MAGNETIC RESONANCE IMAGING STUDIES OF FORCED AND FREE CONVECTIVE HEAT TRANSFER IN PACKED BEDS AND FLUID COLUMNS

by

Matthew Eric Skuntz

A dissertation submitted in partial fulfillment
of the requirements for the degree

of

Doctor of Philosophy

in

Mechanical Engineering

MONTANA STATE UNIVERSITY
Bozeman, Montana

July 2021

©COPYRIGHT

by

Matthew Eric Skuntz

2021

All Rights Reserved

DEDICATION

This dissertation is dedicated to all the family and friends who helped me along the way. I could not have achieved this goal without your love and support. Thank you!

ACKNOWLEDGEMENTS

I would like to acknowledge my wonderful wife Kate. This would never have happened without her love and support.

I would like to acknowledge my chair Ryan Anderson and my committee members Joseph Seymour and Sarah Codd. You three made the lab and department feel like a second home, and your friendship and guidance has been invaluable.

All my lab mates Schamali, Rehab, Dinal, Peng, Madison, Brenden, Jeff and Linn. Thanks for all the laughs, distractions and support!

Finally, the Lab Manager Scott Busse. Your knowledge and expertise were crucial in keeping the spectrometers running.

TABLE OF CONTENTS

1. INTRODUCTION 1

2. CONVECTIVE HEAT TRANSFER 6

The Boundary Layer 6
The Problem of Convection 8
Studying Scaled Systems by Similitude 9
The Conservation Equations 12
Conservation of Mass Equation 12
Conservation of Momentum Equation 13
Conservation of Energy Equation 15
Non-dimensional Conservation Equations 17
Internal Pressure Driven Flow 17
Natural Convection 18
Turbulence 21
Porous Media and Modified Conservation Equations 22
Numerical Simulations 27
Pore-scale Computational Fluid Dynamics 28
Computational and Experimental Studies 32

3. NMR BASICS 35

Introduction to NMR 35
Fourier Transforms 35
Spin Angular Momentum – Quantum Mechanics 38
Vector Model 41
Resonant Excitation 42
Intrinsic Spin Interactions 45
Signal Detection 47
Relaxation and Molecular Interactions 49
Molecular Motions and Spectral Density Functions 51
Pulse Sequences 53
Spin Echo 54
CPMG Train 55
Phase Cycling 56
Signal Averaging 56
Imaging Gradients and $\boldsymbol{k}$-space 57
$\boldsymbol{k}$-space Coverage 59
MRI Resolution 61
Slice Selection and Chemical Selection 62
Imaging Artifacts 64

TABLE OF CONTENTS CONTINUED

The Spectrometer 67

4. ADVANCED NMR TOPICS 71

Molecular Motion and Propagators 72
Motion Sensitized Gradients and Gradient Moments 74
Coherent Motion 78
Incoherent Motion 79
Bloch-Torrey Equation for Diffusion and Flow 80
MRI Velocimetry 82
Imaging the Propagator 83
Velocity Imaging 86
MR Temperature Measurement 86

5. MELT-FRONT PROPOGATION AND VELOCITY PROFILES IN PACKED BEDS OF PHASE-CHANGE MATERIALS MEASURED BY MAGNETIC RESONANCE IMAGING 89

Contribution of Authors and Co-Authors 89
Abstract 91
Introduction 91
Experimental Setup and Methods 93
Results and Discussion 98
Velocity Images of Bead Pack 98
Temperature and the NMR Signal 99
One-Dimensional Profiles 102
Two-Dimensional Images 104
Applications to Heat Transfer 109
Conclusions 112

6. VALIDATION OF DEM-CFD SIMULATION OF PACKED BED HEAT TRANSFER VIA MAGNETIC RESONANCE IMAGING 114

Contribution of Authors and Co-Authors 114
Abstract 116
Introduction 116
Experimental Method 120
MRI Method 124
Hardware and Sequence Details 124
PCM Particle Analysis 127
Simulation Methods 128
DEM Packed Bed Generation 130

TABLE OF CONTENTS CONTINUED

Boundary Conditions and Interfaces....132
Mesh and Time Step....132
Numerical Solvers....134
Numerical Data Processing....135
Results and Discussion....136
Experimental Packed Structure and Velocity Maps....136
Experimental 2D Heat Transfer Results....137
Experimental 1D Intensity Profile Results....139
Experimental Discussion....142
Model Results....144
Model DEM Packed Bed Assessment....144
Model Heat Transfer Results....148
Conclusions....150

7. AXIAL VARIABILITY OF PATTERN FORMATION IN RAYLEIGH-BENARD CONVECTION: MRI VELOCIMENTRY IN A LOW ASPECT RATIO CYLINDER....152

Contribution of Authors and Co-Authors....152
Abstract....154
Introduction....155
Experimental Methods....160
Numerical Method....163
Results....165
Discussion....171
Conclusions....173

8. OBSERVATION OF HEAT TRANSFER DUE TO VARIABLE THERMOPHYSICAL PROPERTIES OF SUB-, NEAR- AND SUPER- CRITICAL FLUIDS IN POROUS MEDIA BY MAGNETIC RESOANCE IMAGING....175

Contribution of Authors and Co-Authors....175
Abstract....177
Introduction....177
Experimental Methods....182
Results and Discussion....184
Conclusions....188

9. MULTI-ECHO T_2 THERMOMETRY OF MICRO-ENCAPSULATED WAX PARTICLES: QUANTITATIVE T_2 MR IMAGING....190

TABLE OF CONTENTS CONTINUED

Contribution of Authors and Co-Authors 190
Introduction 192
Application of T_2 Imaging 193
Temperature Measurement during Phase Change 194
T_2 Imaging Theory 195
Methods 198
Sequences and Hardware 199
Experiment 200
Analysis 202
Results and Discussion 203
Intrinsic T_2 and $CuSO_4$ Concentrations 203
Imaging Timing Parameters and T_2 Observed 204
Melt Process 205
Eicosane Phase Transition as Temperature Indicator 207
Micro-Encapsulated Wax T_2 Images 208
Temperature Maps of Melting PCM 211
Conclusions 213

10. CONCLUSIONS AND RECOMMENDATIONS 214

Recommendations 218

REFERENCES CITED 223

APPENDIX A: High-pressure vessel designed for RBC in SWB 235

Background 236
Design 240
PEEK Cylinder Stress Analysis 242
Thread Stress Analysis 244
Heat Cap Stress Analysis 245
Thermal Effects 246
Pressure Vessel Sealing 246
Flow Loop 247

LIST OF TABLES

Table Page

1. DEM and Experimental Packed Bed Comparison.....146

LIST OF FIGURES

Figure Page

2.1. Boundary Layer 7

2.2. Differential Fluid Elements.....14

2.4. DEM Force Displacement.....30

2.5. PIV/LCT Images.....33

3.1. Fourier Transforms 37

3.2. Energy Levels 41

3.3. Rotating Reference Frame 45

3.4. T_1 and T_2 Relaxation 46

3.5. Electronics Diagram.....48

3.6. Real and Imaginary Spectrum.....50

3.7. Correlation Times 52

3.8. Spin-Echo Pulse Sequence.....54

3.9. CPMG Pulse Diagram.....56

3.10. Phase Helix 59

3.11. Fourier Imaging 61

3.12. Excitation Pulse Shape.....63

4.1. Brownian Particle Displacements.....73

4.2. Average Propagator 74

4.3. PGSE Sequence 75

LIST OF FIGURES CONTINUED

Figure Page

4.4. Effective Gradients 77

4.5. Gradient Moments 79

4.6. PGSE pulse Sequence Diagram 83

4.7. k and q Space Flow Chart 85

5.1. Fluorinert Flow Loop 95

5.2. Fluorinert FC-43 Spectrum 97

5.3. Longitudinal Flow Map 98

5.4. Axial Flow Map 99

5.5. Solid-Liquid 1D Intensity Profiles 101

5.6. 1D Profile Sequences of Melt and Solidification 103

5.7. No Flow Solidification Profile Sequence 104

5.8. Longitudinal Melt Sequence of PCM Bed 106

5.9. Velocity Melt Image Comparison 107

5.10. Axial Melt Sequence of PCMs 108

5.11. Normalized Signal Intensity Data 110

6.1. Experimental Packed Bed 122

6.2. Flow Loop and Inlet Temperatures 123

6.3. PGSE Pulse Sequence and Image Locations 125

39. DSC Data PCM Melt Range 128

6.5. DEM Packed Bed 131

LIST OF FIGURES CONTINUED

Figure Page

6.6. Mesh and Time Step Study 134

6.7. Experimental Velocity Maps 137

6.8. 2D Melt Sequence 138

6.9. Melt Analysis Schematic 140

6.10. 1D Intensity Analysis 141

6.11. 1D Melted Height 142

6.12. Average Melted Height 143

6.13. Simulated and Experimental Packed bed Comparison 145

6.14. Local Porosity and Velocities 147

6.15. Simulation 2D Melt Sequence 149

6.16. Bed Melt and Melted Height Comparison 150

7.1. RBC Flow Patterns 157

7.2. RBC Flow Cell and Set Up 161

7.3. RBC MRI 168

7.4. Numerical RBC Results - Longitudinal 170

7.5. Numerical RBC Results - Transverse 171

8.1. C_2F_6 Thermophysical Properties 181

8.2. PMC Flow Cell 183

8.3. PMC Heat Transfer Images 185

8.4. SteadyState Heat Transfer 187

LIST OF FIGURES CONTINUED

Figure Page

8.5. Transient Heat Transfer 188

9.1. Simple T_2 Sequence 195

9.2. Bruker's MSME Sequence 196

9.3. T_2' vs $T_{2,i}$ 201

9.4. $CuSO_4$ Intrinsic T_2....204

9.5. $CuSO_4$ T_2 Histograms 205

9.6. Intrinsic T_2 of Wax....206

9.7. Intrinsic T_2 vs Temperature....208

9.8. T_2 Maps of Wax 209

9.9. Histograms of Wax T_2....210

9.10. Wax T_2 vs Temperature 211

9.11. Wax Temperature Images....212

A.1. Old Pressure Vessel 237

A.2. Pressure Vessel Detail....239

A.3. Cap Detail 241

A.4. Cylinder Stress Analysis....244

A.5. Heat Transfer Cup Stress Analysis 245

A.7. Heat/Cool loops....248

ABSTRACT

Prediction of fluid flow and associated energy transport is an essential component in many engineering applications where analytical solutions are not possible. In these systems experimentation and numerical simulations are a necessary part of the design process. This work focuses on the experimental study of mass and energy transport in packed beds and pure fluids under forced and natural convection using nuclear magnetic resonance (NMR) imaging (MRI) techniques. It further evaluates the efficacy of commercial computational fluid dynamics (CFD) software to simulate these processes. The study of heat transfer via NMR has proven difficult historically, despite sensitivity of NMR parameters to temperature. Here, a novel experimental setup is pioneered, which enables the study of heat transfer in packed beds. The method employs fluorinated pore-filling fluid and hydrogen-rich core-shell packing particles. Hydrogen and fluorine are NMR-active chemicals that can be imaged with the same experimental equipment by adjusting the resonance frequency; providing means to image the two domains separately. Pore-fluid velocities and particle-wax melting are observed in the same packed bed, at sub-millimeter resolutions, presenting a more complete picture of the conditions in these hard-to-measure systems. In the presented studies, this methodology is demonstrated under forced convection and proven capable in identifying and correlating spatial variations in heat transfer to pore-fluid velocity. The technique is then employed to assess the accuracy of a CFD model in the commercial software package, STAR CCM+, using the melt to quantify energy absorbed by the bed. In natural convection studies of a pure fluid and packed bed in the Rayleigh-Bénard configuration, the axial circulation pattern is found to change with axial position in the long narrow cylinder, a result that is rarely discussed in literature. A CFD model is shown to match well with these experimental findings. In porous media convection with sub-, near- and super-critical fluid, the rapidly changing thermal diffusivity was captured by the rate the particles absorb energy. Finally, a correlation is developed allowing particle-wax T_2 relaxation time to be converted into temperature.

CHAPTER ONE

INTRODUCTION

Presented in this thesis are works applying nuclear magnetic resonance (NMR) imaging (MRI) techniques to study the coupled nature of fluid dynamics and heat transfer. The studies focused on two common template systems: packed beds of spherical particles and Rayleigh-Bénard convection (RBC). The genesis of a packed bed's macroscopic properties on micro-scale interactions has led to recent interest in the prediction of pore-scale conditions and their spatial variations. RBC initiates due to a fluid instability, and the resulting large-scale circulation pattern is therefore inherently sensitivity to small-scale perturbations. In these and many other systems, the small-scale conditions exert controlling influence on the system-scale properties. Spatial resolution of local conditions, as performed in this research, is key for fundamental understanding of large-scale systems.

Packed beds are common in a wide range of industrial applications where mass and energy transport play an important role. In chemical production and emissions mitigation, reactors composed of packed beds of catalyst pellets facilitate reactions to produce desirable products and capture harmful chemicals. Concentrated solar power plants store thermal energy in packed beds of encapsulated salt for on–demand conversion to electricity [1, 2]. In pebble-bed nuclear reactors, a working fluid removes heat from packed beds of nuclear pebbles. In these systems, the local mass and energy transport must remain in a specific range to maintain efficient function and prevent costly overhaul, wasted energy, or dangerous melt-down. Despite the importance of these parameters, the prediction of the local pore-velocity and temperature conditions in specific applications is still poor, requiring expensive pilot-scale systems to test

designs. This barrier to innovation has contributed to the continued use of antiquated systems and prevented the implementation of more efficient designs.

Natural convection is an important mode of heat transfer in the natural world. It moves heat absorbed by the earth into the atmosphere, leading to atmospheric weather. It is the dominant driver of the ocean currents, transporting nutrients from the ocean floor and tempering the earth's temperature. Heat from the earth's solid inner core is transported out by convection in its liquid metal outer core, driving the magnetic field encircling Earth. It is also common in industrial applications. During pasteurization, the fluid is warmed from below and the duration at elevated temperature determines whether bacteria are killed without adverse effect to the product [3]. In monitoring wells natural convection could lead to contamination [4]. In solar heating devices natural convection drives energy transport [5]. RBC is a simple form of natural convection where an enclosed fluid is heated from below and cooled from above, an arrangement which induces an unstable density difference in the fluid. The simplicity of this configuration provides a system in which the fluid flow bifurcation and stability can be studied and insights can be made into the mechanisms driving the aforementioned geophysical [6, 7] and industrial systems.

Acquiring analytical solutions is impossible for many fluid dynamics problems. This is true for both packed beds, due to the complex fluid pathways, and for RBC where sensitivity to perturbation results in non-unique solutions. Since the turn of the 21st century, the proliferation in available computing power has allowed numerical analysis of these systems to flourish [8-12]. It is now possible for simulations to be resolved at the pore-scale in three dimensions (3D) [8, 13]. At the same time, there have been major advancements in imaging methods [14-17]. The most

popular techniques are: particle imaging velocimetry (PIV); particle tracking velocimetry (PTV); laser-Doppler velocimetry (LDV); ultrasound velocimetry (UV); and magnetic resonance imaging (MRI). These advances provide the means for pore-scale prediction of these systems through numerical analysis and the necessary validation through experimental data collection.

Experimental measurements in packed beds and RBC are difficult due to their inaccessibility and sensitivity to perturbation. MRI has the ability to non-invasively image opaque systems with slices positioned in any orientation. This allows non-destructive measurements in sensitive, hard to reach systems [18-22], like packed beds and enclosed cylinders [16, 23-26], inaccessible to other methods. MRI is sensitive to fluid motions over a wide range of length scales, a property that has been exploited to study many porous media systems [16, 27-29].

As the name magnetic resonance implies, MRI is achieved by tuning the spectrometer to the resonant frequency of a specific nuclear species. When more than one chemical species resides in a sample, images can be formed from the different species separately by tuning to their respective resonances. This provides a means of selectively probing different molecular environments or regions of the sample. This is utilized in the present studies of packed beds to image the pore-fluid and the packing structure separately. Here, the two regions are kept chemically distinct by using a fluorinated fluid in the pore-space and hydrogen-rich core-shell particles for the solid structure. The fluid and packing components have resonant frequencies of 282 MHz and 300 MHz, respectively, at 7 Tesla magnet. Tuning to 282 MHz frequency allowed imaging of pore velocities, while tuning to 300 MHz allowed imaging of the particle-core wax structure. Under heating, the wax changed from its solid to liquid state, a transformation easily

identified in MRI. Using chemically distinct pore-fluid and packing material allows the two domains to be imaged separately, without interference [16]. The phase change material (PCM) in the packing provides a means of quantifying the heat transfer in the system, identifying local variations in heat transfer and correlating these variations to local flow conditions. NMR has been successfully employed to study complex porous media systems such as bacterial growth [30], two-phase flow [26], brain structure [31, 32], battery corrosion [33], CO_2 sequestration [34], and chemical production [35], but it has historically been difficult to study heat transfer, the problem of focus in this dissertation.

The work presented here represents an important step forward in the study of packed beds and RBC via MRI. The novel, chemically distinct packed bed arrangement was initially demonstrated for spatially resolved flow-melt correlation, then used to validate a three dimensional (3D) computational fluid dynamics (CFD) model, and finally extended to provide a means for temperature measurement of the wax. Despite MRI's aptitude for studying fluid motions, few studies have focused on RBC [36-38]. In regards to RBC, MRI's ability to provide spatially resolved fluid velocities at many locations and orientations was applied to reveal dependence of circulation pattern with height in long narrow cylinders. Additionally, the packed bed under RBC conditions was imaged, providing a means to observe the variable thermo-physical properties in near-critical fluids. The main challenge for studying RBC via MRI is the ability to control boundary temperatures. This is addressed in Appendix *A*, which details the design of a device which allows precise control over boundary temperature, opening the door for more RBC studies.

An overview of convective heat transfer relevant to the studied systems is presented in Chapter 2. This is followed by an introduction to NMR methods with a discussion on the applied methods in Chapter 3, 4. The chemically-distinct packed bed arrangement is introduced in Chapter 5. In Chapter 6, a CFD simulation created in STAR CCM+ is assessed against the experimental results captured with this technique. In Chapter 7, a study into the dependence of RBC circulation on column height, a feature not mentioned elsewhere, is presented. In Chapters 5 and 6, the local heat transfer is determined qualitatively; in Chapter 8, a method for imaging the temperature of the encapsulated wax is presented. Refinement of this method could provide a means to map both the temperature and velocity fields in the packed bed.

CHAPTER TWO

CONVECTIVE HEAT TRANSFER

Convective energy exchange between a flowing fluid and solid surface is integral to many industrial packed beds and heat exchangers as well as natural phenomena like ocean currents and weather patterns. This mechanism of heat transfer has effects over large length-scales but occurs in a thin layer at the interface with the rate of transfer dependent on local geometry, fluid velocity gradient and temperature difference. There is an enormous body of work covering convective heat transfer. In the following, the works of *Convection in Porous Media* by Nield and Bejan [39], *Introduction to Heat Transfer* by Bergman *et al.* [40], *Fluid Mechanics* by Munson, *et al.* [41], *Viscous Fluid Flow* by White [42], *Transport Phenomena* by Bird *et al.* [43] and *Analysis of Transport Phenomena* by W. Deen [44] are the foundational texts.

The Boundary Layer

The transfer of energy from a flowing fluid to a solid occurs wherever there are velocity and temperature gradients. The rate of this transfer is determined by conditions near the fluid solid interface where intermolecular forces act to reduce the velocity of the fluid. At the surface, it is generally safe to assume there is zero velocity in the fluid, a boundary condition called no-slip. Adjoining fluid layers are inhibited by this stationary fluid, decreasing the fluid velocity some distance into the fluid. This slower moving region is called the velocity boundary layer and extends, by definition, into the fluid until $u = 0.99u_\infty$ where u_∞ is the freestream velocity (see Fig. 2.1) [40]. Velocity gradients and shear forces are high in the boundary layer, and negligible in the freestream flow. The shear forces in this layer act on the solid producing surface drag, an

important parameter for many engineering applications. Knowledge of the velocity gradient at the surface allows the shear force to be calculated as [40],

$$\tau_s = \mu_f \frac{\partial u_f}{\partial y}\Big|_{y=0} \qquad Eq.\ 1$$

The shear shown at the wall is used to define a friction coefficient,

$$C_f \equiv \frac{\tau_s}{\rho u_\infty^2/2} \qquad Eq.\ 2$$

where μ_f is the dynamic viscosity [40].

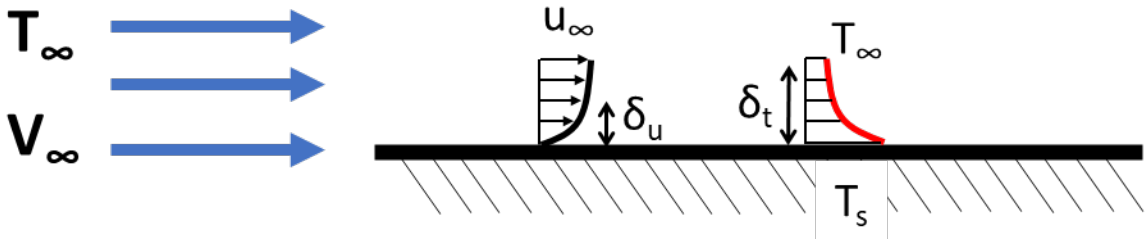


Fig. 2.1. At the interface between a flowing fluid and solid surface velocity and thermal boundary layers develop. The boundary layers are defined to extend into the fluid until the fluid reaches 99% of the freestream velocity or temperature. The surface drag and convective heat transfer depend on the thickness of these layers. In the figure $T_s > T_\infty$.

A similar, thermal boundary layer develops at the fluid/solid interface, extending into the fluid a distance δ_t as shown in Fig. 2.1. This layer arises from the stationary fluid achieving thermal equilibrium with the surface, transferring energy further into the fluid through diffusion (and mixing, in the case of turbulence). Heat transfer from the surface can be described using Fourier's law; as there is no fluid motion, heat is transferred via conduction only. Equating this with Newton's law of cooling, a definition for the heat transfer coefficient h, which has units of $W/(m^2\ K)$, can be found [40],

$$h = \frac{-k_f\ \partial T/\partial y|_{y=0}}{T_s - T_\infty} \qquad Eq.\ 3$$

where k_f is the thermal conductivity of the fluid, and T_s and T_∞ are respectively the temperature of the surface and freestream. The total convective heat transfer rate q into the fluid is [40],

$$q = (T_\infty - T_s) \int h \, dA_s = \bar{h} A_s (T_s - T_\infty) \qquad Eq.\ 4$$

where A_s is the area of the surface and $\bar{h}$ is the average heat transfer coefficient over the surface. The designation of an average heat transfer coefficient $\bar{h}$ is necessary as the local parameter h, depends on the fluid shear, which will change with location on the surface. While fluid shear at the surface will strongly influence heat transfer, the temperature gradient has no effect on the velocity boundary layer, apart from changes to viscosity [40]. This fact suggests seperability of the two governing equations as will be discussed later.

The velocity and thermal boundary layers are of paramount importance in fluid systems as they will control important engineering terms. They will develop wherever a fluid flows over a surface of different temperature. The velocity boundary layer determines the friction coefficient and ensuing pressure loss. Similarly, the thermal boundary layer controls the heat transfer coefficient [40]. Of interest here is the application to heat transfer in packed beds and fluid columns heated from below. The friction coefficient will determine the pressure drop in the packed bed. In RBC, wall drag affects circulation pattern stability. These are important considerations but not the primary focus here. The following discussion will concentrate on h.

The Problem of Convection

The determination of $\bar{h}$ or h is central to the analysis of convective heat transfer. However, this is not easy and is often referred to as *the problem of convection*. The difficulty in finding h stems from its dependence on fluid properties, surface geometry and fluid shear. For example, the thickness of both velocity and thermal boundary layers will increase with distance

from the leading edge (though they rarely grow at the same rate). It then follows that the friction coefficient and heat transfer coefficient change with location on the plate as well. Finding h requires deriving the velocity vector field, which is analytically possible only for simple cases such as laminar flow over a flat plate or around a sphere. For the majority of real-world instances, like packed beds, this is not possible. In order to provide a means to predict heat transfer in geometries that do not have analytical solutions, empirical correlations or numerical solutions are required. Empirical correlations for $\bar{h}$ exist for many common flow configurations such as pipe flow, open channel flow, natural convection, and packed beds. In the case of packed beds, the accuracy of the predictions is highly variable and the correlations of different researchers often do not agree [45]. Packed bed correlations for $\bar{h}$ describe the macro-scale, volume-averaged heat transfer, experimentally determined by measuring inlet and outlet temperatures. These average $\bar{h}$ values provide no information on the spatial variations in heat transfer which have important engineering consequences. For instance, in catalytic reactors, reaction rate is often dependent on temperature e.g. Haber-Bosch process, and can be either endothermic or exothermic. Spatial variations in flow speed and temperature can reduce reaction efficiency or lead to runaway reactions [46]. In thermal energy storage, areas of low flow lead to decreased heat transfer, lowering recharge/discharge efficiencies.

Studying Scaled Systems by Similitude

When studying convective heat transfer, it is often necessary to model the system on a different scale than it is applied. For packed beds, this can mean smaller volumes, different sized particles, lower temperatures or different fluids. When the scale is changed, it is necessary to use

similarity variables to equate the relevant parameters. In forced convection the Reynolds number Re is of paramount importance [41],

$$Re = \frac{\rho V_s L}{\mu} \qquad Eq.\ 5$$

where ρ is the fluid density, V_s the superficial velocity, L relevant length scale and μ is the dynamic viscosity. Re relates the relative strength of the inertial and viscous forces which determines whether the flow will be laminar or turbulent. At low *Re* the flow is laminar as viscous forces can dampen out inertial tumbling. At high *Re* the flow is turbulent, as inertial forces overcome viscous dampening [40]. In porous media *Re* is modified by the porosity φ as,

$$Re_p = \frac{\rho V_s L}{\mu(1-\varphi)} \quad Eq.\ 6$$

The relevant length-scale L dependes on the system of interest. In pipe flow it is the pipe diameter, while in porous media it can be the hydraulic diameter, particle diameter, or pore-size.

When concerned with energy transport in the fluid system, the dimensionless numbers of interest are the Prandtl Pr and Nusselt Nu numbers. Pr is the ratio of momentum diffusivity to thermal diffusivity given as [40],

$$Pr = \frac{\nu}{\alpha} = \frac{c_p \mu}{k} \quad Eq.\ 7$$

where the momentum diffusivity is $\nu = \mu/\rho$, the thermal diffusivity is $\alpha = k/(\rho c_p)$, c_p is the specific heat, and k is the thermal conductivity. Unlike Re, Pr does not contain a length scale and is only dependent on fluid state properties. It is therefore a constant for a given fluid state. The Nusselt number, also known as the dimensionless heat transfer coefficient, is the ratio of convective to conductive heat transfer [40],

$$Nu = \frac{\bar{h}L}{k} \propto \left.\frac{\partial T'}{\partial y'}\right|_{y'=0} \qquad Eq.\ 8$$

where L is the relevant length scale, T' is the dimensionless temperature and y' is the dimensionless distance from the surface. The Nusselt number is therefore the dimensionless temperature gradient at the surface and can be used to calculate $\bar{h}$ or to equate heat transfer rates between different systems. It is therefore of primary concern in packed bed and natural convection studies on heat transfer. The coupled nature of velocity and thermal boundary layers imply that heat transfer is dependent on the flow field. For internal open-tube flow, Nu is constant in the fully developed region, independent of Re or Pr, depending only on the boundary conditions. It can be derived as $Nu = 4.36$ and 3.66 for constant heat flux and constant surface temperature, respectively. The relationship is more complicated for other flow configurations and must be empirically derived as $Nu = f(Re, Pr)$. For instance, Handley and Heggs found the correlation $Nu = \frac{0.255}{\varphi} Pr^{1/3} Re^{2/3}$ for packed beds at $Re > 100$ and $d_t/d_p > 8$. In packed beds at low Re there is a wide range in estimates for Nu [47]. For an asymptotic value as $Re \rightarrow 0$, these range from $Nu = 0.1$ to 12.4 based on mass transfer work of Wakao *et al.* [48] and measurements by Miyauchi *et al.* [49], respectively. For natural convection in enclosures the correlation is dependent on the shape, aspect ratio and Ra. A large number of correlations have been proposed, with an example by Catton [50] in Eq. 9,

$$\overline{Nu} = 0.22 \left(\frac{Pr}{0.2+Pr} Ra \right)^{0.28} \left(\frac{H}{L} \right)^{-0.25} \qquad \textit{Eq. 9}$$

This applies to,

$$\begin{bmatrix} 1 \leq \frac{H}{L} \leq 10 \\ Pr \leq 10^5 \\ 10^3 \leq Ra \leq 10^{10} \end{bmatrix} \qquad \textit{Eq. 10}$$

where H is the enclosure height and L its width. For larger aspect ratios, MacGregor and Emery suggest [51],

$$\overline{Nu} = 0.42Ra^{1/4}Pr^{0.012}\left(\frac{H}{L}\right)^{-0.3} \qquad Eq.\ 11$$

for,

$$\begin{bmatrix} 10 \leq \frac{H}{L} \leq 40 \\ 1 \leq Pr \leq 2x10^4 \\ 10^4 \leq Ra \leq 10^7 \end{bmatrix} \qquad Eq.\ 12$$

These examples emphasize the variability in Nu correlations dependent on the specific geometry and flow conditions, and the difficulty in selecting the appropriate correlation for a specific application.

The Conservation Equations

To understand the importance of these dimensionless numbers, it is necessary to review the conservation equations which govern fluid dynamics along with their modifications for packed beds. The conservation equations are determined through consideration of basic principles. At all points in the flow, mass and energy must be conserved and Newton's second law of motion must be satisfied. By applying these laws to differential volumes, equations for conservation of mass, momentum and energy can be derived.

Conservation of Mass Equation

The conservation of mass may be mathematically represented as [43],

$$\frac{\partial \rho}{\partial t} = -\boldsymbol{\nabla} \cdot \rho \boldsymbol{V} \qquad Eq.\ 13$$

which states that the change in system mass must be equal to the mass flux leaving the system. Mass is therefore neither created nor destroyed. This statement is true for unsteady or steady flow and for compressible or incompressible fluids. The simplification for steady flow of an incompressible fluid yields [43],

$$\boldsymbol{\nabla \cdot V} = \frac{\partial \boldsymbol{u}}{\partial x} + \frac{\partial \boldsymbol{v}}{\partial y} + \frac{\partial \boldsymbol{w}}{\partial z} = 0 \qquad \textit{Eq. 14}$$

Conservation of Momentum Equation

In order to derive the conservation of linear momentum equation, it is convenient to start with Newton's second law applied to a differential volume, $\delta \boldsymbol{F} = \delta m \boldsymbol{a}$, which states that the change in force is equal to the change in the product of mass and acceleration. The relevant forces which must be considered are surface and body forces, with surface forces acting on the element face and body forces being distributed throughout the element volume. Here gravity is the only body force [41],

$$\delta \boldsymbol{F}_b = \delta m \boldsymbol{g} \qquad \textit{Eq. 15}$$

which can be broken into its vector components,

$$\begin{bmatrix} \delta \boldsymbol{F}_{bx} = \delta m \boldsymbol{g_x} \\ \delta \boldsymbol{F}_{by} = \delta m \boldsymbol{g_y} \\ \delta \boldsymbol{F}_{bz} = \delta m \boldsymbol{g_z} \end{bmatrix} \qquad \textit{Eq. 16}$$

The surface forces $\delta \boldsymbol{F}_s$ can be broken into three components as shown in Fig. 2.2: $\delta \boldsymbol{F}_n$, $\delta \boldsymbol{F}_1$, $\delta \boldsymbol{F}_2$. These forces act over a differential area, allowing normal and shear stresses to be defined and resultant surface forces to be expressed, for the *x* direction, as [41],

$$\delta \boldsymbol{F_{sx}} = \left(\frac{\partial \boldsymbol{\sigma_{xx}}}{\partial x} + \frac{\partial \boldsymbol{\tau_{xy}}}{\partial y} + \frac{\partial \boldsymbol{\tau_{xz}}}{\partial z} \right) \delta x \, \delta y \, \delta z \qquad \textit{Eq. 17}$$

These equations can be combined with Eq. 16 to yield the equations of motion shown here for the *x* direction with *y* and *z* similar [41],

$$\rho \boldsymbol{g}_x + \frac{\partial \boldsymbol{\sigma_{xx}}}{\partial x} + \frac{\partial \boldsymbol{\tau_{xy}}}{\partial y} + \frac{\partial \boldsymbol{\tau_{xz}}}{\partial z} = \rho \left(\frac{\partial \boldsymbol{u}}{\partial t} + \boldsymbol{u} \frac{\partial \boldsymbol{u}}{\partial x} + \boldsymbol{v} \frac{\partial \boldsymbol{u}}{\partial y} + \boldsymbol{w} \frac{\partial \boldsymbol{u}}{\partial z} \right) \qquad \textit{Eq. 18}$$

These equations describe the general motions of any incompressible liquid continuum.

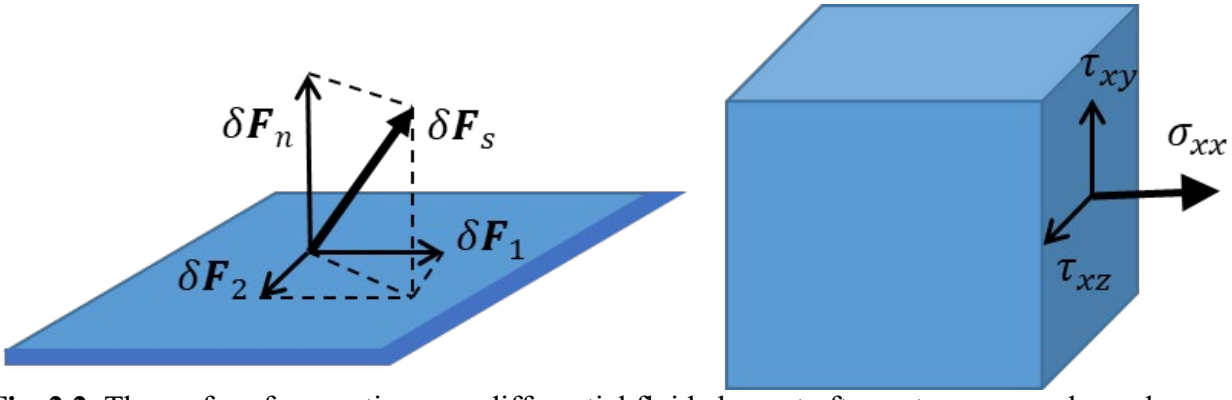


Fig. 2.2. The surface force acting on a differential fluid element often acts on an angle, and can be resolved into a normal force, $\mathbf{F}_1$ and $\mathbf{F}_2$ mutually perpendicular forces. These forces act over a differential area, resulting in stresses.

Solving this equation is difficult or impossible in most cases. For this reason, the equations are generally simplified to some degree. Euler derived one of the most well-known simplified forms by assuming shear stresses are negligible. This is a good assumption when *Re* > 1 [41]. Flows with negligible shear stresses are known as inviscid or frictionless flows. Under this condition, the normal stresses are independent of direction, allowing pressure to be defined as the negative of the normal stresses, $-p = \sigma_{xx} = \sigma_{yy} = \sigma_{zz}$, so that positive pressure is compressive. These simplifications result in Euler's equations of motion, shown here in vector notation [41],

$$\rho \boldsymbol{g} - \boldsymbol{\nabla} p = \rho \left[\frac{\partial \boldsymbol{V}}{\partial t} + (\boldsymbol{V} \cdot \boldsymbol{\nabla}) \boldsymbol{V} \right] \quad \textit{Eq. 19}$$

Euler's equations remain nonlinear partial differential equations, which are not agreeable to general analytical solutions. The nonlinearity results from the $(\mathbf{V} \cdot \boldsymbol{\nabla})\boldsymbol{V}$ term which can be expanded by its identity as [41],

$$(\boldsymbol{V} \cdot \boldsymbol{\nabla})\boldsymbol{V} = \frac{1}{2}\boldsymbol{\nabla}(\boldsymbol{V} \cdot \boldsymbol{V}) - \boldsymbol{V} \times (\boldsymbol{\nabla} \times \boldsymbol{V}) \quad \textit{Eq. 20}$$

Bernoulli developed a solution by applying the use of streamlines, along which $[\boldsymbol{V} \times (\boldsymbol{\nabla} \times \boldsymbol{V})] \cdot d\boldsymbol{s} = 0$, resulting in [41],

$$\frac{p_1}{\gamma} + \frac{\boldsymbol{V_1^2}}{2\boldsymbol{g}} + z_1 = \frac{p_2}{\gamma} + \frac{\boldsymbol{V_2^2}}{2\boldsymbol{g}} + z_2 \qquad \textit{Eq. 21}$$

Subscripts 1 and 2 refer to any two points along a streamline. Additionally, $\boldsymbol{\nabla \times V}$ is known as the flow vorticity. This implies that the Bernoulli equation can be applied to any two points in an irrotational flow, where the vorticity is equal to zero.

In flows involving real fluids, neglecting trivial cases such as free, uniform flow far from any obstruction, there are areas where shear forces are negligible and areas where shear forces are large, that is to say there are regions of both inviscid and viscous flow. The entrance region in pipe flow is one such example. The shear forces are initially negligible for the entire fluid domain but become dominate once flow is fully developed. Viscous flow is synonymous with the incompressible Navier-Stokes equation [42],

$$\rho\left(\frac{\partial \boldsymbol{V}}{\partial t} + \boldsymbol{V} \cdot \boldsymbol{\nabla V}\right) = -\boldsymbol{\nabla} p + \rho \boldsymbol{g} + \mu \boldsymbol{\nabla^2 V} \qquad \textit{Eq. 22}$$

They can be derived by applying relationships between stresses and velocities [41],

$$\boldsymbol{\sigma_{xx}} = -p + 2\mu\frac{\partial \boldsymbol{u}}{\partial x}, \quad \boldsymbol{\sigma_{yy}} = -p + 2\mu\frac{\partial \boldsymbol{v}}{\partial y}, \quad \boldsymbol{\sigma_{zz}} = -p + 2\mu\frac{\partial \boldsymbol{w}}{\partial z'} \qquad \textit{Eq. 23}$$

$$\boldsymbol{\tau_{xy}} = \mu\left(\frac{\partial \boldsymbol{u}}{\partial y} + \frac{\partial \boldsymbol{v}}{\partial x}\right), \quad \boldsymbol{\tau_{yz}} = \mu\left(\frac{\partial \boldsymbol{v}}{\partial z} + \frac{\partial \boldsymbol{w}}{\partial y}\right), \quad \boldsymbol{\tau_{zx}} = \mu\left(\frac{\partial \boldsymbol{w}}{\partial x} + \frac{\partial \boldsymbol{u}}{\partial z}\right) \qquad \textit{Eq. 24}$$

These can then be combined with the equations of general fluid motions to yield the Navier-Stokes equations. These equations are considered the general governing equations of motion for incompressible, Newtonian fluids. They are second-order, nonlinear equations that have only been solved for a few specific cases.

Conservation of Energy Equation

The energy equation can be computed by applying the first law of thermodynamics that states, the energy change in the system is equal to the sum of the work and energy added to the system, $dE = dQ + dW$. In a moving fluid the energy will depend on the internal, kinetic and

potential energy per unit volume. The rate of increasing energy (kinetic and internal) is equal to the net rate supplied via convection, conduction, and rate of work though stresses and external forces. Kinetic energy is determined by the work necessary to accelerate the object in motion from rest to its current velocity. It can be shown to equal $\frac{1}{2}\rho v^2$ for a non-rotating body. The internal energy U is determined by its thermodynamic state containing contributions from rotational and vibrational energies [44]. A general form of the energy equation is [42],

$$\rho \frac{Dh}{Dt} = \frac{Dp}{Dt} + \boldsymbol{\nabla} \cdot \boldsymbol{q} + \boldsymbol{\Phi} \qquad \textit{Eq. 25}$$

where h is enthalpy, p is the pressure, $\boldsymbol{q}$ is heat transfer and $\boldsymbol{\Phi}$ is the thermal dissipation. As temperature is often the parameter of interest, it is often useful to rewrite this in a form with temperature [42],

$$\rho c_p \left(\frac{\partial T}{\partial t} + \boldsymbol{v} \cdot \boldsymbol{\nabla} T\right) = \boldsymbol{\nabla} \cdot (k\, \boldsymbol{\nabla} T) + \beta T \frac{Dp}{Dt} + \boldsymbol{\Phi} \qquad \textit{Eq. 26}$$

where the terms on the left side represent the change in energy with time and the convective heat flux. On the right side, there is the conductive heat flux term, a compressibility term which relates the work required to compress the fluid and a viscous dissipation term relating the rate of conversion of kinetic energy to heat. In the case of incompressible constant viscosity Newtonian fluids, Eq. 26 can be simplified as [42],

$$\frac{\partial T}{\partial t} + \boldsymbol{v} \cdot \boldsymbol{\nabla} T = -\alpha \boldsymbol{\nabla}^2 T \qquad \textit{Eq. 27}$$

where the material derivative had been expanded into the change in temperature with time, convective energy flux terms. The energy conduction term is on the right side with $\alpha = k/\rho c_p$. The viscous dissipation term may also be added to the right, which is described by,

$$\boldsymbol{\Phi} = \mu \left[2\left(\frac{\partial \boldsymbol{u}}{\partial x}\right)^2 + 2\left(\frac{\partial \boldsymbol{v}}{\partial y}\right)^2 + 2\left(\frac{\partial \boldsymbol{w}}{\partial z}\right)^2 + \left(\frac{\partial \boldsymbol{v}}{\partial x} + \frac{\partial \boldsymbol{u}}{\partial y}\right)^2 + \left(\frac{\partial \boldsymbol{w}}{\partial y} + \frac{\partial \boldsymbol{v}}{\partial z}\right)^2 + \left(\frac{\partial \boldsymbol{u}}{\partial z} + \frac{\partial \boldsymbol{w}}{\partial x}\right)^2\right] + \lambda \left(\frac{\partial \boldsymbol{u}}{\partial x} + \frac{\partial \boldsymbol{v}}{\partial y} + \frac{\partial \boldsymbol{w}}{\partial z}\right)^2$$

Eq. 28

Thermal dissipation is significant in high-velocity flows, highly viscous flows and in microchannels.

Non-dimensional Conservation Equations

It is generally more useful to report these equations in their dimensionless forms, achieved through similarity variables, to allow for more general application to similar systems. Assuming steady state, the similarity variables are [40],

$$x_i' \equiv \frac{x_i}{L} \qquad \textit{Eq. 29}$$

$$\boldsymbol{u_i'} \equiv \frac{\boldsymbol{u_i}}{\boldsymbol{V}} \qquad \textit{Eq. 30}$$

$$T' \equiv \frac{T - T_s}{T_\infty - T_s} \qquad \textit{Eq. 31}$$

where L is a characteristic length, V is the velocity in the free stream T_s and T_∞ are the surface and free stream temperatures, respectively. Assuming steady flow, the resulting conservation equations in two dimensions are [40],

$$\boldsymbol{u'}\frac{\partial \boldsymbol{u'}}{\partial x'} + \boldsymbol{v'}\frac{\partial \boldsymbol{v'}}{\partial y'} = -\frac{dp'}{dx'} + \frac{1}{Re}\frac{\partial^2 \boldsymbol{u'}}{\partial y'^2} \qquad \textit{Eq. 32}$$

$$\boldsymbol{u'}\frac{\partial T'}{\partial x'} + \boldsymbol{v}^*\frac{\partial T'}{\partial y'} = \frac{1}{RePr}\frac{\partial^2 T'}{\partial x'^2} \qquad \textit{Eq. 33}$$

The importance of these equations is to show that the fluid momentum and energy transport are completely dependent on Re and Pr. Therefore, by matching these values, systems can be modelled at different scales. Additionally, the equations are coupled by the Reynolds number.

Internal Pressure Driven Flow

Internal pressure driven flow is commonly used in industrial application to enhance heat transfer. Common examples include regenerative-steam energy cycles and HVAC systems. Under internal flow, the boundary layer will expand into the entire region, once fully developed.

Under laminar flow conditions, this results in a parabolic flow profile, dominated by viscous forces [40]. The same conservation equations apply but the relevant length scale is different: pipe diameter for pipe flow, particle diameter for a packed bed, pore diameter for other porous media. When calculating *Re* for internal pipe flow, the average or superficial velocity is used and it is often convenient to use the mass flow rate $\dot{m}$ as [40],

$$Re = \frac{4\dot{m}}{\pi D \mu} \qquad Eq.\ 34$$

where the relevant length scale L has been replaced with diameter D. It should also be noted that once the flow is fully developed, the Nusselt number, and therefore heat transfer, is not a function of position in the pipe but solely temperature difference between the wall and fluid. This leads to the convenient method for calculating total heat transfer through a pipe wall as [40],

$$\boldsymbol{q} = \dot{m} c_p \left(T_{m,o} - T_{m,i}\right) \quad Eq.\ 35$$

where $T_{m,i}$ is the inlet fluid inlet temperature and $T_{m,o}$ is the fluid outlet temperature. This equation is based off an energy balance around the fluid, making it universally applicable irrespective of the nature of the wall surface or tube flow conditions [40]. Under forced convection, the solution to the momentum equation is independent of the energy solution, assuming small changes in viscosity and density. This allows the velocity and temperature fields to be computed sequentially, without iteration.

Natural Convection

In natural, or free convection, fluid motions are driven by fluid density differences. This type of motion is the driving force for many natural fluid motions including atmospheric weather, ocean currents and motion in the earth's mantle, occurring on length scales both small

and large [3-7]. These free convection motions are of great importance and understanding them is of scientific interest. Due to the large scales on which it occurs, it is necessary to study the fundamental mechanisms on a small scale. Rayleigh-Bénard convection (RBC) is one arrangement often employed for this purpose. In RBC, a fluid instability is induced, where density increases with height and convection begins when a critical value is reached. This is normally achieved by uniformly heating the bottom boundary and cooling the top surface. Side walls can be either adiabatic or perfectly conducting. Of notable importance in the study of RBC and other free convection is the dependence of the velocity field on temperature gradients. This imposes additional complexity into solutions as the momentum and energy equations are coupled.

Analytical solutions for RBC flows require linearization of the conservation equations. This was first attempted by Lord Rayleigh in 1916 [52], and refined by Jefferys (1926), Pellew and Southwell (1940) and summarized by Chandrasekhar in 1961 [53]. The linear analysis of RBC is based on the conservation equations for mass, momentum and energy as well as the equation of state for the fluid. The mass conservation equation is [53],

$$\frac{\partial \rho}{\partial t} + \boldsymbol{\nabla} \cdot (\rho \boldsymbol{V}) = 0 \qquad \textit{Eq. 36}$$

The Navier-Stokes equation is used for momentum conservation [53],

$$\rho \frac{d\boldsymbol{V}}{dt} = -\boldsymbol{\nabla} p + \rho \boldsymbol{g} + \mu \boldsymbol{\nabla}^2 \boldsymbol{V} \qquad \textit{Eq. 37}$$

The energy equation for thermal conduction is used, neglecting thermal dissipation from viscosity [53],

$$\frac{dT}{dt} = \alpha \boldsymbol{\nabla}^2 T \qquad \textit{Eq. 38}$$

Finally the equation of state for the fluid is,

$$\rho = \rho_o(1 + \beta\Delta T) \qquad Eq.\ 39$$

where the volume expansion coefficient is $\beta = 1/\rho_o \ \partial\rho/\partial T$. The Oberbeck-Boussinesqu approximation is applied, whereby fluid density is assumed constant in all but the vertical direction where it provides the driving force. The implications of this approximation have been considered and proven valid for small temperature differences [54-56].

It is now necessary to use perturbation equations to consider the response of a fluid to a small disturbance of its stationary state, as described by [53],

$$\boldsymbol{V} = 0, \ \frac{d^2T}{dz^2} = 0, \ \frac{dp}{dz} = \rho_o \boldsymbol{g}[1 - \beta(T(z) - T_o)] \qquad Eq.\ 40$$

Perturbation analysis allows Eqs. 37-39to be linearized, as any velocity which develops from the small perturbation will be so small that the square of the velocity, product of velocity components, or product of velocity and temperature can be neglected. The continuity equations can be made non-dimensional with [53],

$$x_i' = x_i/d, \quad t' = \alpha t/d^2, \ \ \boldsymbol{V'} = d\boldsymbol{V}/\alpha, \ \ T' = \beta \boldsymbol{g} d^3 T/\nu\alpha, \ \ p' = pd^2/\rho_o\alpha^2 \quad Eq.\ 41$$

where d is the depth of the fluid and θ an infinitesimal temperature deviation. The convection equations then become [53],

$$\boldsymbol{\nabla} \cdot \boldsymbol{V'} = 0 \qquad Eq.\ 42$$

$$\frac{\partial \boldsymbol{V'}}{\partial t'} = -\boldsymbol{\nabla} p' + PrT'\boldsymbol{e_z} + Pr\boldsymbol{\nabla^2 V'} \qquad Eq.\ 43$$

$$\frac{\partial T'}{\partial t'} = \boldsymbol{\nabla^2} T' + Ra\, \boldsymbol{w} \qquad Eq.\ 44$$

where $\boldsymbol{w}$ is the vertical velocity component and $\boldsymbol{e_z}$ is the vertical unit vector. The Rayleigh Ra and Prandtl Pr numbers are [53],

$$Ra = \frac{\beta \boldsymbol{g} \Delta T d^3}{\nu\alpha}, \quad Pr = \frac{\nu}{\alpha} \qquad Eq.\ 45$$

where ΔT is the vertical temperature difference across the fluid layer. These equations, Eqs. 42-44, can be used to eliminate the horizontal velocity components, pressure and temperature, resulting in an equation for the vertical component only [53],

$$\left[\frac{\partial}{\partial t'} - \boldsymbol{\nabla}^2\right]\left[\frac{1}{Pr}\frac{\partial}{\partial t'} - \boldsymbol{\nabla}^2\right]\boldsymbol{\nabla}^2\boldsymbol{w} = Ra\boldsymbol{\nabla}_2^2 \quad \textit{Eq. 46}$$

where $\boldsymbol{\nabla}_2^2$ is the two-dimensional Laplace operator. Further consideration of the boundary conditions, the ansatz $\boldsymbol{w} = W_o W(z) e^{i(k_x x + k_y y)} e^{st}$, and the use of the membrane equation as detailed in [53] yields the result [53],

$$\left(\left(\frac{d}{dz}\right)^2 - a^2\right)^3 \boldsymbol{w} = -a^2 Ra\, \boldsymbol{w} \qquad \textit{Eq. 47}$$

In RBC the flow patterns corresponding to the eigenvalue solutions for the wave number a, are entirely dependent on the Rayleigh number.

Many works have been published on stability analysis of RBC flows solving for the critical *Ra* and stable convection patterns in various container shapes and aspect ratios. Charles and Sani investigated axisymmetric convection patterns in various aspect ratio containers [57-59]. Their works were used to predict the expected flow patterns in Chapter 7. Concentric rolls were investigated by Koschmieder and Pallas [53, 60]. Chen and Whitehead used small perturbations to study RBC of arbitrary wave-numbers [61]. In Chapter 8, RBC of a near critical fluid is investigated, a topic that has seen recent interest [62-65].

Turbulence

Absent from this discussion are the effects of and transition to turbulence. Turbulence occurs when the inertial forces dominate the viscous forces leading to the development of eddies and whorls. The transition to and degree of turbulence is characterized by the Reynolds number,

which is the ratio of inertial to viscous forces. At high *Re*, viscous forces are unable to dampen the inertial forces. Small perturbations develop non-linearly, resulting in a chaotic flow with random eddies and vortices [40]. These stochastic fluid motions compress the boundary layer, resulting in a larger velocity and temperature gradient near the wall. These boundary layer effects cause greater shear and heat transfer to occur at the surface [40]. The unsteady nature of turbulence logically lends itself to statistical descriptions where properties are based on time-averages. Turbulence is of great importance in many fields but is beyond the scope of this research and is neglected in this discussion.

Porous Media and Modified Conservation Equations

Porous media is a broad term for a two-phase system composed of a rigid matrix filled with a fluid. The matrix forms a network of interconnected pores through which the fluid can flow. Some examples are the catalytic bed, filters, lungs, coffee grounds, bread, sponges, wood, soil and sandstone. Beds of spherical particles are common in research due to the ease they can be recreated. Porous media are characterized by the volume fraction composed of void space, called porosity, defined as [39],

$$\varphi = \frac{V_V}{V_T} \qquad \textit{Eq. 48}$$

where V_V is the void volume and V_T is the total volume. The volume of the solid is then $V_s = (1-\varphi)V_T$. The porosity of natural media does not exceed 0.6 [39]. More relevant to here is the porosity of a packed bed of uniform spheres, which range from 0.26 to 0.48 representing rhombohedral and cubic packing, respectively. Variation in particle size generally leads to denser packing [39].

Porous media is (often) composed of a random distribution of pore sizes and shapes interconnected by 'throats' of differing size and orientation. Fortunately, these pore scale irregularities are typically smoothed when observed on a larger scale. This naturally leads to volume-averaged properties that vary regularly with time and space, allowing theoretical analysis [39]. The approach to these volume-averaged problems is therefore dependent on the scale of interest. Conventional fluid mechanics can be applied at small scales, on the order of a couple of pores. The multitude of flow paths available at larger scales, *i.e.* more pores, is resolved by assigning volume-averaged properties such as permeability and conductivity, which include contributions from all phases. The factors of greatest interest to engineers occur at the intermediate scale between those described above, as this is where flow can be optimized on the element basis to provide greater efficiency in the assembled structure [39].

The standard approaches to this problem begin with the normal conservation equations described above and are macroscopic equations obtained by averaging over a volume. Averaging can be done either spatially using a representative element volume (REV) [66] or statistically over an ensemble of possible pore sizes [67, 68]. Taking the spatial averaging approach, a velocity averaged over a REV V_m is denoted as $\langle \boldsymbol{v} \rangle = (\boldsymbol{u}, \boldsymbol{v}, \boldsymbol{w})$. The size of V_m is such that average values do not depend on the specific volume element. The intrinsic average fluid velocity $\boldsymbol{V}$ is then related to $\langle \boldsymbol{v} \rangle$ by $\langle \boldsymbol{v} \rangle = \varphi \boldsymbol{V}$. Based on this continuum value, the volume averaged conservation of mass equation is [39],

$$\varphi \frac{\partial \rho_f}{\partial t} + \boldsymbol{\nabla} \cdot \left(\rho_f \langle \boldsymbol{v} \rangle \right) = 0 \qquad \textit{Eq. 49}$$

The volume-average Naiver-Stokes equation is [69],

$$\rho_f \left[\frac{\partial \langle v \rangle}{\partial t} + \boldsymbol{\nabla} \cdot \left(\frac{\langle \boldsymbol{v} \rangle \cdot \langle \boldsymbol{v} \rangle}{\varphi} \right) \right] = -\boldsymbol{\nabla} P + \mu_f \boldsymbol{\nabla}^2 \langle \boldsymbol{v} \rangle + \boldsymbol{F} \quad \textit{Eq. 50}$$

where $\langle \boldsymbol{v} \rangle$ is the volume-averaged velocity, and $\boldsymbol{F}$ is the body forces.

For seepage flow many other simpler momentum equations have seen greater application, starting with Darcy's Law which is applicable to consolidated porous media. Henry Darcy derived this description in 1856, shown here generalized to three dimensions [39],

$$\langle \boldsymbol{v} \rangle = -\frac{K}{\mu} \cdot \boldsymbol{\nabla} P \qquad \textit{Eq. 51}$$

where K is the specific permeability of the medium, dependent on the geometry with unit length squared [m^2]. This equation, known as Darcy's law, has been validated by many experiments and theoretically via deterministic techniques and statistical models. Darcy's law is accurate for creep flow, when *Re* is equal to unity or smaller.

The momentum equation must be formulated differently for application to packed beds above the seepage velocity (*Re* < 1). As the flow velocity increases, Darcy's law breaks down due to form drag, which has a quadratic relation with velocity, reaching the magnitude of surface drag, which is dominant in seepage flow [39]. The transition to non-linear drag occurs smoothly as *Re* increases from 1 to 10, moving from the Darcy regime to the Forchheimer regime. There are various extensions to Darcy's law made in an attempt to account for acceleration and inertial forces (which cause form drag). The validity and accuracy of these extensions has been the topic of much debate. The solution form suggested by Nied and Bejan [39] is known as the Dupiut-Forchheimer equation [39],

$$\boldsymbol{\nabla} P = -\frac{\mu}{K} \langle \boldsymbol{v} \rangle - c_F K^{-1/2} \rho_f \langle \boldsymbol{v} \rangle^{\mathbf{2}} \qquad \textit{Eq. 52}$$

where c_F is a dimensionless drag coefficient and, in the case of packed beds, K can be estimated using the Carman-Kozeny equation,

$$K = \frac{D_{p2}^2 \varphi^3}{180(1-\varphi)^2} \qquad \textit{Eq. 53}$$

where D_p is the effective particle diameter, defined as,

$$D_{p2} = \int_0^\infty D_p^3 h(D_p)\, dD_p \Big/ \int_0^\infty D_p^2 h(D_p)\, dD_p \qquad \textit{Eq. 54}$$

where $h(D_p)$ is the density function for the distribution of diameters D_p. A specific form of this is the Ergun equation, which is commonly used for packed beds of spheres [39],

$$\boldsymbol{\nabla} P = -150 \frac{\mu(1-\varphi)^2}{d_p^2 \varphi^3} \langle \boldsymbol{v} \rangle - 1.75 \frac{\rho_f (1-\varphi)}{d_p \varphi^3} \langle \boldsymbol{v} \rangle^2 \qquad \textit{Eq. 55}$$

It is a special form of the Irmay equation and is valid only for unidirectional flow.

The accuracy of the many forms of the volume-averaged momentum equation is dependent on the geometry of the packed bed being similar to that used to derive the empirical correlation, including tube-to-particle-diameter ratio, porosity and particle shape. Delineation in similarity is accounted for in some part by further empirical variables *e.g.* drag coefficient and permeability. These adjustments can provide good prediction at the cost of in-depth experimentation.

The description for the energy equation is also dependent on the form and properties of the composite medium. Relative thermal conductivities of the fluid and solid, pressure and viscous dissipation effects and thermal dispersion must be accounted for. In the simplest case, an energy balance can be composed for the fluid and solid phases with the assumption of isotropic medium, negligible work from pressure change and viscous dissipation, local thermal equilibrium of the solid and fluid phases, and that the conduction in the two phases proceeds in parallel. The energy equation for each domain is then [39],

$$(1-\varphi)(\rho c)_s \frac{\partial T_s}{\partial t} = (1-\varphi)\boldsymbol{\nabla} \cdot (k_s \boldsymbol{\nabla} T_s) + (1-\varphi) \boldsymbol{q}_s''' \qquad \textit{Eq. 56}$$

$$\varphi \left(\rho c_p\right)_f \frac{\partial T_f}{\partial t} + \left(\rho c_p\right)_f \langle \boldsymbol{v} \rangle \cdot \boldsymbol{\nabla} T_f = \varphi \boldsymbol{\nabla} \cdot \left(k_f \boldsymbol{\nabla} T_f\right) + \varphi \boldsymbol{q}_f''' \qquad \textit{Eq. 57}$$

where the subscripts *s* and *f* represent solid and fluid respectively and $\boldsymbol{q}'''$ is the heat production per unit volume. Setting $T_s = T_f = T$ and summing the two equations yields the single equation model [39],

$$(\rho c)_m \frac{\partial T}{\partial t} + (\rho c)_m \langle \boldsymbol{v} \rangle \cdot \boldsymbol{\nabla} T = \boldsymbol{\nabla} \cdot (k_m \boldsymbol{\nabla} T) + \boldsymbol{q}'''_m \qquad \textit{Eq. 58}$$

where

$$(\rho c)_m = (1-\varphi)(\rho c)_s + \varphi\left(\rho c_p\right)_f \qquad \textit{Eq. 59}$$

$$k_m = (1-\varphi)k_s + \varphi k_f \qquad \textit{Eq. 60}$$

$$q'''_m = (1-\varphi)\boldsymbol{q}'''_s + \varphi \boldsymbol{q}'''_f \qquad \textit{Eq. 61}$$

Eq. 58 is then the single phase formulation of the energy equation, commonly used in many packed bed heat transfer numerical simulations [70].

In the absence of local thermal equilibrium, commonly referred to as local thermal non-equilibrium (LTNE), equations must be maintained for each phase. In this case, the above equations become [39],

$$\left(1-\varphi\right)\left(\rho c\right)_s \frac{\partial T_s}{\partial t} = \left(1-\varphi\right)\boldsymbol{\nabla} \cdot \left(k_s \boldsymbol{\nabla} T_s\right) + \left(1-\varphi\right)\boldsymbol{q}'''_s + h\left(T_f - T_s\right) \qquad \textit{Eq. 62}$$

$$\varphi(\rho c)_f \frac{\partial T_f}{\partial t} = \varphi \boldsymbol{\nabla} \cdot \left(k_f \boldsymbol{\nabla} T_f\right) + \varphi \boldsymbol{q}'''_f + h\left(T_s - T_f\right) \qquad \textit{Eq. 63}$$

These equations include a heat transfer coefficient h which links the two phases. Determination of h for packed beds of spheres was previously discussed in the section on similitude.

Numerical methods are employed to solve these equations. The type of numerical method and resemblance of the discretized equations to those above depend on the aim of the analysis. The macro-scale perspective is often employed for beds with large numbers of particles and particle-to-tube-diameter ratios, and where averaged properties are desirable. These solutions are solved in one, two or three dimensions. When more detailed information on pore fluid dynamics

or local variability is of interest, 3D pore-scale computational fluid dynamics is the preferred approach.

Numerical Simulations

Numerical solutions are generally solved in either one or two dimension and can be either single- or two-phase models. Single phase models assume the instantaneous temperature of the fluid and solid phases remains the same. In two phase models, the fluid and solid are treated separately with the interface described by Nusselt correlations. Common two-phase models are the concentric dispersion model, continuous solid phase model and Schumann's model [70]. The concentric model allows conduction in spheres but not between spheres [70]. The continuous solid phase model treats the packed bed as a continuous porous media but allows for axial and radial conduction components [70]. Schumann's model only accounts for convective heat transfer. In all these models, an average velocity is used, which does not allow the accurate reflection of flow passages [70]. Model accuracy depends on the effective thermal conductivity of the bed and the total heat transfer coefficient between the fluid and solid phases which are usually determined by empirical correlation [70].

In the continuum treatment of packed beds, effective transport properties are used, a constant axial velocity v_z, *i.e.* plug flow, is assumed (or some radial variation $v_z(r)$) and solutions provide averaged properties that can predict only general transport characteristics. In packed beds with large N, the macroscopic perspective is often appropriate, as wall effects are small and porosity is consistent. However, as the tube-to-particle-diameter ratio N decreases, continuum assumptions fail, necessitating the use of more detailed models. In industry beds with $N > 10$ have some undesirable characteristics, such as high pressure drops and low pore-velocities,

which can make them costly to run and can reduce reactor efficiency. For these reasons, beds of low N ($N < 10$) are often employed despite the high channeling which leads to large variations in local temperature and velocity. Small changes in particle shape and N can have large effects on the porosity, pore speed, Nu, reaction rate and residence times. The ability to better predict the local conditions in these systems has the potential to save companies money and increase safety. However, improvement of bed design is hindered by the difficulty in collecting detailed bed data. Fortunately, the low number of particles in these beds is conducive to pore-scale CFD modelling.

Pore-scale Computational Fluid Dynamics: Packed Bed Generation and Meshing

Recent increases in computational power have provided the means for pore-scale CFD, which resolve individual particles and local conditions. Commercial CFD software packages such as STAR CCM+, ANSYS Fluent, and COMSOL provide a convenient framework for modelling fluid systems in 3D, resulting in many pore-scale CFD studies being conducted. The general workflow involves creating the packed bed geometry, breaking it into finite elements or volumes (meshing), and iteratively solving for the result. Pore-scale CFD solves the complete velocity and temperature fields, resolving fluid shear and particle temperature gradients, and allowing local drag coefficient and Nusselt numbers to be obtained. Resolving porous media flows on the pore scale introduces many new complexities that must be addressed for accurate solutions to be found and meaningful conclusions to be made. Some of the most relevant issues are the accurate representation of the packed bed geometry, creation of stable mesh elements and correctly selected time step [8].

The generation of a packed bed that accurately portrays the physical bed is of upmost importance as it is impossible to obtain an accurate model solution without the proper packing

geometry. The generation of synthetic packed beds is therefore vital and has been the topic of much research. Efforts have pursued true 3D scanning and reconstruction, generation through idealized particle arrangements and by random generation. Exact 3D reconstructions have been achieved rarely [71, 72] and are too time consuming in both acquisition of the geometry and conversion to a discretized form. Reconstruction is most useful for complex geometric shapes that other methods have difficulty producing. The generation of packed beds with regularly structured arrangements such as face-center cubic and body-center cubic can be derived explicitly for the position of each particle. These idealized beds are computationally cheap and can be generalized to random packed bed flows [13]. They are well suited for the study of monodisperse spherical particle beds. Ballistic random deposition or similar methods have been coupled with Monte-Carlo compression processes to produce accurate packed beds [73, 74]. This method does not take particle interactions into account, resulting in the generation of non-physical beds [13].

More recently, the discrete element model (DEM) has been used and reviewed extensively for packed bed generation [75, 76]. DEM allows true random synthetic packed bed generation by initializing individual particles with different velocities and trajectories at the top of the domain and calculating interaction forces from collisions as they fall under the influence of gravity. Each particle is governed by a momentum balance equation,

$$m_p \frac{d\boldsymbol{v}_p}{dt} = \boldsymbol{F}_s + \boldsymbol{F}_b \qquad \textit{Eq. 64}$$

where m_p is the mass of the particle, $\boldsymbol{v}_p$ is the instantaneous particle velocity, $\boldsymbol{F}_s$ is the surface force composed of drag, pressure gradient, and virtual mass forces, and $\boldsymbol{F}_b$ is the body force composed of contact, gravity, Coulomb and user-defined forces. The contact force can be

modeled as a linear-spring, non-linear spring-dashpot or Walton-Braun hysteretic linear spring [13]. The CFD software used here, STAR CCM+, uses the linear spring model as shown in Fig. 2.3. The DEM algorithm can only solve these interactions for spherical bodies. Beds of cylinders, rings and other shapes must be produced by representing the shape as many spheres glued together [8]. These representations can have significant impact on model accuracy [77], so DEM is severely limited in its ability to model non-spherical particles. The accuracy and applications of DEM methods have been studied by Marigo and Stitt [78]. Rigid body dynamics (RBD) embedded in the Bullet Physics library and implemented in Blender [79, 80] is another method of generating random packed beds that incorporates contact forces. This method defines particles based on surface meshes allowing complex shapes to be produced. Fleischlen and Wehinger [81] compared the DEM and Blender method, finding that they produced similarly accurate packings but that the Blender required less computational time.

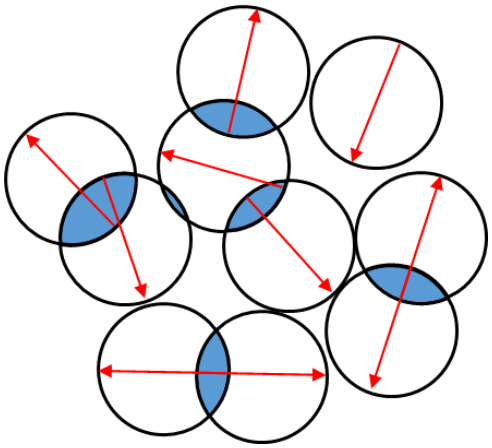


Fig. 2.3. The DEM algorithm tracks the interactions of multiple particles, using the overlapping areas to calculate elastic forces using a force-displacement law. Red arrows indicate the particle velocity vector.

The discretization, or meshing of the packed bed into small subdomains, for solution by the CFD algorithm is another important step which has been intensively studied. There are many

methods of mesh generation, which provide different balances between ease of generation, accuracy of solution and faithfulness representing the original geometry. Meshes can be either structured, where interior nodes are projected from the surface mesh, or unstructured, where a space-filling algorithm generates internal elements [8]. A common mesh for complex geometries uses an unstructured tetrahedral or polyhedral mesh. Thin hexahedral prism layers can be added at the boundaries where there are strong velocity gradients for better fidelity. The dominant trade-off in meshing is between the number of elements and the accurate representation of gradients. The number of elements can quickly become large due to the cubic relation of mesh size to element number, resulting in unacceptable solution times.

A particular problem for packed beds occurs at particle-particle and particle-wall contact points. Moderate mesh size cells can become highly skewed at contact points leading to difficulties in solution convergence [8]. One simple solution is to increase the cell density. With large numbers of particles, this approach can lead to an unacceptable increase in the total number of cells. Other early strategies were to decrease or increase the sphere size by 0.5-2.0% of diameter [82]. Even at 1%, these global methods had too large of an effect on the porosity and pressure drop [83]. The bridge and flattening methods were also suggested [84, 85]. The bridge method is preferred as it maintains thermal conduction between the spheres. The thermal conductivity of the bridges was found to be an important parameter [86]. Implementation of these techniques is straightforward for spherical packed beds but poses a problem for non-spherical particles [13].

The best method for generating accurate synthetic beds is still up for debate with many other issues being addressed. Methods for compacting DEM beds are just being investigated and more research is needed into meshing of complex shapes and methods for their bridging.

The plethora of unresolved problems in CFD modelling highlights the importance of experimental validation. These models are powerful tools for studying packed beds and can provide a more accurate prediction of reactor and storage performance. However, for the full benefit of pore-scale CFD to be realized, experimental methods must be able to supply validation at a similar resolution.

Computational and Experimental Studies

Despite the debate on the nuances of proper CFD setup, many models have achieved remarkable agreement with experimental results and there are many publications with CFD models compared against experimental result. A variety of experimental methods are used to validate the models. Thermocouples are often used in larger systems, in harsh environments, and at high temperatures. Dixon *et al.* used thermocouples attached to catalyst pellets to monitor temperatures in a pilot-scale methane steam reforming reactor [87]. They found good agreement with their model at various inlet temperatures. Cascetta and Serra used internal and external thermocouples to measure thermoclines in a bed of alumina particles. Their results were compared to a CFD thermal storage model [88]. Niu and Wang used archived data from the German organization SANA to study the heat up of a pebble bed nuclear reactor after failure of the forced convection system using Fluent [89].

Where possible, the greater fidelity of imaging techniques provides more confidence in model validation than point-based data methods can provide. Many imaging techniques have

been applied for packed bed studies, each with their own advantages and disadvantages. Particle imaging velocimetry (PIV), particle tracking velocimetry (PTV) and laser Doppler anemometry (LDA) can capture velocity fields in specially designed systems and the fluid temperature field in very limited cases. An example of the images captured with PIV are shown in Fig. 2.4. These methods require optical access, which limits their application to systems that can be refractive index matched. They also require particle seeding with the resulting measurements applying to the seeded particles not necessarily to the fluid itself. The seeded particles can be made temperature sensitive, allowing the acquisition of temperature maps. A final limitation is their ability to image in only one plane. The advantage of these optical methods is the measurement speed and resolutions they are capable of. These techniques are therefore ideal for basic science studies of turbulence [14, 90, 91] and other rapid flows like jets.

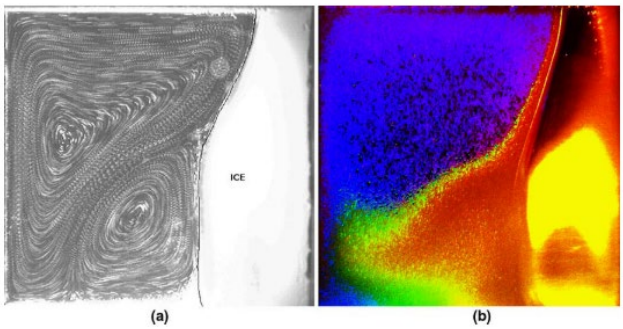


Fig. 2.4. Flow structure (a) and temperature variation (b) in a differentially heated cube captured with PIV.

Ultrasonic velocimetry (UV) and MRI methods can image through opaque objects, which has led to their wide-spread use in the medical field for imaging inside the body. UV has some major drawbacks in its inability to penetrate dense regions, no temperature dependence, and limited resolution. NMR velocity measurement does not require seeding, images are formed from the fluid itself, it can easily penetrate dense objects, and can image in any orientation [92].

Many NMR parameters are temperature sensitive, but low sensitivity and conflicting dependence of different parameters can make temperature mapping difficult to apply in many systems [93]. NMR also has low signal-to-noise ratio (SNR), so images are often formed from multiple acquisitions resulting in a speed of measurement much slower than optical methods. MRI velocity images are therefore spatially resolved time-averages, and can provide the distribution of velocities present in a spatial voxel. The genesis of the NMR signal from the nuclei itself presents data that is rich in information and sensitive to a variety of factors. MRI is capable of characterizing many different parameters via subtle manipulation of spin magnetic moment and analysis of signal. A review of the many applications of MRI to chemical engineering and flow can be found in works by Gladden and Sederman [26, 94], and for porous media by Song *et al.* [95].

The techniques explored in this work provide a means of measuring both the velocity field and heat transfer to the particles. A method to provide particle temperature is also investigated. This combination provides a way to resolve heat transfer spatially in an opaque packed bed and is well suited to validating CFD models.

CHAPTER THREE

NUCLEAR MAGNETIC RESONANCE THEORY BASICS

Introduction to NMR

Nuclear Magnetic Resonance (NMR) utilizes the intrinsic quantum mechanical property of spin angular momentum. This property, known colloquially as 'spin', allows the magnetic field of specific nuclei to be manipulated by applying an oscillating magnetic field. This phenomena was first observed in 1945 by two separate groups, Purcell, Torrey and Pound [96] at Harvard University, and Bloch, Hansen and Packard at Stanford University [97]. The best known application of NMR is magnetic resonance imaging (MRI) for medical purposes, however, it took nearly thirty years for the first NMR image to be produced in 1973, again by two separate groups: Lauterbur [98]; and Mansfield and Grannell [99]. These distinguished researchers are now renowned in the NMR field for their accomplishments. The following two chapters were composed with predominant reliance on two reference texts [92, 100] by another well-loved luminary of NMR, Sir Paul T. Callaghan. Callaghan is remembered for his intellect and exuberance shown to young investigators and his texts are the standard for NMR microscopy today. Other original references will be made where pertinent.

Fourier Transforms

Any thorough investigation into NMR would be incomplete without discussion of the Fourier transform (FT), a mathematical relationship to which NMR is intimately tied. The FT commutes a function between the reciprocal domains of time and frequency, decomposing a time domain function into its constituent frequency components. A pleasant example is the Fourier

transformation of a musical chord which will produce the individual notes, and their respective magnitudes. In NMR the transform informs the range of frequencies affected by an input time domain pulse and the constituent frequency components of the resultant signal. The FT is accomplished with Eq. 65.

$$S(\omega) = \frac{1}{2\pi}\int_{-\infty}^{\infty} S(t)\, e^{i\omega t} dt \qquad \textit{Eq. 65}$$

It is important to note that the FT is a complex relationship, meaning it has real and imaginary (sine and cosine) parts. Consider Fig. 3.1 below which contains some examples of simple waveforms and their respective FT. For the moment, assume the left side corresponds to the time domain and the right frequency, though the inverse would be equally true. The principles of time and frequency scaling are illustrated in Fig. 3.1a. A broadening of a function in time causes a narrowing of the FT function in frequency (time scaling). As shown in the limit, an infinitely long signal would FT to an exact delta function. This necessitates that a broadening in frequency result in a narrowing of the inverse FT function in time. The hat-sinc relationship shown in Fig. 3.1b is critically important in NMR where it is often desirable to excite a range of frequencies equally. This is accomplished by modulating the excitation pulse as a sinc in time. Time scaling of the sinc by constant $\boldsymbol{c}$ controls the width frequency width of the pulse by the $1/\boldsymbol{c}$.

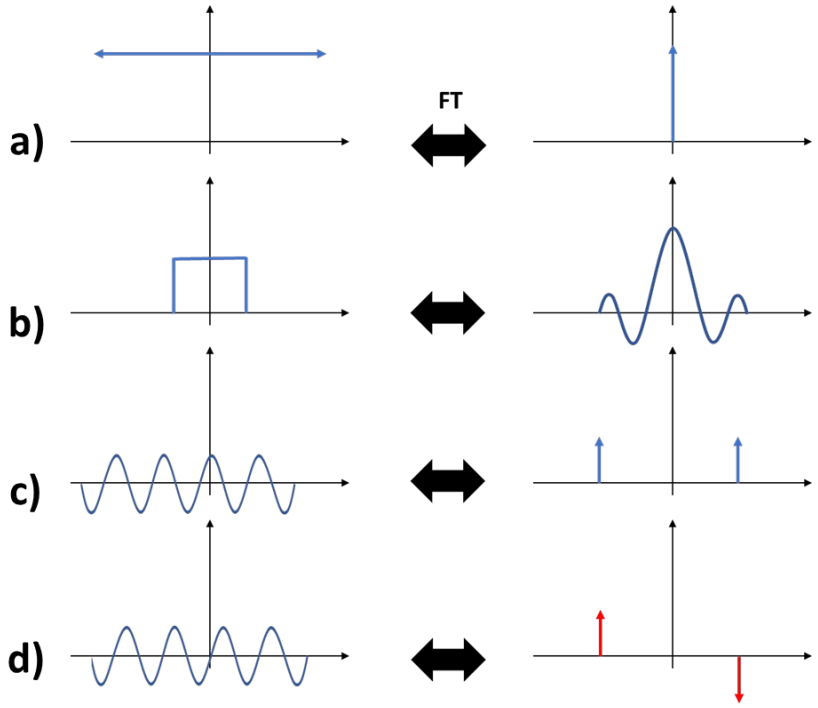


Fig. 3.1. Common waveforms and their corresponding Fourier Transform. a) constant offset transforms to a delta function, b) sine wave transforms into a positive and negative translated delta function both imaginary, c) cosine transforms into two positive, real delta functions, d) a hat function transforms into a sinc.

Other properties of the FT also have important consequences in NMR. The principle of linearity states that the addition of two functions in one space is equal to the addition of their transforms in the other. This principle allows the determination of the frequencies that compose a NMR signal. The principle of convolution requires the multiplication of a function in one domain will result in the convolution of the FT of those functions in the reciprocal space. It is defined by Eq. 66 but is most easily understood as the multiplication of the overlapping area of the two functions as one is translated across the other.

$$(f * g)(t) = \int_{-\infty}^{\infty} f(\tau)g(t-\tau)d\tau \quad \textit{Eq. 66}$$

Convolution is evident in the FT of the digitized NMR signal. Digital sampling acquires signal at discrete time points over a finite duration, effectively multiplying the signal by a

truncated comb, or truncated series of delta function. This causes a convolution of the frequency spectrum with a point spread function. Other important FTs are the sine and cosine function which transform to even and odd dirac delta function, respectively, with offset equal to the frequency of the sinusoid. A Gaussian function transforms to another Gaussian and an exponential to a Lorentzian. The importance of FT in NMR will become apparent in the following chapters.

Spin Angular Momentum – Quantum mechanics

While most NMR experiments can be described using macroscopic ideas originally derived by Bloch in 1946 [97], the basis of all NMR is quantum in nature. It is therefore a logical and informative point to begin a discussion on NMR. Each nuclear isotope possesses a fundamental quantum mechanical property called spin angular momentum which arises from the spin of protons and neutrons. An imbalance of either or both nucleons results in a nonzero angular momentum. The spin state of a nucleus is described by the angular momentum quantum number *I*, which can take on a half-integer or integer value [92]. Nuclei with non-zero spin number possess a non-zero magnetic moment and are thereby available for NMR manipulation. The quantum number *I* defines the number of discrete values of spin angular momentum, *m*, available to each nucleus when measured along an arbitrary axis,

$$m = -I, (-I + 1), \dots (I - 1), I \qquad Eq.\ 67$$

The nuclei used in this work (^{1}H and ^{19}F) are both dipoles with $I = ½$ and have available states of $m = -½$ or ½. These states are often referred to as spin up and spin down, respectively. The spin angular momentum of the atomic nuclei is an intrinsic property but imparts a magnetic moment which behaves mathematically and physically as a spinning object rotating about the direction of

the magnetic field, although the nuclei does not physically rotate. As such angular momentum can be treated as a vector quantity.

Fundamentally in a quantum system, the spin exists in a superposition of all allowed basis states $|\bar{m}\rangle$ and is forced into one spin basis state $\bar{m}$ when a measurement is taken because of interaction between system and measurement. When measuring the I_z component of angular momentum the expectation value is [92],

$$\langle\Psi|\boldsymbol{I_z}|\Psi\rangle = \sum_m |a_m|^2 m \qquad \textit{Eq. 68}$$

During measurement the linear combination of basis states collapses into one of the allowed states based on the probability of each state a_m.

The time evolution of the quantum system is described by the Schrödinger equation,

$$i\hbar\frac{\partial y}{\partial x}|\Psi(t)\rangle = \boldsymbol{H}|\Psi(t)\rangle \qquad \textit{Eq. 69}$$

where $\boldsymbol{H}$ is the Hamiltonian operator, corresponding to the energy of the quantum system. The Schrödinger equation reduces when $\boldsymbol{H}$ is time independent to [92],

$$|\Psi(t)\rangle = exp(-i\boldsymbol{H}t)|\Psi(0)\rangle \quad \textit{Eq. 70}$$

where the exponential is the evolution operator. In the presence of a strong, static magnetic field, $\boldsymbol{B_o}$, the Hamiltonian takes the form of $-\mu \cdot \boldsymbol{B_o}$ where μ is the magnetic dipole moment defined as $\mu = \gamma J = \gamma\hbar\big(I(I+1)\big)^{1/2}$ where J is the quantized spin angular momentum and $\hbar$ is Plank's constant. This Hamiltonian describes the Zeeman interaction that occurs between the field and the magnetic dipole moment. Nuclei with non-zero magnetic dipole moment, or spin, will align with or against the applied magnetic field $\boldsymbol{B_o}$. When this is the case, the Hamiltonian is referred to as the Zeeman Hamiltonian and takes the form $\boldsymbol{H} = -\gamma\boldsymbol{B_o}\boldsymbol{I_z}$ [101].

The two alignments, with or against the magnetic field, correspond to the two spin states available to $I = ½$ nuclei and the spins are constantly switching between them. Each state has an associated energy and the difference between the two states ($\Delta E = \gamma\hbar\boldsymbol{B_o}$) increases with field strength as shown in Fig. 3.2. The emission of the energy which occurs during transition between the states provides the signal detected in NMR. This energy difference is proportional to the frequency at which energy is absorbed, $\Delta E = \hbar\boldsymbol{\omega_o}$, so the transition between the spin up and spin down states occurs at the Larmor frequency. Alignment with the $\boldsymbol{B_o}$ field corresponds to the lower energy state, resulting in more spins residing in this alignment at any given time. A summation of individual spin moments results in a bulk magnetization $\boldsymbol{M}$ in the direction of the $\boldsymbol{B_o}$ field. The signal is therefore proportional to the ratio of the energy state populations and is described by the Boltzmann distribution,

$$\frac{N^+}{N^-} = exp\left(\frac{\gamma \boldsymbol{B_o} \hbar}{k_B T}\right) \qquad Eq.\ 71$$

where k_B is the Boltzmann constant and T is the absolute temperature of the system.

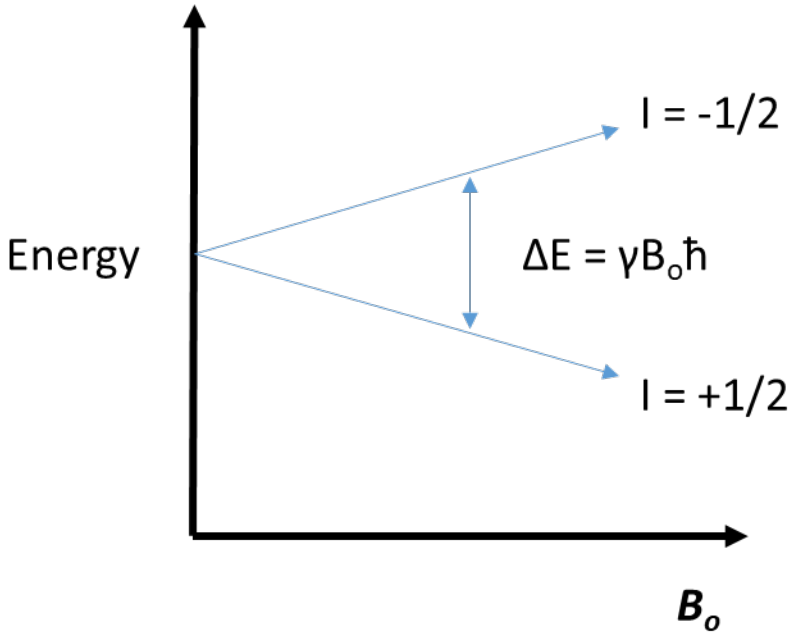


Fig. 3.2. Energy levels available to spin ½ nuclei like ^{1}H and ^{19}F. The energy difference between the spin up and spin down states are proportional to the field strength and gyromagnetic ratio of the nuclei.

Vector Model

Despite quantum origins, most spin-½ nuclei NMR techniques are more easily described mathematically and conceptually as rotating objects in a framework known as the semi-classical representation. This includes the techniques used here and will be the dominant mode utilized to explain the NMR phenomena presented.

As described above, all nuclei are composed of charged particles and those accessible through NMR have an odd number of one or both nucleons which imparts a magnetic moment called spin. This is the source of the magnetization utilized in NMR, however, the magnetization from individual spins is too small to be detected. Instead, a bulk magnetization vector ***M*** is detected, which accumulates from large ensembles of spins. This vector points in parallel with

the polarizing field, $\boldsymbol{B_o}$, due to the preference of spins for their lower energy state and is much smaller than $\boldsymbol{B_o}$ in magnitude. The semi-classical, macroscopic description is therefore preferred to the quantum description as it describes most of the behavior of the detectable signal. Additionally, this perspective allows for a vector description, which is more familiar and easier to use than the quantum descriptions. It is common convention to assign the *z* axis in parallel with the $\boldsymbol{B_o}$ field, and the spins precess around this axis with a frequency of $\boldsymbol{\omega_o}$, called the Larmor frequency. This frequency depends on the specific nuclear species and is proportional to the applied magnetic field strength by,

$$\boldsymbol{\omega_o} = \gamma \boldsymbol{B_o} \qquad \textit{Eq. 72}$$

where $\boldsymbol{\omega_o}$ is the frequency of the precession, γ is the gyromagnetic ratio of the nuclei of interest and $\boldsymbol{B_o}$ is the strength of the magnetic field. The gyromagnetic ratio is an intrinsic property, unique to each nucleus, resulting in different precession frequencies for different nuclear species at the same magnetic field strength.

Resonant Excitation

The spin system is in thermal equilibrium with the surround lattice when the $\boldsymbol{M}$ vector is aligned with the $\boldsymbol{B_o}$ field. It is, however, impossible to detect $\boldsymbol{M}$ in this alignment due to its small magnitude compared to $\boldsymbol{B_o}$. $\boldsymbol{M}$ must be tipped away from the $\boldsymbol{z}$ axis by exciting the spins with an oscillating magnetic field $\boldsymbol{B_1}$ applied in an orthogonal direction to $\boldsymbol{B_o}$. Excitation applied at the Larmor frequency exhibits a torque on the spins, causing a nutation of $\boldsymbol{M}$, about the $\boldsymbol{z}$ axis, while energy applied at other frequencies has no effect on the spins. In high field instruments, like the 7 Tesla magnet used here, the Larmor frequency lies in the radio frequency range, so a

radiofrequency (RF) coil is used to apply power. This RF coil can be turned on and off precisely to allow for precise application of energy into the sample.

The general differential equation which governs the influence of the magnetic field $\boldsymbol{B}$ on $\boldsymbol{M}$ is expressed as,

$$\frac{d\boldsymbol{M}}{dt} = \gamma \boldsymbol{M} \times \boldsymbol{B} \qquad \textit{Eq. 73}$$

It is useful to separate this equation into *x*, *y*, and *z* components, and consider the contributions from the static $\boldsymbol{B_o}$ and pulsed $\boldsymbol{B_1}$ fields separately. With the application of the initial condition $\boldsymbol{M}(0) = M_0\boldsymbol{k}$, the behavior of the magnetization vector in the laboratory frame after excitation is [92],

$$\begin{aligned} \boldsymbol{M_z} &= M_0 cos(\boldsymbol{\omega_1} t) \\ \boldsymbol{M_x} &= M_0 sin(\boldsymbol{\omega_1} t) sin(\boldsymbol{\omega_0} t) \qquad \textit{Eq. 74} \\ \boldsymbol{M_y} &= M_0 sin(\boldsymbol{\omega_1} t) cos(\boldsymbol{\omega_0} t) \end{aligned}$$

where $\boldsymbol{M_o}$ is magnitude of the $\boldsymbol{M}$ vector immediately after excitation, and $\boldsymbol{\omega_1} = \gamma \boldsymbol{B_1}$. This indicates that the magnetic vector precesses about both the $\boldsymbol{B_o}$ and $\boldsymbol{B_1}$ fields with frequencies of $\boldsymbol{\omega_o}$ and $\boldsymbol{\omega_1}$, respectively. During application of a $\boldsymbol{B_1}$ pulse, the $\boldsymbol{M}$ vector would move in the spiral pattern indicated in Fig. 3.3a.

To better visualize the interaction between the spins and the applied oscillating magnetic field, it is useful to adopt the rotating reference frame. This reference frame has the added benefit of simplifying many of the mathematical equations that govern spin dynamics. In the laboratory reference frame, the spins are rotating at the Larmor frequency, but in the rotating reference frame the observer is rotating at the same rate as the spins. From the rotating frame, the spins appear to be stationary, just as an observer from space sees the earth rotating while to someone

on earth the world appears to be stationary. Recall the Hamiltonian due to static magnetic field, $\boldsymbol{B_o}$ is $\boldsymbol{H} = -\gamma \boldsymbol{B_0} \boldsymbol{I_z}$. An additional frequency offset is applied in the rotating frame to account for the rotation of the frame itself [100],

$$\boldsymbol{H}_{rot} = -\gamma \left(\boldsymbol{B_0} + \frac{\boldsymbol{\omega}}{\gamma} \right) \boldsymbol{I_z} \qquad \textit{Eq. 75}$$

The application of the oscillating field $\boldsymbol{B_1}$ tips the magnetization vector into the transverse plane, and the Hamiltonian becomes [100],

$$\boldsymbol{H_{rot}} = -\gamma \left(\boldsymbol{B_o} + \frac{\boldsymbol{\omega}}{\gamma} \right) \boldsymbol{I_z} - \gamma \boldsymbol{B_1} \boldsymbol{I_x} \qquad \textit{Eq. 76}$$

The rotational frame is chosen to be that of resonance, so $\boldsymbol{\omega} = \boldsymbol{\omega_o}$. The $\boldsymbol{I_z}$ term in $\boldsymbol{H}_{rot}$ then collapses, leaving only the transverse term and the $\boldsymbol{B_1}$ field appears stationary in the rotating frame as shown in Fig. 3.3b. The equations describing the time evolution of $\boldsymbol{M}$ are then [92],

$$\begin{aligned} \boldsymbol{M_z} &= \boldsymbol{M_0} \cos(\boldsymbol{\omega_1} t) \\ \boldsymbol{M_x} &= 0 \qquad\qquad \text{Eq. 77} \\ \boldsymbol{M_y} &= \boldsymbol{M_0}\, sin(\boldsymbol{\omega_1} t) \end{aligned}$$

In the rotating frame, the apparent Larmor frequency is zero and the only rotation is due to $\boldsymbol{B_1}$ field.

The rotation or tip angle of $\boldsymbol{M}$ into the transverse plane is equal to $\boldsymbol{\omega_1 t}$. It is easy to control this tip angle by adjusting the duration t or magnitude of $\boldsymbol{B_1}$. The most common tip angles are the 90° and 180°, which tip $\boldsymbol{M}$ into the transverse plane or $-z$ direction, respectively. Back in the laboratory frame with the $\boldsymbol{B_1}$ field switched off, $\boldsymbol{M}$ is oscillating in the transverse plane and can be detected by the RF receiver.

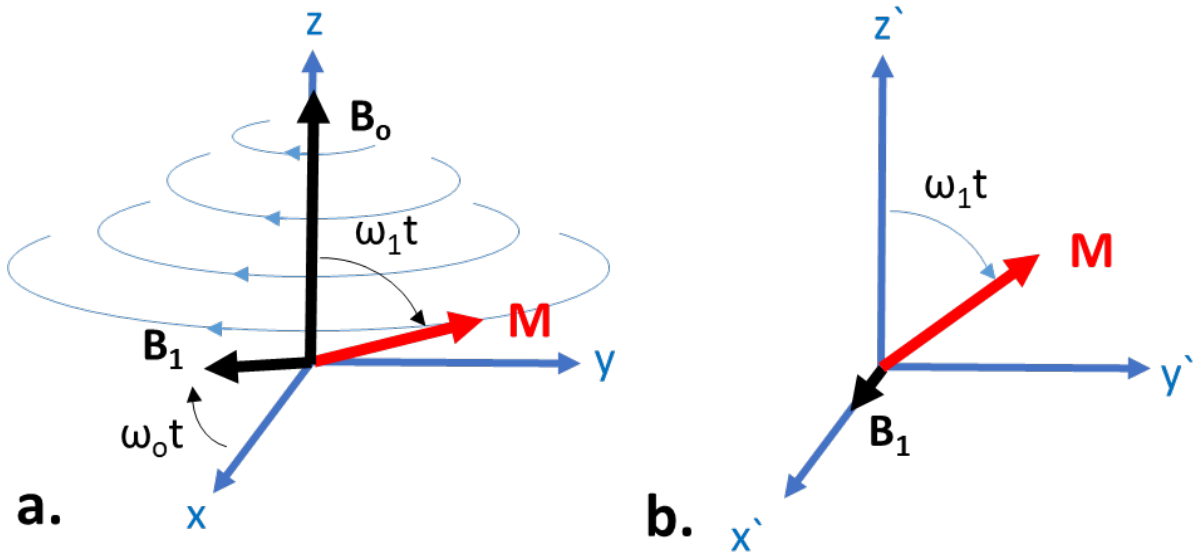


Fig. 3.3. In the laboratory reference shown in (a), the magnetization vector ***M*** precesses around the $\boldsymbol{B_o}$ and $\boldsymbol{B_1}$ axes. It is useful to use the rotating reference frames shown in (b) where the ***M*** vector only rotates about the $\boldsymbol{B_1}$ field.

Intrinsic Spin Interactions

The effect of the RF pulse is to move the nuclear ensemble out of thermal equilibrium. Molecular interactions immediately begin to move the ensemble back to equilibrium through two processes termed T_1 and T_2 relaxation as depicted in Fig. 3.4. T_1 or spin-lattice relaxation is the process by which the spins return to equilibrium with the polarizing field. This relaxation process involves the exchange of energy between the ensemble and the surroundings, or lattice, with which it is in equilibrium. So T_1 relaxation is the time it takes for the ***M*** along the z axis to return to its initial value after it has been disturbed from equilibrium. Due to its relationship with the alignment of ***M*** along $\boldsymbol{B_o}$, it is often termed longitudinal relaxation. The longitudinal magnetization can be described in terms of T_1 relaxation by,

$$\boldsymbol{M_z}(t) = \boldsymbol{M_z}(0) + \boldsymbol{M_o}(1 - e^{-\frac{t}{T_1}}) \qquad \textit{Eq. 78}$$

with the solution,

$$\boldsymbol{M_z}(t) = \boldsymbol{M_z}(0)exp(-t/T_1) + \boldsymbol{M_0}\big(1 - exp(-t/T_1)\big) \qquad Eq.\ 79$$

Typical T_1 relaxation times for protons range from 0.1 to 10 seconds.

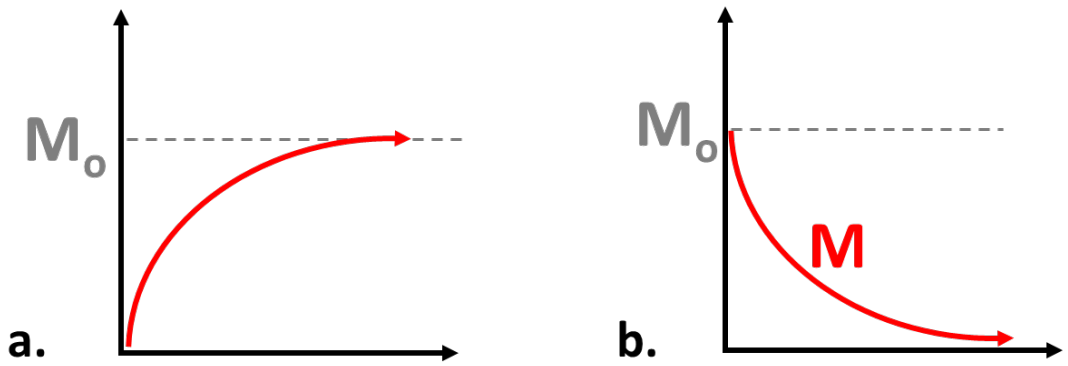


Fig. 3.4. The magnetic coherence excited by an RF pulse will immediately begin to relax back to equilibrium via two characteristic times termed T_1 and T_2 relaxation. Figs. a) and b) show the time evolution of magnetization due to T_1 and T_2 relaxation, respectively.

The second characteristic time describes the decay of the transverse magnetization. It is called spin –spin or T_2 relaxation and is representative of the time it takes the spins to reach equilibrium amongst themselves. It is therefore sensitive to interactions which cause dephasing of the spins. While the same interactions of energy exchange with the lattice will affect the decay of the transverse magnetization, other direct interactions also contribute. For this reason, T_2 is always equal to or less than T_1. T_2 relaxation can be phenomenologically described by,

$$\frac{d\boldsymbol{M}_{x,y}}{dt} = \frac{-\boldsymbol{M}_{x,y}}{T_2} \quad Eq.\ 80$$

with solution,

$$\boldsymbol{M}_{x,y}(t) = \boldsymbol{M}_{x,y}(0)e^{-\frac{t}{T_2}} \qquad Eq.\ 81$$

In spin–½ systems the main mechanisms leading to loss of magnetic coherence are magnetic field inhomogeneity and dipolar couplings. Loss of coherence due to inhomogeneous magnetic

field is reversible with the appropriate pulse sequence, while loss due to random dipolar coupling is not. Differentiation between the reversible and irreversible effects is important enough to warrant the definition of an additional relaxation term known as T_2*. T_2* includes both reversible and irreversible mechanisms while T_2 includes only irreversible losses.

Equations 78 and 80 along with the description for the $\boldsymbol{M}$ vector above can be combined in the rotating frame to yield the Bloch equations shown below.

$$\frac{d\boldsymbol{M_z}}{dt} = -\gamma \boldsymbol{M_y B_1} - \frac{\boldsymbol{M_z - M_o}}{T_1}$$

$$\frac{d\boldsymbol{M_x}}{dt} = \gamma \boldsymbol{M_y}\left(\boldsymbol{B_o} - \frac{\boldsymbol{\omega}}{\gamma}\right) - \frac{\boldsymbol{M_x}}{T_2} \qquad \text{Eq. 82}$$

$$\frac{d\boldsymbol{M_y}}{dt} = \gamma \boldsymbol{B_1} + \gamma \boldsymbol{M_x}\left(\boldsymbol{B_o} - \frac{\boldsymbol{\omega}}{\gamma}\right) - \frac{\boldsymbol{M_y}}{T_2}$$

The Bloch equations completely describe the evolution in time of the magnetic vector after it has been disturbed by a RF pulse.

Signal Detection

The NMR signal can only be detected when $\boldsymbol{M}$ is in the transverse plane as the magnetism from the molecules is negligible compared to that of the $\boldsymbol{B_o}$ field. Once the spins have been tipped into the transverse plane, the precessing magnetization cuts through the RF coil causing an oscillating voltage signal in the receiver. It is important to realize the energy emissions of individual RF protons are too small to be detected alone. We are instead detecting signal from ensembles of spins. The coherence of the excited spins decays away over time, resulting in a free induction decay (FID) of the signal. The duration this signal lasts is directly related to the homogeneity of the $\boldsymbol{B_o}$ field, the physical state of the perturbed nuclei, and their current environment. The FID decays at a rate of $1/T_2^*$ and is given as,

$$S(t) = S_0 exp(i\varphi) exp(i\Delta\omega t) exp\left(\frac{-t}{T_2^*}\right) \qquad Eq.\ 83$$

where S_0 is the signal immediately after excitation.

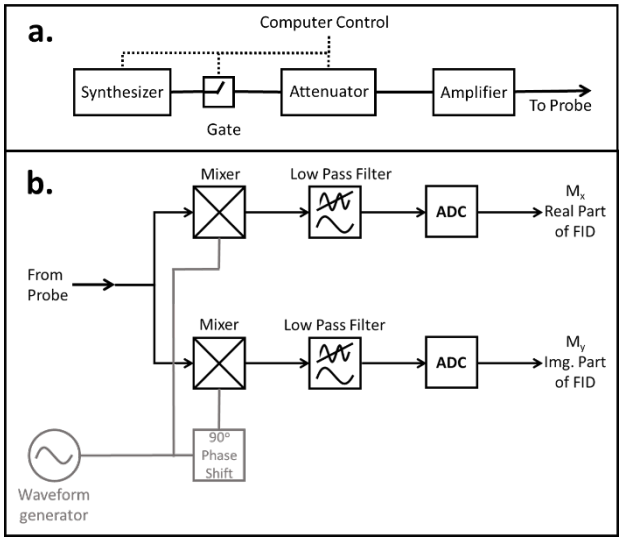


Fig. 3.5. Electronics diagram for excitation (a) and signal detection (b).

A clever arrangement of electronics allows the output from the single RF receiver coil to be converted into a complex output of real and imaginary parts. This process, called quadrature detection, is simply shown in Fig. 3.5. The RF signal is split, run through a mixer, low pass filter and analog-to-digital converter. In the mixer the RF signal is subtracted from two reference signals oscillating 90° out of phase at the Larmor frequency. These low-frequency signals are passed through a filter to remove high-frequency noise and an ADC to digitally sample it. The results are an in-phase and quadrature phase output signal which are effectively the $\boldsymbol{M_x}$ and $\boldsymbol{M_y}$ components of the transverse magnetization decay [102]. This decaying complex signal can be made up of one or many frequencies and is well suited for analysis by Fourier transformation (FT) which converts the data between the conjugate variables of time t and frequency ω,

$$F\{S(t)\} = S(\omega) = \frac{1}{2\pi}\int_{-\infty}^{\infty} S(t)\, exp(i\omega t) dt \qquad Eq.\ 84$$

This process can be demonstrated by considering the simplest case of a decay with $\varphi = 0$, after a single 90° pulse, as shown in Fig. 3.6. The real spectrum is called the absorption spectrum and is a Lorentzian with offset equal to $\Delta\omega/2\pi$ and Full-Width-Half-Maximum (FWHM) of $1/2\pi T_2$. The imaginary spectrum is known as the dispersion spectrum.

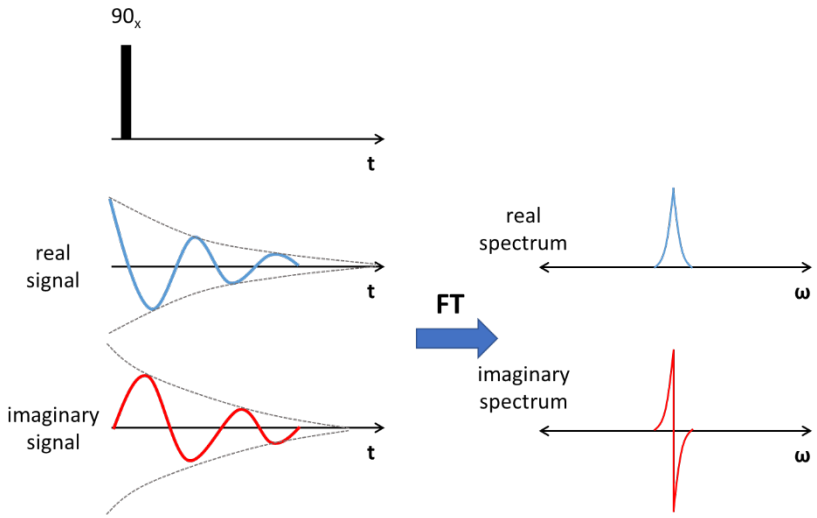


Fig. 3.6. Quadrature detection allows the signal to be decomposed into real and imaginary parts. Fourier transformation of these individual components results in Lorentzian and dispersion spectrum in the frequency domain.

Digital sampling of the analog signal, accomplished by the ADC, imparts some important consequences. A finite number of sampling points, N, are collected at interval T, imparting a bandwidth of $1/T$ and point spacing of $1/NT$ in the frequency space. Finite sampling has the effect of multiplying the data by a hat function in time domain and convoluting the frequency space with the point spread function.

Relaxation and Molecular interactions

The application of energy to the system during excitation tips the magnetic coherence into the transverse plane and out of thermal equilibrium. The time-dependent evolution of the

magnetization vector as it regains thermal equilibrium with the Zeeman field and loses coherence with itself are described by two NMR relaxation timescales T_1 and T_2. The mechanisms underlying these relaxations are stochastic in nature, emerging from random motions of many nuclei. As relaxation is a product of many random interactions, they are well suited to description by autocorrelation functions. Autocorrelation functions are defined by,

$$G(t) = \int_0^\infty A(t')A(t'-t)dt' \qquad Eq.\ 85$$

where A is the stochastic variable. Autocorrelations specify the strength to which a variable remains correlated with its original value over time. NMR relaxation additionally exhibits stationary and ergodic characteristics. The time invariance of stationary variables requires the variable value does not change with the absolute start time but depend only on the duration of the time interval. Additionally, ergodicity signifies that the long-term average of the variable is equal to its instantaneous spatial average. This property allows the autocorrelation function to be extended to the ensemble,

$$G(t) = \langle A(0)A(t)\rangle \quad Eq.\ 86$$

and together, allow a correlation timescale to be calculated. Because of ergodicity, $G(t)$ is equal to the means squared value of A at t=0, $\langle A(0)^2\rangle$. The correlation time can therefore be calculated by normalizing the autocorrelation function to its initial value and integrating over time [100],

$$\tau_c = \frac{\int_0^\infty \langle A(0)A(t)\rangle dt}{\langle A(0)^2\rangle} \qquad Eq.\ 87$$

where τ_c is the characteristic timescale over which any stochastic variable will lose correlation with itself. Relevant here are the timescales over which spins regain thermal equilibrium with the Zeeman field (T_1) and lose magnetic coherence with themselves (T_2). These timescales are very sensitive to the chemical environment, being directly tied to random molecular interactions and

the timescales driving those interactions. This sensitivity provides NMR with its unique perspective on molecular scale interactions and motions.

Molecular motions and Spectral Density Functions

In condensed matter molecules are continuously in random motion and interacting through their magnetic fields via dipolar couplings. Each interaction has an associated energy, dependent on the distance between the molecules, the duration the interaction and orientation of their respective fields. The duration of the interactions is the correlation time, τ_c. Due to random thermal effects, as the molecules move about, they will be tumbling at a range of rates. Spectral density functions, $J(\omega)$, describe the spectrum of molecular rotation frequencies, found by Fourier transform of molecular rotation times. As the rotation times are directly related to the dipolar interactions, $J(\omega)$ governs the magnetic relaxation rates which occur. As discussed earlier, there are only two energy states in spin – ½ systems. Therefore, there are three potential outcomes from an interaction between dipoles in a static magnetic field: no interaction, one spin changes energy, or spins flip energy states. The spectral density functions associated with each interaction are [100],

$$J^{(0)}(\boldsymbol{\omega}) = \frac{24}{\boldsymbol{r}_{ij}^6}\frac{\tau_c}{1+\boldsymbol{\omega}^2\tau_c^2}$$

$$J^{(1)}(\boldsymbol{\omega}) = \frac{4}{15\boldsymbol{r}_{ij}^6}\frac{\tau_c}{1+\boldsymbol{\omega}^2\tau_c^2} \qquad \textit{Eq. 88}$$

$$J^{(2)}(\boldsymbol{\omega}) = \frac{16}{15\boldsymbol{r}_{ij}^6}\frac{\tau_c}{1+\boldsymbol{\omega}^2\tau_c^2}$$

where $\boldsymbol{r_{ij}}$ is the nuclear magnetization vector of the interacting nuclei. These interactions are the genesis of T_1 and T_2 relaxation and can be used to directly define them. The definition of T_1 based on spectral density functions is [100],

$$\frac{1}{T_1} = \left(\frac{u_o}{4\pi}\right)^2 \gamma^4 \hbar^2 \frac{3}{2} I(I+1)\left[J^{(1)}(\omega_0) + J^{(2)}(2\omega_0)\right] \quad \textit{Eq. 89}$$

This relation clearly shows the dependence of the two interactions on ω_o and $2\omega_o$, respectively, indicating that molecular interactions only occur when molecules are tumbling at the Larmor frequency. The dependence of T_1 relaxation on $J^{(1)}(\omega)$ and $J^{(2)}(\omega)$ should come as no surprise as these are interactions which lead to the release of energy back to the lattice.

T_2 relaxation can be given based on spectral density functions as [100],

$$\frac{1}{T_2} = \left(\frac{u_o}{4\pi}\right)^2 \gamma^4 \hbar^2 \frac{3}{2} I(I+1)\left[\frac{1}{4}J^{(0)}(0) + \frac{5}{2}J^{(1)}(\omega_0) + \frac{1}{4}J^{(2)}(2\omega_0)\right] \quad \textit{Eq. 90}$$

All three interactions contribute to T_2 relaxation. $J^{(0)}$ has no dependence on rotation frequency, while $J^{(1)}$ and $J^{(2)}$ retain the same dependence. T_2 will always be less than or equal to T_1 relaxation time due to its dependence on all three interactions.

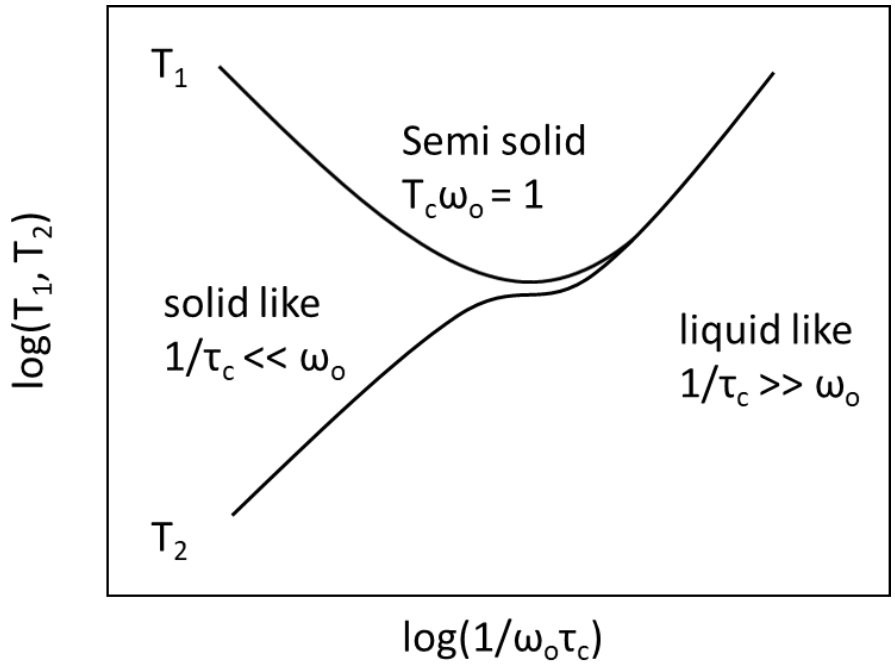


Fig. 3.7. T_1 and T_2 relaxation times plotted as a function of correlation time τ_c. The relative magnitudes of T_1 and T_2 times depend on the structural phase of the substance. T_2 is much shorter than T_1 in solids but become equal in liquid like substances.

The dependence of the spectral density functions on correlation time implies that the relative magnitude between T_1 and T_2 relaxation rates are also dependent on correlation time. This relationship is shown in Fig. 3.7. When correlation times are short, T_1 and T_2 are the same. However, as correlation time increases, T_1 becomes much longer than T_2.

Pulse Sequences

The pulse sequence is a series of excitations, delays and magnetic gradient applications delivered at precise strengths and timing which control the rotation of the $\boldsymbol{M}$ vector and the durations over which the spins sample their environment. A diverse array of sequences have been developed. There are, however, a few basic pulses that are often incorporated in more complicated sequences and can be used as building blocks for more complex, often multidimensional sequences. These base sequences are the Hahn (spin) echo, stimulated echo, gradient echo, the Carr-Purcell-Meiboom-Gill (CPMG) train, and the inversion recovery. The spin echo and CPMG echo train are introduced here as they play a central role in the pulse sequences used in this research.

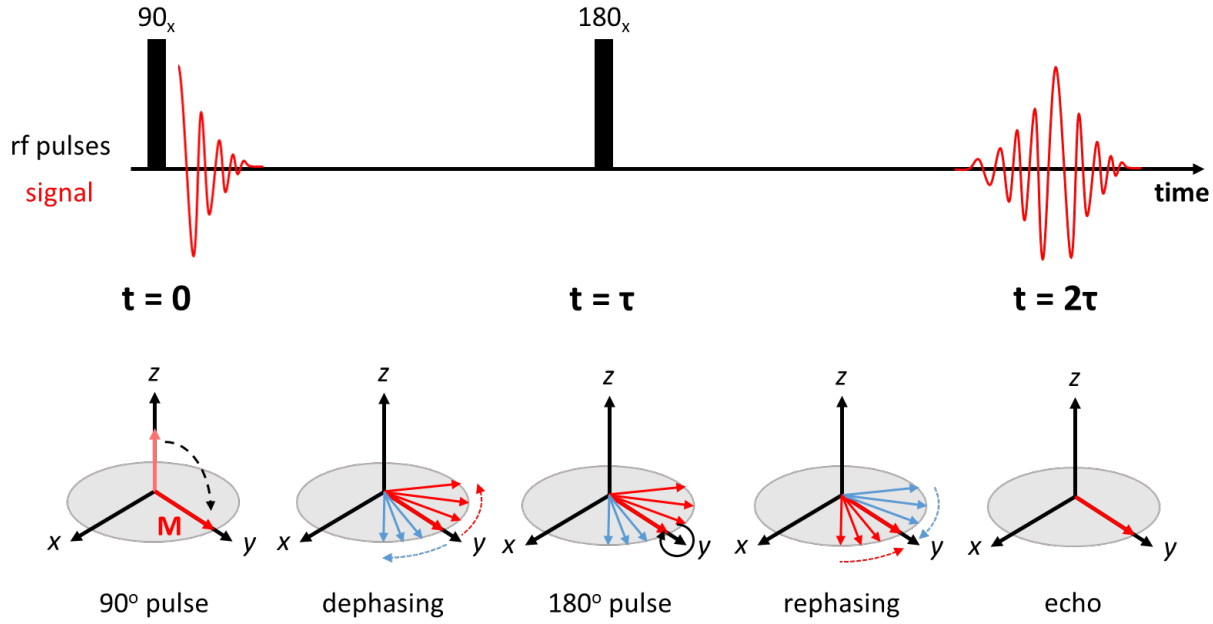


Fig. 3.8. Pulse diagram with generated signal for the spin echo pulse sequence are shown on the top line. The bottom sequence is the evolution of spin phase at select times in the pulse sequence. Excited coherence is initially all in phase after 90° pulse. Phase spreads during the dephasing duration, then reverses during the rephasing duration to form an echo at time 2τ after 90° pulse.

Pulse sequences are typically depicted using a pulse diagram. These diagrams are laid out on multiple *x* axes where time increases to the right. The different axes represent the timing of different experimental elements; often these are, RF pulse transmission and detection, slice gradients, and image gradients in *x, y* and *z* coordinate directions. The individual pulse sequences can often be combined. For example, a multi-echo T_2 sequence can be combined with an imaging sequence to produce a spatial map of T_2 relaxation.

Spin Echo

The spin echo is often called the Hahn echo in honor of Erwin Hahn who first discovered it in 1950. The echo is the refocusing of the magnetization after a user-controlled timeframe, less than the T_2 time. It is one of the simplest and most useful pulse sequence elements for its ability

to reverse the loss of magnetic coherence due to magnetic inhomogeneity. The pulse diagram of the spin echo is shown in Fig. 3.8 with a diagram sequence depicting the evolution of the spins at corresponding times. An initial application of a 90^{o} pulse excites a coherence, rotating the spins into the transverse plane. The term coherence refers to the spins which are in phase with each other and have experienced the same history of rotational manipulations. Immediately after excitation the spins begin to lose coherence (phase), decaying away in the form of a FID. This rapid decay, termed T_2*, is due to small variations in field strength leading to a distribution of rotational frequency. After a time interval τ, during which the magnetization vector often completely decays, an 180^{o} pulse is applied. This pulse has the effect of flipping the rotation direction of the spins, which continue to rotate at their same relative frequencies, ultimately resulting in a convergence of the spins at time 2τ. This convergence is termed an echo and takes the form of a reverse FID, followed by an FID. The magnitude of this echo will be less than the initial FID, as the dipolar couplings which cause T_2 relaxation have had time to occur. The echo provides a mean to control the interaction time of the spins and measure the result. This provides a way for molecular motions, and interaction rates to be measured at the micro-scale. Additionally, the delay of time τ allows gradients to be applied across the sample for imaging and other purposes. For these reasons, most pulse sequences record the echo and not the initial FID.

CPMG Train

The spin echo refocuses the magnetic vector, removing effects from $\boldsymbol{B_o}$ inhomogeneity, providing a decay that is due only to true T_2 effects. The CPMG train sequence links a chain of multiple 180^{o} pulses at fixed 2τ intervals as shown in Fig. 3.9. The amplitude of the echoes will

decay at a rate of $1/T_2$, providing a convenient way to measure T_2 in one pulse sequence. This sequence was first introduced by Carr and Purcell in 1954, and refined by Meiboom and Gill in 1958, hence the CPMG train name. Meiboom and Gill modified the original train to incorporate quadrature 180_y pulses, which compensates for small errors in flip angle which would otherwise lead to an accumulation of errors.

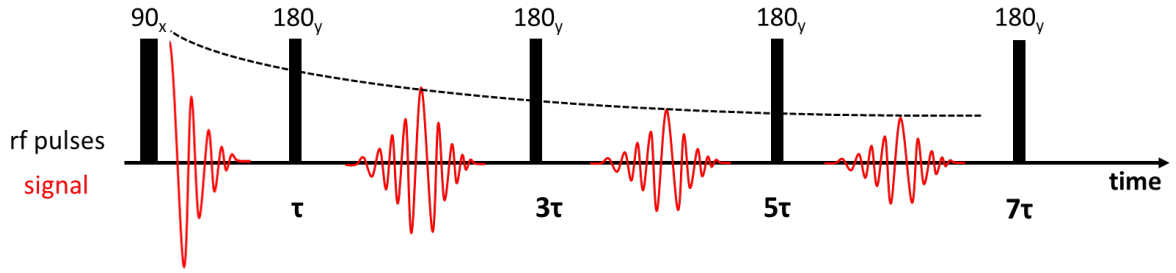


Fig. 3.9. Pulse diagram for the CPMG train, a sequence used to determine the T_2 relaxation time with a single excitation.

Phase Cycling

NMR experiments often require many repeated 90° and 180° pulses. This can lead to accumulated errors due to inexact flip angles. Phase cycling is a method of compensating for these error by flipping the coherence onto different axes in a defined sequence. The four step CYCLOPS sequence of Hoult and Richards is widely used as the basis of other phase cycles. By tipping the coherence into a different axis, spins that receive inexact excitations cancel out over the cycle. An excellent source for information on phase cycling is Chapter 9 of *Understanding NMR Spectroscopy* [102].

Signal Averaging

A signature limitation to NMR is the insensitivity of its measurement. The tiny signal detected by the RF receiver means the desired signal is often on the order of that produced by

random thermal noise, resulting in a signal-to-noise ratio (SNR) too low to allow accurate analysis. To overcome this handicap, each signal acquisition is repeated multiple times and added together. Frequencies of the desired signal will add constructively while those due to thermal noise will not, thus providing a means to improve the SNR. The real signal contribution will scale linearly with the number of averages, *N*, while that from thermal noise will be incoherent following a Gaussian distribution with mean of zero, therefore scaling with $(N)^{1/2}$. This results in an effective SNR scaling of $N^{1/2}$. Incorporating phase cycling with averaging cancels pathological signal contribution while increasing SNR.

Imaging Gradients and $\boldsymbol{k}$-Space

One of the most powerful and flexible tools in NMR is the use of magnetic field gradients. These gradients produce time varying linear deviations in the magnetic field strength in each of the three coordinate directions and can be used to measure molecular displacements, for chemical selection, for spatial encoding, and for slice selection. In magnetic resonance imaging (MRI) the Larmor frequency is made to depend on spatial position. This linear magnetic gradient is achieved using a set of three specially designed magnetic coils, called gradient coils, to produce field gradients in the *x*, *y* and *z* directions. The gradients are of a strength much smaller than the polarizing $\boldsymbol{B_o}$ field, so the frequency variation is small in comparison. The applied gradients add to the $\boldsymbol{B_o}$ field so the local Larmor frequency can be determined by,

$$\boldsymbol{\omega(r)} = \gamma \boldsymbol{B_o} + \gamma \boldsymbol{G} \cdot \boldsymbol{r} \qquad \textit{Eq. 91}$$

The time evolution of the transverse magnetization phase is governed by,

$$\boldsymbol{M_+(r,t)} = \boldsymbol{M_+(r,0)} exp(i\gamma \boldsymbol{r} \boldsymbol{G} t) \qquad \textit{Eq. 92}$$

Under the influence of the gradient, the phase difference increases, winding the helix tighter and shortening the wavelength λ of the helix as shown in Fig. 3.10. Where λ is defined as [92],

$$\lambda = \frac{2\pi}{\gamma \boldsymbol{G} t} \qquad \textit{Eq. 93}$$

It is common to use the reciprocal space vector, $\boldsymbol{k}$,

$$\boldsymbol{k} = \gamma \boldsymbol{G} t \qquad \textit{Eq. 94}$$

which has units of angular spatial frequency, radians m^{-1} or,

$$\boldsymbol{k}' = (2\pi)^{-1} \gamma \boldsymbol{G} t \qquad \textit{Eq. 95}$$

which has units cyclic spatial frequency m^{-1}. Using the $\boldsymbol{k}$ –space nomenclature the phase evolution of an isochromat at position $\boldsymbol{r}$ is,

$$\boldsymbol{M}_+(\boldsymbol{r}, t) = \boldsymbol{M}_+(\boldsymbol{r}, 0) exp(i\boldsymbol{k} \cdot \boldsymbol{r}) \qquad \textit{Eq. 96}$$

This $\boldsymbol{k}$-space, or frequency space, can be scanned and recorded. The signal is collected in the time domain and has the form of [92],

$$S_n(\boldsymbol{k}) = \int \rho(\boldsymbol{r}) exp(i2\pi \boldsymbol{k} \cdot \boldsymbol{r}) d\boldsymbol{r} \qquad \textit{Eq. 97}$$

The image can be formed by Fourier transformation of the reciprocal variables $\boldsymbol{k}$ and $\boldsymbol{r}$,

$$\rho(\boldsymbol{r}) = \int S_n(\boldsymbol{r}) exp(i2\pi \boldsymbol{k} \cdot \boldsymbol{r}) d\boldsymbol{r} \qquad \textit{Eq. 98}$$

where $\rho(\boldsymbol{r})$ is the spin density at position $\boldsymbol{r}$, S_n is the time domain signal collected at all $\boldsymbol{k}$-space points and the exponential is the phase vector. This form of imaging is called Fourier imaging as the image is only recovered after FT.

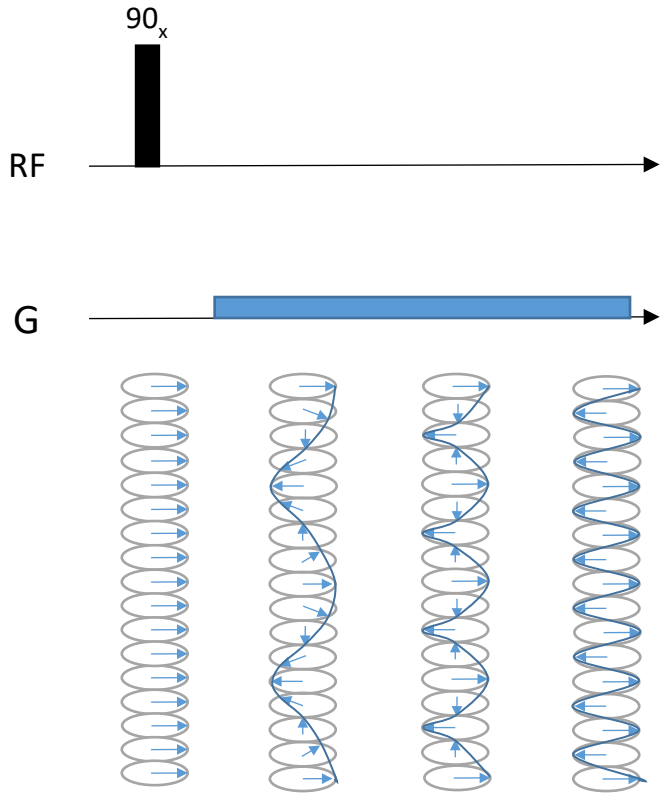


Fig. 3.10. Evolution of spin phase angle under the influence of a linearly varying magnetic gradient. Immediately after the 90° pulse, all spins are in phase. The application of the gradient causes some spins to move faster, resulting in a phase difference. Often the evolution of spin frequency under the influence of a gradient results in the winding of a helix and the shortening of the wavelength λ.

***k*-space coverage**

NMR images are created by modulating the frequency and phase of the spins across the sample in a 2D plane. There are many methods for scanning ***k***-space, with a wide range in efficiency. The simplest (and slowest) method for traversing ***k***-space is the phase-phase method, where gradients are stepped up in each of the two dimensions and a single point in ***k***-space is collected for each echo. Using this method, an image of 64 pixels by 64 pixels would require 64^2 excitations or around an hour to complete with a repetition time (TR) of 1 second. While time is clearly a downside to this method, it provides an image with very few artifacts. To speed up the

imaging processes, phase-frequency encoding is often employed. This method collects one row of ***k***-space for each excitation by applying a read gradient during collection of the FID. The same 64 x 64 pixel image would require only 64 excitations or approximately 1 minute with the same TR = 1 sec. Other gradient based imaging techniques such as FLASH, SPRITE and EPI use precisely controlled gradients to traverse ***k***-space in just a few or a single excitation, creating an entire image in seconds. Ultra-fast imaging sequences use SPRITE or FLASH in conjunction with sparse sampling methods to collect images in under a second. In these sequences only a few ***k***-space points are collected, and the image is recreated using machine-learning techniques.

In the works covered here the spin-warp, frequency-phase method is used nearly exclusively and will be the only method covered in detail. Fig. 3.11 shows the pulse diagram for a standard spin-warp, frequency-phase encoding pulse sequence, and the path traversed during a single excitation on a 2D grid.

The first pulse is a hard 90^{o}. This broadband excitation brings all the spins into the transverse plane. A phase encoding gradient is applied in the *y* direction in *N* independent steps, where the $\boldsymbol{k_y}$ position depends on the strength of the applied *y* gradient. Modulation of the gradient strength while maintaining a fixed duration is what makes this a spin-warp sequence. A read gradient in the *x* direction is applied to move out to the edge of the $\boldsymbol{k_x}$ space. The 180^{o} pulse inverts the phases of the spins, prompting the formation of an echo. A final application of the read gradient during the formation of the echo allows the collection of the entire $\boldsymbol{k_x}$ row. This sequence is then repeated *N* times at different values of the phase encoding gradient to sample all of ***k***-space.

MRI Resolution

k-space is sampled in the time domain at discrete points then Fourier Transformed into the frequency space where the image is resolved. The number of phase steps and points collected in the read direction determine the resolution of the image. With the frequency-phase imaging method, scan time scales linearly with the number of phase steps, as only one step can be collected per excitation. Increasing the number of collected read points scales with the dwell time (TD). This is on the order of microseconds and so has little effect on the total scan time. The number of points in either direction is typically kept at a multiple of 2^N to allow the use of the fast Fourier transform (FFT).

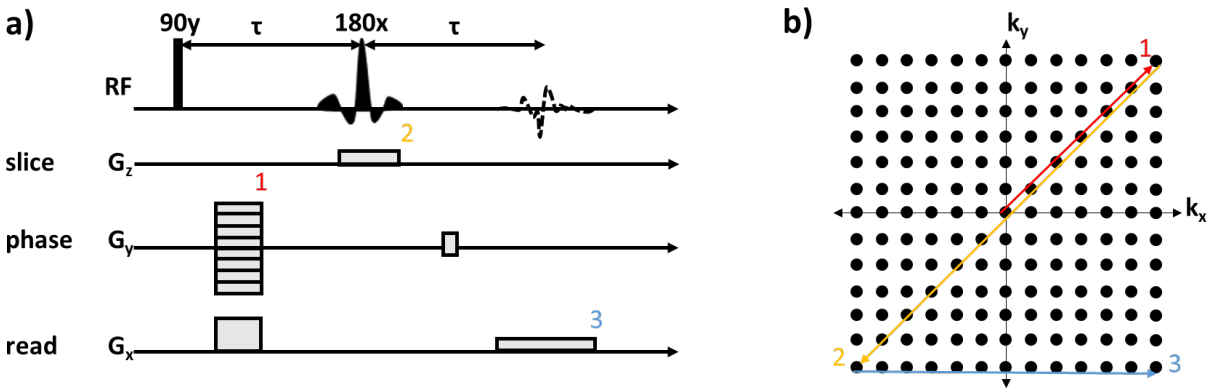


Fig. 3.11. Spin -warp, frequency-phase Fourier Imaging pulse sequence shown in a). The path by which ***k***-space is traversed is shown in b) with three key points located.

The relationship between the resolution and field-of-view (FOV) of an MRI can be described by,

$$FOV = \frac{N}{2\boldsymbol{k}_{max}} = \frac{N}{2}\frac{2\pi}{\gamma \boldsymbol{G}_{max}\delta} \qquad Eq.\ 99$$

where N is the number of points collected in single dimension, $\boldsymbol{G}_{max}$ is the maximum gradient strength and δ is the total gradient duration.

Slice Selection and Chemical Selection

The NMR spectrum is the range of frequencies that are present in a sample at a given field strength. Often the same nuclear species has a different frequency depending on the functional group it is attached to. Oil (or fat) and water are a good example, as they are both present in the human body. The different rotational freedom provided by their respective chemical bonds results in a difference in Larmor frequency of 3.5 ppm. The difference for other compounds can be large or smaller. Regardless, it is often necessary to select just one of these functional groups for imaging or other reasons and this is accomplished through chemically selective excitation.

Chemical selection is performed by exploiting the Fourier relationship between time and frequency to excite only a specific range of frequencies. Consider the product which determines the tip angle of the spins, $t_p = \gamma \boldsymbol{B_1} T$. The duration of the pulse, T, has a Fourier relation with the frequency range, or bandwidth, excited as $\omega_{fr} = 1/T$. The strength of the $\boldsymbol{B_1}$ field can be adjusted to compensate for different durations of the pulse while still providing the same tip angle. Since the field strength does impact the Fourier relationship, changes to its strength do not affect the frequencies excited. Short pulses, termed hard pulses, excite a broad range of frequencies while long pulses, termed soft pulses, excite a narrow range of frequencies. The soft pulse is used in chemical selection to excite a single peak from the spectrum.

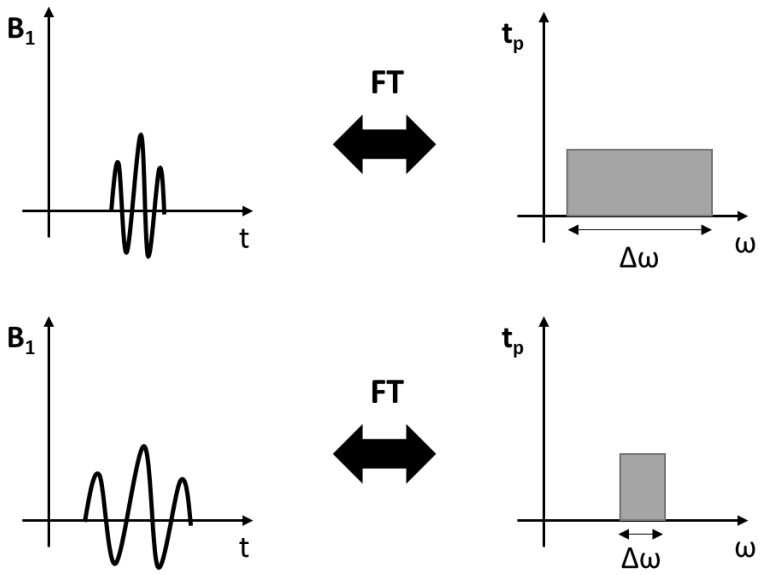


Fig. 3.12. Excitation pulse shape in time domain has a Fourier relationship with the frequencies excited in the frequency domain. A short sinc corresponds to a broad hat or wide range of excitation frequencies. A long sinc is more appropriate for selection of a specific nuclear species or imaging slice as it will excite a smaller range of frequencies.

It is desirable to have all the excited spins experience the same tip angle. It is therefore necessary to modulate the pulse to provide a constant value in the frequency space over a finite range, and zero everywhere else. The inverse Fourier transform of this 'hat' function is a sinc, which is composed of oscillating positive and negative lobes of decreasing amplitude that stretch out to infinity in the time domain. Conveniently, it is generally sufficient to approximate this shape with a three-lobed function which produces a reasonably uniform excitation profile. Fig. 3.12 shows the three-lobed approximation in the time domain and the corresponding hat excitation function in the frequency domain.

In 2D imaging selection of slice position and thickness is accomplished by exploiting this same Fourier relationship. In slice selection a distribution of Larmor frequencies is introduced by applying a gradient in the direction perpendicular to the desired slice plane and a soft, excitation

pulse is applied at the same time. The duration and frequency of the excitation pulse control the bandwidth and its central frequency of the excited spins. When used for slice selection this controls the thickness and location of the excited slice. A gradient is not necessary for chemical selection as the variation in Larmor frequency is already present.

Image Artifacts

The MRI practitioner must be adapt at determining the causes of the many artifacts that can occur during routine imaging. Such artifacts can arise from interactions between the sample and the magnetic field, improperly selected parameters, or imperfect equipment. Many of the artifacts have similar appearance and yet the method which minimizes or eliminates one artifact in one sample, can have no impact for another. An experienced NMR practitioner can determine the cause and improve on the experimental protocol to clean up or correct the data.

Chemical Shift. MRI samples often contain complex spectra, requiring the selection of a single peak. Failure to properly isolate the desired peak can result in an artifact known as chemical shift, where the entire image or parts of it are overlaid on each other but shifted in the read direction. The resulting shift is linearly dependent on the field strength. For instance, in a high-field spectrometer, the chemical shift of water and fat is 1000 Hz at 7 T but in a low-field instrument this shift is only 8 Hz at 0.05 T. Since position r is assigned by the frequency of the spins $\boldsymbol{\omega}$, this results in a miss registration of position to an incorrect voxel.

This type of artifact is identified by switching the direction of the read and phase dimensions, which will switch the axis on which the shift is observed. The severity of this artifact increases with the field strength of the measurement, the ppm offset of the offending peak and the inverse of the bandwidth of sampling. Chemical selection as described above and

increase of bandwidth are two methods for removing or reducing chemical shift artifacts. The first is used if there are more than two peaks, and they are well separated. Increasing the amount of bandwidth per pixel is effective when the two peaks are close together. These methods can be combined when there are multiple peaks, some far away and other close. When applying the frequency encode gradient, its strength will determine the range of frequencies, or bandwidth, across the sample. Each voxel is assigned a discrete ranges of frequencies equal to $\Delta\omega = FOV_f/N_f$, where FOV_f, is the width in the read dimension, and N_f is the number of points collected.

Magnetic Susceptibility. MRI relies on highly homogeneous magnetic fields to which linear gradients can be added to provide field strengths which vary linearly with position along a specific axis. At the boundary of two substances the magnetic field may be distorted due to changes in magnetic permeability, causing a local increase/decrease in the magnetic gradient. The macroscopic effect is for faster relaxation, and results in images with lighter and darker areas which can be similar in appearance to chemical shift, despite different mechanistic origin. Similarly, this artifact can be suppressed by increasing the bandwidth which reduces the size of the artifact.

Gibbs' Ringing. Gibbs ringing occurs most often near high contrast areas of the image and can be recognized as multiple parallel lines. This artifact is also known as the truncation artifact as it is caused by finite sampling of the frequency data. Any signal can be represented by an infinite summation of sine waves; however, we are restricted to a finite number of frequencies when imaging. The Fourier transformation is therefore performed using an incomplete or truncated dataset. Gradual changes in image intensities require only a few Fourier terms but in

high contrast areas the truncated data set may not be enough, resulting in cyclic over- and under-shooting. It can also cause artificial widening and obscure or distort areas adjacent to interfaces. This error is often most pronounced in the phase direction as fewer point are often acquired in that direction but will be present in both directions. Increasing the number of phase/frequency points will minimize this error but cannot eliminate it. Hamming or Tukey filters can also be applied in post processing to help smooth the image.

Data Clipping. The magnitude of the NMR signal is quite small, requiring amplification between the receiver and ADC, but can also be highly variable depending on the sample. It can also change dramatically throughout an experiment. Data clipping occurs when the gain on the amplifier is set too high. This often manifests itself as distortions to the large features and overall contrast, while leaving the finer details unaffected. The low frequency data is clipped because the echo magnitude is always greatest at the center where gradient attenuation is smallest. It is common practice to set the receiver gain so the signal is no greater than 60% of digitizer filling and set the receiver gain relative to the highest expected data of an experiment.

Spatial Aliasing. The spatial aliasing artifact is often called the wrap-around artifact. It occurs in the phase direction when the sample extends beyond the field of view. In the phase encode step, the applied gradient is such that the spins at the center of the FOV have zero phase and those at the edge a phase of π and $-\pi$. Any portion of the sample that extends beyond this FOV will have a higher phase shift. The spectrometer cannot distinguish between a $-\pi/2$ phase shift or a $3\pi/2$ phase shift so the spins with the $3\pi/2$ phase shift will be recorded at $-\pi/2$ location. This affect will occur for the entire portion of the sample extending beyond the FOV, resulting in

that portion being overlaid, or wrapping on the opposite side. This wrap around artifact is corrected by adjusting the phase dimension to be larger than the sample.

Motion Artifact. The ghosting artifact is associated with periodic or non-periodic motion of the sample, relative to the gradient coil. It results in either multiple shifted images, smearing or an overall blurriness most often in the phase encode direction. Motion artifacts occur when the sample moves part way through a scan. This causes a mismatch in the k-space frequency representation of the image. Together this results in two truncated oscillations, effectively an oscillation multiplied by a hat. The Fourier transformation of this is a frequency convoluted with a sinc function, resulting in the image being reformed at a shifted location. Ghosting is less common in the read direction because there is less time for the motion to occur. This artifact can be combated by preventing the motion (i.e. damping vibrations or securing the sample), synchronizing the TR time with the periodic motion or switching the read and phase directions so the artifact does not obscure the region of interest.

The Spectrometer

The manipulation of the magnetization vector and acquisition of data is inherently dependent on the spectrometer system and the limitations of its composite hardware. It is therefore important to understanding the components that make up a spectrometer, their physical limitations and how this restricts measurement. A modern high field MRI spectrometer is composed of four main systems: a superconducting magnet with associated cooling system and shim gradients designed to provide the most homogeneous magnetic field possible; a power transmission/detection system which excites the sample with (radio-frequency) energy pulses

and detects the sample signal; magnetic field gradients designed to apply exact gradient values while minimizing effects of eddy currents; and software used to control each of these individual components.

High-field superconducting magnets provide the strongest and most homogeneous magnetic fields. The solenoids of these magnets are composed of miles of copper wire wound around the magnets central bore. Maintaining a constant cold temperature is essential to the magnets function. To this end, the wire is immersed in a bath of liquid helium which is surrounded by a heat shield of liquid nitrogen and isolated by a vacuum chamber from the surroundings. This system keeps the copper coil at a constant 6^{o} Kelvin. At temperatures so close to absolute zero, the wire acquires superconductive properties where it has essentially zero resistance to electrical flow. The coil is charged once at the beginning of service and will run continually for decades provided the cold environment is maintained. The isolation of the electrical current from external power sources, along with zero resistance, provides an electrical current and therefore magnetic field that is extraordinarily stable and can be maintained at very high field strength. The replacement of liquid nitrogen and helium as it boils off are all that is required to maintain the functioning of the magnet. In older systems the liquids are allowed to boil off, requiring frequent fills. Newer systems are equipped with regenerative capture systems and require very infrequent coolant additions. The first spectrometers along with smaller, desktop and portable systems operate at lower field-strength using electromagnets and permanent magnets. These systems suffer from lower SNR and shorter signal life due to relatively poor magnetic field homogeneity, limiting their resolution. They often lack active shimming coils and

have gradients in only one direction if at all. Despite these limitations they have proven extremely useful when designed for specialty applications.

The homogeneity of a superconducting magnet's field is extraordinary; however, the addition of a sample will distort this field enough to prevent high-resolution spectroscopy. The gradient shim coils are designed to counter sample induced inhomogeneity and expand the homogeneous region of the magnet. The coils, up to 40 in a shim stack, are specifically designed to generate magnetic fields of different gradients or shapes i.e. xy, yz^3, x^4, etc. In normal operation only the linear x, y, z and quadratic z^2 coils are adjusted.

The homogeneous spin system generated by the magnet and shims is excited and recorded by the RF coil which acts as both transmitter and receiver. Just as the magnet and shims are designed to provide a homogeneous magnetic field, the RF coil is designed to apply RF power uniformly to the sample. In high-field systems, where the polarizing field is in-line with the bore access, the RF coils are designed in birdcage coils, saddle coils and cavity resonators configurations. The electronics used to generate excitation pulses and to record the detected signal are shown in Fig. 3.5 is a basic block diagram. A waveform is created by a synthesizer at the Larmor frequency and this runs through a computer-controlled gate. The synthesizer produces RF at stable frequencies and amplitude but low power level, on the order of mW. This RF is then increased by an amplifier to up to 60-100 W. Both the amplifier and synthesizer operate at fixed amplification, so an attenuator is used to adjust the power level before amplification. It is then sent to the probe and the RF coil transmits it to the sample. As the same coil acts as the transmitter and receiver, signal cannot be received while power is delivered, resulting in a short switching delay. The magnetization excited by the RF power oscillates in the

transverse plane, producing an oscillating current in the RF coil. This signal is split and routed through a mixer, low pass filter and analogy-to-digital converter. In the two separate mixers the signal is combined with a reference signals which are 90^{o} out of phase with each other. This produces the real and imaginary parts of the signal from a single RF coil in a method called quadrature detection. The final signal is recorded in digital format. Digitization of the analog signal effectively truncates the frequencies composing the signal. This can lead to errors when FT the data. The use of high bandwidths (rapid digitization) is suggested.

In addition to the shim gradients, high field NMR spectrometers are equipped with three additional gradient coils which provide linear magnetic gradients in the three coordinate directions. These gradients can be much larger than the shim gradients and are switched off and on frequently during a pulse sequence. The rapid, accurate switching of gradients requires a carefully calibrated preemphasis system which counter the induced electrical currents. The gradient ramp times and over-shoot characteristics can have noticeable effects on measurement. This is especially pronounced for rapid imaging sequences e.g. EPI, RARE.

Today the incorporation of computers with NMR spectrometers is ubiquitous. Software programs such as ParaVision (version 5.1WB) and TopSpin v3.7 (used in this research) coordinate and control the various spectrometer components. These programs have preprogrammed sequences which can be refined with desired timing delays, gradient powers, resolution, field of view, etc. User-defined sequences can also be implemented. These programs calculate gradient moments and incorporate spoiler gradients. In addition to software which controls the spectrometer, post-processing must be performed in a separate program. Prospa and in-house MATLAB code was used here.

CHAPTER FOUR

ADVANCED NMR TOPICS

The previous chapter provided a foundational understanding of NMR and MRI. This chapter will discuss the methods used in this research in more depth. Of greatest interest is how NMR can be used to measure and image quantities other than spin density, namely molecular motions and temperature. The ability of NMR to measure molecular motions of both diffusive and convective nature is the result of a fortuitous coincidence of time scales between the lifetime of the magnetic coherence in fluids, on the order of milliseconds to seconds, and relevant fluid motions. NMR can measure fluid velocities of order 10^{-6} to 10^{-1} m s^{-1}. Magnetic relaxation is dependent on the dipolar interactions among nuclei and accelerated by surface interactions and magnetic field inhomogeneity [92]. This combined with its non-invasive and non-optical nature provide a technique optimally suited to study fluid motions and interactions in opaque systems and porous media. The advantages of NMR for fluid motion studies has become apparent in recent decades from the proliferation of papers published [15, 17, 24, 36, 103-105], spurred by hardware advances which provide the necessary sensitivity to capture fluid motions.

Changes to temperature result in greater motions of molecules which influences many NMR parameters. The relaxation rates T_1 and T_2, magnetization transfer rate, signal magnitude and diffusion rate are all temperature dependent [93]. It is therefore often possible to use NMR to non-invasively measure temperature. However, with more than one parameter effected by temperature it is often difficult to disentangle the often-conflicting effects on the detected signal [93]. Despite the challenges, methods for temperature measurement have been successfully employed in many systems [36, 94, 106-108]. The results are worth pursuing, as temperature

measurements are difficult in opaque systems and complex geometries, where other optical techniques or positioning of a sensor are not feasible.

Molecular motion and Propagators

Brownian motion describes the stochastic processes of molecular motions. It was first observed by botanist Robert Brown in 1827 while observing pollen under a microscope. The random fluctuations and dislocations are proportional to the thermal (kinetic) energy in the system and are characterized by their self-diffusion coefficient as described by the Sutherland-Einstein relation,

$$D = \frac{k_B T}{6\pi\mu a} \qquad Eq.\ 100$$

where k_B is the Boltzmann constant, μ is the dynamic viscosity, T temperature and a the effective particle size. The translational motion of the Brownian particles is described using probability densities due to the large numbers of molecules involved in measurements. The propagator describes the probability a molecule will displace a certain distance over a period of time. This description works well with NMR where large ensembles of spins are dealt with. The probability spins with a density $\rho(\boldsymbol{r})$ at time $t = 0$ will displace $\boldsymbol{R} = \boldsymbol{r}' - \boldsymbol{r}$ by time t is described by [109],

$$\bar{P}(\boldsymbol{R}, t) = \int \rho(\boldsymbol{r})\, P(\boldsymbol{r}|\boldsymbol{r} + \boldsymbol{R}, t) d\boldsymbol{r} \qquad Eq.\ 101$$

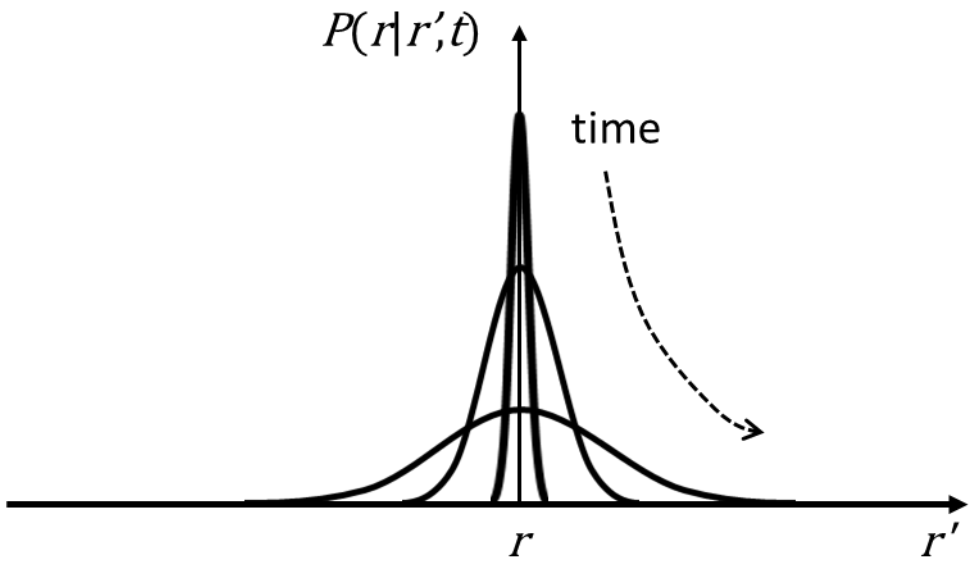


Fig. 4.1. The displacement of Brownian particles follows a Gaussian distribution which broadens over time. The displacement propagator shown above shows the probability of a molecule being at position $\boldsymbol{r'}$ at time t when it started at position $\boldsymbol{r}$, t = 0.

Under unrestricted self-diffusion, the average propagator results in a Gaussian distribution. Since particles have an equal probability of moving in any direction, this distribution is centered at zero. As time advances the particles will move away from their starting positions, resulting in a broadening of the Gaussian. This broadening describes the mean squared displacement of the particles, a result known as Einstein's equation [109],

$$\langle(\boldsymbol{r'} - \boldsymbol{r})^2\rangle = 2nDt \quad \textit{Eq. 102}$$

where *n* is the number of dimensions. The evolution of the displacement probability distribution over time is shown in Fig. 4.1. This Gaussian can be described with [109],

$$\bar{P}(\boldsymbol{R}, t) = (4\pi Dt)^{-1/2} exp\left(-\frac{|\boldsymbol{R}|^2}{4Dt}\right) \quad \textit{Eq. 103}$$

Stochastic Brownian motion occurs in a fluid otherwise motionless and in a fluid experiencing bulk flow. When a coherent displacement is present, the Gaussian described above is shifted by a constant related to the fluid velocity [92, 101],

$$\bar{P}(\boldsymbol{R},t) = (4\pi Dt)^{-3/2} exp\left(-\frac{(\boldsymbol{R}-vt)^2}{4Dt}\right) \qquad Eq.\ 104$$

The effect of this constant is to convolute the Gaussian with a delta function as shown in Fig. 4.2. The propagator can be measured directly by NMR through the thoughtful application of magnetic field gradients as will be described in the next section.

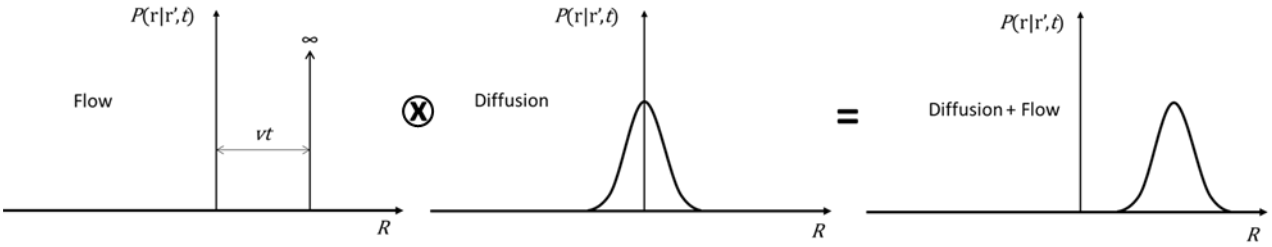


Fig. 4.2. The average propagator produced under coherent flow conditions is shown at right. This distribution is the result of a shift due to bulk motion convoluted with a Gaussian caused by underlying Brownian motion.

Motion Sensitized Gradients and Gradient Moments

The origin of NMR's signal from the particles themselves provides a unique technique with which to study molecular motions of both a coherent and incoherent nature. Most methods for measuring fluid displacements are Eularian, measuring quantities from a fixed position. NMR provides a measurement which follows the particle (Lagrangian) from a fixed starting position. The basic method for measuring molecular motions using NMR involves applying a gradient to encode for initial position in the sample and then observing the effects on the signal over a fixed duration[101]. The simplest manner of achieving this is by applying a steady gradient ***g(r)*** with amplitude ***g*** for a time *t*. Carr and Purcell calculated this effect for diffusive motion as [110],

$$\frac{S(\boldsymbol{g})}{S(0)} = E(\boldsymbol{g}) = exp\left(-\frac{1}{3}\gamma^2\boldsymbol{g}^2Dt^3\right) \quad Eq.\ 105$$

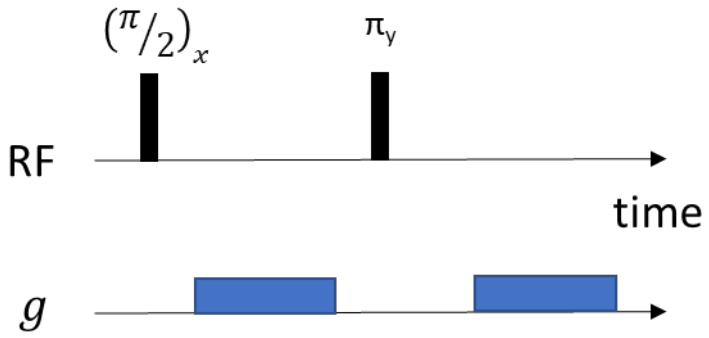


Fig. 4.3. Simple representation of the PGSE sequence. The pair of identical gradient pulses exactly compensate when there is no motion due to the reversing effect of the π pulse.

where *E(**g**)* is the signal normalized to the initial signal amplitude called signal attenuation. The application of a steady gradient quickly attenuates the signal completely due to the signals t^3 behavior, severely limiting application. A more flexible method known as the pulsed gradient spin echo (PGSE) sequence was developed by Stejskal and Tanner [111]. This sequence is simply represented in Fig. 4.3. It contains an initial π/2 pulse to excite the sample, after which two gradient pulses of duration ***δ***, magnitude ***g***, separated by an observation time **Δ** are applied to encode for motion. The π pulse occurs between the gradient pulses and has the effect of reversing the phase accumulated from previous gradients [101]. Consider a molecule encoded to position ***r*** by the first pulse, remains at that location over the observation time **Δ**. The second pulse will exactly reverse the phase from the first pulse and the spin will refocus at the correct time, contributing to the echo. Now consider a molecule which moves to position ***r'*** during the observation time **Δ** between the gradient pulses. This spin will be rotating at a different frequency and will refocus at a different time resulting in a phase shift at the center of the echo. Under random (Brownian) motion, molecules will accumulate random phase shifts resulting in a broadening and attenuation of the echo. Under coherent motion, where many spins are moving at the same velocity, the spins will refocus coherently at a different time, resulting in a uniform and

measurable phase shift [92]. The effects of incoherent and coherent motion are separable, so the attenuation from each may be considered in isolation, with a general solution being the product of the two. In the following it is assumed that the narrow gradient pulse condition is met. This condition requires the gradient pulse to be short compared to the measured molecular motion and is generally expressed as $\delta << \Delta$ and $\tau_c < \delta$ [92].

The phase shift experienced by a spin is proportional to its dynamic displacement $\boldsymbol{R} = \boldsymbol{r}' - \boldsymbol{r}$ and the wave vector $\gamma \boldsymbol{g} \delta$,

$$\phi(\boldsymbol{R}) = \gamma \boldsymbol{g} \delta \cdot (\boldsymbol{r}' - \boldsymbol{r}) \qquad \textit{Eq. 106}$$

The normalized echo signal will take the form of [92],

$$E(\boldsymbol{q}, \Delta) = \int \int \rho(\boldsymbol{r}) P(\boldsymbol{r}|\boldsymbol{r}', \Delta) exp(i\gamma\delta \boldsymbol{g} \cdot [\boldsymbol{r}' - \boldsymbol{r}]) d\boldsymbol{r}' d\boldsymbol{r} \qquad \textit{Eq. 107}$$

The product of the first two terms is the definition of the propagator $\bar{P}(\boldsymbol{r}|\boldsymbol{r}', \Delta)$, which gives the probability of displacing $\boldsymbol{R} = \boldsymbol{r}' - \boldsymbol{r}$ over time Δ. It is additionally useful to introduce the reciprocal space vector $\boldsymbol{q}$ defined as,

$$\boldsymbol{q} = \frac{i\gamma\delta \boldsymbol{g}}{2\pi} \qquad \textit{Eq. 108}$$

This allows us to write Eq. 104 as [92],

$$E(\boldsymbol{q}, \Delta) = \int \bar{P}(\boldsymbol{R}, \Delta)\, exp(i2\pi \boldsymbol{q} \cdot \boldsymbol{R}) d\boldsymbol{R} \qquad \textit{Eq. 109}$$

This form makes it clear there exists a Fourier relationship between the propagator $\bar{P}(\boldsymbol{R}, \Delta)$ and the normalized signal $E(\boldsymbol{q}, \Delta)$, this relationship is analogous to Eq. 94 for $\boldsymbol{k}$ space where the transform contains the spin density function. In the case of Eq. 106 the transform contains spin displacement which can easily be converted into velocity.

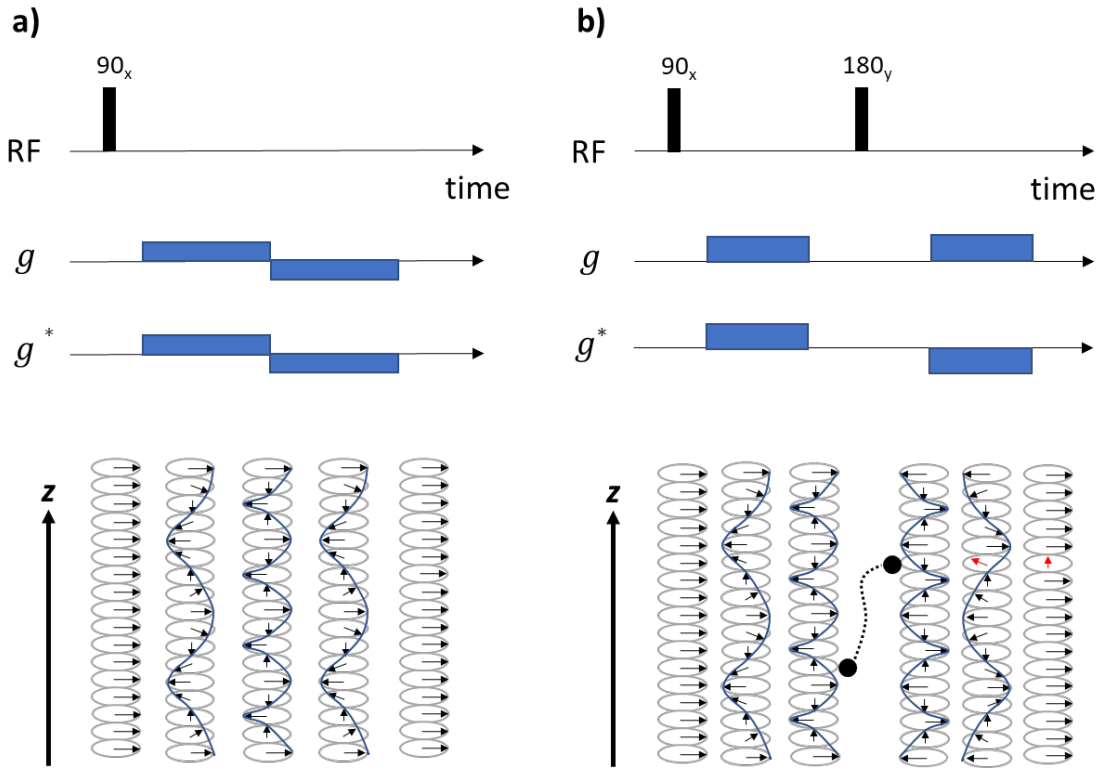


Fig. 4.4. The PGSE gradient pair can be applied either with or without an 180° pulse separating the pair. In (a) phase is unwound by switching gradient direction. In (b) an 180° pulse is used with an identical pulse pair.

The two pulsed gradients cause a de-phasing and re-phasing of the spin coherence, resulting in spins being restored to their original state and an echo to be formed. This echo formation can be accomplished through a gradient echo as in Fig. 4.4a or a spin echo as in Fig. 4.4b. The formation of an echo occurs when the echo condition is met [92],

$$\int_0^t \boldsymbol{g}^*(t')dt' = 0 \qquad \textit{Eq. 110}$$

The echo will occur at 2τ, where τ is the time between excitation and refocusing pulse. The spin echo is often preferred as it refocuses dephasing caused by inhomogeneities in the local Zeeman field.

The phase shift experienced at time *t* by a spin is equal to the product of the time dependent Larmor frequency $\omega(t')$ and its position $\boldsymbol{r}(t')$ [100],

$$\phi(\boldsymbol{r},t) = \int_0^t \omega(t') \cdot \boldsymbol{r}(t')dt' = \gamma \int_0^t \boldsymbol{g}^*(t') \cdot \boldsymbol{r}_j(t')dt' \quad \textit{Eq. 111}$$

where $\boldsymbol{g}^*(t')$ is the effective gradient which accounts for phase inversions caused by π pulses. The effective gradient can be defined by equivalence to its Hamiltonian [100],

$$\begin{aligned} \boldsymbol{\mathcal{H}}(t) &= -\gamma \boldsymbol{g}^*(t) \cdot \boldsymbol{r_j}(t)\boldsymbol{I_{jz}} \qquad \textit{Eq. 112} \\ &= -\boldsymbol{g}(t) \cdot \boldsymbol{r}_j(t)U_{rf}^{\dagger}\boldsymbol{I_{jz}}U_{rf} \end{aligned}$$

where U_{rf} is the ordered product of evolution operators from the history of RF pulses. The effect is shown pictorially in Fig. 4.4.

Coherent Motion

In real systems fluid movement is affected by contributions from velocity, acceleration, and higher order moments of the motion. Expanding the spin position into a Maclaurin series decomposition clearly presents these contributions. The ensemble averaged Maclaurin series for spin position is [109],

$$\overline{\boldsymbol{r}(t)} = \overline{\boldsymbol{r_0}} + \frac{d\overline{\boldsymbol{r}(t')}}{dt'}\Big|_0 t' + \frac{1}{2!}\frac{d^2\overline{\boldsymbol{r}(t')}}{dt'^2}\Big|_0 t'^2 + \cdots \frac{1}{n!}\frac{d^n\overline{\boldsymbol{r}(t')}}{dt'^n}\Big|_0 t'^n = \overline{\boldsymbol{r_0}} + \overline{\boldsymbol{v}_0}t' + \frac{1}{2}\overline{\boldsymbol{a}_0}t'^2 + H.O.T. \qquad \textit{Eq. 113}$$

where $\boldsymbol{r_0}$ represents the initial position, $\boldsymbol{v_0}$ the velocity (1st moment), and $\boldsymbol{a_0}$ the acceleration (2nd moment). Higher order terms (H.O.T.) have negligible impact and are generally neglected. The third moment, known as jerk is included in some special cases. Substituting Eq. 113 into Eq. 111 reveals the zero, first and second moments of the effective gradient,

$$\phi(\boldsymbol{r},t) = \gamma\left[r_0 \int_0^t \boldsymbol{g}^*(t')dt' + v\int_0^t \boldsymbol{g}^*(t')t'dt' + a\int_0^t \boldsymbol{g}^*(t')t'^2dt' + \cdots H.O.T.\right] \qquad \textit{Eq. 114}$$

This equation defines how each moment of the gradient impacts the accumulated phase shift. The echo condition (Eq. 110), requires that the zeroth moment is equal to zero, preventing

position from impacting phase in the PGSE experiment. Other gradient waveforms can be used in the PGSE sequence to produce sensitivity to velocity, acceleration, or jerk. An example of waveforms for either velocity or acceleration sensitivity are shown in Fig. 4.5. It is useful to evaluate the gradient moments [92],

$$m_1 = \int_0^t \boldsymbol{g}^*(t')t'dt' = \boldsymbol{g}\delta\Delta \qquad \textit{Eq. 115}$$

$$m_2 = \int_0^t \boldsymbol{g}^*(t')t'^2dt' = \boldsymbol{g}\delta^2\Delta \quad \textit{Eq. 116}$$

Based on these evaluations and assuming negligible impact from acceleration, the velocity can be found as,

$$\boldsymbol{v} = \frac{\phi(\boldsymbol{r},t)}{\gamma \boldsymbol{g}\delta\Delta} \qquad \textit{Eq. 117}$$

The normalized echo signal can finally be given in the moment expansion form,

$$E(t) = \frac{E(t)_{\boldsymbol{g}^*(t)\neq 0}}{E(t)_{\boldsymbol{g}^*(t)=0}} = exp\left(i\gamma \boldsymbol{r}\cdot\int_0^t \boldsymbol{g}^*(t')dt' + i\gamma \boldsymbol{v}\cdot\int_0^t t'\boldsymbol{g}^*(t')dt' + i\gamma \boldsymbol{a}\cdot\int_0^t t'^2\boldsymbol{g}^*(t')dt'\right) \qquad \textit{Eq. 118}$$

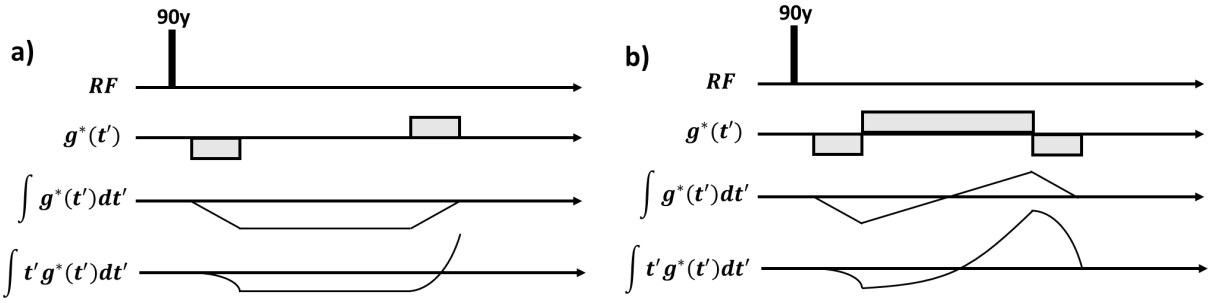


Fig. 4.5. Gradient moments can be manipulated so sequences are sensitive to velocity (a), acceleration (b) or even jerk (not shown).

Incoherent Motion: the Stejskal-Tanner Relation

Stejskal and Tanner proposed the use of the PGSE sequence for measuring diffusion in 1965 [111]. Since then it has been widely used to measure free and restricted diffusion in pure

fluids, polymers, tablets and rocks. As explained earlier, the average propagator takes the form of a Gaussian (Eq. 101). Substituting this into Eq. 107 yields [92, 101],

$$E(\boldsymbol{q},\Delta) = \int (4\pi Dt)^{-1/2} exp\left(-\frac{\boldsymbol{Z}^2}{4D\Delta}\right) exp(2\pi \boldsymbol{q}\cdot\boldsymbol{Z}) d\boldsymbol{Z} \qquad \textit{Eq. 119}$$

Evaluating this integral gives,

$$E(\boldsymbol{q},\Delta) = exp(-4\pi^2\boldsymbol{q}^2 D\Delta) \;\; \textit{Eq. 120}$$

To account for finite pulse duration and any motion which occurs during the pulse an adjustment of $\left(-\frac{\delta}{3}\right)$ is needed, resulting in the famous Stejskal-Tanner equation [92],

$$E(\boldsymbol{q},\Delta) = exp\left(-4\pi^2\boldsymbol{q}^2 D\left(\Delta - \frac{\delta}{3}\right)\right) \; \textit{Eq. 121}$$

To measure diffusion, the signal attenuation is measured at a number of $\boldsymbol{q}$ points. The data is plotted with $ln\big(E(\boldsymbol{q})\big)$ against $b = \gamma^2\delta^2\boldsymbol{g}^2\left(\Delta - \frac{\delta}{3}\right)$ with the resulting slope equal to the diffusion coefficient *D*.

In systems where both diffusion and bulk flow are present the normalized signal attenuation becomes [100],

$$E(\boldsymbol{q},\Delta) = exp\left(i2\pi\boldsymbol{q}\cdot\boldsymbol{v}\Delta - 4\pi^2\boldsymbol{q}^2 D\left(\Delta - \frac{\delta}{3}\right)\right) \qquad \textit{Eq. 122}$$

where the first term in the exponent represents the phase shift due to coherent bulk flow and the second corresponds to broadening from diffusion.

Bloch-Torrey Equation for Diffusion and Flow

In many engineering applications it is standard practice to apply conservation equations to solve for dependent properties. This was the approach taken by Torrey in 1956 when he modified Bloch's equations to account for the effects of diffusion and flow [112]. Torrey's

insight was to consider magnetization as a conserved quantity and to treat it as a fluid. This now famous result describes the general behavior of the NMR signal in complex sequences. The Bloch-Torrey equations describe phase evolution accounting for position, advection and relaxation affects.

Torrey applied Fick's Law to magnetization, accounting for relaxation as a sink term. The resulting transport of magnetization equation is given as [92],

$$\frac{\partial \boldsymbol{M_x}}{\partial t} = \gamma \boldsymbol{M_y}\left(\boldsymbol{B_o} - \boldsymbol{\omega}/\gamma\right) - \frac{\boldsymbol{M_x}}{T_2} + \boldsymbol{\nabla} \cdot D \cdot \boldsymbol{\nabla} \boldsymbol{M_x} - (\boldsymbol{v} \cdot \boldsymbol{\nabla}) \boldsymbol{M_x} \quad \textit{Eq. 123}$$

This equation can be simplified by using complex representation for magnetization $\boldsymbol{M}_+$, applying the rotating reference frame with zero frequency offset and assuming isotropic diffusion, resulting in,

$$\frac{\partial \boldsymbol{M}_+}{\partial t} = -i\gamma \boldsymbol{r} \cdot \boldsymbol{g}^*(t) \boldsymbol{M}_+ - \frac{\boldsymbol{M}_+}{T_2} + D\boldsymbol{\nabla}^2 \boldsymbol{M}_+ - (\boldsymbol{v} \cdot \boldsymbol{\nabla}) \boldsymbol{M}_+ \qquad \textit{Eq. 124}$$

The solution to this equation for a general pulsed-gradient sequence is [92],

$$\boldsymbol{M}_+(\boldsymbol{r}, t) = A(t) exp\left(-i\gamma \boldsymbol{r} \cdot \int_0^t \boldsymbol{g}^*(t')\, dt'\right) exp(-t/T_2) \quad \textit{Eq. 125}$$

where $A(t)$ is a modulation factor. The first exponential reduces to one at the echo center due to the familiar echo condition. The second exponential term accounts for T_2 relaxation. When the echo condition is met, $A(t)$ reduces to the normalized echo amplitude resulting in [92],

$$E(t) = exp\left[-D\gamma^2 \int_0^t \left(\int_0^{t'} \boldsymbol{g}^*(t'')dt''\right)^2 dt'\right] exp\left[i\gamma \boldsymbol{v} \cdot \int_0^t \int_0^{t'} \boldsymbol{g}^*(t'')dt''dt'\right] \quad \textit{Eq. 126}$$

with zeroth, first and second gradient moments of,

$$\int_0^{2\tau} \boldsymbol{g}^*(t')dt' = 0$$

$$\int_0^t \int_0^{t'} \boldsymbol{g}^*(t'')dt''dt' = -\boldsymbol{g}\delta\Delta \qquad \textit{Eq. 127}$$

$$\int_0^t \left(\int_0^{t'} \boldsymbol{g}^*(t'')dt'' \right)^2 dt' = \boldsymbol{g}^2\delta^2(\Delta - \delta/3) \quad \textit{Eq. 128}$$

MRI Velocimetry

When studying fluid dynamics, the perspective being used to describe the flow is very important. The perspective can be Eulerian, that of a stationary observer who describes the fluid as it moves past a specific point in the flow. This is the perspective of most experimental techniques, such as PIV, or hot-wire-anemometry. The other perspective is known as the Lagrangian perspective, where the perspective is that of the flowing fluid. These equations describe the path the fluid takes over time. In many ways this is the natural perspective for describing fluid dynamics when transport is of interest. The perspective provided by NMR measurement is fundamentally Lagrangian, as it is the motion of the fluid molecules that is measured, in stark contrast to other methods which infer a particles motion based on diffraction of light passed perpendicular to the flow. Where instantaneous measurements provide little insight into the dispersive components of complex flows, the tag and observe approach of NMR can provide greater insight into the transport process.

Velocity imaging can be accomplished with the PGSE sequence by incorporating one of the imaging schemes described in Chapter 3. Once the signal is processed, the result is an image where each voxel contains the average velocity in the direction of the displacement encoding gradient [92]. A standard PGSE velocity imaging sequence is shown in Fig. 4.6 below. The sequence includes imaging gradients $\boldsymbol{G}$ for encoding spatial position $\boldsymbol{r}$ and pulsed gradients $\boldsymbol{g}$ for encoding displacements $\boldsymbol{r'} - \boldsymbol{r}$. The signal encoded for both $\boldsymbol{k}$ and $\boldsymbol{q}$ space is described by,

$$S(\boldsymbol{k}, \boldsymbol{q}) = \int \rho(\boldsymbol{r}) exp(i2\pi \boldsymbol{k} \cdot \boldsymbol{r}) \int \bar{P}(\boldsymbol{r}|\boldsymbol{r'}, \Delta) exp\big(i2\pi \boldsymbol{q} \cdot (\boldsymbol{r'} - \boldsymbol{r})\big) d\boldsymbol{r'} d\boldsymbol{r} \quad \textit{Eq. 129}$$

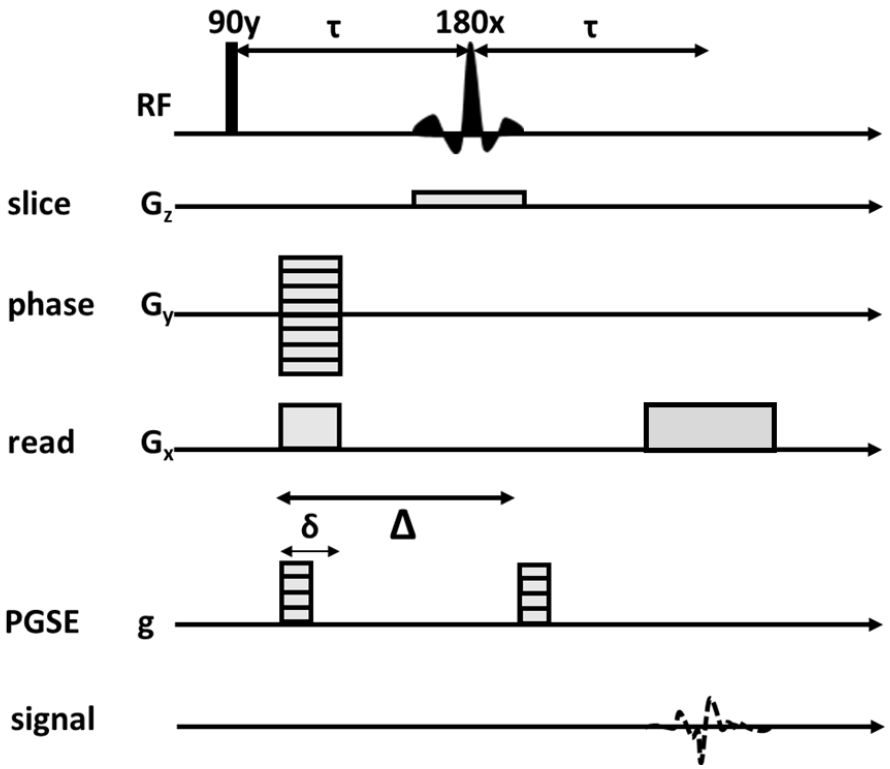


Fig. 4.6. Timing diagram for the PGSE sequence with phase-frequency imaging.

Imaging the Propagator

The direction of ***k***- and ***q***- space are independent so the imaging slice and measured velocity can be oriented in the same or different coordinate directions. Generally, slice selection is performed, resulting in a two-dimensional image of $\boldsymbol{k}_{read}$ x $\boldsymbol{k}_{phase}$ and a third ***q***-encoded dimension [109]. This is a time intensive sequence, requiring an acquisition for each spatial phase step, at least two for phase cycling, all repeated for each ***q***-step. The spatial phase is usually 64, 128 or 256 point and ***q***-steps from 8 to 32, resulting in at minimum of 1024 acquisitions [109]!

Data processing for the combined ***k*** and ***q*** space encoded signal follows the scheme outlined in Fig. 4.7. The complex signal is Fourier transformed with respect to the ***k*** space

dimensions, resulting in a stack of $\boldsymbol{q}$ encoded images of complex signal. The normalized signal takes the form of [92],

$$E(\boldsymbol{q},\Delta,\boldsymbol{r}) = E(0,\Delta,\boldsymbol{r})exp(i\boldsymbol{q}\boldsymbol{v}\Delta)exp(\boldsymbol{q}^2 D\Delta)$$

$$= \rho(\boldsymbol{r})exp\left(i(\gamma\delta\Delta\boldsymbol{v})\left(\frac{\boldsymbol{g_m}}{n_D}\right)n\right)exp\left(-\gamma^2\delta^2\left(\frac{\boldsymbol{g_m}}{n_D}\right)^2 Dn^2\Delta\right) \qquad \textit{Eq. 130}$$

Further Fourier transformation along the $\boldsymbol{q}$ dimension for n voxels, results in a spectrum of the dynamic disablement for each voxel. The propagator resulting from the product in Eq. 130 is the convolution [92],

$$\bar{P}(k/N,\Delta) = \left(\frac{\pi n_D^2}{\gamma^2\delta^2 g_m^2 D\Delta}\right)^{1/2} exp\left(-\frac{\pi^2 k^2 n_D^2}{\gamma^2\delta^2 g_m^2 N^2 D\Delta}\right) \otimes \delta\left(\frac{k}{N} - \frac{\gamma\delta v\Delta g_m}{2\pi n_D}\right) \qquad \textit{Eq. 131}$$

where N is the number of points in the digital FT (phase points plus zero-fill), k (not to be confused with $\boldsymbol{k}$) is the digital value ranging from -N/2 to N/2 – 1. The peak center occurs at,

$$k_v = \frac{N\gamma\delta\boldsymbol{v}\Delta\boldsymbol{g_m}}{2\pi n_D} \quad \textit{Eq. 132}$$

which can be reordered to find the mean molecular velocity,

$$\boldsymbol{v} = \frac{2\pi n_D k_v}{N\gamma\delta\Delta\boldsymbol{g_m}} \qquad \textit{Eq. 133}$$

The full-width-half-maximum (FWHM) of $\bar{P}$ can be used to find the diffusion coefficient as,

$$D = \frac{(n_D k_{FWHM})^2}{[(4ln(2)/\pi^2)\gamma^2\delta^2\boldsymbol{g}_m^2 N^2\Delta]} = 3.56\frac{(n_D k_{FWHM})^2}{\gamma^2\delta^2\boldsymbol{g_m^2}N^2\Delta} \quad \textit{Eq. 134}$$

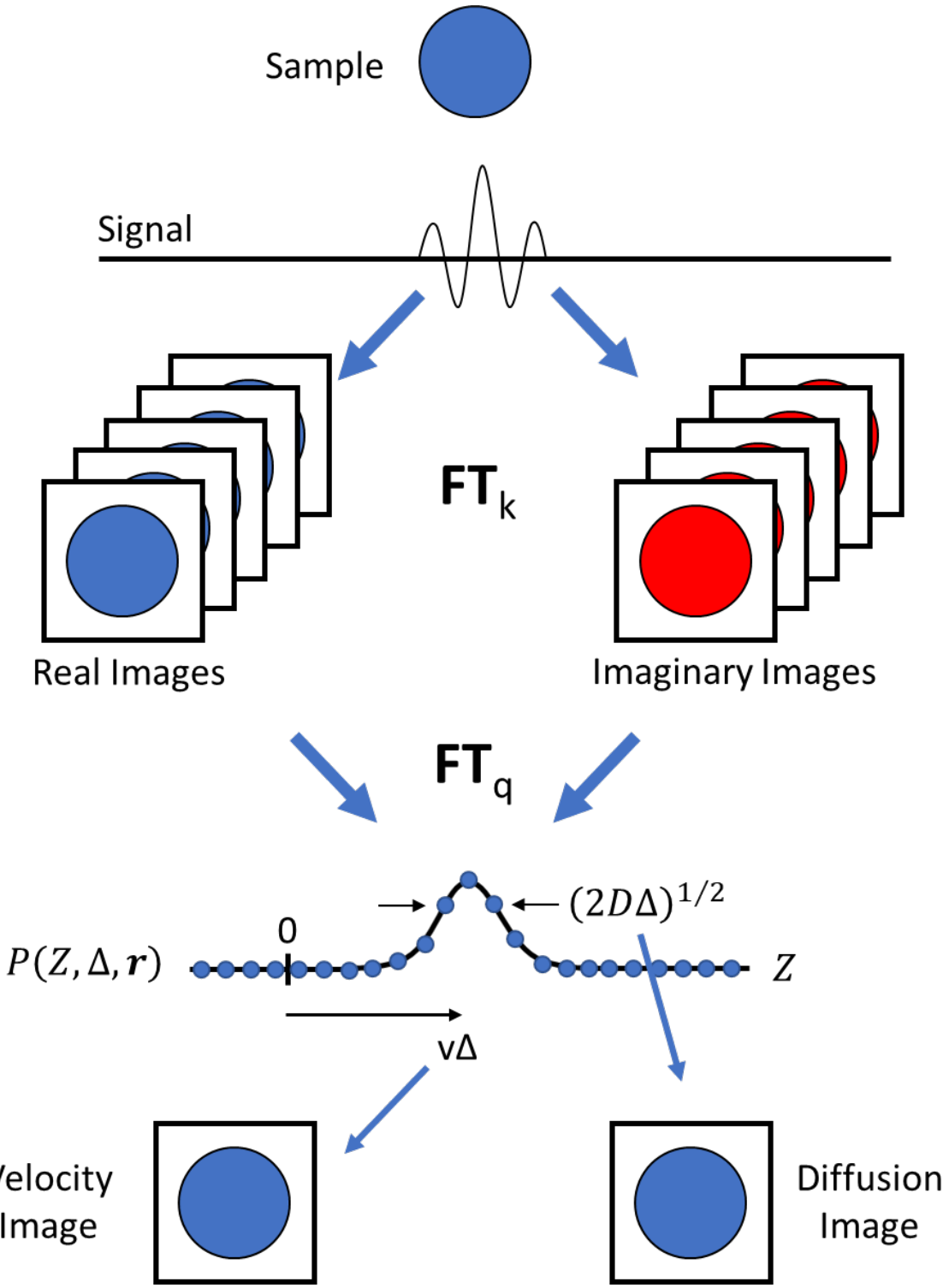


Fig. 4.7. Flow diagram for processing combined ***k***-and ***q***-space imaging data. FT in ***k***-space direction produces real and imaginary images each ***q*** step. An additional FT in the ***q***-direction produces a displacement propagator for each pixel which can be used to produce images where each pixel represents the average velocity or diffusion rate.

Velocity Imaging

Images of the full propagator contain an extraordinary amount of information on the fluid dynamics occurring. The long scan times required to form these images are fine when studying steady state systems but can be unacceptable where flows are evolving quickly. When only the average velocity at each pixel is of interest a single $\boldsymbol{q}$-step can be collected along with a null $\boldsymbol{q}$ image in a technique called single-step phase-encoding [92]. This two-step experiment results in,

$$\frac{E(q_1,\Delta,\boldsymbol{r})}{E(0,\Delta,\boldsymbol{r})} = A\ exp(i\boldsymbol{q_1}I\Delta) \qquad Eq.\ 135$$

where A is an attenuation factor of < 1.

The velocity image can also be found by Fourier transformation in the $\boldsymbol{k}$ and $\boldsymbol{q}$ space dimensions. However, since there are only two $\boldsymbol{q}$ space points, FT essentially only returns one piece of information, the velocity.

MR Temperature Measurement

Fluid flow and heat transfer are complex processes highly dependent on secondary flows, stagnation, and separation which make prediction of it difficult. This is compounded by limitations in available techniques for measurement and validation. NMR provides a means to spatially resolve fluid velocities and temperatures in optically inaccessible locations. The study of fluid motions via magnetic resonance velocimetry techniques is well established; however, methods for magnetic resonance thermometry (MRTh) have proven more difficult due to low sensitivity and occurrence of multiple dependencies which obscure temperature measurement [93].

NMR parameters sensitive to temperature include proton resonance frequency (PRF), diffusion coefficient, magnetization transfer, T_1 and T_2 relaxation rates, proton density and through temperature-sensitive contrast agents [93]. MRTh based on PRF, diffusion and T_1 relaxation have received the most attention due to the applicability to medical applications *i.e.* ablation and hyperthermia therapy [113]. PRF techniques have also been used recently to study engineering flows [114-116]. T_2 relaxation has received much less attention due to its dependence on dipolar interactions which introduces a dependence on changes to spin environment other than temperature. For example, during ablation therapy, degeneration of tissues changes the structural environment of the spins, shifting the T_2 relaxation rate on the same scale as temperature changes, thereby confounding temperature measurement. In systems where the environment of the spins is controlled, the speed of measurement and sensitivity to temperature give T_2 relaxation-based methods an advantage.

T_2 relaxation is a measure of how long the transverse magnetization takes to decay, as described by,

$$S(t) = S_o exp\left(-\frac{t}{T_2}\right) \quad Eq.\ 136$$

T_2 is determined by plotting the signal at different times after excitation and fitting the result to the above equation. The evolution of signal magnitude can be recorded with either a multi-echo (CPMG-like) or multi-excitation technique. The CPMG technique has the advantage of faster acquisition times, recording signal magnitude at each echo with spacing of 2τ. With this technique, T_2 can be measured with a single excitation (imaging still requires an excitation for each phase step). With the multi-excitation technique, a single echo is recorded for each excitation and echo time is increased until the signal completely decays. This technique is

generally only performed when the sample is very sensitive to RF power input (melting ice) or during multi-dimensional sequences which require multiple excitations regardless (T_1-T_2 sequence).

The rate of relaxation is directly related to the correlation time τ_c of molecular motion, where τ_c characterizes the time between molecular collisions. This time can be defined as,

$$\tau_c = \frac{4\mu a^3}{k_B T} \qquad Eq.\ 137$$

where μ is the viscosity, a the effective radius, k_B the Boltzmann constant and T temperature. The inverse relation to temperature suggests the correlation time will decrease with increasing temperature. The dependency of viscosity on temperature will also affect how correlation time changes with temperature.

The decreases in correlation time with increased temperature, reduces the interaction time between molecules. This leads to a decreased probability of dipolar couplings and associated energy release (relaxation). As a result, T_2 times are inversely related to correlation time and proportional to temperature. T_2 relaxation can be defined based on correlation time as,

$$\frac{1}{T_2} = C\left(3\tau_c + \frac{5\tau_c}{(1+\omega_o^2\tau_c^2)} + \frac{2\tau_c}{(1+4\omega_o^2\tau_c^2)}\right) \qquad Eq.\ 138$$

where C is a constant related to molecular diameter, and the three terms related to the spectral density functions associated with quantum transitions as discussed earlier.

CHAPTER FIVE

MELT-FRONT PROPOGAION AND VELOCITY PROFILES IN PACKED BEDS OF PHASE-CHANGE MATERIALS MEASURED BY MAGNETIC RESONANCE IMAGING

Contribution of Authors and Co-Authors

Manuscript in Chapter 5

Author: Matthew E. Skuntz

Contributions: Wrote manuscript. Collected and analyzed data. Implemented experimental system. Incorporated revisions and provided feedback on reviewer comments.

Co-Author: Dinal Perera

Contributions: Edited manuscript. Assisted in data collection. Helped implement experimental system.

Co-Author: James E. Maneval

Contributions: Edited manuscript. Wrote Temperature and NMR section. Provided training on experimental methodology. Assisted in data collection.

Co-Author: Joseph D. Seymour

Contributions: Edited manuscript. Conceived experimental method. Assisted with data collection. Provided training on experimental methodology. Secured funding.

Co-Author: Ryan Anderson

Contributions: Edited manuscript. Conceived experimental method. Secured funding.

Manuscript Information Page

Matthew E. Skuntz, Dinal Perera, James E. Maneval, Joseph D. Seymour, and Ryan Anderson

Chemical Engineering Science

Status of Manuscript: (Put an x in one of the options below)
___ Prepared for submission to a peer-reviewed journal
___ Officially submitted to a peer-reviewed journal
___ Accepted by a peer-reviewed journal
_X_ Published in a peer-reviewed journal

Elsevier Volume 190, pages 164-172, November 2018

https://doi.org/10.1016/j.ces.2018.06.019

MELT-FRONT PROPOGATION AND VELOCITY PROFILES IN PACKED BEDS OF PHASE-CHANGE MATERIALS MEASURED BY MAGNETIC RESONANCE IMAGING

Abstract

Fluid flow and heat transfer characteristics in packed beds are of importance in many fields of study. However, experimental characterization and model validation of the numerical methods used to study packed beds is difficult. Utilizing nuclear magnetic resonance (NMR), we present a novel approach to track the melt front (and thus melt temperature) in a non-isothermal packed bed. The approach tracks the melt front through packed beds of wax encapsulated phase change material (PCM) by taking advantage of the change in T_2 associated with phase change. Additionally, velocity maps of the flow in the pore space of the same packed bed sample are obtained. The approach uses the ^{1}H signal from the PCM packing and a ^{19}F signal from the flowing fluid to allow monitoring of both particle bed structure/phase and flow velocities in the same sample with the use of a dual tune coil. Together, this information can be used to probe the heat transfer characteristics of packed beds experimentally.

Key words: heat transfer, packed beds, NMR, velocity mapping, phase-change materials

Introduction

Packed beds are widely used in operations such as thermal energy storage from solar-power facilities [117, 118], industrial waste heat recovery [119], and fixed bed catalytic reactors [120]. While current design approaches for these systems are well guided by principles at the input-output macroscale, further improvements to design next-generation versions of these units will have to rely on better understanding of transport processes at the pore microscale. A key

challenge to the development and use of effective microscale models is the lack of detailed experimental measurements of temperature and velocity fields at the same scale. Such measurements are critical for assessing the performance of models at the microscale. Current experimental approaches are limited to temperature and flow measurements at the input and output of the units [120, 121] or via thermocouple measurement of temperature at fixed locations within the bed [122-124]. The relatively low spatial density of these measurements does not provide enough information at the spatial resolution needed for pore scale model validation and cannot correlate the results to the local velocity. As a consequence, the use of only macroscale measurements for testing predictions of the microscale has led to wide scatter in correlations for key design parameters such as interphase heat-transfer coefficients [47] as well as larger-than-desired uncertainties in the sizes of final unit designs.

Nuclear magnetic resonance and magnetic resonance imaging (MRI) methods have proven to be powerful techniques for measuring features of transport in porous media [30, 95, 101, 125-133]. For example, NMR and MRI have been used to measure dispersion in packed-bed flows, porosity and density maps, pore surface to volume ratios and pore size distributions at length scales from 10 microns to 100 mm. Importantly, the non-invasive nature of NMR allows for these measurements to be made *in situ*, and real-time observations are possible. Hence, NMR and MRI methods are uniquely suited for observation and measurement of transport processes at the length scales needed to assess and validate proposed microscale models that can improve designs of packed-bed devices.

Many NMR parameters are sensitive to temperature [134]. These include active nuclei density, T_1 and T_2 relaxation rates, diffusion coefficients, magnetization transfer rates, and

changes in chemical shifts [108, 114, 134-142]. While these parameters provide ample means for temperature mapping, many of them interact and can depend on sample heterogeneity. The approach here provides a robust alternative method for the study of energy transport processes. In the current study, bed particles containing ^{1}H and a pore fluid containing ^{19}F enables monitoring of both the solid phase and the pore space separately in the same sample akin to the approach of Boyce *et al.* applied to fluidized beds [143]. Porous media structure was composed of wax encapsulated in a plastic shell, PCM particles. Pore space was filled with fluorinated oil heated to a specific temperature by a heat bath, and pumped through an insulated flow loop. By tuning to the ^{1}H frequency (300 MHz), one dimensional (1D) and two dimensional (2D) imaging of the melt front propagating through the bed was possible. In addition to this, velocities in the pore space were recorded from the ^{19}F frequency (282.4 MHz), allowing for visual comparison of melt dynamics to velocity distribution *in situ*, with no signal degradation due to signal in the pore space and particle bed interacting.

The work reported here entails three main points. First, we present and discuss aspects of the experiment, particularly the materials used for the study, and how the changes in T_2 for the material can be interpreted. Second, we summarize imaging and flow measurements of the transport dynamics of a packed bed whose solid phase contains a phase-change material. Finally, we assess the results with a view toward what can currently be measured and the connections of this approach to detailed quantification of heat transfer processes in PCM units.

Experimental Setup and Methods

The key elements of the experiment are a continuous-flow loop for circulating a fluorinated heat-transfer fluid through a packed bed inside the magnet system. The packed bed

was constructed from a high-performance liquid chromatography column (Kinesis USA, OmniFit Benchmark HIT 10-150-AF) with a 10 mm inner diameter. The inlet and outlet fittings could be adjusted to allow bed lengths of 50-150 mm. A flow system was built to allow for continuous flow and heating of the pore-phase fluid through the bed, shown in Fig. 5.1. Flow rates were varied from 200 mL/hr to 400 mL/hr with inlet temperatures of approximately 39ºC. The solid phase of a packed bed was composed of 5-15 μm encapsulated eicosane wax capsules agglomerated into 3.7-5 mm diameter spheres (Microtek Encapsulation Technologies). Two waxes of different melting points are shown to have NMR relaxation properties useful for application here, octadecane filled macroPCM28 (T_M = 28˚C) and the eicosane filled macroPCM37 (T_M = 37˚C). The packed bed of macroPCM37 is studied in detail. The fluid phase was Fluorinert FC-43 (3M Corporation), a heat transfer fluid, chosen for its heat transfer characteristics and high fluorine density. The fluid system used a dual syringe pump (Pharmacia P-500) to pump the fluid through a temperature-controlled bath. On exit from the bath, the fluid line temperature was maintained by using a counter-current double-pipe heat exchanger that spanned the distance from the bath to the base of the magnet. Calibration experiments were performed to obtain the actual probe-inlet temperature from the settings on the temperature-controlled bath.

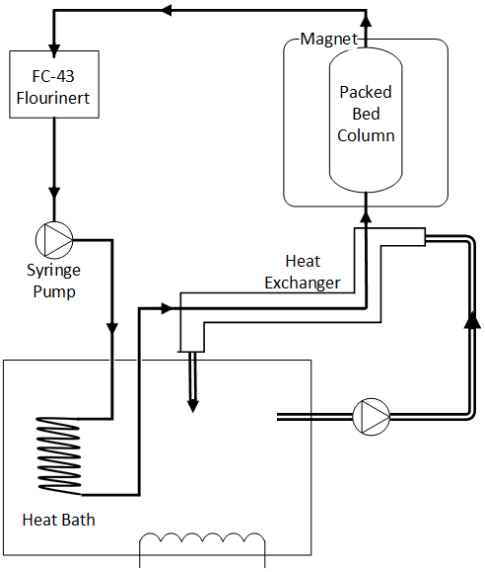


Fig. 5.1. Schematic of the heated Fluorinert flow loop. Fluid was heated after the pump with a heat bath, and the temperature was maintained to the base of the probe with a counter-flow heat exchanger. Relationship between sample inlet and bath set temperatures was determined in a separate experiment.

NMR and MRI measurements were performed on a vertical wide-bore Bruker Avance III 300 Spectrometer at 7 Tesla (300 MHz nominal proton frequency, 282.4 MHz nominal fluorine frequency) controlled by ParaVision 5.1 software on a Linux operating system. The receive/transmit coil was a $^{1}H/^{19}F$ dual tuned bird-cage with an internal working diameter of 25 mm and an active imaging length of about 40 mm. Shielded gradient coils (Micro 2.5, Bruker) for imaging and flow measurements had maximum gradient strengths of 1.5 T/m at 60 A. Images were formed using both the ^{1}H and ^{19}F resonances. The ^{1}H images of the PCM material were made using a multi-echo spin-warp imaging sequence. Imaging methods included one-dimensional frequency-encoded profiles in the direction of flow through the bed, as well as two-dimensional (phase- and frequency-encoded) images of either the bed cross-section (transverse images) or the bed profile (longitudinal images). 1D profiles could be acquired rapidly (< 15 seconds needed for image acquisition) while the (2D) images required a somewhat longer time

(between 1 and 2 minutes for full acquisition). Different regions of the bed were probed using varying slice position with set thickness. Image processing used Prospa V3.13 (Magritek) and MATLAB R2016a (Mathworks).

The field of view for transverse images was 12 mm by 12 mm and were acquired using 128 frequency-encode and 64 phase-encode data points. For longitudinal images, the field of view was 40 mm by 12 mm and acquisition of 256 by 64 data points. Nominal image spatial resolutions were 94 μm by 188 μm in transverse images and 156 μm by 188 μm in the longitudinal images based on the fields of view and number of acquisition points. For longitudinal images, three slices were acquired per scan without significant image acquisition time increase, each with a slice thickness of 1 mm and offsets of 3 mm in the direction perpendicular to flow. For transverse images, five slices were acquired per scan, each with a slice thickness of 1 mm and with slice offsets of 5 mm in the direction of flow. The 1D profiles were collected with 128 points without slice selection so that the slice thickness covered the entire sample in order to clearly show the melt propagation in the axial direction. Image acquisition parameters were Echo Time (TE) = 8.06 ms, Repetition Time (TR) = 1000 ms, Number of Averages (NA) = 4 for 1D profiles, and TE = 10.6 ms, TR = 1000 ms for 2D longitudinal and TE = 8.06 ms, TR = 1000 ms, NA = 1 for 2D transverse images.

Velocity images were obtained from the ^{19}F signal with a two-step phase-encode pulsed-gradient spin echo (PGSE) sequence using both transverse and longitudinal imaging slices [92]. Slices were centered in packing and taken post melt at elevated temperature. Typically, 16 averages were acquired for longitudinal scans and 8 averages for transverse scans with total acquisition times lasting 68 min for longitudinal and 34 min for the transverse. The gradient

separation time (Δ) was 11.1 ms and the duration (δ) was 1 ms. Gradient amplitudes were varied with flow rate. A range of +/-0.0395 to +/- 0.0198 T/m provided a suitable window for the longitudinal velocity and +/- 0.198 to +/- 0.0741 T/m for the transverse velocities. The spatial resolution of the velocity images was the same as the corresponding ^{1}H images with TE = 16.4 ms and TR = 1000 ms.

The ^{1}H NMR spectrum of the PCM material consisted of one peak while the ^{19}F spectrum of Fluorinert had multiple peaks (Fig. 5.2) that introduced chemical shift artifacts into the PGSE velocity images. To eliminate these artifacts a chemical selective 180° radiofrequency (RF) pulse was used with a slice selective 90° pulse of 900 Hz ~ 3.2 ppm, thus refocusing and fully encoding only the ^{19}F signal from the resonance at 0 ppm in Fig 5.2. The bandwidth of the selective pulse was also reduced to a small value and the slice positions were limited to a zero offset from the gradient center.

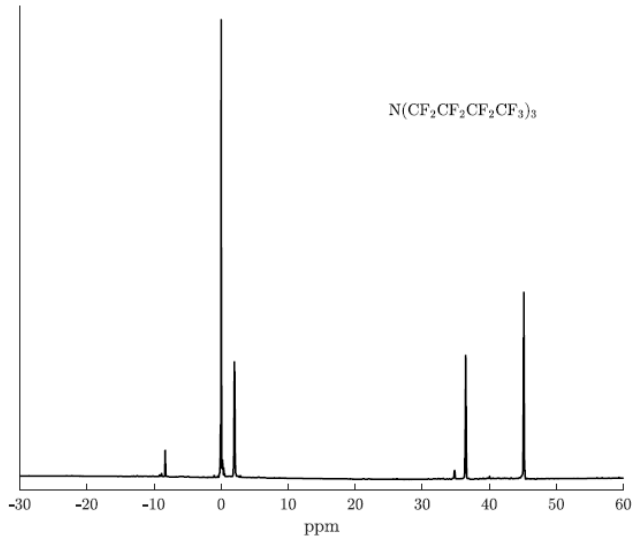


Fig. 5.2. Fluorinert FC-43 spectra with multiple peaks required a narrow bandwidth slice selective RF pulse centered on the largest peak at 0 ppm in the velocity imaging sequence to prevent chemical shift artifacts.

Results and Discussion

Velocity Images of Bead Pack

Velocity images for flow in the *x*, *y* and *z* coordinate directions are shown for longitudinal (Fig. 5.3) and transverse (Fig. 5.4) image orientations.

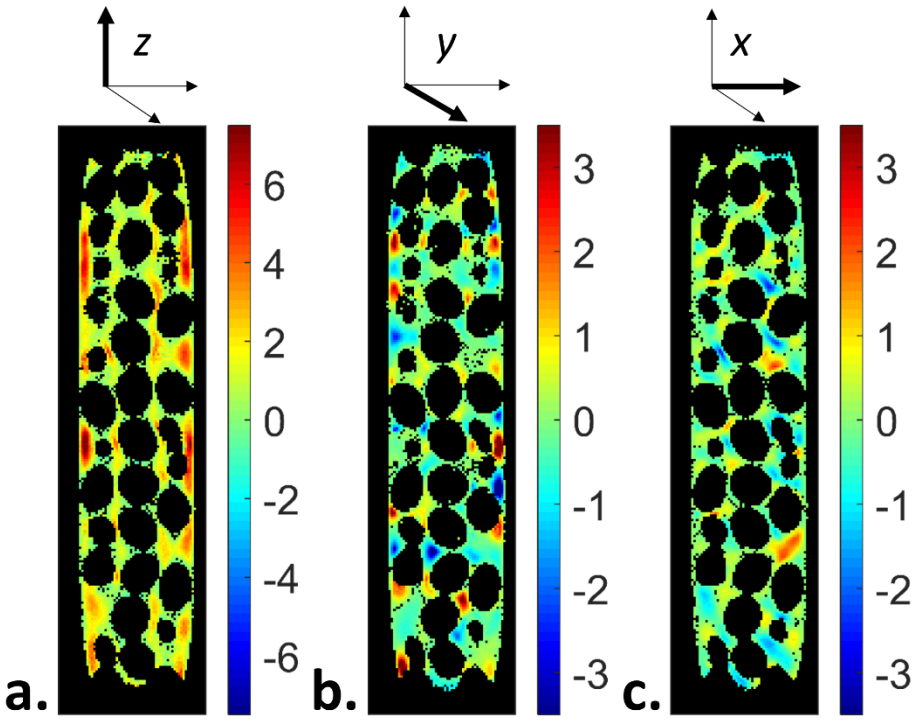


Fig. 5.3. Longitudinal velocity maps of flow at a fixed volumetric flow rate of 200 ml/hr in the z, y and x coordinate directions with melted PCM37 (at 39o C). Velocity maps are located along the center of the packed bed. Resolution is 0.156 mm/pixel in the z direction and 0.188 mm/pixel in the x direction. Image 3a shows z velocity, 3b y velocity and 3c x velocity. Max velocity in mm/s for the images are 8.70 (a), 6.74 (b), 2.30 (c).

The velocity maps show expected features of flow in the pore space with maximum velocities occurring at locations furthest away from the walls of the column and the particle surfaces. Comparing Fig. 5.3 and 5.4, the helical like flow paths are evident. Direct

measurement of the spatial distribution of velocity allows for direct correlation with the spatial distribution of the temperature front through particle melting.

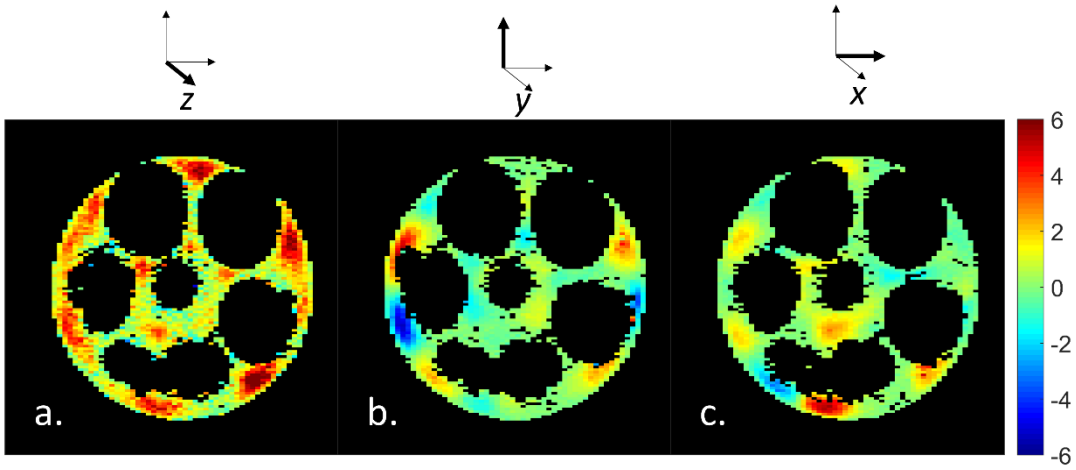


Fig. 5.4. Transverse images of velocity in z, y and x coordinate directions centered longitudinally in imaging area. Images are taken with constant volumetric flow rate of 200 ml/hr with 8 averages and were acquired over a 34 min time frame. Spatial resolution of images is 0.188 mm/pixel in y and 0.094 mm/pixel in the x direction. (a) Velocity into/out of the page, (b) top to bottom, and (c) left to right. Max velocity in mm/s for each image is 7.53 (a), 5.57 (b), 5.53 (c).

Temperature and the NMR Signal

The ^{1}H in the encapsulated eicosane wax is the source of signal for the temperature front imaging. Since no ^{1}H bearing materials are added or removed from the sample in the experiments, image intensity changes over the course of an experiment are due to changes in the energy state of the wax molecules. For the melting experiments here, changes in the energy state of the PCM are due to the change in temperature as the sample warms from the initial bed temperature to the temperature of the heating fluid, and the change in energy due to the melting transition i.e. the latent heat of melting.

The effects of temperature on the NMR signal for a single phase system are well known, and chemical shift, T_1 and T_2 relaxation times, diffusion coefficients and magnetization transfer

properties are all impacted by changes in temperature [134]. The susceptibility of the material follows the Curie Law with the magnetization being proportional to the reciprocal of the absolute temperature [144]. For most materials, this effect is modest but represents an effect that can connect the NMR signal to changes in the sample temperature. NMR chemical shifts are sensitive to temperature; however, spectral resolution in images requires pure phase encoding and longer acquisition times. The primary effect of temperature on NMR signal is that from the solid to liquid phase change due to changes in molecular mobility of the material. When the molecular mobility changes, as measured by the rotational and translational correlation times of a material, the NMR T_1 and T_2 relaxation rates are significantly impacted [93]. Measurements taken at different temperatures but fixed echo times then give signal intensities that reflect the impact temperature has on the T_2 relaxation. Hence T_2-mapping methods provide temperature measurements due to energy changes altering molecular mobility [145].

This indirect effect of temperature on the signal through changes in mobility has a further important impact on the observations here. As the PCM warms from its initial temperature, the material reaches a phase-transition temperature (T_m) where the sample goes from a solid to a liquid state. At this point, the hydrogens associated with the wax in the PCM experience a step jump increase in mobility. Hence, large signal changes are observed at a specific temperature that reflects the melting of the PCM as it absorbs or releases energy at its solid/liquid transition temperature.

Fig. 5.5 demonstrates the changes that can be monitored in these materials as they pass from solid to liquid states. The 1D signal profiles shown in each plot consist of a room temperature profile (21˚C, lower traces) and a profile for the same material at a temperature

approximately 22˚C above the nominal melting temperature of the encapsulated wax (T_m = 28˚C for PCM28 and T_m = 37˚C for PCM37, upper traces). The effect of the melting phase transition noted above is clear and significant. The magnitude of signal gain on melting thus suggests that the imaging of melting fronts will be robust.

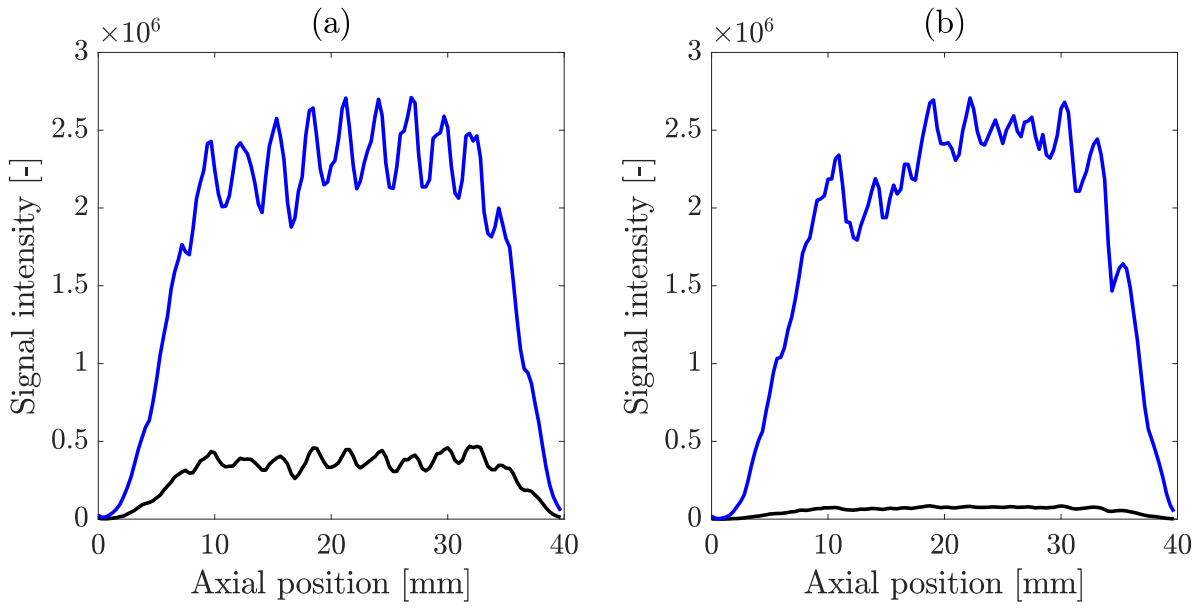


Fig. 5.5. One-dimensional axial signal profiles for (a) PCM28 and (b) PCM37. In (a), the lower trace was taken at room temperature while the upper trace was taken at 50˚C. In (b), the lower trace was also at room temperature but the upper trace was at 60˚C.

The lower traces in Fig. 5.5 also provide insights into other thermal effects leading up to a melting transition that might be usefully connected to NMR measurements. For PCM28 (Fig. 5.5a), the room temperature profile is only about 7˚C below the melting temperature while for PCM37 (Fig. 5.5b), that difference is about 16˚C below the melting temperature. The higher signal intensity of the PCM28 relative to PCM37 at the same temperature suggests that mobility changes in a material as its melting point is approached could also lead to useful NMR signal changes suitable for temperature changes associated with non-phase-change (sensible) heat

effects. In what follows, however, we focus on the dominant effects of the melting phase transition to track phase front motion.

One-Dimensional Profiles

One-dimensional longitudinal profiles (Fig. 5.6) quantitatively track the axial progression of the melt front through the packed bed. The measurements are acquired rapidly and contain spatial information on the axial energy transport. Fig. 5.6a shows 1D profiles for melting with fluid flow at 39˚C while Fig. 5.6b shows 1D profiles for solidification of the bed with flow at 22˚C. Fig. 5.7 shows solidification under no flow conditions. Profiles in Fig. 5.6 and 5.7 are all 2.5 minutes apart. The profiles in Fig. 5.6 and 5.7 provide a range of data useful for understanding the dynamics of the melting/solidification process. The progression of a melting front from the fluid inlet to outlet is clear in the changes of 1D signal with time (Fig. 5.6a). There is a slow increase in the signal, likely due to temperature changes associated with sensible heat changes of the material ahead of the larger change in signal associated with the material phase change. Finally, the profiles coalesce into a final profile that corresponds to the fully-melted material at its final temperature. The series of profiles in Fig. 5.6b shows a solidification front moving in a similar way through the bed but with signal intensities that fall with time.

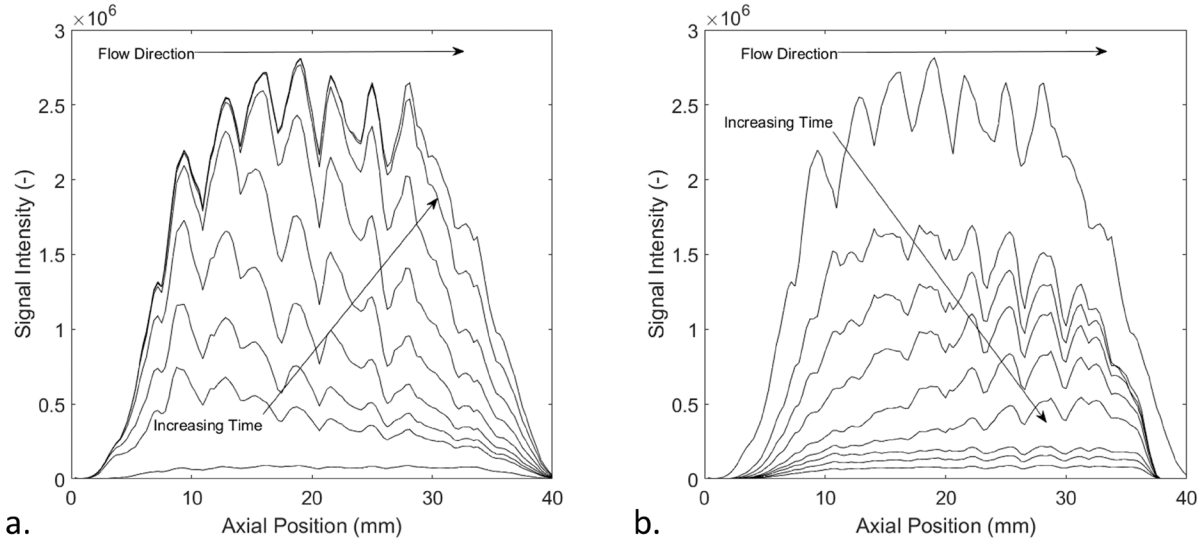


Fig. 5.6. 1D profiles for two different phase changes of PCM37 (a) melting and (b) solidification during flow of fluid. The interval between each line is 2.5 minutes. Flow is from left to right, where the abscissa is location from inlet in the vertical packed bed.

The peaks and valleys seen in the Fig. 5.6 profiles are the result of the ordered packing of the 5 mm PCM spheres in a tube with a diameter of 10 mm. This particle-to-tube diameter ratio leads to poorly packed beds with the PCM spheres forming distinct layers within the bed, which lead to packing inhomogeneities. This bed-structure is clearly observed in the 2D images shown below. The packing of the bed allows the pore scale fluid velocity to be imaged and the melt-front signal quantified. It should be noted that Fig. 5.6a, Fig. 5.6b, and Fig. 5.7 are of different packed beds *i.e.* the column was emptied and refilled between experiments, resulting in different profiles. This does not impact the determination of the melt front location.

The no-flow profiles in Fig. 5.7 show a steady, uniform decline in signal across the whole sample, consistent with a cooling process that is dominated by energy transfer from the sample via conduction rather than advection, as was the case for Fig. 5.6a and 5.6b. The rate of convective energy exchange can be observed to change with the temperature difference between

the PCMs and the heated fluid as diminishing vertical jumps in signal between adjacent profiles. The effect can be observed at long times under heating and cooling conditions. At long times in Fig. 5.6a, the dominant heat transfer mechanism changes from convection to conduction, identified as the uniform signal decrease in the last three profiles. These results demonstrate that the NMR measurements are sensitive to the nature of the transport processes in the bed.

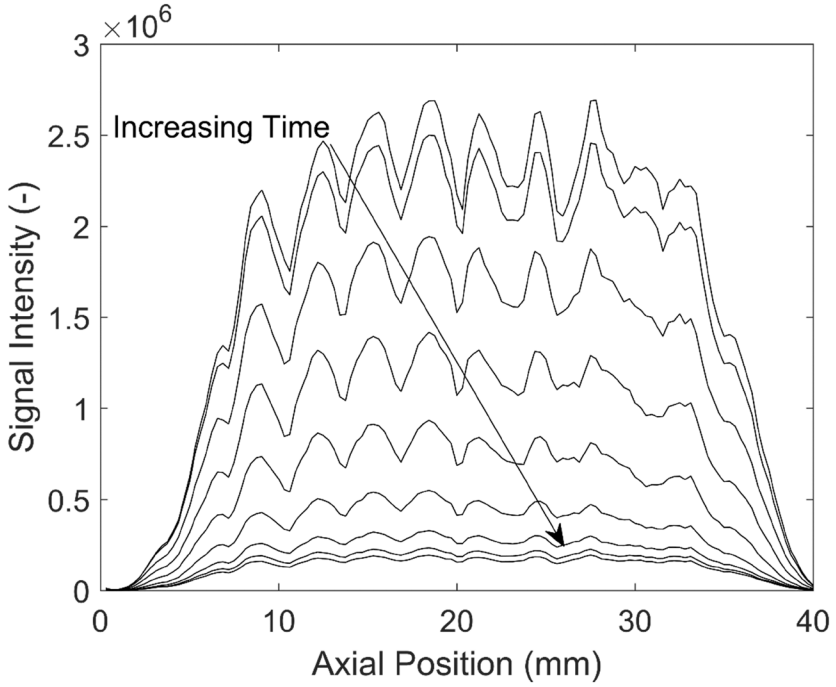


Fig. 5.7. Cooling of a previously melted bed of PCM37 with no internal flow. The interval between each line is 2.5 minutes. Results are consistent with cooling via conduction.

Two Dimensional Images

The one-dimensional profiles capture the fine details of time dependent energy transport during axial melting of the bed. Two-dimensional images provide more detailed spatial information about melt variations across the sample but do so at the cost of temporal resolution. In addition, these images provide direct connections to the pore scale fluid dynamics measured in the velocity maps.

The 2D longitudinal images in Fig. 5.8 correspond to the 1D profiles shown in Fig. 5.6a. Complementary spatial and temporal data provide insights into the details of the heat-transfer dynamics in the system. The melting within individual PCMs beads is evident and significant spatial variations in heat transfer rates, and the subsequent melting process, in both the radial and longitudinal directions are seen throughout the bed as well as around individual spheres due to the flow profiles such as those observed in Fig. 5.3 and 5.4. This more detailed view of the coupling of flow and heat transfer is a good complement to the view of the bulk melting front shown in the 1D profiles of Fig. 5.6.

The 2D T_2 weighted intensity images in Fig. 5.8 and 5.9 have been normalized by the intensity of the images of the fully melted bed (not shown). Hence image intensities in these images span the range from 0 (unmelted) to 1 (melted at 39ºC). This scaling was done to remove the effects of pixels that enclose both PCM and pore fluid allowing for clearer observation of inter- and intra-particle gradients.

Fig. 5.8 shows a time sequence for three longitudinal images of the macroPCM37 packed bed as it is heated by a flow of Fluorinert at 200 mL/hr with an inlet temperature of 39˚C. The images allow for visualization of the transport processes in the bed and the nature of non-uniformities over the cross-section of the bed. There are clear indications of inter- and intra-particle heat transfer processes as the particles display internal gradients in signal that grow and decay in time. Note also that the heating is asymmetrical with spheres on the left side melting faster than the balance of material in the cross-section for times up to 27.5 min. This pattern is then reversed with accelerated melting on the right side of the sample.

Comparison of slice 2 in Fig. 5.8 to the corresponding velocity maps in Fig. 5.3 shows the interaction of fluid flow and heat transfer in the bed. Accelerated melting occurs along the edges where the longitudinal fluid flow is fastest (e.g., white circled bed particle in Fig. 5.8). Areas of high transverse flow (white boxed bed particle in Fig. 5.8), also melt at faster rates than other spheres in the cross section. The white boxed bed particle has both high transverse flow and moderate longitudinal flow in its surrounding pores, resulting in an overall faster melt rate compared to its neighbors. A magnified view of the boxed and circled areas are shown in Fig. 5.9 with zoomed-in areas of the velocities of interest.

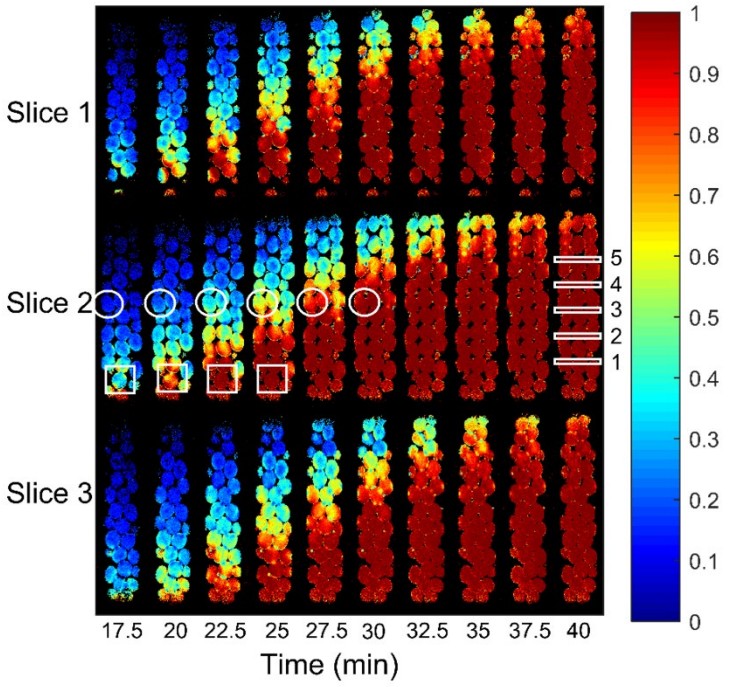


Fig. 5.8. Images show melt progression at 200 mL/hr with inlet temperature of 39°C of three longitudinal slices, 1, 3 are near the wall of the column in and 2 is in the column center. Slices are 1 mm thick, 3 mm apart and were acquired over 1.25 min. Flow is from bottom to top. Time increases to the right and is relative to the start of heated flow. Transverse slice positions in Fig. 5.10, are shown as white rectangles in the far right image of slice 2. Image intensity has been normalized to the final image taken at 42.5 min, which is not shown. Normalized images better represent melting by accounting for effects on intensity from pixels that were part PCM and part pore.

Five 2D transverse slices are shown in Fig. 5.10 with slice 3 corresponding to the position of the transverse velocity maps shown in Fig. 5.4. The transverse images in Fig. 5.10 show similar behavior to that of the longitudinal images in Fig. 5.8. Slices 1-3 are characterized by accelerated melting in the lower left quadrant. However, this feature diminishes until there is a near even melting rate at longer times (slices 4 and 5). Intra-particle melting, visualized as an intensity gradient across particles, is very evident in these images. Particle surfaces near high flow regions melt first, with energy being conducted through to the center over a period of 5-10 minutes.

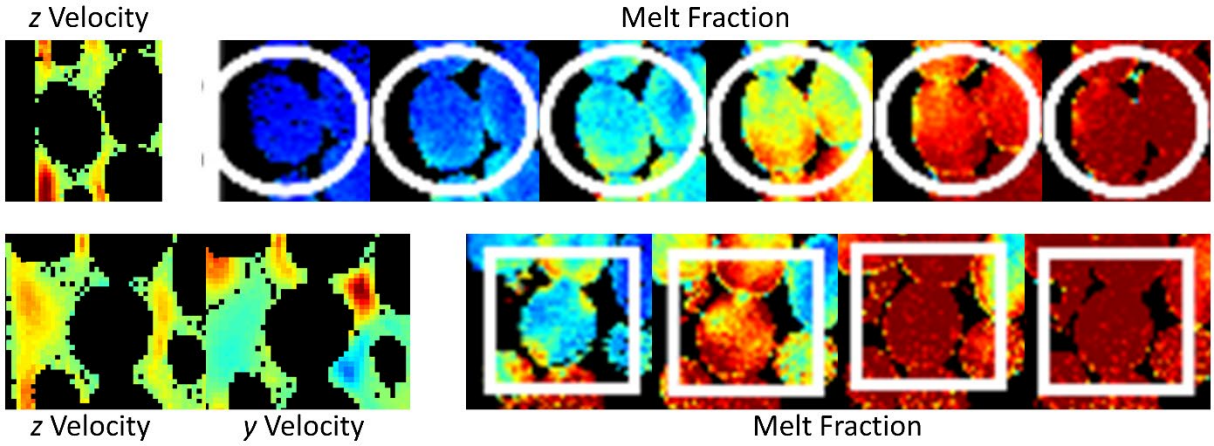


Fig. 5.9. Magnified images of the circled and boxed areas shown in Fig. 5.8 (right) along with magnified velocity images of interest (left). Accelerated melting can be seen near areas of high flow.

A visual coupling of the velocity field (Fig. 5.4) with the time course of the particles at the same location (Fig. 5.10 slice 3) clearly shows the interaction of flow and heat transfer in the bed. Interestingly, the pores with the highest longitudinal velocity do not always correspond to spheres that melt quickest. Instead, the spheres adjacent to pores with high transverse flow melt at higher rates than the balance of material in the same cross-section. Whether this is an effect

due to longitudinal position in the bed, which is hard to determine from the axial images alone, or due to lower local temperatures in the fluid in these pores has not been determined.

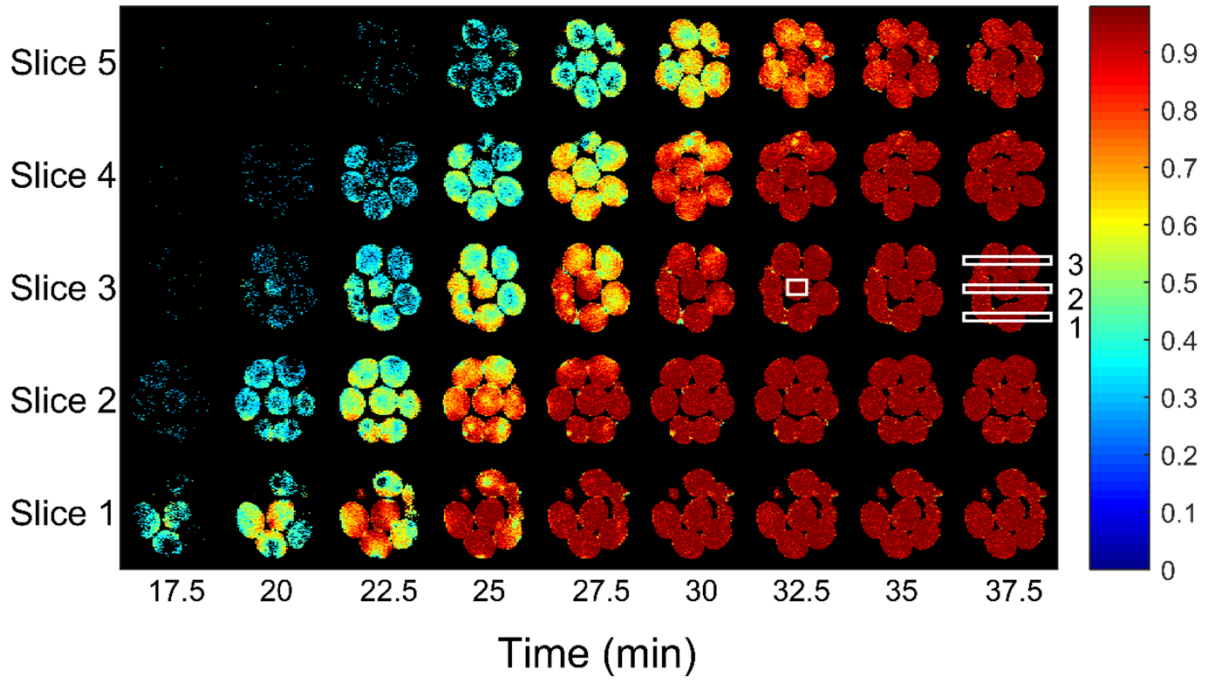


Fig. 5.10. Transverse images corresponding to slice positions shown in Fig. 5.8. Slices are 1 mm thick, 5 mm apart and were acquired in 1.25 min. Image acquisition time (*x* axis) is relative to the start of heated flow. Internal signal gradients that grow and decay in time can be seen. Position of longitudinal slices from Fig. 5.8 are shown as white rectangles overlaid on slice 3, far right. White box in slice 3 image at 32.5 min shows the approximate area of signal plotted in Fig. 5.11a-b. Signal intensity has been normalized to the intensity at 42.5 min.

Spatial gradients in the ^{1}H signals are in accord with overall gradients in the velocity profile, suggesting that the expected interplay of fluid shear and enhanced heat-transfer rates can be observed at length scales smaller than any existing method in this field. As referenced earlier, current methods for monitoring temperatures in packed beds use thermocouples placed at fixed locations in the bed to measure axial and/or radial temperatures in a packed bed [122-124]. Most experiments record temperatures at the inlet and outlet before and after entering the packed bed and at limited axial locations within the bed, such as three thermocouple measurements over a

1.5 m long bed [146]. Efforts to measure intra-particle temperature gradients are also limited to the use of thermocouples embedded within the beads, such as the analysis of a single encapsulated PCM sphere [147] or within a few PCM particles in a larger bed [2]. As the images show above, our method can resolve both intra- particle gradients as well as axial and radial variations at high spatial resolution, which is not possible with thermocouple based methods.

Applications to heat transfer

Imaging of the melt front in 1D and 2D is an important step toward determining spatial temperature profiles within a packed bed. There is, however, other information about the heat transfer conditions in the bed that can be explored with this method. Plots in Fig. 5.11 compare normalized signal against time for different locations longitudinally and axially. All the plots have gradual increases in signal before leveling off at a maximum. As discussed above, image data were collected at a fixed echo time so that increases in signal can be attributed solely to changes in mobility, specifically increases in temperature and change from solid to liquid state in the PCM. The increase in signal is then attributed to melting of the bed and so the signal levels off after all material has transitioned to the liquid.

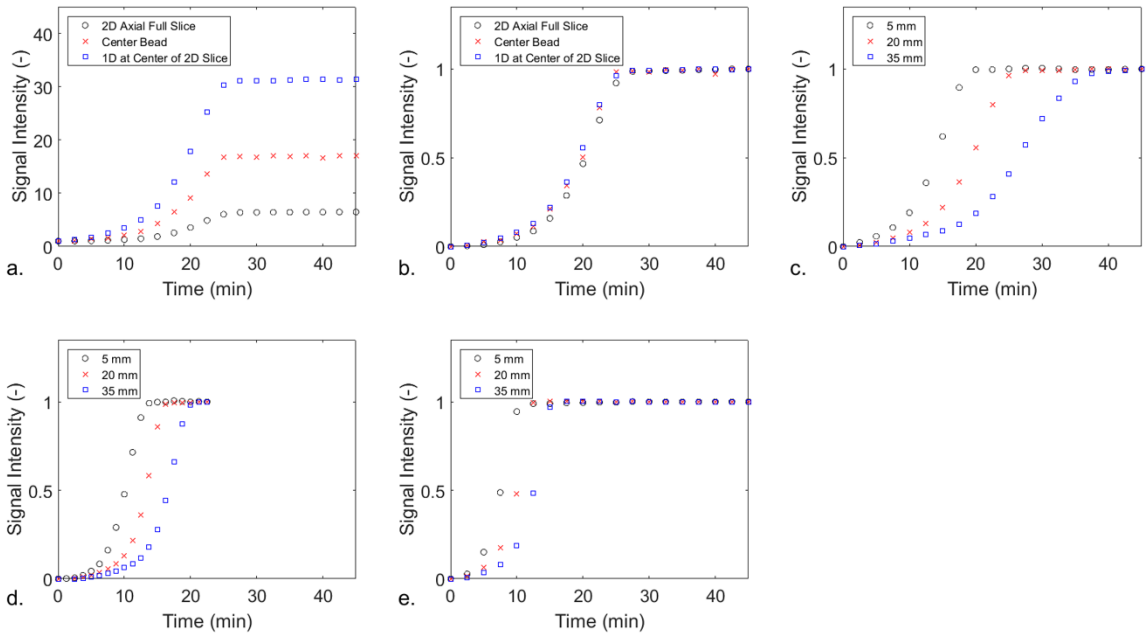


Fig. 5.11. Normalized signal intensity data over time is shown in plots. In plot a) signal intensity is normalized to the lowest signal in: the entire center axial slice, the center PCM in said axial slice and the point on the 1D profiles that corresponding to the center of the 2D slice. This plot makes clear the varying levels of signal to noise in each domain. In plot b) the same locations are plotted, but normalized from 0 to 1. This shows that despite the differences in SNR, they all measure the same rate of transport. Plot c) is signal at three transverse slices, separated by 15 mm, normalized from 0 to 1. The rate of melting is different at each slice, in line with thermal dispersion in the packed bed. Plots d) and e) show the same information as plot c) but for flow rates of 300 mL/hr and 400 mL/hr respectively.

In Fig. 5.11a three signals, each normalized to their own lowest signal and collected at the same longitudinal position in the bed, are presented. The signals are: the average signal for an entire 2D slice of 1 mm thickness, the center bead of the 2D slice, and the point on the 1D profiles corresponding to the center of the 2D slice. The point from the 1D profile represents a slice of 156 μm thickness. This plot shows that the magnitude of the signal increase varies spatially within a single slice and that the signal depends on slice thickness. The 1D slice has the greatest signal increase, while the entire 2D slice had the least. This is due to large areas of no

signal from the pore space filled with ^{19}F. This plot suggests that 1D profiles are the most sensitive to increases in signal magnitude even with an effective smaller slice.

Fig. 5.11b shows the same three signals but normalized from 0 to 1 by subtracting the initial signal from each time step, then dividing by the signal maximum. When normalized in this manner, all signals collapse into a single profile, suggesting that, despite differences in the change of total signal intensity, they all measure the same transport process. In Fig. 5.11c, signal from three different longitudinal positions are plotted. The slope of the position nearest the entrance is steepest and the slope of each subsequent melt profile decreases. This behavior is indicative of thermal dispersion in the packed bed. Fig. 5.11d-e display signal at the same locations as Fig. 5.11c but at flow rates of 300 mL/hr and 400 mL/hr respectively. The increase in flow rate has the effect of decreasing thermal dispersion, seen as slopes that steepen progressively with flow rate. A line was fit at the location of steepest slope at each position and flow rate. It was found that at 200 mL/hr the slope near the entrance was twice as steep as the slope near the exit. For 300 mL/hr the change in slope was 20% and at 400 mL/hr there was no change. The rate of thermal transport increased at higher flow rates and is visualized by the data. Full melt at the last position was achieved in only 15 min at 400 mL/hr compared to 22 min at 300 mL/hr and 38 min at 200 mL/hr.

Numerical simulations are used extensively to model PCM packed bed systems. In a recent review by Gracia and Cabeza [70] on the various numerical models used to simulate PCM packed bed systems, it was clear that empirically correlated parameters for solid-fluid heat transfer coefficient, thermal gradients in the PCM, and thermal conductivity of the bed were of

key importance. The method outlined above will allow for these parameters to be more accurately derived, which will allow for more efficient design of thermal energy systems.

Conclusions

A robust approach for following temperature fronts through packed beds of novel PCMs has been demonstrated. Capturing melt fronts and melt fractions allows assessment of the fine details of heat transfer processes by NMR. Use of bed particles with ^{1}H and a fluid with ^{19}F nuclei allows observation of the interaction of the bed structure and the pore velocity field at a spatial resolution that has not been available to date. Visualization of different modes of axial energy transport is possible using 1D profiles. Melting due to heated internal flow, solidification via cooled internal flow and solidification via no flow are easily measured. 1D profiles also provide high temporal resolution of melt front motion while 2D images provide high spatial resolution of individual PCM's and bed structure during melt, with inter- and intra-particle melt gradients visible. Velocity maps show the range of velocity values and gradients in the pore space. Comparison of intensity images and velocity maps show enhanced heat transfer in areas of high fluid flow, as expected for a heated fluid. The length scales of these internal observations are smaller than that of any existing experimental method for packed bed heat transfer studies and represent a novel approach to the study of porous media heat transfer by NMR. Ongoing research is focused on direct comparison of the data and computational fluid dynamics models of fluid flow and energy transport.

Acknowledgements: This research is supported by the National Science Foundation under Grant Number 1511045 to RA and JDS. Any opinions, findings, and conclusions or recommendations expressed in this material are those of the authors and do not necessarily

reflect the views of the National Science Foundation. JDS thanks the M.J. Murdoch Charitable Trust and NSF MRI program for equipment funding.

CHAPTER SIX

EXPERIMENTAL IMAGING OF PACKED BED HEAT TRANSFER BY MRI WITH ASSESSMENT OF DEM-CFD SIMULATION

Contribution of Authors and Co-Authors

Manuscript in Chapter 6

Author: Matthew E. Skuntz

Contributions: Wrote manuscript, collected, analyzed data. Implemented experimental system. Finalized CFD simulation. Incorporated revisions and provided feedback on reviewer comments.

Co-Author: Dinal Perera

Contributions: Assisted in data collection. Developed CFD simulation.

Co-Author: Brenden G. Pelkie

Contributions: Assisted in data collection. Progressed CFD simulation.

Co-Author: Sarah L. Codd

Contributions: Edited manuscript. Provided technical support in data collection and analysis.

Co-Author: James E. Maneval

Contributions: Performed DSC analysis on PCM particles. Edited manuscript

Co-Author: Erick L. Johnson

Contributions: Technical Assistance in simulation development and running simulations on cluster.

Co-Author: Joseph D. Seymour

Contributions: Edited manuscript. Conceived experimental method. Provided training on experimental methodology. Secured funding.

Co-Author: Ryan Anderson

Contributions: Edited manuscript. Conceived experimental method. Secured funding.

Manuscript Information Page

Matthew E. Skuntz, Dinal Perera, Brenden G. Pelkie, Sarah L. Codd, Erick L. Johnson, Joseph D. Seymour, and Ryan Anderson

American Institute of Chemical Engineers

Status of Manuscript: (Put an x in one of the options below)
___ Prepared for submission to a peer-reviewed journal
_X_ Officially submitted to a peer-reviewed journal
___ Accepted by a peer-reviewed journal
___ Published in a peer-reviewed journal

EXPERIMENTAL IMAGING OF PACKED BED HEAT TRANSFER BY MRI WITH ASSESSMENT OF DEM-CFD SIMULATION

Abstract

Packed beds are studied with a unique experimental setup allowing imaging of the pore-fluid velocities and the energy absorbed by the packed bed. The setup utilizes a fluorinated pore-fluid and a hydrogen-rich packed bed to allow measurements in each domain separately. The packed particles are micro-scale core-shell particles agglomerated into larger 3.5 mm macro particles with the micro-core composed of eicosane. The energy absorbed by the bed is captured by the phase-change of particle-bound wax bound that is easily identified by MRI. The resonant signal intensity is a direct measure of the alkane k_BT energy. The experimental rate of energy transfer, rendered by the wax melting, is compared to a particle-resolved model constructed in a commercial CFD package. It is found that the total energy transferred was in good agreement but differences occurred in the liquidus front propagation.

Introduction

Packed beds are widely used in industry as catalytic beds [45, 120], in pebble-bed nuclear reactors [148], and for thermal storage [149]. They are also used to model food drying, storage, and processing. Quality, safety, and efficiency of these packed beds and their end-products depend on the local pore temperature, velocity, and fluid concentration. In fixed catalytic beds small tube-to-particle-diameter ratios ($N < 10$) are desirable to keep pressure drops to a minimum and pore velocities high [120]. Low N prevents dense, ordered particle packing, resulting in inhomogeneous porosities that fluctuate in the axial and radial directions. Design of such systems

should not rely on empirical correlations, *e.g.* Ergun, Carmen-Kozeny as those correlations are based on volume-averaged properties, which assume plug flow and evenly distributed porosity [45]. Adaptations to account for v_z(r) dependence (*i.e.* extended Brinkman-Forchheimer-Darcy equation) can yield improved prediction but provide little insight into the underlying mechanisms necessary for improved system design [45]. The inability to accurately predict maximum pore velocities, stagnation and residence time can lead to problematic conditions like hotspots, which are detrimental to performance [150]. Accurate prediction of transport in these systems requires numerical models and experimentation that capture pore-scale behavior of the packed bed.

Computational fluid dynamic (CFD) modelling and discrete element modelling (DEM) techniques naturally lend themselves to these problems [84, 151, 152]. These models allow detailed prediction of local properties and provide a platform to test new arrangements cheaply and quickly. Three-dimensional (3D) particle-resolved CFD is a relatively new technique, rising with computational power at the turn of the 21st century [8]. Many consequential issues associated with packed beds still lack definitive solutions [8, 77, 83, 86, 153]. This includes methods for generating random sphere packs which reflect their real-world counterparts [154] and generation of volume meshes where sphere-sphere and sphere-wall contacts cause high element skew [8, 86]. For example, in STAR CCM+ contact-point induced skew is avoided by enforcing a small distances between DEM particles. Questions remain on the appropriate method for fluid-particle heat transfer coupling where solid-particle and operator-splitting methods are both in use [8]. Less important to the present study is the choice between large eddy simulation or the Reynolds-averaged Navier-Stokes method for turbulence modeling [8] and difficulty in incorporation of micro kinetics [8]. Packed beds are complex systems which require large

numbers of mesh elements to accurately represent their geometries at the resolution sufficient to model convection. The limit in the number of elements that can be handled restricts the packed bed size that can be simulated [8] and limits the application of particle-resolved simulations to low *N* arrangements.

CFD models require high resolution experimental results to verify and guide improvement numerical methods. Experimental measurements for this purpose are challenging due to the system opaqueness and sensitivity to perturbation, limiting the available techniques. Point-based methods are of limited utility in low *N* packed beds which have high spatial variability in temperature and velocity. Additionally, accuracy of local temperatures determined by thermocouples (TC) are questionable due to the likelihood of system perturbation from TC wires and measurement [155]. Optical techniques like Laser Doppler Velocimetry (LDV) and Particle Image Velocimetry (PIV) for velocity have been applied by refractive index matching of the fluids and solids [156-158]. These techniques give high spatial and temporal information on local particle velocities but are limited in the systems to which they can be applied and the planes images can be oriented. Also, PIV techniques measure the velocities of the tracer particles, not the fluid itself, resulting in a measurement that is influenced by buoyancy and inertial forces. Liquid Crystal Thermometry (LCT) is an optical technique that uses polychromatic tracer particles for temperature measurements [156, 159]. However, the refractive index of a fluid is dependent on temperature, which has limited most PIV to isothermal systems. One outlier is the recent study by Ataei-Dadavi *et al.* who used PIV and LCT to resolve velocity and temperature images of natural convection in a coarse-grained porous media [159].

Magnetic resonance imaging (MRI) can measure velocity fields internal to opaque systems without perturbation to the measured system or the addition of tracer particles [92, 94, 101, 129, 160, 161], providing a Lagrangian measurement of the fluid itself [92]. Spatial resolution of measurements can be on the order of 10-100 microns, allowing pore-scale images and local velocities to be captured [92]. The most common method of MRI velocimetry encodes fluid displacements into magnetization phase using the pulsed gradient spin echo (PGSE) pulse sequence which allows fluid motion to be tracked over a controlled duration [100]. The time to acquire a PGSE velocity map depends on the resolution and signal-to-noise ratio of the measurement with typical times ranging from 8-68 minutes, unless a rapid imaging method is used [92, 94]. MRI velocity measurements are now fairly routine and have been applied to porous media in studies such as biofilm growth [30], convection in mushy layers [162], two phase flow [163], natural convection [38], and shale rock characterization [22]. Other MRI pulse sequences, *e.g.* echo planar imaging, can provide velocity measurement in much less time, as fast as ~7 ms in special circumstances [25]. Groups have developed methods of MRI temperature measurement in packed beds. Gladden *et al.* used ethylene glycol isolated in glass spheres as thermometers located in an active catalytic reactor [164]. Lysova *et al.* have correlated signal intensity of ^{27}Al to temperature allowing them to monitor catalyst temperature in an active reactor [165]. Both techniques allow temperature measurement but have not included velocity mapping. Our experiment provides the ability to measure heat transfer to the packed bed particles while still imaging pore-fluid velocities in the same packed bed.

In this paper MRI methods are used to measure pore-fluid velocities and energy absorbed in a low tube-to-particle-diameter packed bed, $N \sim 3$, and the results are compared to a particle-

resolved CFD model. This is accomplished by selecting fluid and solid components that have different MRI active resonant nuclei of fluorine and hydrogen, respectively. This arrangement provides a robust way of imaging each domain by adjustment to the resonant frequency [16]. The packed bed core-shell particles contain micro-encapsulated wax and the pore-fluid is heated above the wax's melting point. The resulting solid-liquid phase change within the particles is easy to identify in the MRI, and its signal intensity is proportional to its k_BT energy providing an indicator of local temperature and a quantitative measure of the energy absorbed by the bed at any spatial location. Here images of the melting process and pore-fluid velocities are recorded for three experimental packed beds tested in triplicate at Re = 2.3 and 4.5. One-dimensional signal intensity profiles, spatially resolved in the longitudinal direction, average the signal over the full width of the bed. This data is compared to discrete element modelled (DEM) packed beds simulated in the CFD software package STAR CCM+ (Seimens PLM Software). Five DEM packed beds are studied under the same flow conditions to consider the effects of variability in packing structure.

Experimental Method

MRI measurements were performed on a packed bed composed of hydrogen-rich alkane-containing core-shell particles with a fluorinated liquid (Fluorinert FC-43, 3M Corporation) filling the pore-space. The pore working fluid was pumped through the bed at a temperature 38^{o}C, 2^{o}C above the liquidus temperature of the wax (eicosane T_{liq} = 36^{o}C) contained in the packed bed particles. Heating at this fluid temperature allowed the wax-melting process to be observed in detail with MRI. The particles are core-shell micro-capsules (10—20 um) agglomerated into near-spherical larger particles of mean diameter 3.5 mm (macroPCM37C,

Microteck Encapsualtion Technologies). The core of the micro particles is eicosane wax and the core-shell a hard plastic. Microencapsulation of the wax prevents particle-scale convection and provides structural integrity when the wax is liquid. A packed bed of these particles is shown in Fig. 6.1a and an illustration of the agglomerated particles in Fig. 6.1b. Heating of the wax through its solid-liquid phase transition results in signal increase at the ^{1}H resonance. The signal increase is a quantitative indicator of the energy transferred from the pore-fluid to the solid packing [16] and can be used as a narrow range temperature indicator effective around the wax melt temperature (T_{range} = 34-36^{o}C).

MRI can be performed on any active isotope, *e.g.* ^{1}H, ^{3}He, ^{13}C, ^{19}F, ^{31}P. In this experiment images were formed at the ^{1}H and ^{19}F resonances of the particle-bound alkane and pore-fluid respectively, as shown in Fig. 6.1c. The right hand image was taken at the ^{1}H resonance, formed from alkane proton ^{1}H signal. Signal intensity is represented by the colorbar, ranging from dark blue, the solid alkane, to red, the liquid alkane. The increase in signal intensity results from the increase in mobility of the CH- chains when melting or liquid. The left hand image in Fig. 6.1c is of the ^{19}F resonance from the pore-fluid. The color bar represents the axial fluid velocity ranging from 0 to +7 mm/s with light green indicating low velocity and red indicating high velocity.

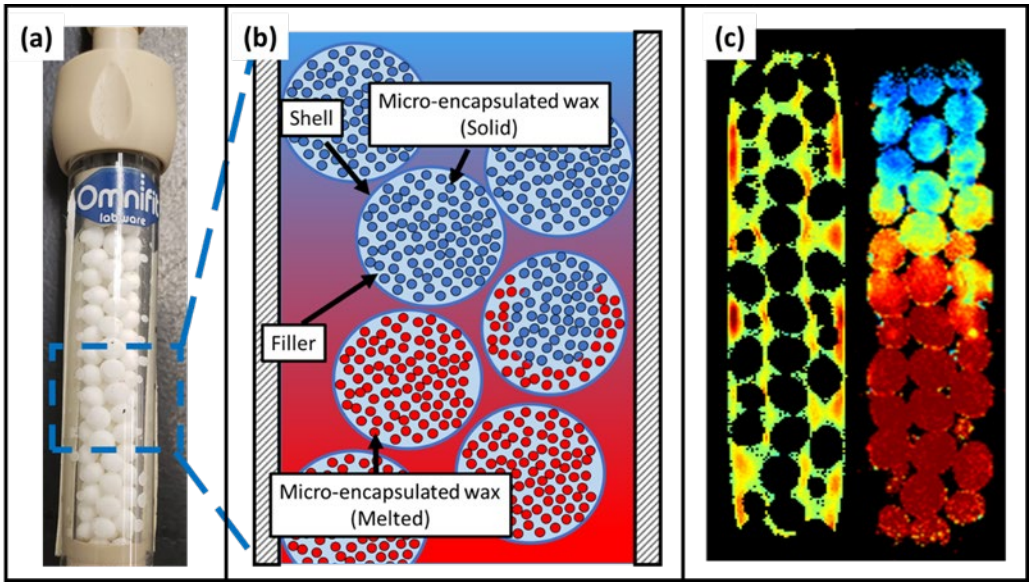


Fig. 6.1. The packed glass column used in the experiments is shown in (a).The particles are composed of micro-scale core-shell particles filled with wax, combined with a binder to form 3.5 mm semi-spherical particles as illustrated in (b). MRI of experimental packed bed at ^{1}H and ^{19}F resonances are shown in (c). The signal from the image in the right-hand image is generated by the wax encapsulated in the particles. The wax is liquid in the areas with greater intensity (red) and solid in areas of less intensity (blue). A velocity map of the $v_z(r,z)$ velocity component is shown in the left-hand image generated from the fluorinated, pore-filling fluid. Areas of high velocity are red and low velocity are light yellow/green, ranging from 0 to +7 mm/s.

A continuous-flow loop circulates the heated fluorinated oil through the packed bed. The system consisted of a fluid reservoir, a dual-syringe pump (Pharmacia P-500), a heat bath, a double-walled heat exchanger, and a cylindrical packed bed vessel plumbed as depicted in Fig. 6.2a. The packed bed column was a high-performance glass liquid chromatography column with PEEK plastic fittings (Kinesis USA, OmniFit Benchmark HIT 10-150-AF) filled with the core-shell particles (Fig.6.1) and placed in the MRI probe and magnet bore. The column had a bed length of 85 mm and an interior diameter of 10 mm (N ~3). An inline double-walled heat exchanger warmed the pore-filling, heat transfer fluid after the syringe pump while it travelled to the base of the spectrometer bore. Outflow from the top of the packed bed column was directed back to the fluid reservoir.

Three different experimental packed beds were heated in triplicate each at Reynolds numbers of 2.3 and 4.5, both in the laminar region. $Re = \frac{\rho v D}{\mu(1-\epsilon)} < 10$ where ρ is the fluid density, v fluid superficial velocity, D the particle diameter, ϵ is the porosity and μ the fluid dynamic viscosity. Dense random packed beds were generated by loading the phase change material (PCM) particles into the glass column and tamping to settle the particles as densely as possible. A compressive force was then applied to the bed through the adjustable-screw end-cap. This compressive force was necessary to prevent the particles from moving under flow as the density of the pore-fluid ($\rho_f = 1860\ kg\ m^{-3}$) was greater than that of the particles ($\rho_p = 890\ kg\ m^{-3}$). Three packed beds were generated in this manner and each was tested in triplicate.

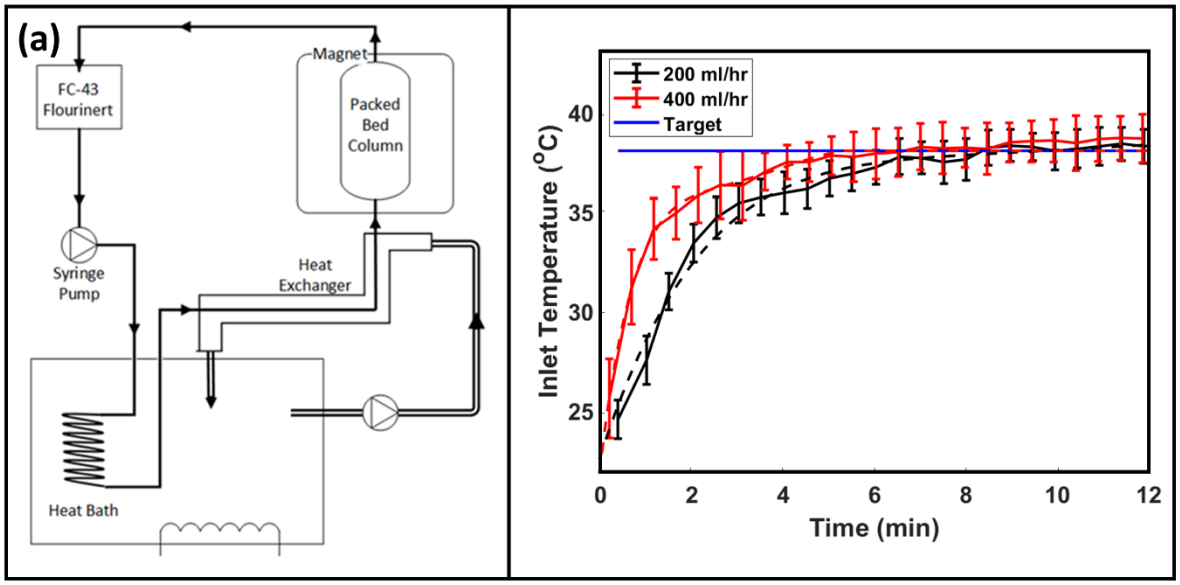


Fig. 6.2. (a) Experimental flow loop composed of fluid reservoir, syringe pump, heat bath, double walled heat exchanger, and packed bed. MRI system is a Bruker Avance III 300 MHz spectrometer integrated with a vertical super-wide-bore 7 Tesla magnet. (b) Averaged temperature at packed bed inlet (n = 10) measured with two k-type thermocouples for 200 and 400 mL/hr flow rates. Temperature measurements could not be recorded during experiments due to space limitations. Fits to averaged temperature curves (dashed lines) were used for inlet boundary conditions in numerical model.

Monitoring of the inlet and outlet packed bed temperatures during the MRI experiment was not possible due to space limitations interior to the magnet bore. Instead, calibration experiments (n=10) were performed without MRI measurement where the inlet temperature was recorded with thermocouples. The average temperature ramp is displayed in Fig. 6.2b for 200 and 400 mL/hr flow rates corresponding to Re = 2.3 and 4.5. The target inlet temperature was 38^{o}C shown in blue and 6th order polynomial fits to the curves were used as the simulation inlet temperature plotted as dashed lines. Residual surface wax was removed from the particles by the heat transfer oil during initial heating of the packed bed. So preliminary runs, twice at Re = 4.5 and once at Re = 2.3, were used for removal.

MRI Methods

Hardware and Sequence Details

MRI images were acquired with a vertical super-wide-bore 7 Tesla magnet integrated with a Bruker Avance III Spectrometer (300 MHz nominal proton frequency, 282 MHz nominal fluorine frequency) equipped with Micro 2.5 shielded gradient coils with maximum gradient strengths of 1.5 T/m at 60 A in all three coordinate axes, and controlled by Bruker ParaVision 5.1 software on a Linux operating system. The transmit/receive radio frequency (RF) coil was a ^{1}H /^{19}F dual-tuned birdcage with internal diameter of 25 mm and active imaging length of 40 mm.

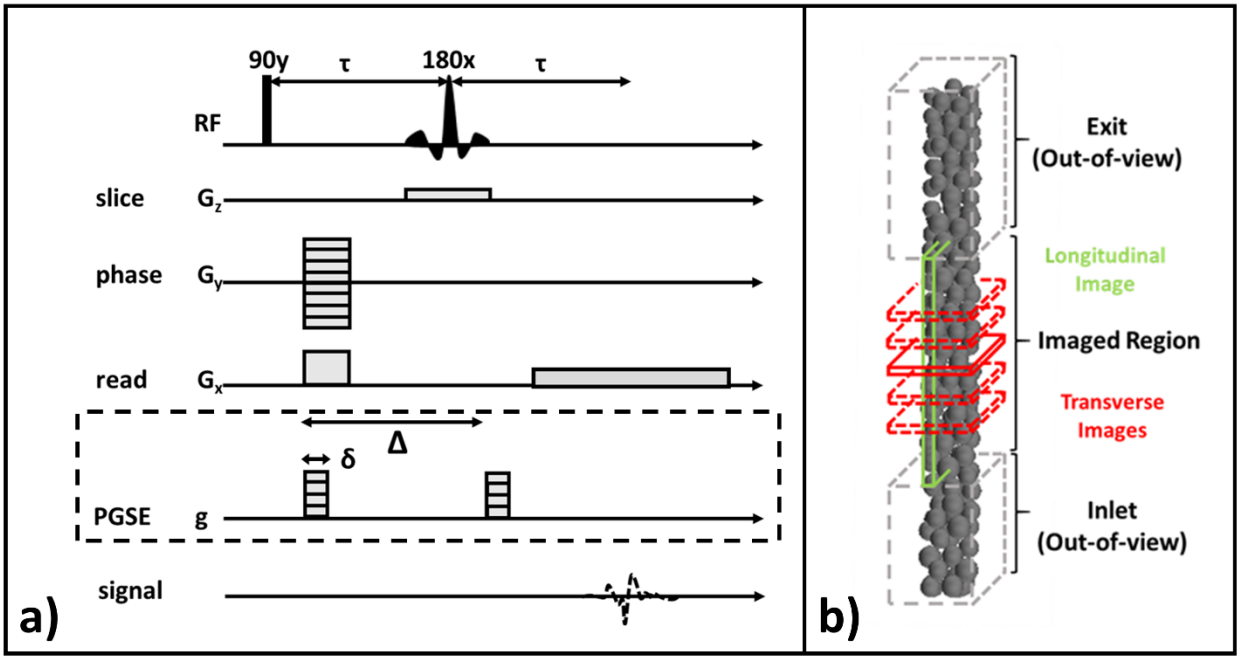


Fig. 6.3. (a) Pulse sequences used to acquire MRI images. The dashed box includes the gradients used to encode velocity into the acquired signal phase. (b) Orientation and position of images. Imaging region is 40 mm in height, 12 mm in diameter, positioned with 20 mm above the bottom of the packed bed. The central transverse image was located 40 mm above bottom of the packed bed with 5 mm between images. The pore-fluid had multiple ^{19}F resonant peaks that prevent multi-slice velocity imaging.

Images were formed at both the ^{1}H and ^{19}F resonances. The MRI pulse sequences are illustrated in Fig. 6.3a. Using the ^{1}H resonance, a spin-warp imaging sequence was used with a single acquisition to acquire one-dimensional frequency-read encoded profiles in the direction of flow through the bed, and two-dimensional (phase- and read-encoded) images of both bed cross-section (transverse) and bed profile (longitudinal) [92] as shown in Fig. 6.3b. The field of view was 12 mm by 12 mm for transverse images and 12 mm by 40 mm for longitudinal images. The imaging region was located from 20 to 60 mm above the bed inlet. 1D profiles were acquired rapidly (~4 sec) with 128 points giving a 313 μm nominal resolution in the longitudinal direction. The transverse 2D images required 68 seconds to acquire 128 frequency- and 64

phase-encoded data points, providing a nominal spatial resolution of 94 μm by 188 μm. Five transverse slices were acquired per scan without noticeable increase in scan duration. Slices were 1 mm thick and with separation of 5 mm between slice locations. The longitudinal images were acquired with 256 frequency- and 64 phase-encoded data points for a nominal spatial resolution of 156 μm by 188 μm and required the same 68 seconds to acquire. One longitudinal image was obtained perpendicular to the main flow with 1 mm thickness. Image acquisition parameters were Echo Time (TE) = 8.06 ms, Repetition Time (TR) = 1000 ms, Number of Averages (NA) = 1 for 1D profiles, and TE = 10.6 ms, TR = 1000 ms for 2D longitudinal and TE = 8.06 ms, TR = 1000 ms, NA = 1 for 2D transverse images. All images processed using MATLAB R2019b (Mathworks). The order of scans was: 1D longitudinal, 2D longitudinal, 2D transverse, repeated until all PCM particles in the field of view were melted.

Velocity images were obtained from the ^{19}F signal with a two-step phase-encode pulsed-gradient spin-echo sequence in both transverse and longitudinal orientations [92]. Images were positioned as shown in Fig. 6.3b with only the central transverse slice acquired. Sixteen averages were acquired for longitudinal scans and eight averages for transverse scans with total acquisition times lasting 68 min for longitudinal and 34 min for the transverse. The gradient separation time to encode for displacement (Δ) was 11.1 ms and the duration (δ) was 1 ms. Gradient amplitudes were varied with flow rate. A range of +/-0.0395 to +/- 0.0198 T/m provided a suitable window for the longitudinal velocity and +/- 0.0198 to +/- 0.0741 T/m for the transverse velocities. The spatial resolution of the velocity images was the same as the corresponding ^{1}H images with TE = 16.4 ms and TR = 1000 ms.

The ^{1}H NMR spectrum of the PCM eicosane consisted of one peak while the ^{19}F spectrum of Fluorinert had multiple peaks as shown in [16]. To eliminate the chemical shift artifacts introduced by the multiple peaks, a chemical selective 180^{o} RF pulse was used with a slice selective 90^{o} pulse of 900 Hz ~ 3.2 ppm, thus refocusing and fully encoding only the ^{19}F signal from the resonance at 0 ppm [101]. The bandwidth of the selective pulse was also reduced to a small value and the slice positions were limited to a zero offset from the gradient center.

PCM Particle Analysis

Physical characterization of the experimental bead properties was necessary to ensure proper model-experiment equivalence. The core-shell particles used in the experiments were composed of straight chain alkane (eicosane, T_m = 34-36^{o}C), micro-encapsulated (10-20 μm) into polymer shells and agglomerated into larger particles with average diameter of 3.5 mm. The composition of the shell and binder were not disclosed by the manufacturer. The product data sheet (PDS) provided by the manufacturer reported the micro-particles contained 85%-90% eicosane and 10%-15% shell, had a density of 890 kg/m^3, and a heat of fusion of 190 J/g. Differential scanning calorimetry (DSC) measurements performed on pure eicosane, the microencapsulated particles and the mm scale particles found their heat of fusion to be ΔH_{fusion} = 233 J/g, 191 J/g, and 184 J/g, respectively. Based on this analysis, the alkane percentage of the macro particles is calculated to be 79% with a specific heat of 9500 J/(kg K) and matched well with manufacturer's PDS. The DSC results for the mm scale particles is shown in Fig. 6.4a.

The temperature range over which the encapsulated wax melted was determined by analysis of the DSC heat curves. The initiation of melt was estimated by extending the slope of the heat flow curve downward from its half-maximum point. The zero-crossing of this line was

then used to define the onset of the phase change. The temperature where maximum heat flow is observed was taken to be the point where the phase change was completed. In these particles the melt range was found to be 34 to 36ºC. The micro-encapsulation of the wax prevented internal, particle-scale wax convection and minimized wax leakage into the pore fluid. These properties allowed wax motion internal to the particles to be neglected in the model, and for use of volume averaged constants for mass and enthalpy.

Melt physics were implemented in STAR CCM+ by inputting the temperature at which transition begins and ends, termed $T_{solidus}$ and $T_{liquidus}$ respectively. These values are used to define a T^* (Eq. 139). By default the energy required for phase transition, defined as the enthalpy of fusion, is distributed over the melt range as shown in Fig. 6.4b. The range over which the phase transition occurs has a large effect on the melt rate of the simulated packed bed.

$$T^* = \frac{T - T_{solidus}}{T_{liquidus} - T_{solidus}} \qquad Eq.\ 139$$

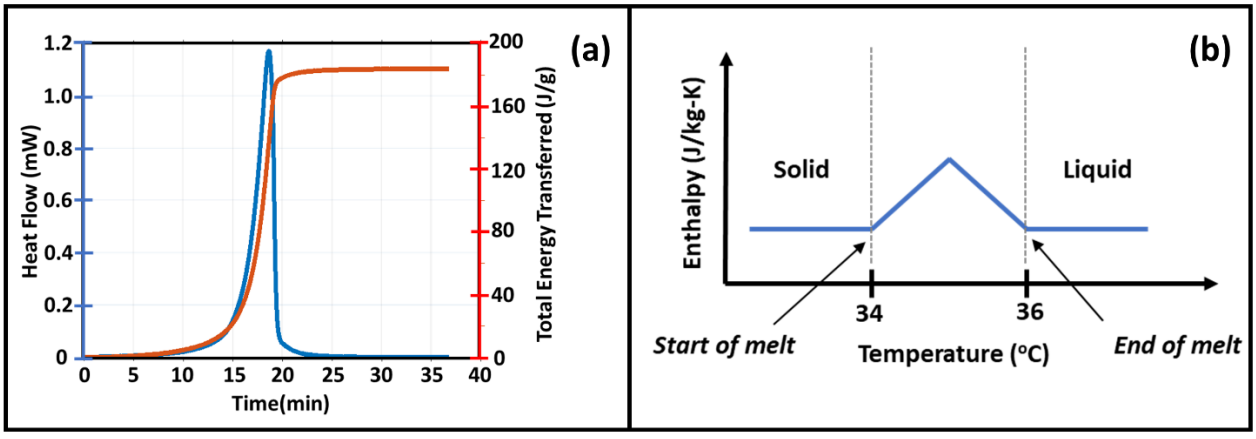


Fig. 6.4. (a) DSC heat flows for the macro particles. b) In STAR CCM+ the user can define the temperature range over which melting occurs. The enthalpy of fusion required for transition from solid to liquid state is distributed over this range in a triangular function.

Simulation Methods

The 3D particle resolved simulation of the packed bed was constructed in the commercially available software STAR CCM+ 2020.1 build 15.02.007 (Siemens PLM Software, Munich). The packed bed was generated using the built-in discrete element modelling (DEM) solver using spherical particles with a Gaussian diameter distribution. Five random packed beds were generated. Similarity between the numerical and experimental packed beds was determined though particle counts, pore-fluid velocities, porosity and visual comparison. The Eulerian Multiphase physics model was selected to simulate particle-bound alkane melt. During the simulation, images positioned similarly to the MRIs were stored at the same time intervals as the experimental acquisitions. A plot of the melted fraction of the wax and table recording positional temperature and energy of particle-phase were also compiled. The table of simulated data was used to generate 1D figures analogous to the 1D experimental data.

For all simulations, full 3D governing equations were solved using the finite volume approach. The conservation of mass, momentum and energy were maintained by the discretized Navier-Stokes equation where fluid is assumed to be incompressible. Constant properties were used based on the average temperature of the system. This leads to the following governing equations.

$$\frac{\partial(\rho \boldsymbol{v})}{\partial t} + \boldsymbol{\nabla} \cdot (p\boldsymbol{v} \times \boldsymbol{v}) = -\boldsymbol{\nabla} \cdot p + \boldsymbol{\nabla} \cdot \boldsymbol{T} + \boldsymbol{f}_b \qquad \textit{Eq. 140}$$

$$\boldsymbol{\nabla} \cdot (\rho \boldsymbol{v}) = 0 \qquad \textit{Eq. 141}$$

$$\frac{\partial(\rho E)}{\partial t} + \boldsymbol{\nabla} \cdot (\rho E \boldsymbol{v}) = \boldsymbol{f}_b \cdot \boldsymbol{v} + \boldsymbol{\nabla} \cdot (\boldsymbol{v} \cdot \boldsymbol{\sigma}) - \boldsymbol{\nabla} \cdot \boldsymbol{q} + S_E \qquad \textit{Eq. 142}$$

where E is the total energy per unit mass, $\boldsymbol{q}$ is the heat flux tensor and S_E is the energy source per unit volume. Special effort was made to ensure the physical properties of the model particles and fluid match those of the experiment.

DEM Packed Bed Generation

The built-in DEM solver in STAR CCM+ was utilized to generate the simulated packed beds. In the DEM processes, spheres were injected at the top of the column with a random position. STAR then generated a force balance equation for each particle, which governed its interactions with gravity, the wall, and other particles as the sphere falls to the bottom (Fig. 6.5a). STAR enforces a minimum allowed distance between DEM spheres to prevent high skew of the nearby volume elements. This method has been shown to reduce computational errors and have minimal effect on particle-particle heat transfer [166]. This method generates the packed beds that closely approximate the randomness of experimental beds [8]. The parameters used to define solid-solid interactions during DEM were similar to those used by Eppinger *et al.* [84]. Initial velocity vector was -2 ms^{-1} in the vertical direction and were injected at a rate of 1000 per second. The particles had a Gaussian diameter distribution with mean diameter of μ = 3.35 mm, standard deviation of $\sigma = 1.0x10^{-4}$ mm and minimum and maximum cut-offs of 3 and 3.8 mm, respectively. The experimental particles had a distribution of sizes and were not perfect spheres (see Fig. 6.5b). The majority of particles had a flattened spherical shape with a major diameter of μ = 3.8 mm, σ = 0.1 mm, and minor diameter of μ = 3.0 mm, σ = 0.1 mm. Packed beds generated from non-spherical particles which closely resembled the experimental particles were investigated, but the particle shapes were too irregular to be accurately reproduced (Fig. 6.5b) and the arbitrary non-spherical shapes did not yield any clear advantage. Additionally, meshing of non-spherical particles is a known difficulty.

The DEM generated packed beds were settled by running until all velocities fell below $1x10^{5}$ m s^{-1}. The porosity of the beds compared well with the empirical correlation of Dixon for low *N*, mono-disperse packed beds [167]. The average porosity of the numerically generated

packed bed was 0.45 and the correlation predicted porosities between 0.45 to 0.48 based on the imposed particle diameter limits of 3.0 and 3.8 mm. Numerical packed bed porosities are in line with experimental packed beds of others [168]. A diagram of the DEM generated packed bed is shown in Fig. 6.5c.

The quality of the numerical bed's representation of the experimental beds was assessed by the particle count, porosity, maximum/mean pore-velocity in an axial slice, and visual similarity. After packed bed generation, the geometry was extracted from the DEM model as surfaces and reinitialized with the correct physical properties in the CFD simulation.

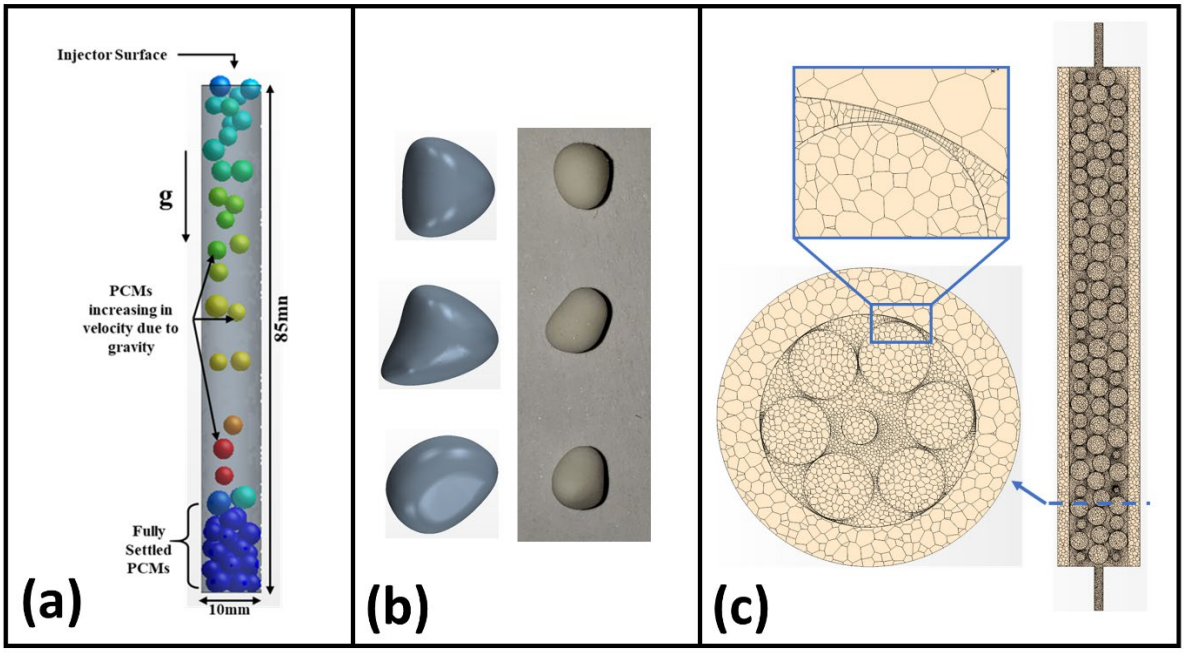


Fig. 6.5. DEM packed bed generation shown in (a), non-spherical particles and experimental particles in (b) and packed bed mesh in (c).

Boundary Conditions and Interfaces

The model consisted of three domains: the fluid pore space, DEM particles, and an exterior glass column. Heat loss through the bottom and top boundaries was neglected due to the

minimal surface area and low thermal conductivity of the PEEK fittings. The exterior boundaries of the glass column were modelled as convection boundaries with heat transfer coefficient of 4 W m^{-2} K^{-1} based on recommendations of Churchill and Chu [169] with ambient temperature of 296 K. For the fluid, a mass flow inlet and pressure outlet were applied. The inlet fluid temperature was controlled by a 6^{th} degree polynomial fitted to the experimental inlet temperatures. Fluid-wall and particle-wall boundaries were adiabatic conducting with conjugate heat transfer. In STAR CCM+ the domain undergoing phase change is designated as a fluid. This required the use of baffle boundaries at fluid-particle interfaces. Baffle boundaries act like thin, perfectly conducting membranes, which prevent mixing of the adjacent fluids. The baffle boundaries had conjugate heat transfer condition applied with no thermal resistance. Individual surfaces and interfaces were created for each particle.

Mesh and Time Step

Each of the domains are meshed separately using polyhedral elements. Separate meshing allows for more efficient allocation of the total mesh elements so mesh density could be increased in the fluid near the particles for proper representation of the fluid thermal boundary layer. In the Wall and Particle domains, polyhedral elements were used with the Surface Remesher, and Automatic Surface Repair routines applied. In the Fluid domain, the Thin Mesher option is applied additionally with four thin mesh elements. Mesh quality was assessed using face validity, cell quality, volume change, and skewness angle. The number of invalid cells was small, less than 0.5%, and STAR's cell quality remediation routine was applied to reduce the effect of these cells on the solution. The addition of prism layers at the fluid-solid interfaces was considered but did not provide more accurate results and greatly increase computation time. In

STAR CCM+ no flattening at particle-particle or particle-wall contacts is implemented. Instead a minimum allowed distance between solids ensures a small fluid gap remains between adjacent solid objects. This prevents computational contact errors without noticeable influence on solid-solid conductive heat transfer [84].

Mesh and time step studies were performed with element base size varying from 0.1 – 1 mm and time steps from 0.125 – 1 seconds. Their influence on melt rates are shown in Fig. 6.6. Increasing the time step with a small mesh size (0.09 mm) led to slower melt rates but did not change the melt rate on the larger mesh size. These trends are explained by the Courant numbers, which compare the rate of thermal convection based on the mesh size and time step. The Courant number is defined as ($\boldsymbol{v}\, dt/dx$). At large Courant numbers, the fluid moves energy multiple mesh elements in each time step, resulting in poor convergence. In Fig. 6.6 the expected trend of increasing melt rate with decreasing Courant number are observed with convergence occurring as Courant number approaches a value of one. Based on these studies a time step of 0.5 seconds and base element size 0.5 mm were selected as providing a good balance of mesh resolution and solution time. With this mesh size, the average number of elements in the fluid, PCM and wall domains was 2.0×10^6, 2.5×10^5 and 5×10^4, respectively.

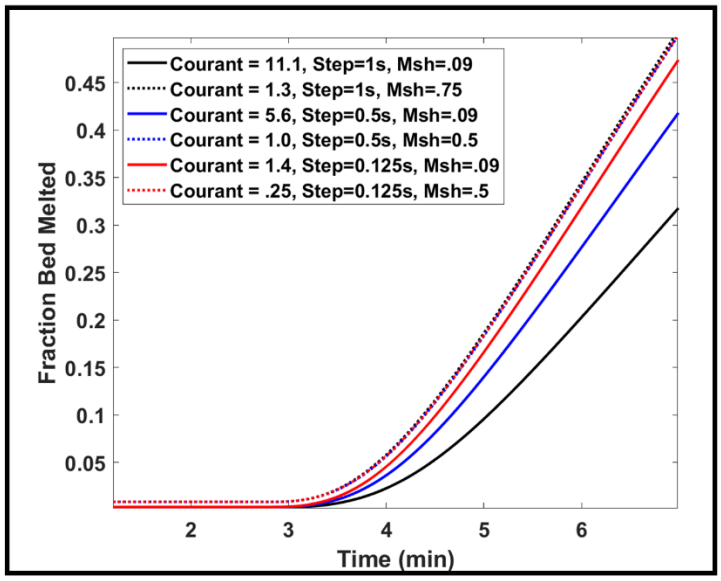


Fig. 6.6. Mesh and time step study. Time steps and meshes were tested from 1 to 0.125 seconds and 0.75 to 0.09 mm base size, respectively. The plot shows convergence when courant number approached a value of 1.

Numerical Solvers

The full three-dimensional (3D) volume was solved using a 1st order implicit unsteady solver with constant density, gradients, gravity, laminar, segregated flow and fluid temperature models with solution interpolation and cell quality remediation options. Phase change particles additionally included Eulerian multiphase, melt-solidification flow stop and volume of fluid models. The micro-encapsulation of the wax prevented internal particle alkane convection. In the model this was enforced by setting the flowability threshold to zero, preventing the alkane from moving.

Segregated flow and energy equations were used to speed up simulation solution time. The AMG linear solver used a Gauss-Seidel relaxation scheme. Thirty cycles were allowed and the convergence tolerance was 0.1. A flex cycle was applied to the segregated flow with a conjugate gradient acceleration method applied to the pressure terms and under-relaxation

factors of 0.8 and 0.2 for the velocity and pressure, respectively. In the segregated energy equation, a *V* cycle was applied to the AMG solver with fluid/solid under-relaxation factors of 0.99 and 0.999, respectively.

Numerical Data Processing

Numerical results are visualized using a combination of STAR CCM+ built in images, reports, plots and tables. The compiled tables are further analyzed in MATLAB version 2020a. Images are positioned in the same longitudinal and transverse locations as the experimental images and are recorded at one minute intervals. The images are composed of the pore-fluid velocities and PCM liquid fraction. Longitudinal images extend the full length of the bed and transverse images are captured at 10, 20, 30, 35, 40, 45, 50, 60, 70 and 80 mm. In the experimentally imaged region, the liquid fraction of the bed over time is recorded. Plots of the average bed temperature, mean pore velocity and outlet mass flow provide confirmation that the solution converged at each time step. One table was compiled at with a sampling of every 64 seconds, composed of the PCM liquid volume fraction, internal energy and Cartesian coordinate location. This table is used to find the axial height up to which the wax has fully melted. In order to keep its size small enough for MATLAB to compile, the table was composed from 272 axial-cut planes spaced at the same distance as the 1D experimental resolution, 0.3125 mm. A second data table reported information on the pore-fluid velocities and is composed of axial cuts distributed at half the sampling rate as the energy table. The pore-velocities were compiled once as they did not change with time. In the table, the element position, axial velocity and axial area are extracted and used to find the local porosity, local mean velocity, and local maximum

velocity for comparison to the experimental velocity maps. Lastly, the packed bed porosity is found using a report.

Results and Discussion

Experimental results are presented first starting with the packed bed structure and velocity maps. The heat transfer is characterized using the energy absorbed by the bed and propagation velocity of the fully melted front. The simulation results are introduced in a manner similar to the experimental results. The geometric similarity of the DEM generated bed and velocity field with the experimental beds is assessed, followed by comparison of the energy absorption rate in the model and the velocity at which the melt front propagates.

Packed Bed Structure and Velocity Maps

The experimental column was packed three separate times to produce three random packed beds. Each of these beds was melted three times at two different Reynolds numbers. The beds had an average particle count of 192, mass of 3.7 grams, and porosity of 0.43. The tamped packed bed typically had six exterior pores (near wall) and six interior pores around the central particle.

MRIs of pore-fluid velocity are shown in Fig. 6.7a-b for the two flow rates. The velocity images are located 40 mm above the bottom of the 85 mm long bed. The outer pores are well defined and have high pore-fluid velocities while the inner pores have lower velocity and are less well defined. The mean and maximum velocities observed in the images were 1.2 and 8 mm/s at *Re* = 2.3 and 2.6 and 15 mm/s at *Re* = 4.5. The flow rates in these images can be calculated as $\sum v_{pixel} \cdot area_{pixel}$, summing over all pixels. Flow rates found in this manner averaged 17%

lower than set at the pump. A lower flow rate is expected when measured in this way due to the effects of pixel volumes partially containing the solid domain. The majority of flow occurred in the pores adjacent the wall, which accounted for 83-87% of the volumetric flow at both of the *Re* values investigated. The velocity images can be analyzed to produce distribution of pore-velocity histograms, as shown in Fig. 6.7c where the arrows locate the mean value for each distribution. The histograms show some negative velocities due to recirculation, which occur in the narrow regions between particles and more high velocity at higher flow rate.

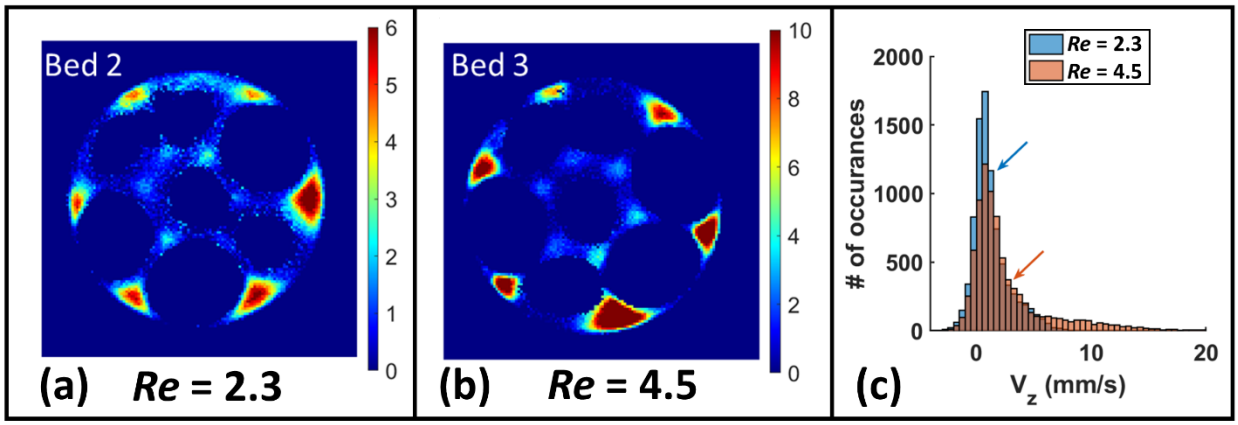


Fig. 6.7. Transverse images of pore- fluid axial velocity are shown for two different beds at *Re* = 2.3 and 4.5. Colorbar represents velocity in mm/s. The images are located 40 mm above inlet and were captured with MRI. Histograms of the pixel velocities can be created for the images (c). Arrows locate the mean pixel velocity for the histogram for each flow rate. At *Re* = 2.3 the mean velocities was 1.2 mm/s and at *Re* = 4.5 the mean velocity was 2.6 mm/s.

Experimental 2D Heat Transfer Results

The sequence of 2D signal intensity images of a typical trial at *Re* = 2.3 are shown in Fig. 6.8. Alternating transverse and longitudinal images are shown in the order acquired, taken at 136 second intervals. The longitudinal image extends from 20 to 60 mm above the bottom of the packed bed. The dashed lines on the longitudinal image show the location of the transverse images. The multiple slices and orientations clearly show initial heating near the walls. This

outside-to-inside heating was expected due to the strong channeling expected at this *N* value [170] and observed in the velocity images. In the displayed packed bed, melting occurred nearly evenly around the radius for the initial 20 mm, then became asymmetric in the top half. In the trials, side melting often preceded that of the center by five or more bead lengths, commonly forming a deep 'V' in the melt front but occasionally extending along a single side. Particle melting generally initiated along the wall-side and conducted inward. These images show the large degree of thermal dispersion and radial variations in melt rate indicating similar radial and axial variations in temperature.

At *Re* = 2.3, it took between 25 and 35 minutes for the imaging area to completely melt and between 15 and 20 minutes at *Re* = 4.5. In Fig. 6.8, melting in the observed region begins 12.8 minutes after the start of flow and the visible region was completely melted after 31 minutes. The average time for the imaged extent of the packed bed to melt was 30 and 19 minutes at *Re* = 2.3 and 4.5, respectively.

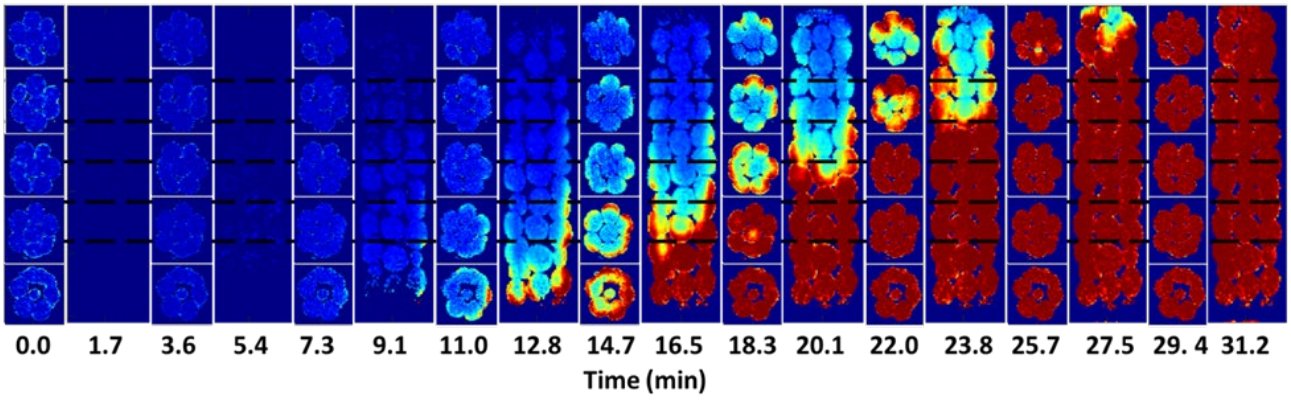


Fig. 6.8. MRI sequence of packed bed during heating at *Re* = 2.3. The transverse and longitudinal images were taken alternately at intervals of 136 seconds, reported minute times are rounded to nearest 1/10 min. The dashed black lines on the longitudinal images indicate approximate locations of the transverse images. Heating is shown to occur near the wall first, as expected due to channeling flow of the fluid.

Experimental 1D Intensity Profile Results

The 2D images were formed over a duration of 68 seconds, resulting in images where the pixel intensities are time averaged over this duration [131]. As a result, the melt front recorded in these images is not instantaneous but smoothed over the image duration. Higher temporal resolution of the melt progression in the packed bed can be acquired by sacrificing spatial resolution with 1D profiles of signal intensity oriented longitudinally with the packed bed, which are acquired in four seconds. The 1D profiles are composed of signal from the full volume of the packed bed (see Fig. 6.9 bottom right inset), providing a better measure of the axial progression of the melted front. The 2D images were formed from a 1 mm thick slice of the packed bed, providing no information on the wax-phase outside this region. The 1D signal can be analyzed to provide information on the fraction of bed melted in the imaged region and the longitudinal melt progression. As shown in Fig. 6.9, the fraction of the bed melted in the imaged region is proportional to the area under the 1D profile curves. Fig. 6.9 also shows how the melted front can be determined from the 1D profiles and 2D images. Averages for each bed and flow rate are readily attainable. In the 1D analysis, the dataset was necessarily truncated to exclude data outside center of the RF coil by +/-15 mm. As seen in Fig. 6.10a, the signal decays to zero at either end of the profiles due to loss of RF excitation homogeneity leading to a decrease in signal-to-noise ratio (SNR) and is not representative of the particle-wax state. The truncation of the dataset prevented the miss-registration of the melt front position.

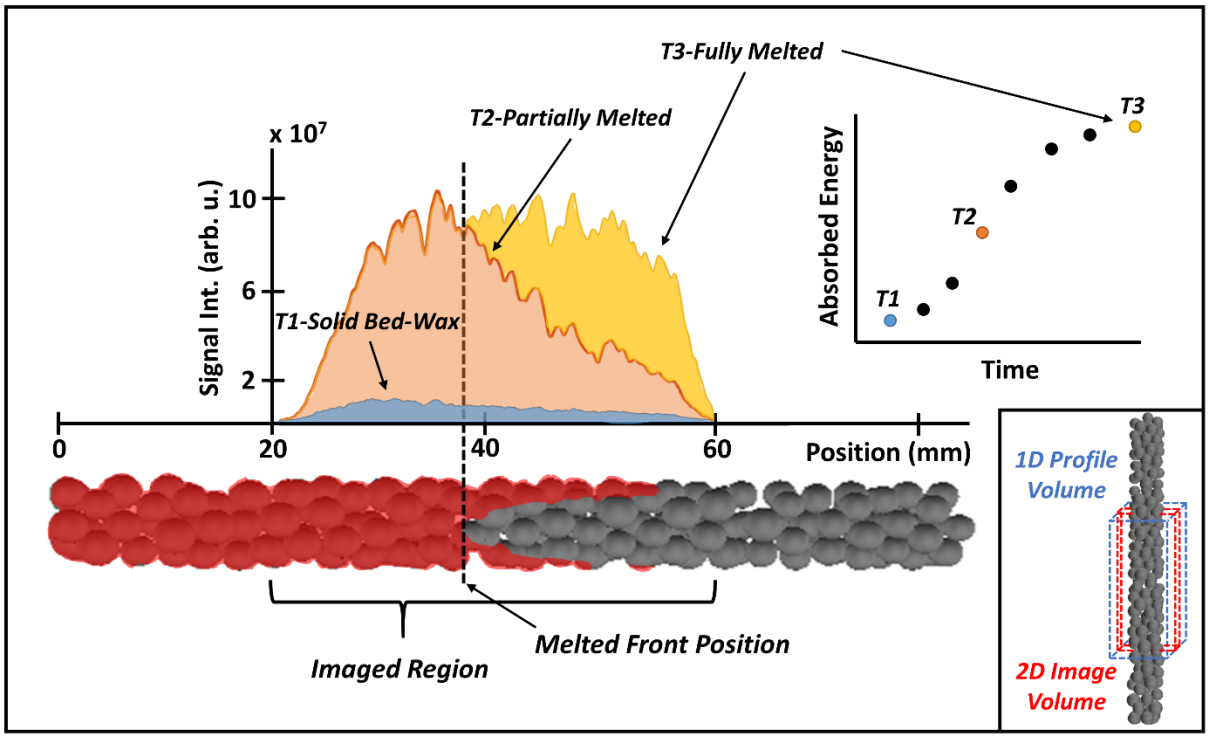


Fig. 6.9. Schematic of how 1D profiles can be used to determine the melt front position, and fraction of the bed melting. In the center three 1D profiles are plotted corresponding to solid alkane profile (blue), partially melted profile (orange) and fully melted profile (yellow). Below these profiles is an illustration of a partly melted bed. The dashed black line locates the melted height in b0th the 2D illustration and the partially melted 1D profile. In the upper right, the melting fraction is plotted against time. These time points correspond to the area under each 1D profile.

Longitudinal intensity profiles are displayed in Fig. 6.10a for flow at *Re*=2.3, where each line was recorded 2.25 minutes apart. The layered packing structure and low tube-to-particle-diameter ratio results in porosity fluctuations in the longitudinal direction, observed as jagged profiles. The areas of high/low particle density and the axial progression of the melt are clearly identifiable. Initially, the increase in signal intensity between time steps is small. During this time, energy absorption causes the solid particle-alkane to increase in temperature. Once melting initiates, larger step increases in intensity are observed until the alkane has completely melted,

after which there is little further increase in signal intensity. The 1D profiles show that some melting occurs over a broad region, extending across the full imaging region for some time steps.

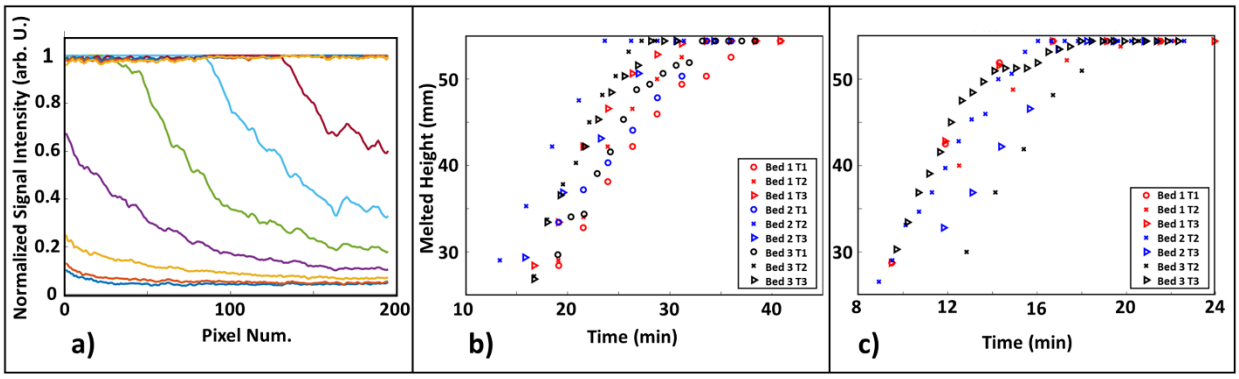


Fig. 6.10. 1D signal profiles can be acquired rapidly, providing a snapshot of the packed bed conditions. Figure (a) is a sequence of 1D profiles of signal intensity collected during melting at *Re* = 2.3. The jagged appearance is a consequence of the low tube-to-particle diameter ratio generating an ordered packing. These profiles were used to produce (b), which plot the area under each profile over time for each trial at *Re* = 2.3 and 4.5. These curves are then normalized and averaged for each *Re* value (c) where the normalized curves are representative of the fraction of the eicosane melted in the imaged area and measures absorbed energy.

The total signal intensity under each profile is directly proportional to the liquid fraction of the alkane and is therefore directly correlated to the amount of energy absorbed by the bed. This area is plotted against time in Fig. 6.10b for each trial, with the color indicating the packed bed number and the solid/dashed lines indicating flow at *Re* = 2.3 and 4.5, respectively.

Each melt trial can be normalized to its final intensity to remove the signal intensity variations due to differences in the mass of alkane in each of the packed beds. Normalization from 0 to 1 was performed by subtracting the signal intensity of the solid (cold) bed and dividing by the signal intensity of the final profile. The normalized results (Fig. 6.10c) represent the melt fraction of the bed-alkane. The individual curves can be averaged for each flow rate with the result shown in Fig. 6.10c where error bars represent one standard deviation. The mean melt fraction for individual beds are shown as dashed lines in c) for comparison. At *Re* = 2.3, the

mean melt rate of each bed was nearly identical. At *Re* = 4.5, beds 1, 2 were very similar, while bed 3 melted slightly slower. The greater variation in melt rates at higher *Re* is due to the convective heat transfer being more dominant at higher *Re*, so that changes in flow paths, caused by differences in packed bed structure, have a greater effect on the heat transfer rates.

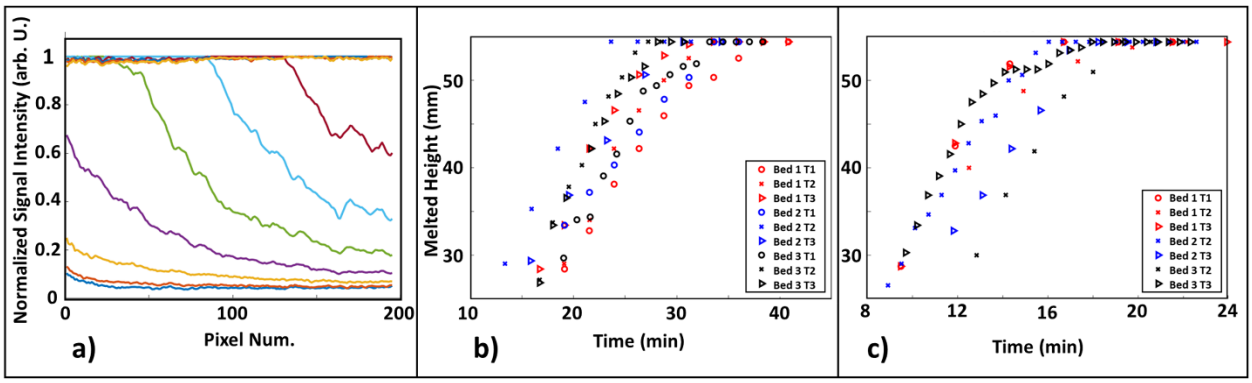


Fig. 6.11. Location of the fully melted front can be tracked by normalizing the 1D intensity profiles (a) and using a code to identify the furthest location with value > 0.97. These values can then be plotted against time for the *Re* = 2.3 (b) and 4.5 (c) flow rates to show melt front progression in the bed. In these plots, common color indicates the same packed bed and symbol indicates different trials.

The location of the melt front can be identified and tracked with the 1D profiles. This is accomplished by normalizing the profile to its completely melted value on a pixel-by-pixel basis. An example of the normalized profiles are shown in Fig. 6.11a. The furthest pixel with a value of 0.97 or greater was used to determine the position of the melt front. The value of 0.97 was selected to prevent noise fluctuations from affecting the identified position. These locations are plotted against time in Fig. 6.11b-c for *Re* = 2.3 and 4.5.

Experimental Discussion

Results plotted in Fig. 6.11b-c can used to find the mean overall beds of the axial height to which all eicosane has been melted. This result is plotted in Fig. 6.12a with error bars at one

standard deviation. The symbols in Fig. 6.12a represent the same position data estimated from the longitudinal 2D images, different symbols representing the different packed beds. The 2D image data matches well with the fit derived from the 1D plots, with most estimates falling within one standard deviation. At times past 14 and 26 min for *Re* = 2.3 and 4.5, respectively, the melt front extended past the visible region for some of the packed beds, resulting in an average dominated by the slower melting beds. These regions were excluded from the plot.

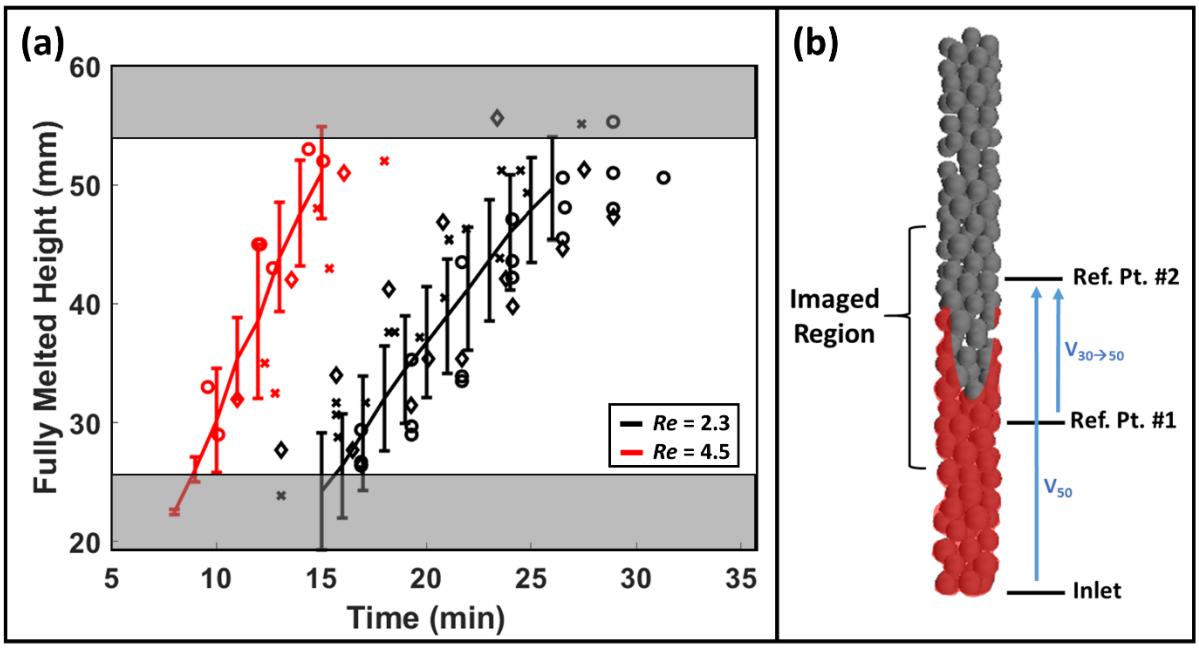


Fig. 6.12. The location of the completed melt front is an important parameter for validating the CFD model. In (a) the mean position of the melted height is plotted for both *Re* values with error bars representing one standard deviation. The symbols represent the melted front as determined in the 2D images. Melted height is the axial location below which all wax has been melted as indicated by the red dashed line in (b). An average speed at which the melted front propagated through the bed was calculated based on the time to reach Reference points 2, located at 50 mm above the inlet, and the time taken to proceed from reference point 1 to 2.

In Fig. 6.11b-c and 6.12a there are some obvious trial-to-trial variations in the axial position to which the wax has fully melted. However, tracking each trial over time, it is observed that the rate at which the melted height changes is fairly consistent, suggesting the propagation

velocity of the fully melted height is a better metric for comparison. Indeed, Fig. 6.2b shows that there was variation in the inlet temperature ramp rate during the first 4-5 minutes which may have contributed to the translational offsets observed. The ramped temperature also suggests that the propagation velocity should be found using two reference points in the imaged region *e.g.* the time taken to melt from 30 mm to 50 mm, and not based on a single reference point which would take the initial ramp time into account. This is illustrated in Fig. 6.12b where $\bar{v}_{30\rightarrow50}$ will be a more accurate comparison metric than $\bar{v}_{50}$, as it will be less affected by the temperature variations during start up. The selected reference points were 30 and 50 mm above entrance to packed bed (10 and 30 mm into the imaging window). This results in average melt front propagation velocities, $\bar{v}_{30\rightarrow50}$, of 2.3 and 4.1 mm/s at Re = 2.3 and 4.5, respectively.

Model Results

In the above results, mean and maximum pore-fluid velocities in the experimental data were determined and the heat transferred to the packed bed was characterized using the particle-bound alkane melt rates with a propagation velocity for the fully melted front. Additionally 2D images of the melting wax provided detail on the spatial variations in the packed bed. In the following sections the CFD model results will be presented and discussed with the aims to assess first the quality of the DEM generated bed in representing the experimental beds, including flow and second, the accuracy of the heat transfer which occurs. The primary metrics of assessment will be the packed beds structure, flow velocities and eicosane melt rates.

Model DEM Packed Bed Assessment

The five DEM packed beds generated with spherical particles were visually similar to the experimental packs. The difference between the simulation and experimental beds can be

attributed to the non-spherical shape of the experimental particles. Replication of the non-spherical shapes in the model was not possible due to the many organic variations. The non-spherical DEM particles were judged to be too arbitrary to represent the experimental distribution of shapes well. The use of non-spherical particles would also introduce the well-known difficulties in mesh generation and solution convergence [8].

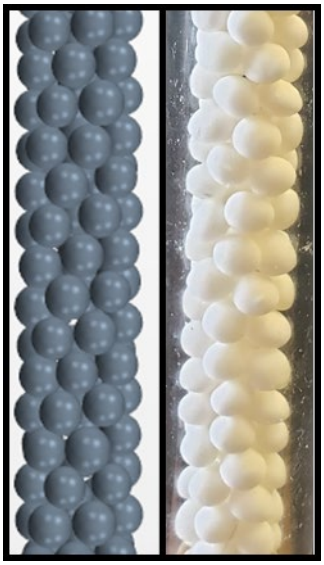


Fig. 6.13. Comparison of DEM generate packed bed and optical image of an experimental packed bed.

Despite the difference in shape, good agreement was found with the quantitative metrics used to assess the representation quality of the simulation packed beds with Gaussian diameter distributions. Table 1 reports the particle count, bed mass, porosity, mean pore-fluid velocity and maximum pore-fluid velocity for each simulated bed along with the average values for the experimental beds. In the simulation, the particle count ranged from 185 to 194 with an mean of 188. This was only 2.5% less than the experimental average. A greater difference occurred in the mass of the beds where the simulations beds contained 14.4% less eicosane than the experimental beds. The maximum velocity observed in the simulation and experiment match

well but the mean fluid velocity in the simulation was greater at both *Re* values. There are two considerations that nullify these differences. The spatial averaging, that occurs in the experimental velocity maps, especially at solid interfaces, will cause a decreased velocity measurement. This effect will be greatest in the axial direction, which is averaged over a 1mm slice thickness. The second consideration is the variability in local porosity which will cause similar variability in the local mean velocity.

Table 1. Metric comparison between the DEM generated simulation packed beds and experimental packed beds.

				Re = 2.3		*Re* = 4.5	
Bed #	PCM Count	Bed mass (g)	Porosity	Mean Velocity (mm/s)	Max Velocity (mm/s)	Mean Velocity (mm/s)	Max Velocity (mm/s)
1	187	3.17	0.45	1.6	7.4	3.2	14.2
2	186	3.15	0.45	1.6	7.4	3.3	14.3
3	185	3.14	0.45	1.6	7.8	3.2	15.0
4	194	3.15	0.46	1.6	6.0	3.1	11.9
5	186	3.15	0.43	1.6	7.8	3.2	14.3
Simulation Mean:	187.6	3.15	0.45	1.6	7.3	3.2	13.9
Experiment Mean:	192.4	3.68	0.43	1.2	8.0	2.6	15.0
Percent Difference:	2.5	14.4					

In the simulation, it is possible to investigate the spatial variability of porosity and its effects on the mean and maximum velocities. This is accomplished by compiling a table composed of the axial velocity, area perpendicular to the z axis (main flow direction) and (x, y) location in transverse slices evenly spaced at 0.625 mm increments. This table is then used to calculate porosity, mean velocity and maximum velocity in each transverse slice. The result is plotted in Fig 6.14 with the axial height oriented along the plot's x axis. There is a clear scatter in the data, which cycles regularly over the distance of a particle diameter. Each panel in the figure displays data from a single packed bed so the fluctuations are not obscured by averaging over multiple packings. Four of the five beds had variability similar to the result in panels (a) and (b) where porosity and velocities at *Re* = 2.3 are plotted respectively. The final bed had larger

variance, as shown in panel (c) of mean and maximum velocity at *Re* = 4.5. In the plots, the red markers represent the experimental values while the black o's and blue x's represent the average and maximum simulation values, respectively. The experimental values were taken at only a single location, so all are located at the same axial position. Note, the experimental values all fall within the scatter of the simulation results. Based on the visual similarities and agreement between local porosity, mean and maximum velocities and particle count, the simulation beds were determined to acceptably represent the experimental packed beds.

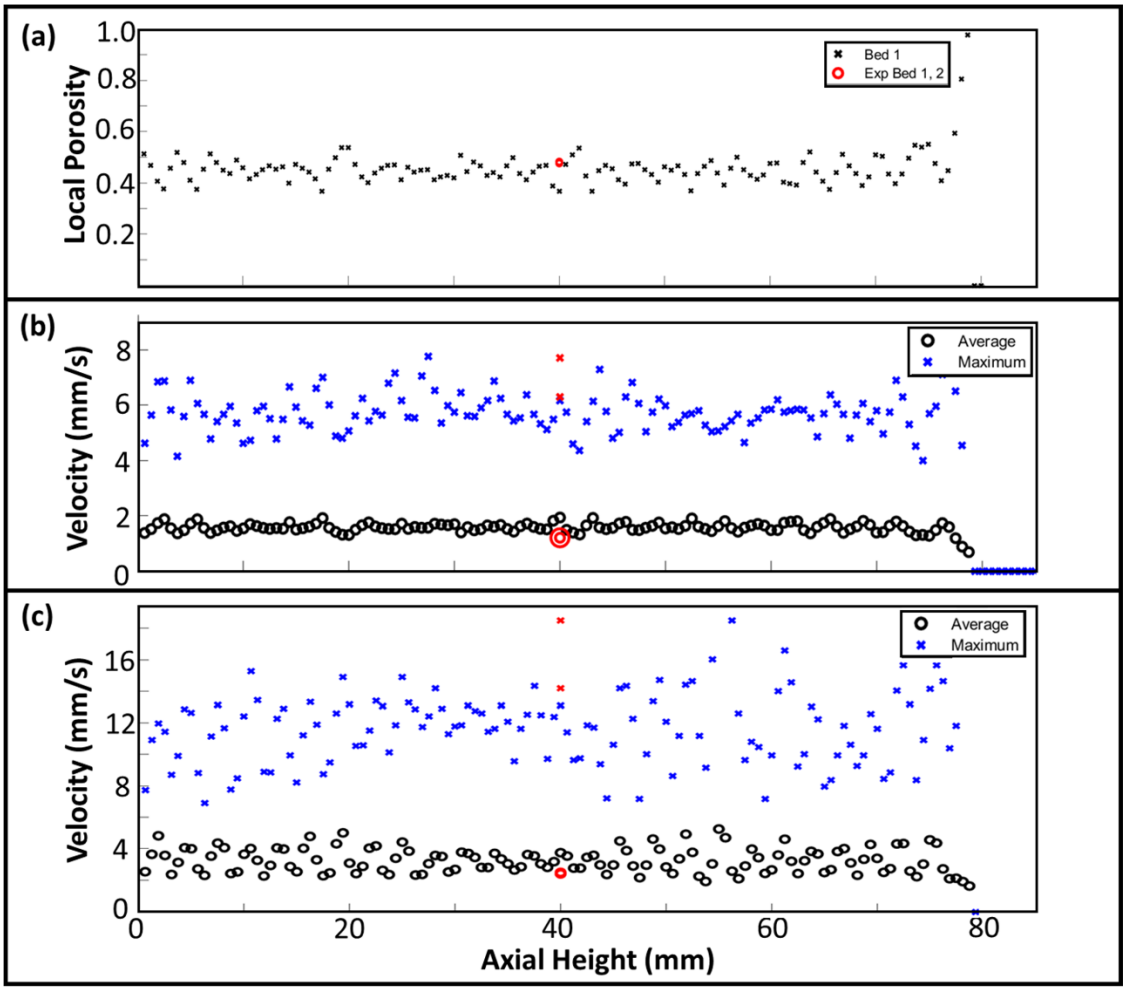


Fig. 6.14. Local porosity (a), mean and maximum velocities at *Re* = 2.3 (b) and 4.5 (c) are plotted against axial position in the column (on the *x*-axis). Simulation values are displayed at

0.625 mm spacing in black and blue. Experimental values are plotted in red at the single height they were collected. In (a) the porosity in axial slices from the simulation ranged from 0.357-0.55 with an average of 0.45. This compared well with the experimental porosity of 0.48. The local average and maximum fluid velocities are plotted in (c) and (d) with the experimental values falling within the scatter of the simulation values.

Model Heat Transfer Results

In Fig. 6.15, a simulation melt sequence is shown with alternating longitudinal and transverse images and time increasing to the right. These images show a combination of pore-fluid velocities and particle eicosane liquid volume fraction. In the velocity images, blue represents low velocity and red high velocity, ranging from 0-6 mm/s. In the transverse slices there are six pores along the wall but interior pores are indistinct. In the longitudinal images channeling is clearly evident, with the high flow regions only occurring along the walls. The liquid volume fraction colorbar ranges from dark brown (solid) to white (liquid). Melting occurs along the walls first and conducts inward, similar to the experimental MRI results. There appears to be greater thermal dispersion occurring in the simulation images with the melting along the walls extending seven or more bead lengths ahead of the fully melted position.

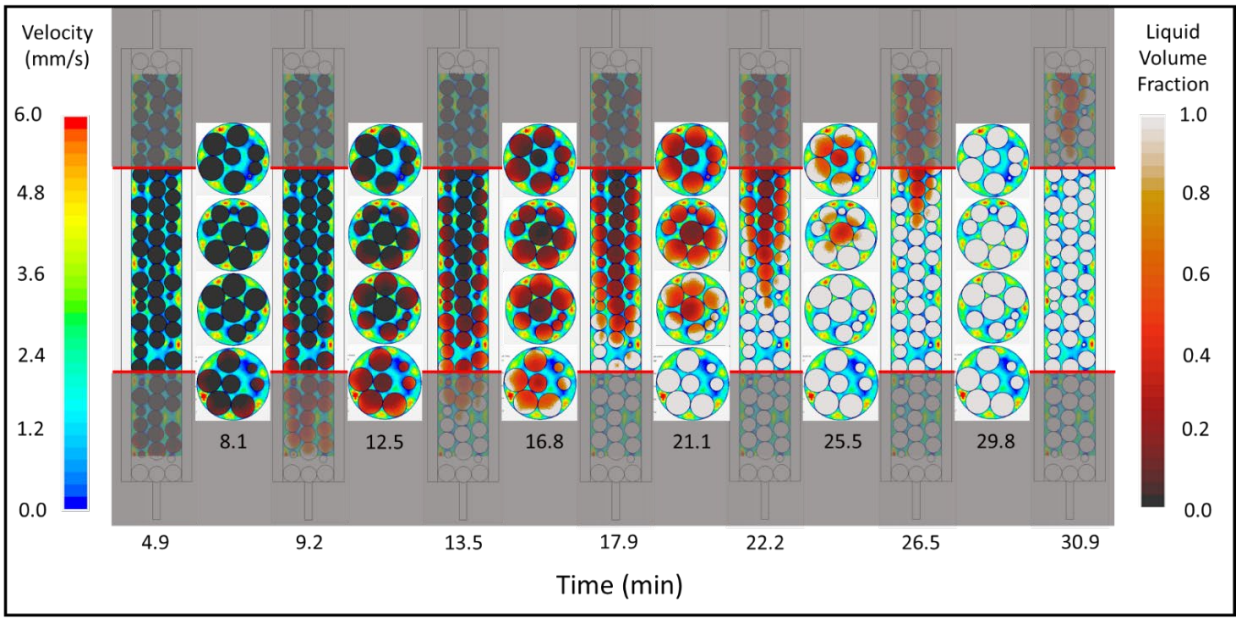


Fig. 6.15. Longitudinal and transverse combination images of pore-fluid velocity and particle liquid volume fraction with *Re* = 2.3. In the pore-space, blue represents low velocities and red represents high velocities. The particle colorbar ranges from dark brown for solid to white for liquid. The greyed out regions are regions of the simulation that are outside of the experimentally imaged region.

In Fig. 6.16a-b, the simulation and experimental data are compared. Fig. 6.16a plots the melt fraction of the bed in the region imaged in the experiment from 20 to 60 mm. This plot is represents of the energy absorbed by the packed bed. At the higher *Re* value, the two curves are nearly identical with the simulation starting to melt a couple minutes sooner. At *Re* = 2.3, the melt fraction of the simulation lags the experiment by approximately three minutes however, the two curves remain within one standard deviation. These results show the total energy transferred in the experiment and simulation are identical.

In Fig. 6.16b, the position to which the packed bed has fully melted is plotted against time. At both *Re* values, this position in the simulated bed is lower than in the experiment. In all cases, the propagation velocity of the fully melted front is consistent over time. At the lower *Re* value, the time dependent melt front propagation velocities agree well with 2.2 and 2.3 mm/s for

the simulation and experiment respectively. At the higher *Re*, the simulation melt front is considerably faster with a propagation velocity of 4.9 mm/s compared to the simulation finding of 4.2 mm/s.

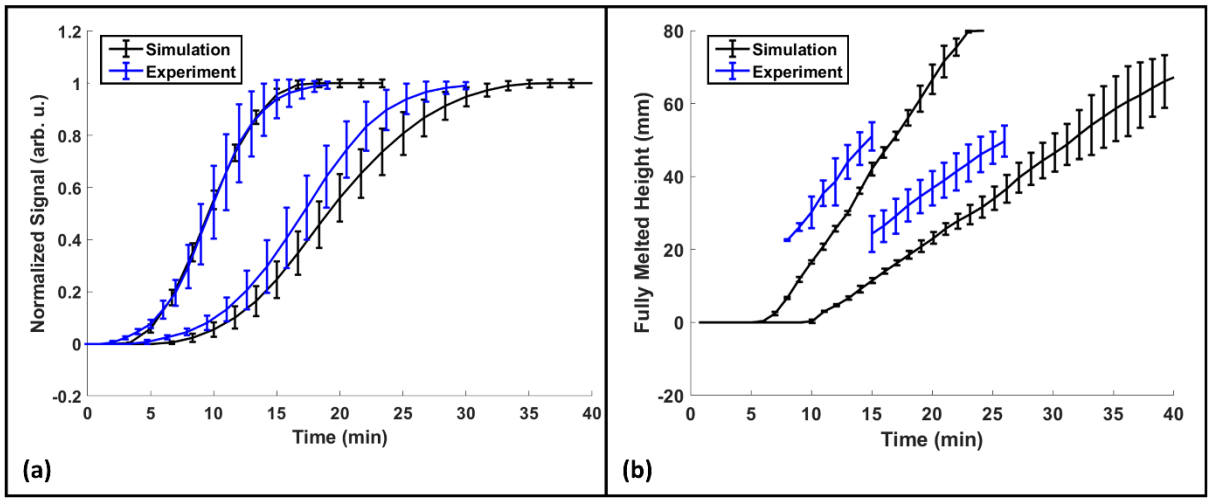


Fig. 6.16. Simulation and experimental data are compared at both *Re* values. In (a), the melt fraction of the packed bed for the imaged region is plotted against time with simulation in blue and experiment in black. In (b), the vertical height to which the wax was completely melted is plotted. There is good agreement in (a), which is indicative of the total energy absorbed by the packed bed. In (b) there is a translational offset in the fully melted height. In the lower *Re* data, the melted position proceeds at the same rate.

Conclusions

A novel experimental set up was presented which uses MRI to image pore-fluid velocities and heat transfer to the particles in the same packed bed, on the micro scale. This was achieved by using a fluorinated pore-filling liquid and hydrogen rich macro-scale particles composed of an agglomerate of micro-scale, eicosane-filled, core-shell particles. The solid particle shell remained rigid when the encapsulated wax was melted under heated pore-fluid flow and the solid-liquid phase change of the alkane provided an easily identified increase in signal intensity proportional to the energy absorbed. A combination of pore-fluid velocity images and particle-

alkane signal intensity images recorded the propagation of the particle-bound alkane melting. 1D profiles of signal intensity were used to track the position the fully melted front and the fraction of the imaged bed melted. These results were compared to a particle-resolved 3D CFD simulation constructed in STAR CCM+. DEM packed beds were generated that represented the experimental packed beds. The PCM particles were modeled using Eulerian multiphase physics based on material properties determined through DSC analysis. The energy transferred to the bed was found to match well with the simulation. The position of the melt front did not match the experimental values but the melt front propagation velocity matched well for the low *Re* model.

CHAPTER SEVEN

AXIAL VARIABILITY OF PATTERN FORMATION IN RAYLEIGH-BENARD CONVECTION: MRI VELOCIMETRY IN A LOW ASPECT RATIO CONTAINER

Contribution of Authors and Co-Authors

Manuscript in Chapter 7

Author: Matthew E. Skuntz

Contributions: Wrote manuscript. Collected and analyzed data. Implemented experimental system. Incorporated revisions and provided feedback on reviewer comments.

Co-Author: Brenden G. Pelkie

Contributions: Assisted in data collection. Developed CFD simulation.

Co-Author: Sarah L. Codd

Contributions: Edited manuscript. Provided technical support in data collection and analysis.

Co-Author: Ryan Anderson

Contributions: Edited manuscript. Conceived experimental method. Secured funding.

Co-Author: Joseph D. Seymour

Contributions: Edited manuscript. Provided training on experimental methodology. Secured funding.

Manuscript Information Page

Matthew E. Skuntz, Brenden G. Pelkie, Sarah L. Codd, Ryan Anderson, and Joseph D. Seymour

International Communications in Heat and Mass Transfer

Status of Manuscript: (Put an x in one of the options below)
___ Prepared for submission to a peer-reviewed journal
___ Officially submitted to a peer-reviewed journal
___ Accepted by a peer-reviewed journal
_X_ Published in a peer-reviewed journal

Elsevier Volume 118, November 2020

https://doi.org/10.1016/j.icheatmasstransfer.2020.104869

AXIAL VARIABILITY OF PATTERN FORMATION IN RAYLEIGH-BENARDCONVECTION: MRI VELOCIMETRY IN A LOW ASPECT RATIO CYLINDER

Abstract

Natural convection is a fundamental hydrodynamic instability and a template process for the study of pattern formation. It is also an important mode of energy transport in natural geophysical and environmental systems, as well as technological applications. In solar heating devices, pasteurization processes, industrial mixing, and pebble-bed nuclear reactors, low aspect ratio systems of greater depth than width are widely used for their favorable convection properties. Here, magnetic resonance imaging was used to quantify the axial spatial variation of flow patterns in a narrow cylinder. Fluid velocity maps were acquired in multiple transverse and longitudinal planes. It is shown that the flow patterns vary significantly as a function of the height above the heated bottom boundary. The large scale circulation varies among predicted azimuthal mode patterns. Azimuthal 180^{o} reorientation of the upward and downward flow cells was observed over short axial distances. The complex circulation patterns observed suggest acquisition of velocity data in only one plane could lead to mischaracterization of flow patterns in low aspect ratios systems, an aspect of the current literature which is lacking quantification. A preliminary computational fluid dynamics model in STAR-CCM+, corroborated by the experimental results, provided velocity and temperature data for the full fluid column height. Together these results indicate the need for further investigation into circulation characteristics in long narrow cylinders. Enhanced understanding of these rapid axial variations in flow pattern will allow better modeling of heat and mass transport in low aspect ratio natural convection flows.

Key words: natural convection, MRI, velocity mapping, low aspect ratio, Rayleigh-Bénard convection

Introduction

Flow patterns in Rayleigh-Bénard convection (RBC) have fascinated scientists for over a century due to significant diversity of the flow patterns generated, which self-organize in response to an applied temperature gradient. In RBC, an unstable density gradient is introduced by bottom heating and/or top cooling, inducing motion when the instability exceeds a critical gradient. The flow pattern formed by the circulation is dependent on the Prandtl number of the fluid ($Pr = \nu/\kappa$), shape of the container, and the Rayleigh number (Ra) of the system. Ra is calculated in terms of the coefficient of volumetric thermal expansion α, gravitational acceleration g, the temperature difference ΔT applied across the fluid of depth L, thermal diffusivity κ and kinematic viscosity ν, was $Ra = \alpha g \Delta T L^3/\nu\kappa$. Motion initiates at the critical Rayleigh number Ra_c, which corresponds to a critical temperature gradient for a specific fluid, here water. The Ra_c required to generate flow decreases with increasing container aspect ratio (Γ= fluid width/depth which for a cylinder is d/L), asymptotically converging on $Ra_c = 1708$. Our data shows that in low aspect ratio cylinders the large scale circulation generates cross sectional flow patterns which change rapidly with height in the cylinder. This is an characteristic of low aspect ratio RBC which has not been considered in detail as indicated by publications which analyze the flow pattern without consideration of axial variation [58] in a single fixed plane in the system [4, 171] or study the large scale circulation with little discussion of the in plane pattern variation [172-175].

RBC for high aspect ratio systems is well studied, in part due to mathematical simplifications that can be applied to the theoretical analysis, *e.g*. neglection of lateral wall effects, application of the Boussinesq approximation, and use of constant fluid properties [53]. These simplifications allow an analytical solution to the buoyancy-driven convection problem using linear analysis [52, 53, 59, 176-178]. At aspect ratios larger than 3, the analytical eigensolutions of the linear theory are close together and oscillate with Γ [58, 176]. This results in the potential for multiple circulation patterns at the same *Ra* number. Ra_c is within 10% of the asymptotic value when $\Gamma > 4$, implying that viscous dissipation at the side wall has only a minor effect on these systems [58]. Below this aspect ratio, viscous wall effects have an increasing impact on system transport and must be accounted for. Growing interest in these low aspect ratios systems has been driven by their applicability to a wide range of fields and advancement in numerical simulations. Low aspect ratio systems are important in geophysics [6, 7], crystal growth [179], pasteurization [3], monitoring wells [4], solar heating devices [5] and nuclear reactors [180]. Despite these applications, low aspect ratios systems have received considerably less attention in the literature, particularly regarding flow pattern formation.

The flow pattern can be described by the number of zero-velocity flow planes in a 360° rotation around the cross-section following the approach of Charlson and Sani [58]. Fig. 7.1 shows magnetic resonance (MR) velocimetry data that demonstrates flow patterns with $n = 0$, 1, 2 in the cross-section of a cylinder. In the images, red denotes upward flow and blue downward flow. The $n = 0$ system has no zero-velocity planes and two flow cells in a concentric arrangement, while $n = 1$ has one zero-velocity plane and two flow cells, while $n = 2$ has two zero-velocity planes and four flow cells.

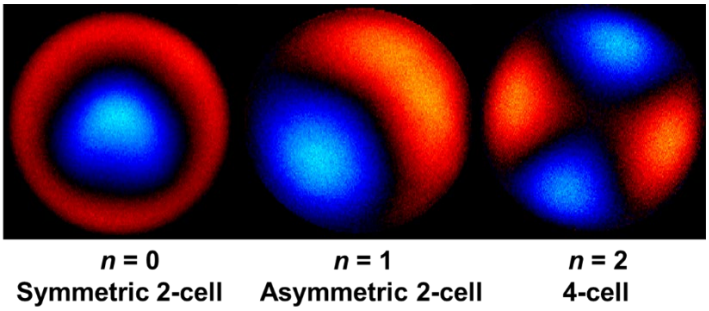


Fig. 7.1. Flow patterns are described by the number of flow cells and the number of zero velocity planes in a 360° rotation about the cross-section dependent on context. Red indicates regions of upward flow and blue downward flow.

Experimental investigations into RBC have been accomplished with several methods. Imaging with the shadowgraph technique and measurement of heat flux rates with thermopiles were long the only methods available [52, 53, 60, 61, 171, 181-185]. The shadowgraph technique is still reported in experiments today [186-188]. Additionally, large scale circulation patterns have been inferred from temperature measurements using multi-thermal-probes which monitor wall temperature to infer locations of upward and downward flows [172, 173, 175, 189]. Recently, particle image velocimetry (PIV) and magnetic resonance imaging (MRI) have been applied to aspect ratios near one [37, 156-158]. Experimental data on low aspect ratio RBC flows is minimal for PIV [4], and MRI [190, 191]. Other RBC studies by MRI have investigated aspect ratios from 1 to 6 [192-195]. Application of MRI and PIV to natural convection has the advantage of measuring fluid velocity and temperature, making these methods well suited for comparison to numerical simulations.

Due to the difficulty in experimentally studying RBC, much research has focused on computational fluid dynamics (CFD) simulations [11, 196-199]. Building on shadowgraph experimental observations of Hof *et al*. [171], numerical simulations investigating hysteresis effects on pattern selection have mapped flow pattern bifurcations. Hof *et al*. (1999) observed a

multitude of flow states in a container of $\Gamma = 4$ filled with water at $Ra = 14{,}200$ ($Ra = 8.3\ Ra_c$). The bifurcation diagram developed numerically [196-198] covered the same conditions [171] with both insulating and conducting lateral walls. Sixteen different bifurcations and more than twelve different flow patterns were observed to be stable at $Ra = 14{,}200$ with even more stable patterns probable. It is important to point out that these diagrams are only valid for $\Gamma = 4$. A change in Γ will change the location of bifurcations and influence which patterns are stable. Notably, these studies do not provide data or analysis on the axial variation of the flows.

In low aspect ratio cylinders, imaging in a single plane does not elucidate the complex fluid dynamics occurring in the system. Our data clearly show that single images of the flow can be incorrectly interpreted as three stacked counter-rotating cells. It is also shown that a single flow pattern composed of long straight flow cells was not stable. The data presented demonstrate that the spatial velocity patterns are strongly dependent on axial position. Wall effects induce a variation, with axial location, of fundamental aspects of the flow, such as the number of cells present. Theory, such as that of Charlson and Sani [58], predict a fixed number of cells. In our experiments the flow evolved from a symmetric bullseye ($n = 0$) to a four-cell pattern ($n = 2$). The downward stream was also observed to abruptly shift across the column in a short distance. These results indicate that measurements at a single axial location or vertical plane are not enough to characterize the entire system. Simulations need to consider axial variation as done in some simulation and theory work [200, 201] but not all [202]. Our own simulations indicate highly variable patterns in low aspect ratio cylinders.

RBC investigations of flow have also considered cessation, reversal and bimodal frequency in lower aspect ratio systems. Recent studies have focused on turbulent RBC at aspect

ratios of 1/3 to 2 with an emphasis on heat transfer behavior (e.g. Nu (Ra)). Turbulent RBC can exhibit strong corner flow [203], meandering [204], mode transitions [204], multiple vertical rolls, cessations and reversals [174]. As noted by Ahlers *et al.* [173], how the flow varies with aspect ratio is understudied. Our MRI data indicates the large scale circulation is associated with systematic variations of the transverse flow pattern which varies among predicted patterns of mode n. A very low aspect ratio container with $\Gamma = 0.05$ was studied by Berthold *et al.* [4] via PIV. The longitudinal flow pattern was imaged and showed time-dependent flow patterns with increasing Ra. Their work captured the velocity field in one longitudinal plane for the full column height. They noted a transition from a quasi-stationary to time-dependent flow where multiple rolls developed in the height. Their analysis did not capture the transverse flow field, so it was unable to consider transverse flow pattern variation with height.

In this work MRI is used to quantifying RBC flow pattern formation in a system with $\Gamma = 0.12$. Application of MRI allows the vertical velocity field (*i.e.* v_z) to be imaged at multiple horizontal (transverse) and vertical (longitudinal) cross-section positions in the lower portion of the convective column [92]. MRI velocimetry is well established as a tool for studying fluid dynamics in a range of flows and systems [92, 94, 101, 160]. Studies of hydrodynamic instabilities [161] and particularly applications to natural convection [36, 205] have been somewhat more limited focusing on porous media [17, 38, 206], convection in mushy layers [162] and sea ice [207] have been reported, but not of fundamental flow pattern formation. Here, the convection patterns of water were observed for Ra numbers from 8.4×10^7 to 2.3×10^8. A CFD model was constructed in the commercial solver STAR-CCM+ to provide qualitative comparison to the experimental system. Importantly, the MRI data indicate the pattern formation

varies significantly as a function of axial position, indicating that a single imaging plane is not enough to characterize the flow in low aspect ratio systems, and challenging theory to incorporate such variations.

Experimental Methods

MR velocimetry allows non-invasive measurement of fluid displacements at any position within the sensitive region of the spectrometer's radio frequency (RF) coil [94]. MRI measures velocity in the direction of the applied motion-sensitizing gradient, in this case the long axis of the cylinder. MRI velocity data is both time [28] and volume averaged. The number of points collected determines the spatial resolution of the image and size of the imaging volume (voxel) over which the velocity is averaged. Images were acquired with 256 frequency encoded points and 128 phase encoded points for a spatial resolution (voxel size) of 70 by 140 μm over a 1 mm slice thickness (x, y, z) for transverse images and 1 mm by 140 μm by 156 μm (x, y, z) for longitudinal images. The total acquisition time during which voltage signals are averaged determines the temporal averaging. Ten images were acquired over a period of 3 hours with each image taking 17 minutes, thus providing the stationary velocity averaged over 17 minutes. Velocities in all three coordinate directions were measured in this experiment but only the axial velocity images (vertical z-component of velocity) are reported as they provide the flow pattern characterization. Velocity maps were measured with a two-step pulsed-gradient spin echo (PGSE) pulse sequence with pulsed gradient durations of $\delta = 0.5$ ms and a displacement averaging time of $\Delta = 7.545$ ms [92]. Transverse MRI velocity images were acquired at five axial locations and two longitudinal orientations 90 degrees apart, as shown in Fig. 7.2b. The five

transverse axial cross-section slices were collected at heights of 10, 20, 24, 30 and 34 mm above the container bottom.

Experiments were performed in a vertical super-wide-bore 7 Tesla superconducting magnet networked to a Bruker Avance III 300 Spectrometer equipped with micro2.5 shielded gradient coils with maximum gradient strength of 1.5 T/m at 60 Amps in all 3 coordinate directions. Proton (^{1}H) nuclei of the water sample were used for MR signal at a nominal frequency of 300.19 MHz. A 25 mm interior diameter ^{1}H birdcage coil with an active imaging length of 40 mm was used.

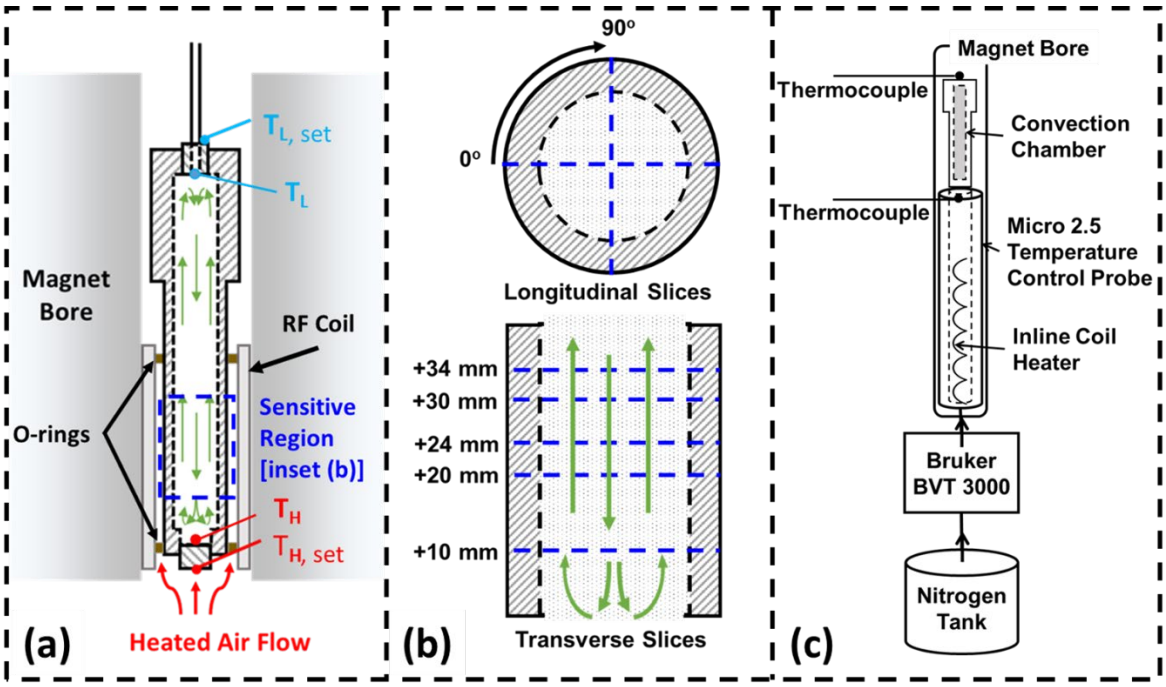


Fig. 7.2. (a) MR compatible convection chamber. $T_{L, set}$ and $T_{H, set}$ were the temperatures set in experiment. (T_H - T_L) was the temperature differential applied to the fluid, which determined the Ra of the flow. (b) Position of MR images inside the dashed box in (a). (c) PID controlled heating system with air flow heated by a helical coil.

MR introduces size, instrumentation, material and experimental flow cell constraints. The entire flow cell, heating, and instrumentation were designed to fit inside the 40 mm bore of the

super-conducting magnet and 25 mm RF coil within the RF probe. The thin walled (2 mm) convection vessel had thick (10 mm) top and bottom to allow pressurized attachments, shown in Fig. 7.2a, and was made of polyetheretherketone (PEEK). The size restrictions limited velocity measurements to the bottom 34 mm of the convection chamber. The interior dimensions of the flow chamber were 140 mm in length, *i.e*. depth of fluid, and 17 mm in diameter, *i.e*. width of fluid, for an aspect ratio $\Gamma = 0.12$. Thermocouples (TCs) and other metal objects interfere with MRI measurements and cannot be in the sensitive region of the RF coil during MRI experiments. This means temperatures at the fluid boundaries could not be monitored during velocity measurement. Instead, repeat experiments were performed to measure system temperatures and velocities separately. Temperatures were measured via TCs attached to the exterior and interior of the vessel. On the exterior, TCs were attached to the top, mid-point, and bottom of the vessel. On the interior TCs similarly located were attached to a probe inserted into the fluid. The experiments were then repeated to measure velocities with all TCs removed except for the top exterior TC and bottom exterior TC connected to the heater PID controller, neither interfered with MRI. Spectrometer bore temperature was set indirectly to 22.8ºC by a temperature control water bath used to internally cool the magnetic field gradient coils. The gradient cooling system maintains a constant temperature during use. The bore temperature was monitored by a thermocouple located near the top of the flow cell and was used as the ambient temperature in the numerical simulations. Temperature at the bottom boundary was controlled via a Bruker BVT 3000 in-line temperature controller composed of a resistance heating element, a thermocouple located just below the convection chamber and a PID controller, which maintained an N_2 gas stream external to the flow cell at a constant temperature. At the base of the convection

vessel, the spectrometer bore was blocked with rubber O-rings fitted tightly between the convection chamber and the RF coil. These O-rings prevented direct convective heating of the vessel sidewalls. The N_2 gas was thereby forced out the bottom of the probe base and magnet bore. The temperature control system is shown in Fig. 7.2c. Heat transfer from the vessel lateral and top walls was only through natural convection of the surrounding air. The system was allowed to equilibrate for one hour after increasing the temperature. After scans were completed, the temperature gradient was increased, and the process repeated with flow data collected after a stable stepwise increase in temperature was realized.

Numerical Method

A dimensionally accurate CFD model was built in STAR-CCM+ (Version 14.02.010 by Siemens PLM) with a fluid region surrounded by a PEEK shell. Energy transport within the solid and fluid regions of the flow cell were simulated with STAR CCM+ solving the three dimensional (3D) continuity, momentum, and energy equations.

$$\frac{\partial \rho}{\partial t} + \boldsymbol{\nabla} \cdot (\rho \boldsymbol{v}) = 0 \qquad \textit{Eq. 143}$$

$$\rho \frac{d\boldsymbol{v}}{dt} = -\boldsymbol{\nabla} p + \rho(T)\boldsymbol{g} + \mu \boldsymbol{\nabla}^2 \boldsymbol{v} \qquad \textit{Eq. 144}$$

$$\frac{dT}{dt} = \kappa \boldsymbol{\nabla}^2 T + \boldsymbol{v} \cdot \boldsymbol{\nabla} T \qquad \textit{Eq. 145}$$

Boundary conditions were applied to the exterior envelope of the convection vessel where conditions were known. A fixed temperature boundary condition was applied to the bottom of the PEEK region. This temperature was set according to the recorded experimental conditions. A general convective heat flux boundary condition was applied to the exterior of the lateral wall and top of the PEEK region which simulated the heat loss due to natural convection in the

spectrometer bore. The spectrometer bore air and PEEK vessel exterior temperatures were experimentally recorded and used to estimate the convective heat transfer coefficient to be 4 W/m^2K. The fluid and PEEK solid phase regions were discretized with a rectangular mesh with base size of 5 x 10^{-4} m, and growth rate of one. A rectangular mesh with even spacing was chosen to remove asymmetric variations noted in the polyhedral mesh, removing the mesh's influence on the resulting asymmetric flow patterns. Segregated flow and energy solvers were used with an implicit unsteady time model. A time step of 10 seconds with 50 internal iterations was used. An independence study on the fluid velocity and heat flux were performed on the time step and mesh size. In STAR CCM+ the velocity and pressure fields are coupled via the SIMPLE algorithm and a second order upwinding discretization scheme is used for the convective term. The Boussinesq approximation was not applied, rather, fluid thermo-physical properties were defined as polynomial functions of temperature from 200-400 K by fitting to NIST data [64], yielding polynomial fits for the viscosity in Eq. 146, density Eq. 147, heat capacity Eq. 148, and thermal conductivity Eq. 149.

$$\mu = 0.0297 \cdot T^2 - 1.71 \times 10^{-4} \cdot T + 2.49 \times 10^{-7}\ Pa \cdot s \qquad \textit{Eq. 146}$$

$$\rho = 717.45 \cdot T^2 + 2.12 \cdot T - 0.004\ kg/m^3 \qquad \textit{Eq. 147}$$

$$c_p = 13228.5 \cdot T^3 - 81.9 \cdot T^2 + 0.246 \cdot T - 2.44 \times 10^{-4}\ J/(kg \cdot K) \qquad \textit{Eq. 148}$$

$$\lambda = -0.75 \cdot T^2 + 0.00745 \cdot T - 9.68 \times 10^{-6}\ W/(m \cdot K) \qquad \textit{Eq. 149}$$

The bottom temperature of the simulation was stepped up in the same manner as the MRI experiments. By modeling the PEEK vessel and applying the temperature boundary conditions to the vessel exterior, knowledge of the interior experimental temperature was not necessary for model setup. Both velocity and temperature numerical data were recorded from the simulations. Transverse numerical data images were located incident to MR images and at locations higher in

the convection chamber. Longitudinal numerical images were incident to MRI maps but at full length of the convection chamber. It should be noted that this is not a validation of our simulation model, rather, the simulation results are presented to provide corroborating evidence on the variability of flow pattern with axial height observed experimentally. In the simulation, flow patterns continue to evolve above the region experimentally imaged, reinforcing the need for further investigation.

Results

In most RBC experiments the top and bottom plates are composed of high thermal conductivity materials in order to maintain boundary temperatures that are constant and even. The PEEK plastic vessel used here had low thermal conductivity which allowed temperature to vary radially at the top and bottom boundaries. This variation was apparent in the simulation results where the temperature variability was greater, with more asymmetry, at higher *Ra*. A similar variation in boundary temperatures was observed experimentally with repeat experiment temperatures differing by up to 1.5^{o}C with the same boundary conditions. These experimental temperatures fell within the bounds of the simulation results. Due to our inability to monitor the spatial temperature distribution of the experimental boundaries in this system, the *Ra* values reported below were calculated using the simulation temperatures with the maximum temperature at the bottom boundary and minimum temperature at the upper boundary used to determine the temperature differential seen by the fluid.

In the experiment, five transverse velocity images were obtained at 10, 20, 24, 30, and 34 mm above the heated bottom, along with two perpendicular longitudinal velocity images that bisect the transverse images at 0^{o} and 90^{o} as shown in Fig. 7.2b. In these images, blue indicates

downward velocity and red upward velocity. MR velocity images at four *Ra* are shown in Fig. 7.3. The flows in these images are stable and steady over the 17 minutes they were acquired. The MR images are time averages of the velocity profile and the velocity of each pixel is a volume average over the pixel in-plane dimensions and 1 mm slice thickness. The steadiness of the flow is indicated by the absence of signal decay that would occur in the presence of fluctuations in velocity [63]. With an acquisition averaging time of 17 minutes, these images are effectively a snapshot in time, approximately $0.008\tau_c$ (τ_c = 1.3e5 s) relative to the thermal diffusive timescale ($\tau_c=L^2/\kappa$) of the system. For this cylindrical column with an aspect ratio Γ = 0.12, Ra_c = 4.5 x 10^6 for insulating walls and 1.4 x 10^7 for conducting walls [10]. Considering the thermal conductivity ratio between the fluid and PEEK vessel (5:2 water:PEEK), an assumption of insulating walls was used to determine all ratios of Ra/Ra_c. Both *Ra* number and its ratio to the critical value are reported for clarity.

In Fig. 7.3a, b experimental results at 8.4 x 10^7 and 1.2 x 10^8 *Ra* are shown. The transverse images show two-cell, n = 1, flow at both *Ra*. Near the flow cell bottom, similar ‘C’ shape patterns rise to a height of 10 mm and 20 mm. In Fig. 7.3a at 24 mm, the warm upward rising fluid split around the cooler stream and reconverged on the side opposite its starting position. This manner of rapid reorientation of the two flow cells was observed consistently in experiments. At 8.4 x 10^8 *Ra* this transition of the flow pattern occurred in only Δz = 6 mm (24 mm to 30 mm). The warmer rising fluid then begins to merge as the vertical height increases, generating a nearly symmetric n = 1 flow at 34 mm. The sharp transition across the column can be clearly seen in the horizontal longitudinal image as a movement of the falling fluid to the right.

The MR velocity data in Fig. 7.3c, d corresponds to 2.0 x 10^8 and 2.3 x 10^8 *Ra*. The wall near the cylinder bottom is sufficiently warm due to the higher temperature to cause an $n = 0$ two-cell flow pattern (*i.e.* 'bullseye') up to a height of 10 mm, with some asymmetry. The rising fluid contracts into a 'C' shape by $z = 20$ mm, extending to 24 mm, while the cool sinking fluid shifted to the wall. At 30 mm both streams begin to split, with an $n = 2$ four-cell flow pattern emerging at a height of 34 mm. The flow was not imaged higher in the cylinder, leaving it unclear whether the four-cell flow was stable over a larger distance. This indicates a need for construction of a high flexibility temperature control flow cell, capable of being positioned vertically within an MRI RF coil over the entire flow cell length. A challenge for future experiments.

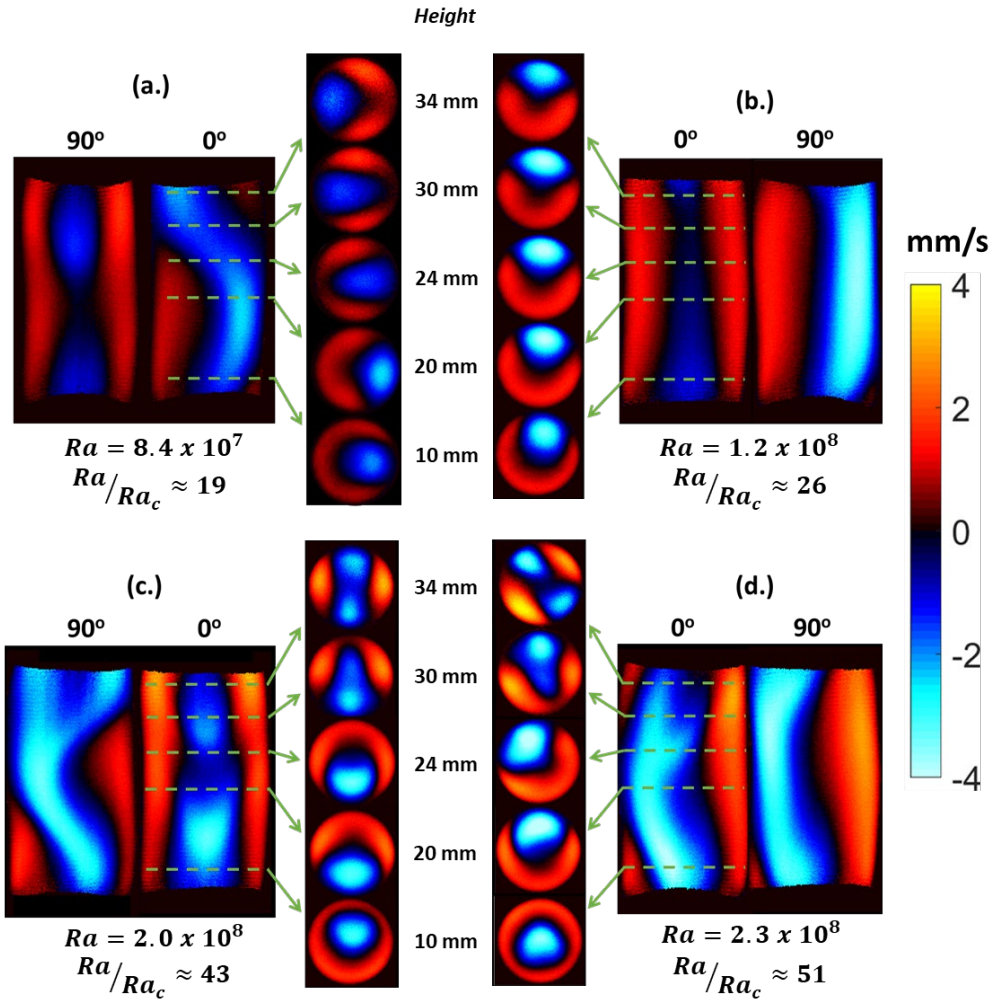


Fig. 7.3. Longitudinal and transverse MRI velocity maps taken in the bottom 40 mm of the fluid column, compared at four *Ra* values. With respect to transverse images, longitudinal images are oriented horizontally (0°) and vertically (90°).

Simulation results for *Ra* 8.4 x 10^7 to 2.3 x 10^8 (19 to 51 Ra_c) are shown in Fig. 7.4. The flow features observed in the numerical results develop in the same manner as observed experimentally. At 19 Ra_c and 26 Ra_c, 'C' shaped flow is observed at the bottom. By 20 mm, n = 1 two-cell flow develops and maintains its stability within the MRI imaged region. Higher in the column, the same manner of cell reorientation as seen in Fig. 7.3a is observed. Flow

development was similar at 43 Ra_c and 51 Ra_c, with 'C' shaped flow at the bottom, which quickly transitioned to $n = 2$ flow by a 20-24 mm height.

Unlike the experiment, the full column height of the simulation could be investigated. Similar flow patterns were observed in the top 40 mm (except for the four-cell pattern which was not observed near the top). In the upper region, when 'C' shaped flow was observed, the downward flow hugged the walls, with the upward flow confined near the center. Similarly, it was the upward flow which passed through the center of the column, bisecting the downward cell, the opposite as seen near the bottom. In the center of the column height two-cell flow was seen at every *Ra* value. Moving axially along the column height, the upward and downward flow cells spiraled at 19 Ra_c, and transitioned through the center of the column at all other *Ra* values.

Temperatures and velocities are available from the numerical results. The maximum values in the simulation ranged from 1.4 to 3.6 mm/s while in the experiment the maximum velocities ranged from 2.7 to 4.8 mm/s. The velocities calculated in the MRI are volume averages over the imaging voxel. For the axial images, the voxel dimensions were 140 x 156 μm in plane by 1 mm in depth. Given the high spatial variability in the flow velocities, the MRI velocities could be expected to be slightly lower than the simulation values. Further velocity amplitude analysis will require a highly accurate temperature measurement flow cell compatible with MRI magnets to exactly match the experiment and simulation temperatures and hence *Ra* conditions.

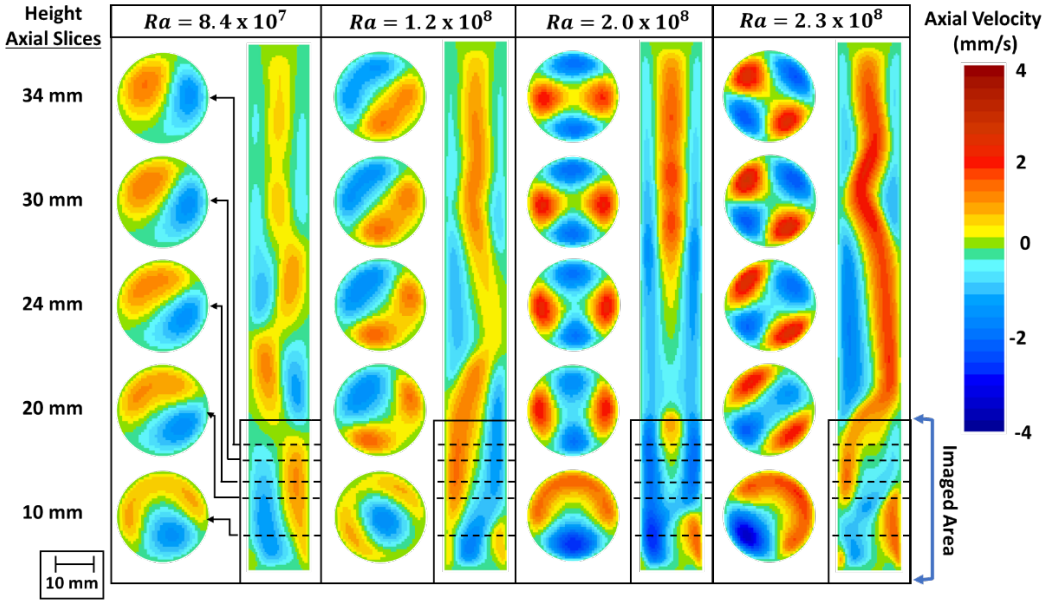


Fig. 7.4. Numerical longitudinal and transverse velocity images. Transverse images are coincident to experimental images.

A similar number of hot/cold regions, and up/down flow cells are observed at coincident axial locations. The highest velocities occur away from the walls, where local warm and cold spots occur. In Fig. 7.5, transverse velocity and temperature maps are compared at the lowest and highest investigated *Ra*. Note, the temperature scaling is different in the two image sets to provide better contrast.

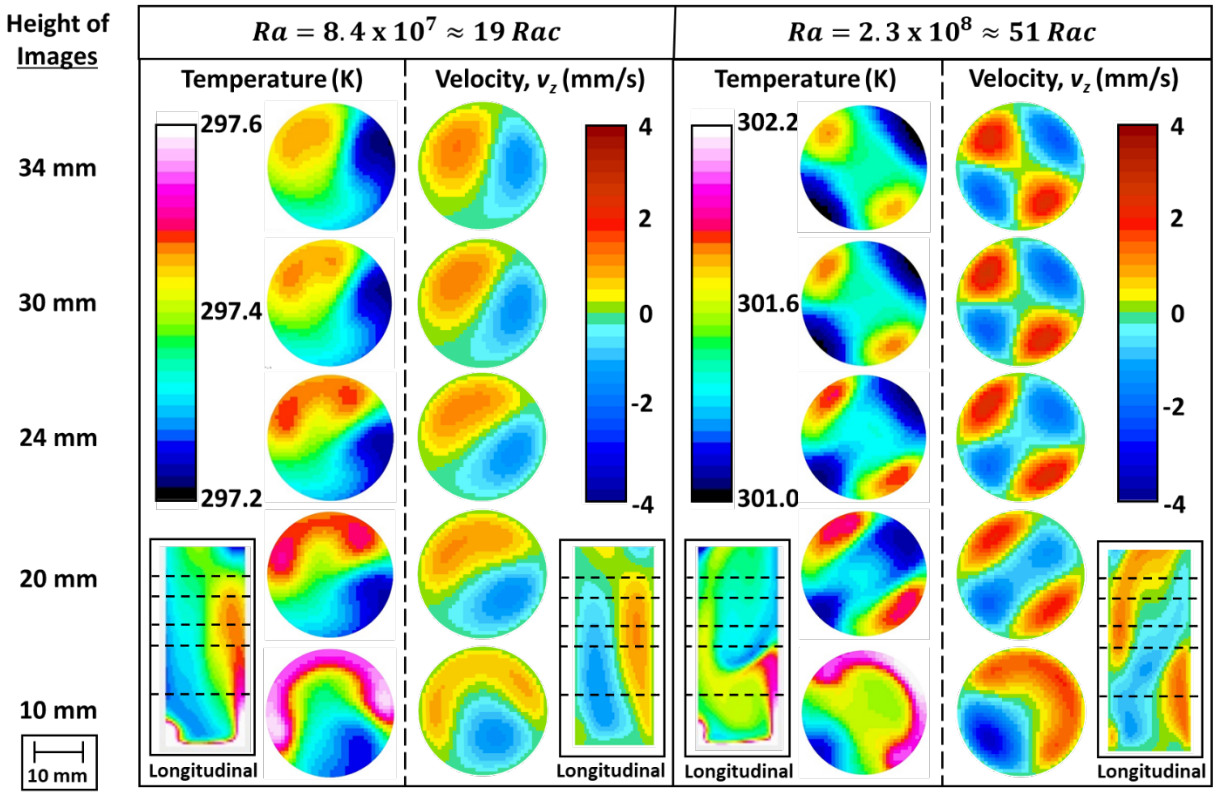


Fig. 7.5. Numerical transverse temperature and velocity images at *Ra* = 8.4 x 10^7 and 2.3 x 10^8. Position of images is coincident to experimental images.

Discussion

In this investigation of RBC in a low aspect ratio column, convection patterns were observed to change with axial location in the bottom third of its height. Numerical results suggest this dependence continues for the full column height. Two-cell flow is seen at *Ra* below 1.2 x 10^8, the flow pattern then transitioned to a four-cell pattern up the maximum *Ra* investigated. In the simulation at 8.4 x 10^7 *Ra*, the downward flow does not pass through the center as seen experimentally and the four-cell pattern developed more quickly with height than in the experiments.

The MRI velocity maps revealed a few new traits of RBC in low aspect ratio cylinders and a discrepancy with theory. The rapid 180^{o} reorientation of two cell flow where one cell bisects the other has not, to the best of our knowledge, been previously discussed in literature. Practitioners of the multi-thermal-probe method [50] should be aware of this mechanism when investigating low aspect ratio cylinders as it could be interpreted as the presence of convection rolls stacked in the vertical direction.

The simulation results at 19 Ra_c in Fig. 7.4 display an instance where imaging in a single plane can be misleading. With only the longitudinal slice for reference the flow could be interpreted as three counter rotating flow cells stacked vertically. The transverse slices at the same location reveals a slight rotation in the up and down flow cells has occurred. This reinforces the importance of imaging in multiple planes when investigating convection in low aspect ratio cylinders.

The flow patterns formed in the studied cylinder and their axial pattern transition behavior are not directly predicted by analytical theory such as that of Charlson and Sani [58], nor discussed in recent experimental works of similar *Ra* [49, 50]. For instance in Fig. 7.3a with $Ra = 8.4 \times 10^7$, theory in [58] predicts a symmetric four-cell flow ($n = 2$), while experimental results show asymmetric two-cell flow with $n = 1$. Even assuming a 40% temperature related error in *Ra* theory predicts either $n = 2$ or 3 pattern which are not observed at this *Ra*. In Fig. 7.3d for $Ra = 2.3 \times 10^8$, theory [58] predicts an eight-cell flow with ($n = 4$). However, multiple patterns are noted experimentally including an $n = 0$ two-cell flow pattern at low heights and an $n = 2$ four-cell pattern as the cylinder height increases. More direct comparison to theory [58, 176] and simulation [11, 196, 197] is restricted by the lack of details in the literature on the

height, or fluid depth, dependence of the flow patterns, analytical theory or simulations. The experimental data presented here and supported by numerical results, clearly indicate an interesting onset and transition behavior of the spatial flow pattern as a function of height in the fluid column. This indicates a significant transition zone in which the impact of the bottom heated boundary impacts the fluid motion and an initiation height which is required for a flow pattern to form. The simulations indicate a significant radial gradient in temperature at the top and bottom solid boundary due to the inflow and outflow of the fluid at the solid-liquid interface. The presence of such a distribution will also impact the flow pattern initiation height. In terms of modeling energy transport in systems of technological interest, where finite heights or controlled design of system height are pertinent, this flow pattern development is significant.

Conclusions

MR velocimetry has been applied to characterize flow patterns in RBC in a low aspect ratio column ($\Gamma = 0.12$) for *Ra* numbers ranging from 0.84-2.3 x 10^8. Experimental MRI velocimetry and numerical simulation results were combined in a complementary manner to highlight the complexity of RBC in long narrow cylinders. The MRI provide a 3D understanding of the complex fluid interactions occurring in the bottom 40 mm of the column via velocity maps at five axial locations in the cylindrical flow cell and two orientations around the major axis. Numerical results supplied information on the behavior for the full column height and demonstrate similar height dependent flow pattern transitions. Observed flow pattern behavior does not align directly with analytical solutions [58] as a function of *Ra,* although flow patterns indicated by the theory were observed including flow patterns with $n = 0, 1$. Variation in flow pattern and velocity with height in the flow cell not predicted by analytical theory were clearly

demonstrated. For instance, at $Ra = 51\ Ra_c$, flow patterns with $n = 0$, 1, and 2 were measured with increasing height over 34 mm. This is evidence of an interesting mode of azimuthal flow cell reorientation in a small axial distance. Numerical results indicate flow development similar to experimental results with small differences in onset of flow transitions. The results of this ongoing investigation indicate the necessity of imaging in more than one plane when studying low aspect ratio systems. Current theory and numerical simulations do not address the axial dependence in these low aspect ratio systems and the data presented indicate the importance of doing so.

Acknowledgments: The authors would like to thank Dr. Erick Johnson, Department of Mechanical and Industrial Engineering at Montana State University, for his help and expertise in developing the STAR CCM+ model. Simulations were solved using the Hyalite cluster, Montana State University's research computing cluster.

Funding: This research is supported by the National Science Foundation under Grant Number 1511045 to RA and JDS. Any opinions, findings, and conclusions or recommendations expressed in this material are those of the authors and do not necessarily reflect the views of the National Science Foundation. JDS and SLC thank the M.J. Murdoch Charitable Trust and NSF MRI program for equipment funding.

CHAPTER EIGHT

OBSERVATION OF HEAT TRANSFER DUE TO VARIABLE THERMOPHYSICAL PROPERTIES OF SUB-, NEAR- AND SUPER- CRITICAL FLUIDS IN POROUS MEDIA BY MAGNETIC RESONANCE IMAGING

Contribution of Authors and Co-Authors

Manuscript in Chapter 8

Author: Matthew E. Skuntz

Contributions: Wrote manuscript. Collected and analyzed data. Conceived and implemented experimental setup. Incorporated revisions and provided feedback on reviewer comments.

Co-Author: Joseph D. Seymour

Contributions: Wrote and edited manuscript. Provided training on experimental methodology. Secured funding.

Co-Author: Ryan Anderson

Contributions: Wrote and edited manuscript. Secured funding.

Manuscript Information Page

Matthew E. Skuntz, Joseph D. Seymour, and Ryan Anderson

International Communication in Heat and Mass Transfer

Status of Manuscript: (Put an x in one of the options below)
___ Prepared for submission to a peer-reviewed journal
_X_ Officially submitted to a peer-reviewed journal
___ Accepted by a peer-reviewed journal
___ Published in a peer-reviewed journal

OBSERVATION OF HEAT TRANSFER DUE TO VARIABLE THERMOPHYSICAL PROPERTIES OF SUB-, NEAR- AND SUPER- CRITICAL FLUIDS IN POROUS MEDIA BY MAGNETIC RESONANCE IMAGING

Abstract

Local velocity and temperature profiles are measured non-invasively using nuclear magnetic resonance (NMR) imaging (MRI) in porous media with a sub-, near-, and supercritical fluid. Heat transfer is driven by natural convection via heating from below. The C_2F_6 fluid fills the pore spaces in a packed bed of encapsulated phase change material (PCM). As the PCMs melt, ^1H signal intensity increases with temperature. Physical properties of C_2F_6, *e.g.* thermal diffusivity, vary substantially at the critical point, affecting the rate and magnitude of heat transfer. The changes in bead signal, *e.g.* temperature, are imaged and measured over time at 27 bar (sub-critical), 32, 34 and 36 bar (near-critical), and 66 bar (supercritical). Despite velocity profile similarities, the temperature in the packed bed varies significantly with thermal diffusivity, the magnitude of which decreases and increases with temperature around the critical point. NMR spatially and temporally captures the resulting dynamic heat transfer processes.

Introduction

Fluids near and above the thermodynamic critical point exhibit transport phenomena behaviors due to physical property variations that are of technological and scientific interest. Supercritical fluids have unique properties, particularly high liquid-like density, with gas-like viscosity. Near-critical fluids are highly compressible due to large fluctuations in density [208, 209]. Systems that use near- and supercritical fluids include extraction [210], nuclear reactors

[211], and refrigeration and power cycles [212-216]. However, many processes that use supercritical fluids are relatively new and designs were formed without considering the unique heat transfer behavior that occurs in supercritical fluids [217]. The thermal diffusivity ($\alpha = k/\rho c_p$) of a near-critical fluid varies strongly as a function of temperature and pressure, approaching zero at the critical point due to divergence of the heat capacity c_p [209]. At the critical point, the heat capacity scales as $c_p \propto \tau^{-1.24}$ with the reduced temperature $\tau = (T - T_c)/T_c$ [217, 218]. The critical scaling of the thermal diffusivity with reduced temperature is $\alpha \propto \tau^{0.67}$.Thus, the heat transfer should slow down according to the timescale for thermal diffusion $t_T \sim L^2/\alpha$, this being the well-known critical slowing down due to long correlation times in near critical systems [219].

Far from phase transition, energy transport is described by the hydrodynamic mode [218, 219] convection-diffusion energy conservation equation.

$$\frac{\partial T}{\partial t} + \bar{u} \cdot \boldsymbol{\nabla} T = \boldsymbol{\nabla} \cdot \alpha \boldsymbol{\nabla} T \qquad \text{Eq. 150}$$

The strong variation of α with temperature in near- and supercritical fluids coupled to the variation in compressibility means the rate of heat transfer in non-isothermal systems will change with changes in local temperature. As this work shows, this effect can both slow down and speed up heat transfer in a packed bed under natural convection heat transfer conditions.

Strong natural convection occurs in near-critical fluids under gravity due to the large density fluctuations which generate high compressibility of the fluid and heterogeneity of density [208]. Natural convection stability in a free fluid, not porous media system, is determined by a modified Rayleigh number

$$Ra = \frac{\rho \boldsymbol{g} C_v L^4}{\lambda \mu} \left(\frac{\partial \rho}{\partial T}\right)_P \left[\frac{\partial T}{\partial z} + \rho \boldsymbol{g} \left(1 - \frac{C_v}{C_P}\right) \left(\frac{\partial T}{\partial P}\right)_\rho\right] \qquad \textit{Eq. 151}$$

where the first term is the standard Rayleigh number for incompressible fluids and the second term comes from the Schwarzschild criteria, which indicates the adiabatic lifting of a fluid particle against the hydrostatic pressure gradient by expansion [208, 218]. The Schwarzschild criteria only applies for the presented data near the critical point. The length scale L^4 in the Rayleigh number may be modified to account for permeability of the porous media [39]. In the literature, most studies of natural convection focus on high aspect ratio systems ($d >> L$) with viscous liquids for Rayleigh-Bénard convection (RBC) research in part due to the mathematical simplifications [52, 53, 59]. Studies in super- and near-critical fluids are extremely limited, but are differentiated by small deviations in temperature leading to large differences in density [217], and commensurate large convection currents. Few studies exist with near-critical fluids of RBC in free fluids, and we are not aware of near-critical fluid natural convection studies in porous media [220]. MRI techniques can non-invasively image inside opaque porous systems, an advantage applied here to address this knowledge gap.

MRI is able to measure velocity distributions with protonated [221] and fluorinated [222] fluids. A novel technique to couple the velocity measurements to heat transfer is described in [16] by exploiting the phase change of a wax. In the packed bed arrangement, the bead is a core-shell particle encapsulated-wax phase change material. Near the melt point of the wax, there is a significant increase in generated ^{1}H signal, providing a narrow temperature range where signal magnitude increases sharply with temperature due to increasing molecular mobility. In the current study with octadecane as the encapsulated wax, this range is between 23.3-27.3ºC. To develop robust thermometry techniques that leverage the non-invasive nature of MRI in medical and biological systems, magnetic relaxation temperature contrast has been developed [93, 115,

140, 223]. Temperature measurements by MRI rely on changes in NMR parameters with respect to temperature, including the magnitude of the signal (changes in the material magnetic susceptibility) [224], the phase of the NMR signal (chemical shift) [225], the NMR relaxation times (spin-lattice, T_1, and spin-spin, T_2 dependent on molecular mobility) [226], and apparent diffusion coefficient (translational molecular mobility) [116, 227]. Spin-spin (T_2) relaxation methods can be made fast in both bulk and imaging modalities. MRI mapping of temperature has recently been demonstrated for T_2 maps of the fluid in gas phase reactions [136]. In images of spin-spin T_2 magnetic relaxation $T_2 = T_2(T)$ for a fluid, so T_2 images can be converted to temperature images [134, 228]. The dependence of T_2 on temperature is small, restricting temperature resolution to ~1°C [36, 113]. The large increase in signal intensity associated with the solid-liquid phase change provides a window where thermal transport can be determined at a finer resolution and without the need for a temperature correlation. Methods for converting wax T_2 relaxation time to temperature $T = T(T_2)$ are under investigation in the NMR field. Current measurements exploiting wax-phase change are limited to a qualitative nature.

Encapsulated core shell particle PCMs provide a template packed bed particle for MRI, where the solid polymer shell remains a solid particle and the interior PCM melting process provides a temperature dependent T_2 measurement. This work uses C_2F_6 as the heat transfer fluid in a packed bed of encapsulated phase change octadecane particles (T_{melt} = 23.3-27.3°C). C_2F_6 allows for the velocity to be spatially resolved in the pore-space without interference from the particle's ^1H signal. It has an accessible critical point (P_{crit} = 30.5 bar and T_{crit} = 19.9°C), and the thermophysical properties vary strongly with temperature and pressure in the near- and supercritical regions. The thermophysical properties at five pressures as a function of

temperature are shown in Fig. 8.1 [229]. Fig. 8.1a-b show the density and specific heat, respectively. In both cases, the gas phase (27 bar) and supercritical phase (66 bar) show less variation than the near-critical phase (32-36 bar) where larger fluctuations occur as a function of temperature. Based on the thermal diffusivity in Fig. 8.1c, non-isothermal systems will experience variations in the heat transfer rate as a function of temperature and differences in steady state temperature values. The melt range of the octadecane wax aligns with the fluids critical properties, which shift to higher temperatures with increasing pressure.

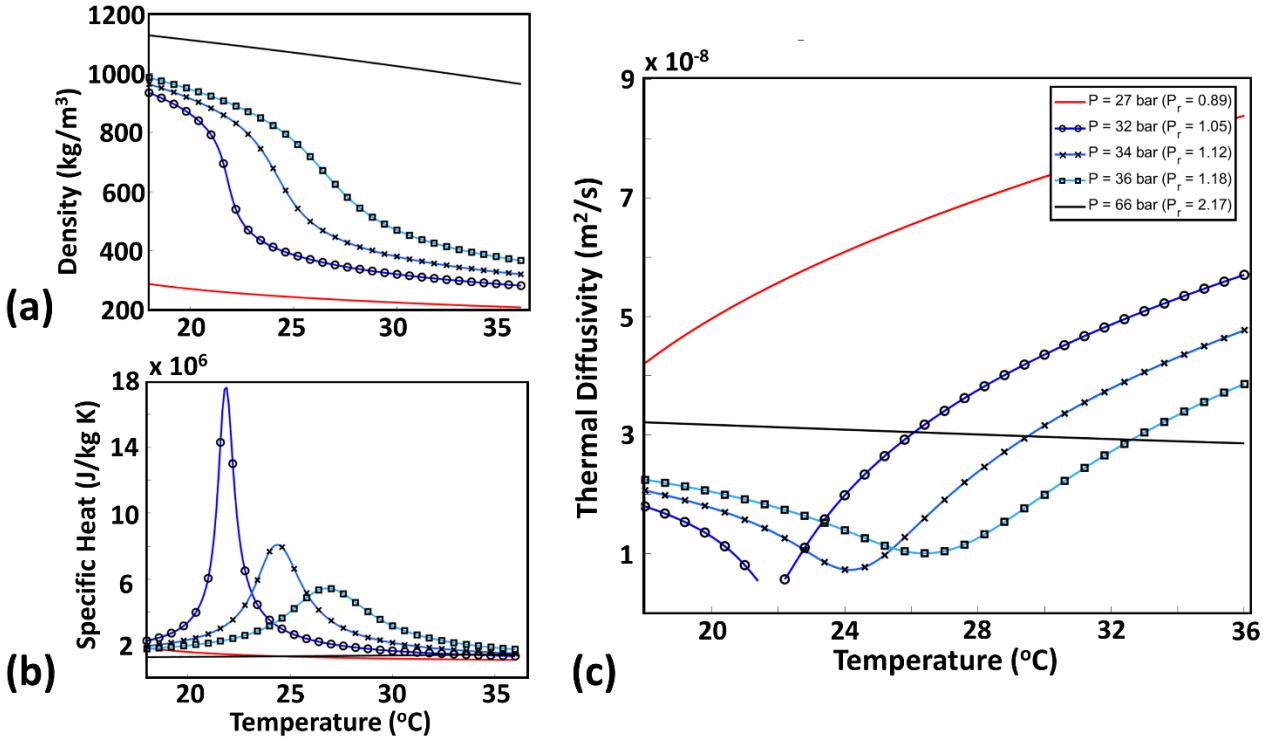


Fig. 8.1. Variation of a) density and b) specific heat for C_2F_6 as a function of temperature and pressure. The resulting c) thermal diffusivity diverges at the critical point and is a strong function of temperature at near-critical pressures, $P_r = P/P_{critical}$.

The effect of the fluids temperature/pressure dependent thermal diffusivity is studied experimentally in this work with MRI in a packed bed under natural convection conditions. MRI provides the means to spatially resolve conditions interior to the packed bed at pore-scale

resolution. Longitudinal images of melt in the bed are generated at each pressure, where an increase in signal is directly correlated with an increase in temperature. The velocity profile is imaged in multiple transverse planes along the axial height of the bed. Bulk NMR signal data from the entire bed provides high temporal resolution of heat transfer behavior.

Experimental Methods

A fixed bed was created by filling a PEEK cylinder (d = 18 mm, L = 140 mm) with encapsulated phase change materials (Mictotek, macroPCM28C). Its placement in the magnet bore is shown in Fig. 8.2a. The average particle diameter was approximately 3.5 mm and the particle shape was approximately spherical. Heated gas flow from below maintained the bottom boundary at 65^{o}C at all pressures, with the top exterior temperature a constant 19.5^{o}C. An O-ring at the bottom of the cylinder ensured the heated gas did not reached the lateral container wall. Only the bottom 40 mm of the 140 mm could be imaged due to heater probe configuration. As shown in Fig. 8.2b, a longitudinal slice and three transverse slices at 10, 20, and 30 mm from the bottom were collected at each pressure.

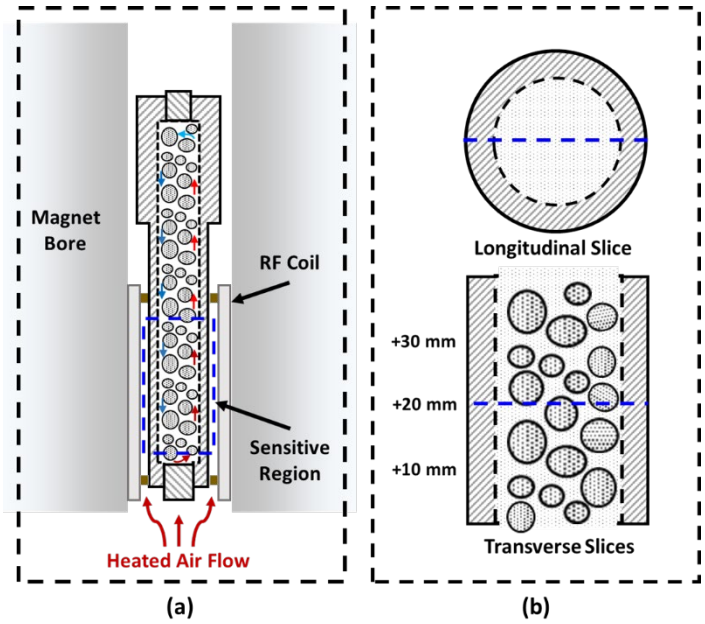


Fig. 8.2. a) Schematic of the packed bed system in the magnet bore, where air flow at 65ºC heated the container bottom at all pressures. The upper boundary is fixed at 19.5ºC. b) Wax signal intensity and velocity are measured in one longitudinal slice and three transverse slices.

Magnetic resonance imaging provides non-invasive measurements without the need for tracer-particles or optical clarity. Experiments were performed in a 7 Tesla, vertical super-wide-bore superconducting magnet interfaced with a Bruker Avance III 300 Spectrometer equipped with micro2.5 shielded gradient coils of maximum gradient strength 1.5 T/m at 60 A in all three coordinate directions. A dual tune $^{19}F/^{1}H$ birdcage radiofrequency (RF) coil of 25 mm internal diameter and 40 mm active imaging length was used in all experiments. Proton nuclei (^{1}H) of the octadecane wax and the fluorine nuclei (^{19}F) of the pore-fluid had resonant frequencies of 300.1936 and 282.4382 MHz, respectively. At the proton frequency, signal intensity images were captured in the above mentioned two-dimensional (2D) planes along with a one-dimensional (1D) longitudinally oriented intensity profile. All scans had an echo time of 7.6 ms, slice thickness of 1.0 mm (18 mm slice thickness for 1D profile) and a repetition time of 1000 ms. Transverse and longitudinal images had nominal in-plane resolutions of 313 x 313 μm/pixel

and took 64 seconds to acquire (four seconds for 1D profile). At the fluorine frequency, two-step velocity images using the pulsed-gradient spin-echo pulse sequence were acquired in the same transverse and longitudinal planes. Velocity scans had an echo time of 6.355 ms (7.416 ms for longitudinal), repetition time of 700 ms, slice thickness of 1.0 mm and took 6 min to acquire with the same spatial resolution as the proton images. For velocity encoding, gradient strength was 0.29 T/m with a duration of 0.4 ms and a separation of 4 ms. Typical experiments switched between the ^{19}F and ^{1}H frequencies multiple times, collecting pore-fluid velocity maps at each plane separately, then ten repeats of the particle-wax intensity in 1D and 2D before switching back to velocity imaging. This cycle took approximately one hour to complete.

Results and Discussion

The bed's axial melt behavior along with the natural convection velocity profiles of the pore fluid are shown in Fig. 8.3 at the multiple axial cross-section locations. These images demonstrate the transient heat transfer behavior with fluid at gas, supercritical, and near-critical conditions in the bed. In all cases, the transverse velocity profile in the pores is shown at three packed bed heights. The flow patterns show similarity between fluid phases, but all exhibit flow patterns that vary with axial height. Analogous variation in the flow pattern with axial height has been measured in the flow cell without packing material [230]. Main flow patterns observed are: a) bullseye with upward, hot flow along the walls and cooler fluid falling in the center; b) symmetric two-cell pattern where the upward warm fluid occurs in one half of the cell with the downward flow on the other plane; and c) a 'C-shape' similar to the two-cell pattern but without a symmetry plane. The flow pattern changes from the bottom bullseye, through a 'C-shape' transition to two-cell. The transition from bullseye to two-cell is further developed in the central

velocity imaged plane for the near critical fluids than the gas or supercritical fluids. Interestingly, for all fluid phases the temporal variability of the pattern indicates the flow pattern is established rapidly relative to the thermal timescale and remains temporally stationary. Analysis of the pore-velocities exhibit the expected dependence on pressure with the fastest mean pore velocities occurring at 32 bar (closest to the critical point) and the slowest occurring in the supercritical fluid.

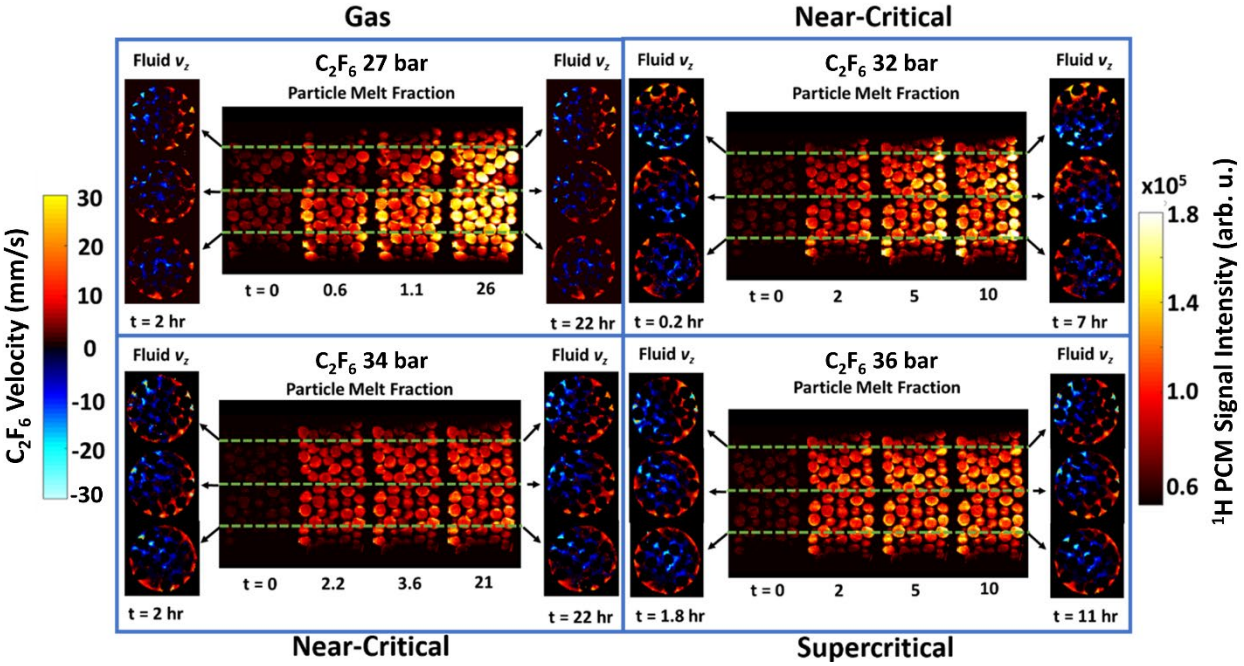


Fig. 8.3. Coupled velocity and heat transfer images at sub-, near-, and supercritical conditions. At each pressure, axial variation in the flow pattern is noted. The bead signal increases with temperature over time, shown in hrs. The image time for the bead signal and velocity varies at each pressure as the rate of heat transfer is a function of the fluid conditions. The velocity images are taken at 10, 20 and 30 mm from the bottom of the heated column.

The bead pack signal intensity rises with temperature as the molecular mobility of the encapsulated octadecane wax increases. The signal intensity increase is driven by a decrease in dipolar coupling of alkane protons [16]. In the images, a greater signal intensity value correlates to a higher temperature. Each case in Fig. 8.3 is shown with the same signal intensity scaling. In

the near-critical region, the thermal diffusivity of the fluid is low in these cases relative to the gas, and the steady state signal intensity is less due to less heat transfer. In all cases, spatial heterogeneity of signal exists *i.e.* a temperature distribution is imaged. This is clearly seen in the gas phase where more melting first occurs along the wall. More uniform signal increase is noted at 32, 34 and 36 bar, despite similar velocity profiles compared to the gas phase. This may evidence thermomechanical effects, though additional experimentation in a precisely controllable system is needed. As $\alpha \rightarrow 0$ near the critical point [217], the heat transfer should slow down; however the opposite effect has been measured due to the coupling of thermal and mechanical effects [217, 218]. Via the piston effect, heat can be transmitted through mechanical (compression and expansion) thermoacoustic waves, which are caused by the sudden expansion of the thin thermal boundary layer into which heat has diffused [217]. This causes thermal behavior not described by the standard convection-diffusion equations. MRI thermometry can measure the response of the thermal resonance in the system, which can help detect anomalous heat transfer behavior. The piston effect has been isolated in micro gravity [208], and the interaction of buoyancy driven convection due to fluid compressibility and the piston effect has not been extensively experimentally studied [218].

Complementing these 2D MRI data, bulk NMR data measures the total signal magnitude averaged over the RF coil active region (the entire volume vs. the planar slices), and can be sampled at higher temporal frequency, providing a more exact measure of total heat transfer in the systems at a specific time. As shown in Fig. 8.4, the bulk NMR signal intensity was measured to near the thermal equilibrium time, ~10^3 min. The data clearly quantifies the total

energy transport in the system, which is correlated to the thermal diffusivity of the fluid with pressure and phase (at steady state $\alpha_{27} > \alpha_{32} > \alpha_{34} > \alpha_{36} > \alpha_{66}$).

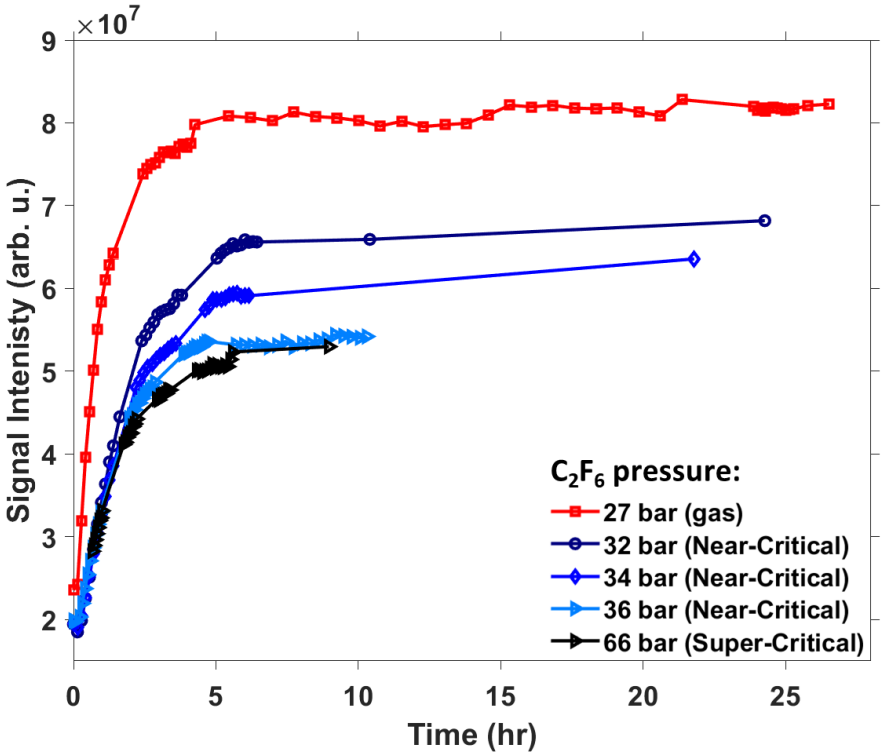


Fig. 8.4. Bulk NMR signal at sub-, near-, and supercritical fluid phases over time. Increased signal is indicative of enhanced thermal transport. At long times, these are consistent with trends in the fluid's thermal diffusivity.

Of significance, the 32, 34 and 36 bar signal intensity data intersect over the transient energy transport time due to the temperature dependent thermophysical properties. This is shown in Fig. 8.5. At early times, the bed is cool (~20ºC), and $\alpha_{36} > \alpha_{34} > \alpha_{32}$. This occurs for $t < 1$ hr. As the system heats up, the thermal diffusivity changes with $\alpha_{32} > \alpha_{34} > \alpha_{36}$ at temperatures greater than ~27ºC. The NMR signal data directly show this transition, where the final signal intensity of the pressures greater than p_c is highest for 32 bar, followed by 34 bar and then 36

bar. Thus, both a slowing down and speeding up of heat transfer is observed at these temperatures and pressures.

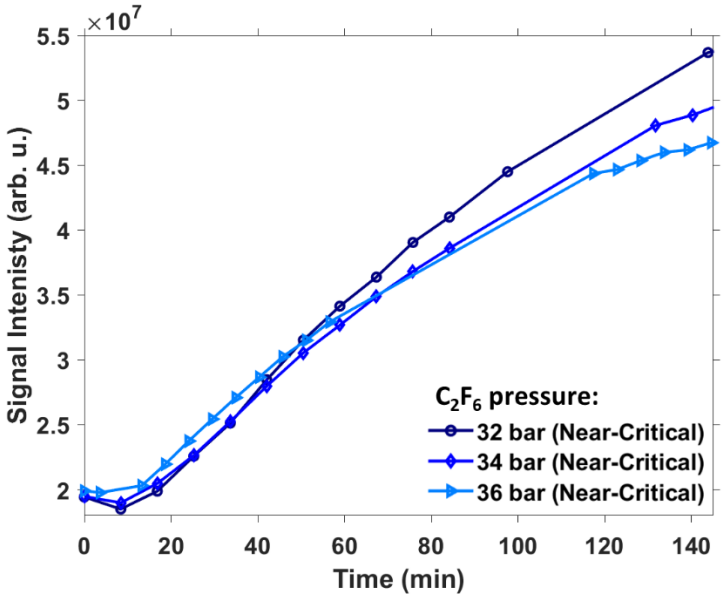


Fig. 8.5. Heat transfer behavior in near- and supercritical conditions at early times. The intersection and magnitude of the signal intensities is consistent with the thermal diffusivity as a function of temperature.

Conclusions

Natural convection heat transfer in porous media was studied at sub-, near-, and supercritical fluid conditions by varying the pressure of the C_2F_6 in the pore space. The effect of the strongly temperature and pressure dependent thermophysical properties on heat transfer was studied non-invasively with NMR. A packed bed of encapsulated phase change materials was the template porous media, and it exhibited increased signal with increased temperature, providing insights into the thermal transport processes. The velocity profile of the fluid, regardless of phase, showed variation in the bed with axial height. Noted flow patterns included bullseye, symmetric two-cell, and asymmetric two-cell. The velocity images were complemented by

intensity images showing the spatial heterogeneity of heating. Less heterogeneity in heat transfer was seen in the near-critical fluids. The heat transfer behavior correlated directly to the thermal diffusivity α of the fluid. At sub-critical conditions, α is high, leading to faster thermal transport and a higher temperature at long times. The total heat transferred to the packed bed at each pressure matched the thermal diffusivity of the fluid at steady state. In near-critical phases, the thermal diffusivity decreases and then increases as a function of temperature. For the three near-critical pressures studied here (32, 34, and 36 bar), the thermal diffusivity values intersect as a function of temperature. This behavior is captured temporally in the NMR signal as the bed is heated. At early times, when the bed temperature is lowest, $\alpha_{36} > \alpha_{34} > \alpha_{32}$, and the signal magnitudes for each pressure increase in this order. However, as the bed heats up, this trend in thermal diffusivity is reversed. This effect leads to an increase of heat transfer at 32 bar and less heat transfer at 36 bar. This dynamic heat transfer response is captured non-invasively by NMR for the first time.

Funding: This research was supported by the National Science Foundation under Grant Number 1511045 to RA and JDS. Any opinions, findings, and conclusions or recommendations expressed in this material are those of the authors and do not necessarily reflect the views of the National Science Foundation. Additional funding was provided by a grant though Montana State University via Montana NASA EPSCoR. JDS thanks the M.J. Murdoch Charitable Trust and NSF MRI program for equipment funding.

CHAPTER 9

QUANTITIATIVE T_2 MRI: MULTI-ECHO T_2 THERMOMETRY OF MICRO-ENCAPSULATED CORE-SHELL WAX PARTICLES

Contribution of Authors and Co-Authors

Manuscript in Chapter 9

Author: Matthew E. Skuntz

Contributions: Wrote manuscript. Collected and analyzed data. Implemented experimental system. Incorporated revisions and provided feedback on reviewer comments.

Co-Author: Ryan Anderson

Contributions: Edited Manuscript. Provided technical support in analysis. Secured funding.

Co-Author: Sarah L. Codd

Contributions: Edited manuscript. Provided technical support in data collection and analysis.

Co-Author: Joseph D. Seymour

Contributions: Edited manuscript. Provided training on experimental methodology. Secured funding.

Manuscript Information Page

Matthew E. Skuntz, Ryan Anderson, Sarah L. Codd, and Joseph D. Seymour

Journal of Applied Magnetic Resonance

Status of Manuscript: (Put an x in one of the options below)
_X_ Prepared for submission to a peer-reviewed journal
___ Officially submitted to a peer-reviewed journal
___ Accepted by a peer-reviewed journal
___ Published in a peer-reviewed journal

QUANTITIATIVE T_2 MRI: MULTI-ECHO T_2 THERMOMETRY OF MICRO-ENCAPSULATED CORE-SHELL WAX PARTICLES

Introduction

NMR relaxometry is widely applied in porous media [22, 94], food science [231, 232], plant studies [233], and human soft tissue [234], to non-destructively characterize internal structure. NMR relaxometry allows monitoring of system changes, such as biofilm growth [30], hydrate formation [23] and reaction [24]. It has the ability to characterize molecular dynamics, from random Brownian motion [235], hydrodynamic dispersion [131] and turbulence [28] to coherent velocities to provide direct measurement of transport phenomena. Determination of temperature using NMR is accomplished by measurement of chemical shift, relaxation and diffusion, among other parameters [36, 107, 134].

Spin-spin or T_2 relaxation measures molecular mobility, chemical environment, restrictions to motion, and molecular exchange [92]. Quantitative T_2 MRI combines the benefits of imaging and relaxometry, allowing detailed spatial heterogeneity information on the image scale to be determined in terms of the microscale rotational diffusion mediated dipolar coupling. The T_2 decay rate determined from imaging is dependent on the imaging gradients and pulse sequence parameters which introduce additional attenuation mechanisms that must be accounted for in order for T_2 decay rates to be quantitatively determined [236]. Repetition time must be long enough (~5*T_1) to prevent T_1-weighting effects, echo time must be fast enough to capture initial decay, and signal should be sampled into the noise for good relaxation fits. In particular, additional attenuation from molecular diffusion during imaging gradient application must be accounted for. The focus of this paper will be on the effects of the imaging gradient attenuation

on the observed spin-spin relaxation $T_{2,obs}$ in terms of spatial resolution based optimization of gradient amplitudes and timings *e.g.* acquisition sweep width and read gradient amplitude, and how this attenuation is determined. Theoretical T_2 signal analysis will be compared to two experimental systems: variable $CuSO_4$ concentration phantoms and core-shell alkane-filled particles used for MRI heat transfer contrast at different temperatures [16].

Application of T_2 imaging

Edzes *et al.* [233] discussed the limitations and challenges of quantitative MRI when the T_2 relaxation rates in a single sample, plant tissue, range over three orders of magnitude. The theory developed in that paper is used to determine imaging induced signal attenuation in this work. In porous media, T_2 relaxation correlated to velocity in rock cores has been used to calculate permeability [237]. The Cambridge group has developed a 1D z-T_2-T_2 imaging sequence allowing chemical production to be spatially determined as a function of height in an active catalytic column [24]. In the medical community, this method has attracted recent attention for its ability to easily identify different microstructures from their T_2 components [32, 238], improving contrast between important soft tissues. Combination diffusion-relaxation weighted images of the brain [234, 239], and spinal column show promise as a means of identifying early signs of multiple sclerosis [240], tumor growth [31] and brain/nerve trauma from concussions [241].

One area of interest and progress has been in temperature measurement. In the medical field MR thermometry has been applied to ablation therapy [242], where proton resonance frequency shift has been the preferred method of temperature measurement. NMR thermometry has also been used for catalyst temperature monitoring of a chemical reactor correlating

temperature to signal intensity in ^{27}Al catalysts [165], phase mapping to study microwave food heating [139] and capture of fluid temperature maps during free convection by T_2 relaxation rate of silicone oil [36]. For an in-depth description of the different methods of MRI temperature measurement see [93].

In this study, T_2 relaxation is correlated for temperature measurement of micro-encapsulated alkane that has application to dynamic heat transfer monitoring experiments [16]. Thermometry based on T_2 relaxation has the advantage of being relatively fast compared to other MRI temperature sensitive methods and, near melting points, has large variation over a narrow temperature band. Temperature maps here are acquired in 68 seconds, rapid enough to capture transient energy transport behavior.

Temperature measurement during phase change

There are two imaging implementation methods for determining a materials T_2 relaxation rate from the spin echo. The Carr-Purcell-Meiboom-Gill (CPMG) multi-echo sequence using multiple 180^o radiofrequency pulses with a fixed τ time allows a T_2 map to be acquired. Simply acquiring multiple images with a different τ time for each single-echo acquisition to highlight T_2 contrast [92]. The dependence of T_2 relaxation on temperature in liquids is around 0.3%/^{o}C, which limits the uncertainty of the temperature measurement to approximately 1^{o}C [93]. During a solid to liquid phase change, there is a much stronger variation in T_2 with temperature, decreasing measurement uncertainty, albeit in a limited temperature window. This study uses micro core-shell particles containing eicosane $C_{20}H_{42}$, a straight chain alkane that have been mixed with a binder to form macro particles with an average diameter of 3.5 mm. The melt range

of particle-bound eicosane is 34-36ºC, as determined by differential scanning calorimetry (DSC) and the T_2 increases from 200 ms to 650 ms during the solid-liquid phase change.

T_2 Imaging Theory

In non-imaging T_2 measurement, the CPMG pulse sequence is applied with no magnetic field gradients and τ times short enough to prevent sampling of local susceptibility gradients in the magnetic field [92]. This results in a measurement of the intrinsic spin-spin relaxation $T_{2,i}$. During spin-warp imaging, magnetic field gradients are applied in the read, phase and slice directions. These gradients introduce additional attenuation mechanisms, resulting in a shorter, observed spin-spin relaxation, $T_{2,obs}$ [236]. In its simplest form, a T_2 image sequence resembles that used by Edzes *et al.*[236], shown in Fig. 9.1 where only the read gradient is

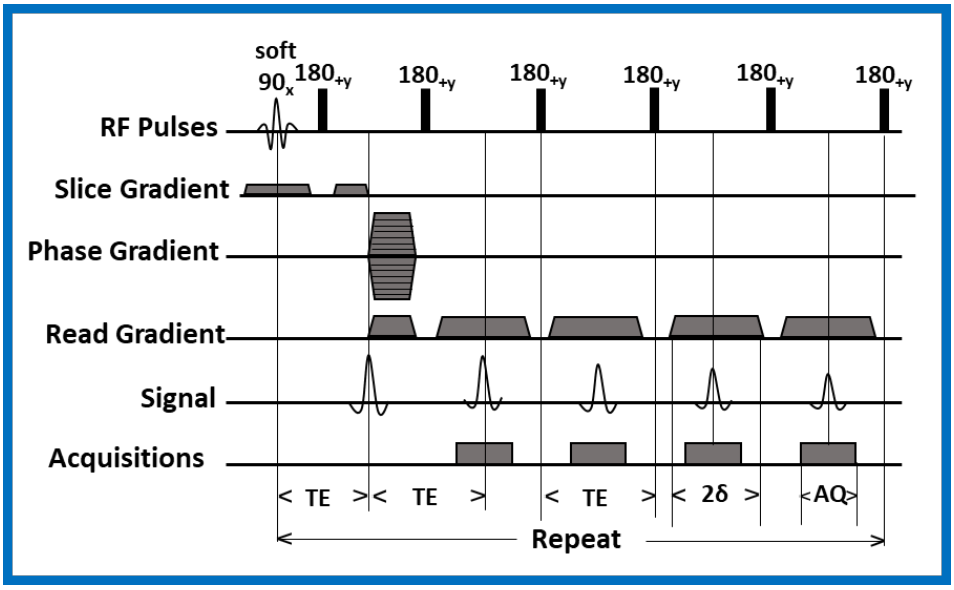


Fig. 9.1. Simple spin-warp T_2 imaging sequence used by Edzes *et al. [236]*.

applied at each echo. In standard imaging sequences, like Bruker's multi-slice-multi-echo (MSME) sequence in ParaVision 5.1, the timing diagram includes gradients in the slice, phase

and read directions at each echo as well as spoiler and crusher gradient pulses as shown in Fig. 9.2a. These additional gradients will also contribute to the signal attenuation and must be accounted for to quantify $T_{2,i}$ relaxation from the image. Expressions have been derived for the attenuation effects of the imaging gradients by Brandl and Haase [243] who started from Torrey's diffusion term [112]:

$$A(t) = exp\left[-\gamma^2 D \int_0^t \left\{\int_0^{t'} \boldsymbol{G}(t'')dt''\right\}^2 dt'\right] \qquad Eq.\ 152$$

where $\boldsymbol{G(t)}$ is the gradient pulse temporal waveform, $A(t)$ the attenuation and this equation must be formulated for each gradient applied. Edzes *et al.* [236] incorporated the read gradient impact on $T_{2,obs}$, deriving an expression composed of imaging time parameters. In the following, the theory of Edzes *et al*. [236] is summarized using the same notation, as it provides an easy connection to the effects the imaging parameters have on the observed T_2.

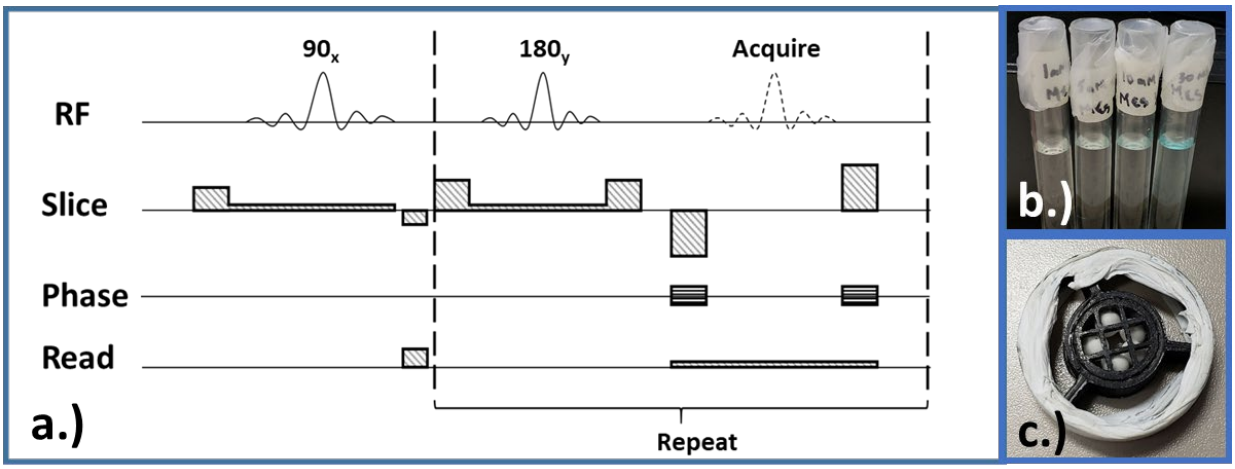


Fig. 9.2. (a) Multi-echo imaging sequence used for T_2 maps (b) Samples used in experiment 1: four vials filled with 1, 3, 6, and 30 mM concentrations of $CuSO_4$ in water. c.) Experiment 2, 3 sample: five particles secured in cage to prevent movement. Particles are ~3 mm diameter agglomerates of micro-encapsulated (~15um) Eicosane mixed with a binder and encased in a hard-plastic shell.

The transverse signal decay at time *t* after excitation can be described by the well-known equation:

$$S(t) = S_0 exp\left(^{-t}/_{T_{2,obs}}\right) \quad Eq.\ 153$$

where the observed decay rate $T_{2,obs}$ is composed of the inverse sum of the intrinsic decay, a local field gradient term, and an imaging gradient term, written as:

$$\frac{1}{T_{2,obs}} = \frac{1}{T_{2,i}} + \frac{1}{T_2{}'} + \frac{1}{T_2{}''} \quad Eq.\ 154$$

The intrinsic spin-spin relaxation time $T_{2,i}$, is due to dipolar coupling. The local field gradient term T_2' accounts for variability in the local field strength caused by magnetic susceptibilities in the sample. This variability is proportional to the gyromagnetic ratio γ, mean squared distribution of local field gradients $\langle \boldsymbol{g_z} \rangle$, echo time *TE*, and diffusion coefficient *D*:

$$\frac{1}{T_2{}'} \propto \gamma^2 \langle \boldsymbol{g_z}^2 \rangle TE^2 D \propto (B_o TE)^{-2} \quad Eq.\ 155$$

The mean squared inhomogeneous field gradient distribution can be measured [244] and is proportional to the square of the applied field strength and *TE*, which implies low magnetic fields are advantageous. In practice, the echo time must be long enough to allow $\boldsymbol{k}$-space to be traversed with the read gradient.

Molecular diffusion in the presence of the imaging gradients generates the T_2'' term. This attenuation is generally much stronger than T_2', and imposes a limit on the longest $T_{2,i}$ that can be imaged. For the imaging sequence used by Edzes *et al.* [236], this term is calculated with:

$$\frac{1}{T_2{}''} = \left(\frac{\pi}{\Delta x}\right)^2 \left(\frac{2\delta}{AQ}\right)^2 \left(1 - \frac{2}{3}\frac{2\delta}{TE}\right) D \quad Eq.\ 156$$

$$\Delta x = \frac{1}{AQ}\frac{2\pi}{\gamma \boldsymbol{G}} \quad Eq.\ 157$$

where AQ is the acquisition time, 2δ the duration of the read gradient and TE the echo time. In the above analysis, T_2'' accounts for only read gradient attenuation. The sequence used here, shown in Fig. 9.2a, has slice, spoiler, phase and read gradients applied at each echo, which all contribute to signal attenuation. T_2'' is dependent on the imaging gradients and timing sequence applied and can therefore be controlled and refocused with 180° pulses to some extent. Mindful tuning of the acquisition time, dwell time, read gradient strength and duration, and echo time can have a large effect on the observable $T_{2,obs}$ decay. Echo time should be kept short for maximum SNR and to capture the initial signal decay. Important timing parameters are the dwell time, which determines the acquisition rate or sweep width, and the gradient strength, which determines how quickly $\boldsymbol{k}$-space is traversed. At a fixed resolution, a shorter dwell time, or higher sweep width ($SW = \frac{1}{dwell\ time}$), necessitates a stronger read gradient in order for $\boldsymbol{k}$-space to be digitized at the proper resolution. The strength of the read gradient has a greater effect on T_2'' than the duration as Eq. 156 implies $1/T_2'' \propto \boldsymbol{G}^2\delta^2(1 - \delta/TE)$. In many standard method implementations such as MSME in ParaVision 5.1 used here, gradient strength is set based on the input sweep width and acquisition time is determined by the number of read points collected (digitized) *i.e.* resolution and field of view.

Methods

In this paper the attenuation effects caused by imaging gradients on $T_{2,obs}$ will be analyzed using a model phantom system consisting of four separate vials of different concentrations of $CuSO_4$ and water. For these solutions, the T_2 values are known and range from 260 – 980 ms, and the effects of imaging parameter variations will be determined. The

quantification of T_2 relaxation in 3.5 mm core-shell particles composed of micro-encapsulated (10-20 um) eicosane mixed with a binder, is studied in order to use these core-shell particles to image temperature distributions in packed bed heat transfer [16]. The intrinsic relaxation time $T_{2,i}$ of the encapsulated alkane is a function of temperature, ranging from 200 ms when the eicosane is solid at 30°C to 650 ms for liquid eicosane at 40°C. Imaging sequence timing parameters will be adjusted to maximize the difference in T_2 of the solid and liquid eicosane. The intrinsic T_2 value is determined from a CPMG sequence with τ = 1 ms. The change in $T_{2,i}$ as a function of temperature is exploited to create a $T_{2,i}$-temperature correlation for the wax particles. This correlation is then validated by monitoring the temperature of the wax particles heated by an air stream of varying temperatures.

Sequences and Hardware

Non-imaging T_2 relaxation spectra were acquired with a CPMG pulse sequence with 200-500 echoes, using hard RF pulses with 50W for 68.4 μs for a 90° pulse and 136.8 μs for a 180° pulse. The number of echoes was adjusted to sample the magnetization decay into the noise. The CPMG sequence was performed with τ = 1 and 2.8 ms controlled with TopSpin 3.5v7 software. Imaging was performed using a multi-echo read-phase spin-warp imaging sequence shown in Fig. 9.2a with 100 echoes controlled with ParaVision 5.1 software. The diffusion attenuation term T_2'' was changed by systematically adjusting the resolution and sweep width of the imaging sequence to investigate the effects on $T_{2,obs}$ and the ability to recover the intrinsic spin-spin relaxation $T_{2,i}$ value using the pulse sequence timing parameters. A TE of 5.6 ms was used in all imaging experiments. This echo time was short enough to capture the initial decay of all the

samples including the solid alkane (except at 500 kHz sweep width), and provide good SNR with the use of moderate read gradients.

All measurements were performed at high field on Bruker Avance III 300 MHz Spectrometer with a 7 Tesla superconducting magnetic equipped with micro 2.5 gradient coils. The maximum gradient strength is 1.5 T/m at 60 A in all three coordinate directions. A birdcage coil with 25 mm internal diameter and active length of 40 mm was used with soft hermite RF pulses 90º 2 ms at 1.06 W and 180º 1.267 ms at 10.6 W for imaging.

Experiment

Three experiments are discussed in the following, a $CuSO_4$ phantom experiment and two core-shell alkane particle experiments with different heating protocols. The first uses the four concentrations of $CuSO_4$ prepared in 10 mm glass NMR tubes (Fig. 9.1b). These samples are imaged four times each with different resolutions and/or bandwidth. These are two commonly adjusted MRI parameters that change either the gradient pulse duration or amplitude. Slice thickness is kept constant at 1 mm during these experiments but variation in slice thickness will have a similar effect as changing the resolution in the read and phase directions.

$CuSO_4$ at 1, 5, 10, and 30 mM concentrations were loaded separately in the RF coil and their T_2 decay rates were measured to be 0.932, 0.535, 0.395, and 0.239 seconds, respectively, by the CPMG sequence. In the encapsulated alkane experiments, five particles were held motionless in a cage of ABS plastic printed on an Ultimaker 2+ three dimensional printer (Fig. 9.1c) and heated via an airstream controlled by a Bruker BVT 3000 temperature control unit.

Based on a minimum resolution of 32 read points *i.e.* 0.625 mm/pixel, the longest T_2'' possible was 1.97 *s* for the CuSO4 and 12 *s* for the encapsulated alkane, with difference due to

their respective diffusion coefficients. The $CuSO_4$ phantoms were imaged at four T_2'' values ranging from 0.06 to 1.97 s. Two of the images had a resolution of 0.313 mm/pixel but different bandwidths (50 and 500 kHz) and two had different resolution (0.156 and 0.625 mm/pixel) but the same bandwidth (100 kHz). Field of view was 20 mm by 20 mm for all images. Fig. 9.3a shows the experiment based calculated T_2'' values used to image the $CuSO_4$ (shown in black and red) along with the intrinsic $T_{2,i}$ of each concentration from the bulk CPMG measurements in blue lines.

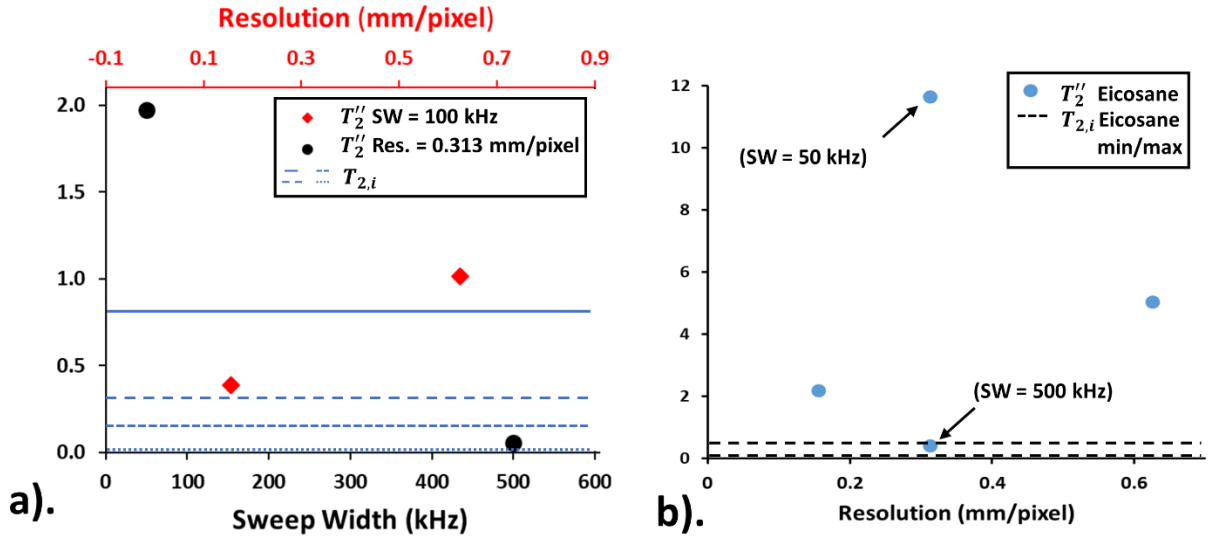


Fig. 9.3. Comparison of calculated T_2'' induced by imaging gradients and $T_{2,i}$ the sample's intrinsic T_2. In (a), the $T_{2,i}$ of the $CuSO_4$ samples are shown in blue and T_2'' theoretical estimates are plotted in red and black symbols for variable imaging sweep width and resolution, respectively. In (b), the $T_{2,i}$ of the liquid and solid wax are shown as dashed lines along with the T_2'' estimates for the four imaging parameters. Decreasing dwell time and increasing resolution both cause a shorter in T_2''. The resolution at which T_2 can be imaged without attenuation from imaging gradients *i.e.* T_2'' controlling decay is limited. The order of magnitude slower diffusion of the wax compared to the $CuSo_4$ solution water decreases the effect of T_2''.

In eicosane particle experiments, the imaging and non-imaging T_2 values are measured at isothermal conditions in a step-wise manner from 30° to 42°C at 1°C intervals, exceeding the melt range of 34° to 36°C as determined from DSC. Accurate temperatures were achieved using

a Bruker VTU system with pressurized air flow. Temperatures were verified using a system of three thermocouples attached to the particle sample cage in the RF coil and magnet bore during calibration experiments when NMR data was not collected. T_2 imaging was performed at four T_2'' values shown as blue dots in Fig. 9.3b. As with the $CuSO_4$ phantom experiments, two had the same resolution of of 0.313 mm/pixel (64x64 points collected) with sweep widths of 50 and 500 kHz, respectively, and two had resolution of 0.156 and 0.625 mm/pixel with a sweep width of 132 kHz. The minimum and maximum $T_{2,i}$ of the eicosane in the investigated temperature range are plotted as black dashed lines in Fig. 9.3b.

In a third experiment to validate a $T_{2,i}(T)$ correlation, the particles were melted via an air stream at temperatures ranging from 35° to 40°C with a 400 L/hr flow rate. Each temperature was measured three times with a different set of particles to test the consistency of the temperature correlation and any particle to particle variation.

Analysis

The non-imaging CPMG results were processed using an in-house MATLB script which applies an Inverse Laplace transform (ILT) to the NMR data. $T_{2,obs}$ from the imaging data was calculated using both Prospa (Magritek, Aachen) and an in-house MATLAB script. A magnitude mask was applied to the image data after Fourier transform, eliminating pixels less than 60% of the max intensity. A secondary mask was applied to the T_2 image, removing data outside one standard deviation of the mean T_2 value to refine the edges of the particles. In Prospa the makeRelaxMap macro was used, which fits a single exponential using the Levenberg-Marquardt method. The in-house script calculated T_2 relaxation rate on a pixel-wise basis using a nonlinear

least-squares fitting method with a trust-region algorithm to fit decays to a single exponential of the form:

$$S(t) = a \cdot e^{\left(-t/T_2\right)} + constant \qquad Eq.\ 158$$

The use of a single exponential is justified in the discussion below.

The T_2'' attenuation term was calculated using Eq. 156 and 157, for each combination of imaging parameters. The diffusion coefficient of water at 25ºC (D = 2.295 x 10^{-9} m^2 s^{-1}) was used for the $CuSO_4$ phantoms and of pure liquid eicosane at 40ºC (D = 2.8 x 10^{-10} m^2 s^{-1}), as a maximum limit for the wax particles. The $T_{2,i}$ and T_2' were determined by running the non-imaging CPMG train sequence at two τ times of 1 and 2.8 ms. The first includes less T_2' effects and the second has the same T_2' experienced in the image. The T_2' under imaging conditions could then be determined by solving Eq. 154 with $T_2'' = 0$ for the non-imaging CPMG data. The theoretically calculated T_2'' and experimentally determined T_2' terms can then be used to estimate expected $T_{2,obs}$.

Results and Discussion

Intrinsic T_2 and $CuSO_4$ Concentration

The results of the CPMG experiment at two τ times is shown in Fig. 9.4 with the dotted and solid lines representing the shorter and longer τ respectively. The relaxation $T_{2,i}$ decreases with the concentration of $CuSO_4$, as expected due to increased paramagnetic centers for relaxation. T_2'' and T_2' are identically zero in the bulk CPMG $CuSO_4$ solution data as shown by the same $T_{2,obs} = T_{2,i}$ for varying τ.

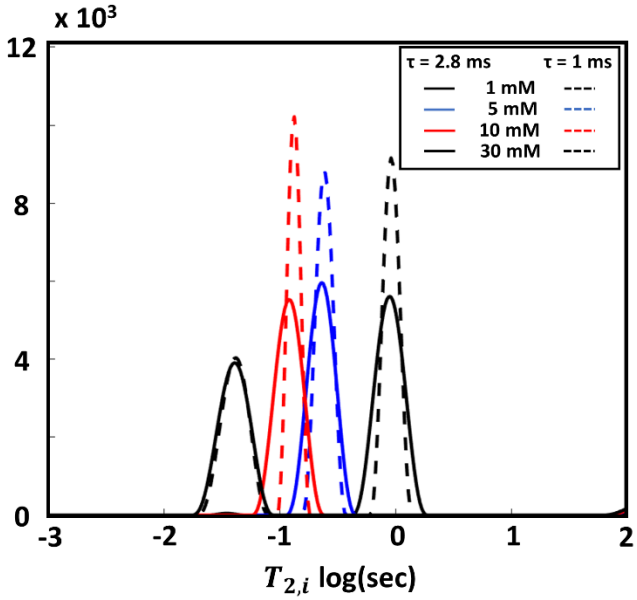


Fig. 9.4. (a) CPMG T_2 distributions of four $CuSO_4$ concentrations at τ = 1 and 2.8 *ms* times after ILT.

Imaging Timing Parameters and T_2 observed

Each of the $CuSO_4$ phantoms was imaged four times with different timing parameters so the characteristic attenuation T_2'' from the imaging gradient varied from 2 to 0.06 seconds. The expected $T_{2,obs}$ can be calculated using Eq. 154 with the $T_{2,i}$ from the CPMG data and a T_2' = 0 for homogeneous solutions. In all cases, $T_{2,obs}$ should be less than $T_{2,i}$ from CPMG due to T_2'' affects. This limit was always the case but the $T_{2,obs}$ of the samples was consistently shorter than expected based on the read gradient analysis of Edzes *et al.* [236] for T_2''. This indicates the need to incorporate the additional crusher and slice selection gradients applied in the Bruker MSME pulse sequence into the calculation of T_2''.

Fig. 9.5a shows the histograms of $T_{2,obs}$ in the $CuSO_4$ solutions at the four different T_2'' values. The color represents the different T_2'' values, caused by changing the gradient timing parameters. The four different $T_{2,obs}$ populations can be distinguished at each T_2'' value and shift

toward shorter times with the increased attenuation from the imaging gradients *i.e.* shorter T_2''. The difference in $T_{2,obs}$ between the lowest and highest $CuSO_4$ concentrations decreases from 180 ms to 25 ms. In Fig. 9.5b, $T_{2,obs}$ has been corrected to $T_{2,i}$ using the theory. The corrected $T_{2,obs}$ are clearly similar for like CuSO4 concentration, except at the shortest $T_2'' = 0.06\ s$ where the large difference between T_2'' and $T_{2,i}$ produces scattering and introduces errors. The clustering of the corrected results indicates the T_2 attenuation from the read imaging gradient was corrected. However, these corrected values are less than 27% (25.9%, 27.1%, 21.7%, 14.3% for 1, 5, 10, 30 mM) of the intrinsic values measured by CPMG, indicating additional attenuation due to the other gradients applied and the need for the correction to take them into account.

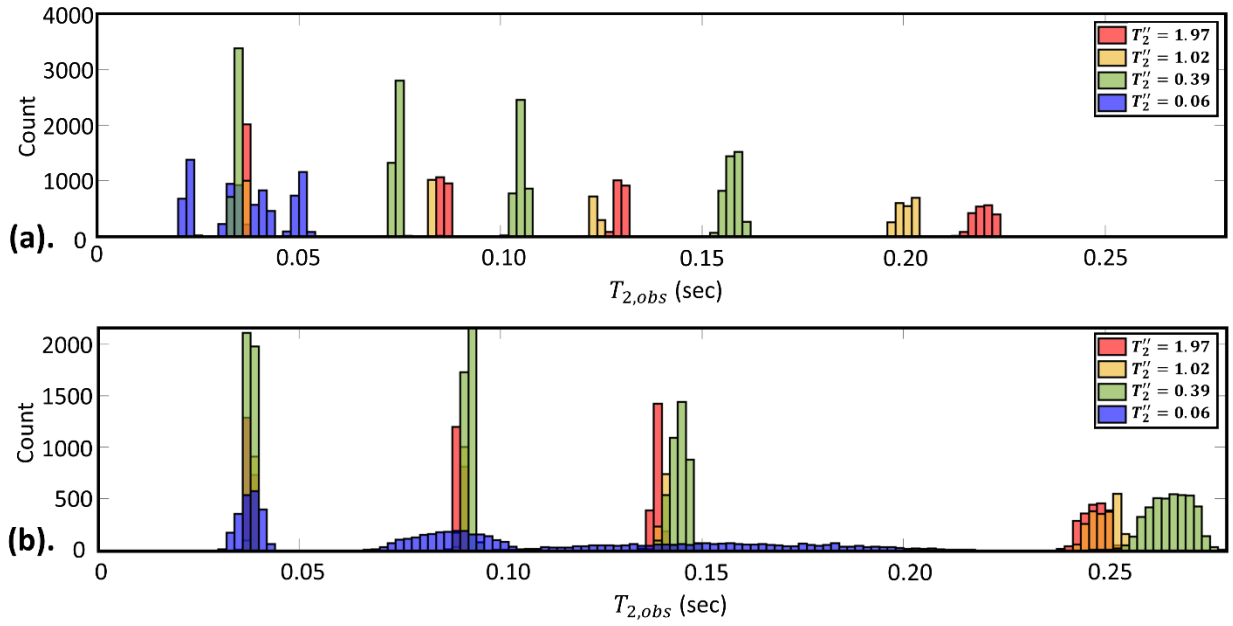


Fig. 9.5. Histograms of the measured T_2 decay rates for each pixel in the images. The color indicates the four different images taken with different timing parameters. Four T_2 populations are visible corresponding to each of the $CuSO_4$ concentrations. The $T_{2,obs}$ are plotted in an (a). In (b), $T_{2,obs}$ has been corrected by the gradient attenuation T_2''.

Eicosane Melt Process

Pure eicosane undergoes a solid to liquid phase change over the range of 36°-37°C. The melt range of these particles is 34°-36°C as measured by DSC. As the encapsulated wax is heated from 30°C, little increase in $T_{2,i}$ occurs until the mobility of the protons increases above 33°C. Upon further heating the impurities cause the liquid transition to occur below the pure-phase melting point. The $T_{2,i}$ time continues to increase as the eicosane melts and smoothly increases with the percentage of melted eicosane in the particles. $T_{2,i}$ then plateaus, as the entire domain transitions to a liquid. In the liquid state, the $T_{2,i}$ time increases slowly with temperature, proportional to the increase in the rotational diffusion coefficient $D \propto {k_B T}/{8\pi\mu a}$.

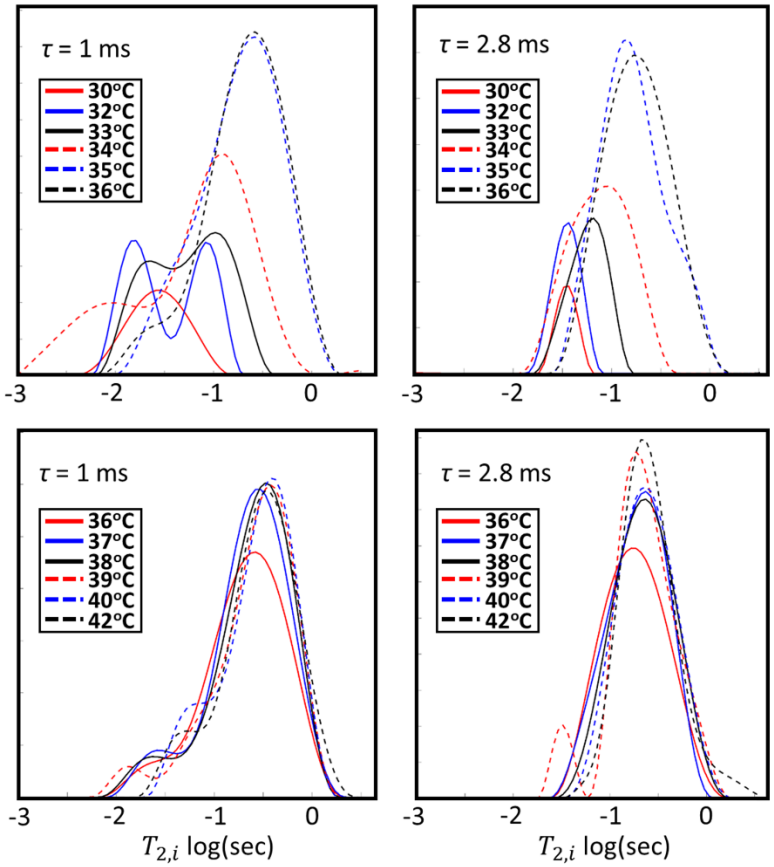


Fig. 9.6. T_2 of micro-encapsulated eicosane at temperatures from 30-42°C captured with CPMG sequence at two τ times, 1 ms in the left column and 2.8 ms in the right column. Top row

displays T_2 distributions from 30-36ºC, bottom from 36-42ºC. The x axis is log(T_2). Two peaks are resolved with τ = 1 ms and a single peak when τ =2.8 ms.

Fig. 9.6 shows the CPMG results for τ = 1, 2.8 ms at temperatures from 30-36ºC and 36-40ºC separately. At the short τ time the T_2 distributions at T<34ºC are bimodal, indicating the less mobile CH_2 protons at lower T_2 and more mobile CH_3 at higher T_2 in the solid eicosane. At longer τ, these bimodal distributions are not present due to averaging between the CH_2 and CH_3 magnetization. This averaging and resulting single peak, justify the use of a single exponential fit to the signal data. The T_2 increases with T providing the means for direct correlation.

Eicosane Phase Transition as Temperature Indicator

The simple T_2 decay provided by the longer τ time is beneficial when eicosane is used as a temperature indicator. With τ = 2.8 ms, the T_2 increases smoothly with temperature during phase transition. Plotting the primary T_2 peak against temperature in Fig. 9.7 shows that T_2 increased from ~ 200 ms to ~530 ms over temperature range from 30º to 40ºC. The results at τ = 2.8 ms indicate that, above 37ºC, there is a linear increase in T_2 at a rate of 0.3%/ºC. This value matches well with T_2-temperature dependence reported elsewhere [36, 93] which have found 0.2-0.6% increases in T_2 with temperature for various liquid phase materials. During melting from 32-37ºC, the increase in T_2 is nearly linear at a rate of 5.8%/ºC. The τ = 2.8 ms data is well fit by three linear regimes in the solid, melt and liquid regimes. The decrease in $T_{2,i}$ from τ = 1 ms to 2.8 ms in the liquid at T > 37ºC is due to the T_2' relaxation effects increasing with τ.

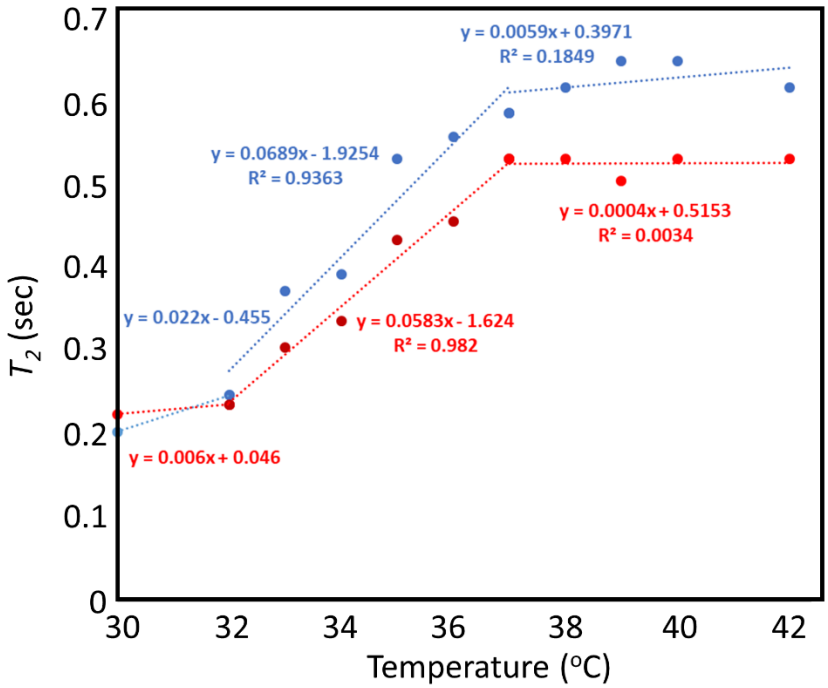


Fig. 9.7. T_2 distributions of encapsulated eicosane as it transitions from solid to liquid captured with CPMG at two τ times. Eicosane is solid below 32°C and fully liquid above 37°C. Top set of data in blue was collected with a τ = 1 ms and bottom set of data in red was collected with a τ = 2.8 ms. The dotted blue/red lines are fits for the solid, melt and liquid regions.

Micro-encapsulated Eicosane T_2 images

The $T_{2,obs}$ measured with the spatially resolved images were shorter than values expected from theory. In Fig. 9.8, T_2 images at sweep widths of 50 and 500 kHz are shown at temperatures from 32-42°C. The increase in T_2 between the solid and melted wax was greatest at the lowest bandwidth (longest T_2''), where T_2 increased from 20 to 200 ms. When T_2'' = 0.06 seconds, the range in eicosane T_2 was reduced to 20 to 120 ms over the same temperature range. In order to produce a $T_2(T)$ correlation from these images, a mask, indicated by the black outline, was applied to these images to remove influence of partial volumes, uneven heating, and any eicosane which had escaped the outer shell. Voxels inside the mask were used in calculation of T_2 at each temperature.

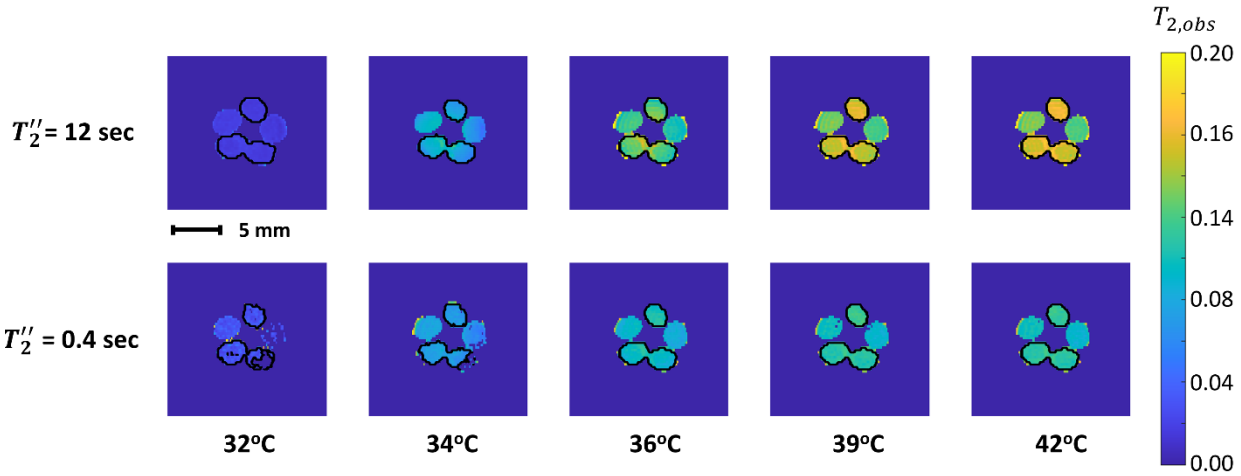


Fig. 9.8. T_2 maps of five spheres composed of micro-encapsulated eicosane captured with a multi-echo spin-warp imaging sequence. The images in each row were captured at different T_2'' decay rates sweep widths of 50 (top) and 500 kHz (bottom). Temperature increases to the right. Shown in black is the mask applied to each image for T_2-temperature correlation. The encapsulated eicosane is solid 32°C and liquid by 38°C.

It is informative to view the result of the T_2 images in a probability histogram *i.e.* data normalized to the same number of voxels. In Fig. 9.9, histograms of T_2 values in the 50 and 500 kHz sweep width images are shown at 1°C increments from 32°-42°C. Below 32°C and above 37°C the change in observed T_2 with sweep width was not significant. Results below 32°C and between 37-42°C are not shown as they change little and obscure the other T_2 distributions. Melting begins at 34°C and continues until 37°C, resulting in a smooth increase in the observed T_2 and wider distributions with increasing T. These results are consistent with those found in the non-imaging CPMG data.

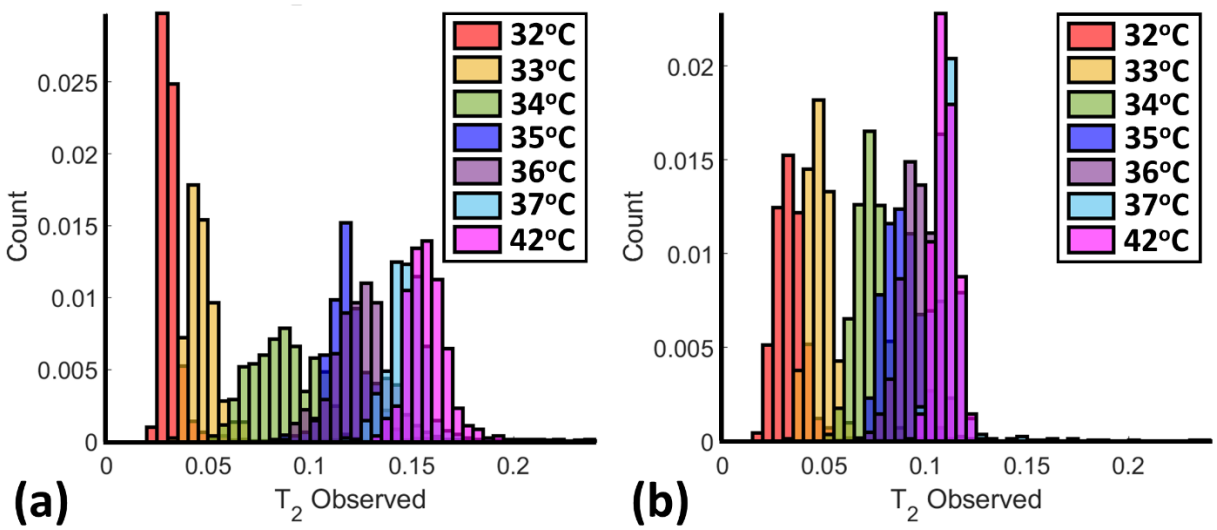


Fig. 9.9. Histograms of T_2 for pixels within mask at temperatures from 32°-42°C. Histograms (a), (b) corresponds to images at 50, and 500 kHz sweep widths (T_2'' = 11.6, 0.4 sec). Histograms at T_2'' = 2.2, 5 sec (not shown) are similar to (a). In (b) the peaks have been shifted to shorter T_2 times making it difficult to resolve the peaks.

The mean of the T_2 distributions from the histograms are plotted against temperature in Fig. 9.10a along with the results when $T_2'' = 2\ s$, sweep width of 132 kHz. In the figure, the error bars indicate the one standard deviation of the T_2 distribution. There is little differnce between the two lower sweep width results. The lower sweep width, $T_2'' = 11.6\ s$, has a slightly larger increase in T_2 and similar standard deviation. At the 500 kHz sweep width, $T_2'' = 0.4\ s$, there is a smaller increase in $T_{2,obs}$ and this results in inaccurate calcualtion of T_2 in the solid phase, $T <$ 33°C, due to low SNR (from large gradient attenuation). The T_2 from the τ = 2.8 ms CPMG (black dots) and mean T_2 from the $T_2'' = 11.6$ second images (blue dots) are shown in Fig. 9.11b. The solid curves are the fits to the image data used for T_2-temperature correlation.

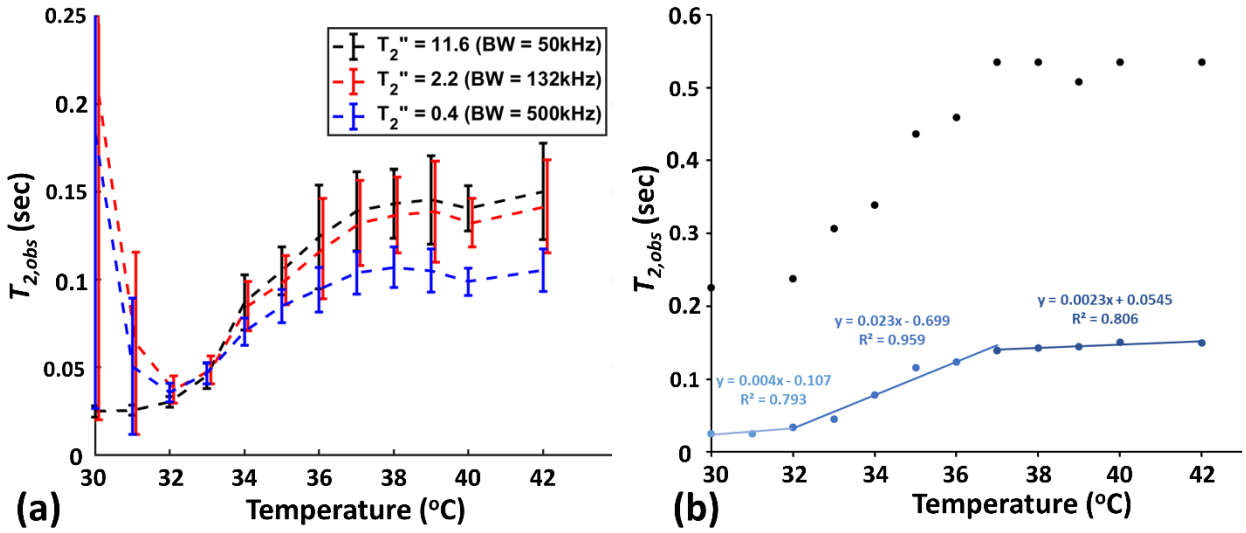


Fig. 9.10. (a) T_2 of micro-encapsulated eicosane imaged at a 0.3125 mm/pixel resolution. The red, blue and black lines correspond to images taken with a sweep width of 50, 132 and 500 kHz, respectively. Increase in sweep width drives up the standard deviation of the measurement due to increased gradient strength causing SNR to decrease. In the solid-phase at 500 kHz, the noise causes poor fitting to attenuation data. (b) T_2 relaxation rate vs temperature with τ = 2.8 ms CPMG results (black dots) shown with 50 kHz T_2-imaging mean (blue dots). Polynomial 3rd degree fit used for temperature correlation shown in blue.

Temperature Maps of Melting Encapsulated Eicosane

To test the accuracy of the correlation, images of the particles were repeated at 137 second intervals under various heating conditions. Resolution was 0.3125 mm/pixel (64x64 points) with a 50 kHz bandwidth, 5.6 ms *TE* and two averages. The air stream used for heating was set to 35°, 36°, 37° and 40°C at 400 L/min flow rates. The results shown in Fig. 9.11 are for five tests at the four temperatures with one (35°C) repeated. The rise in temperature initiates adjacent to the central gap where the heated air flow is highest. The heat can be seen to conduct through the particles outwardly in rings. While the T_2 relaxation rate of the majority of the particles/voxels match well with the temperature correlation, there are areas of particles and whole particles which do not. These variations seem to be of two types. One are isolated areas

with longer than expected T_2 decays. These are likely due to imperfections in the microencapsulation, areas where the wax has escaped confinement and has greater mobility. The other variation seems to apply to whole particles. These were identified during the development of the correlation and excluded. These particles were created in large batches for the purpose of storing thermal energy and the size of the microencapsulated eicosane particles within the 3.5 mm outer shell was said to be 10-20 micron. It is possible particle size variations (i.e. shorter than expected T_2 decays) are caused by micro particles which are smaller in diameter or have greater density of impurities which could influence relaxation. The error in the temperature measurement caused by this variation in pore size is < 1°C.

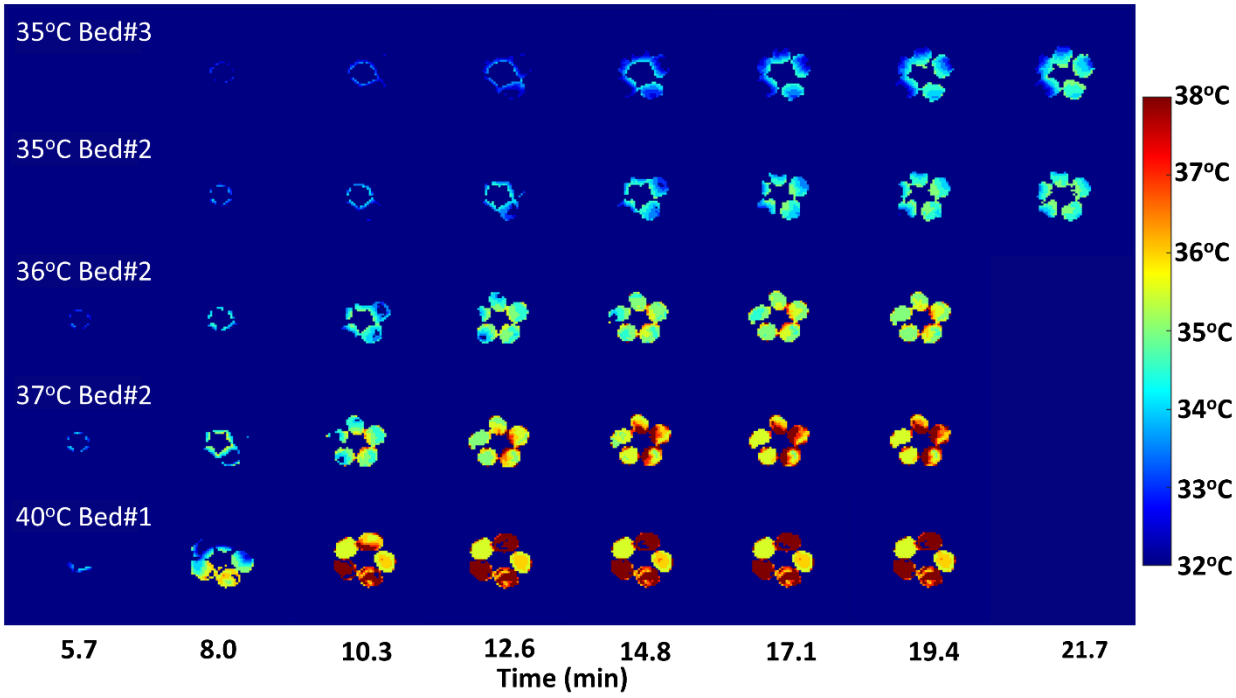


Fig. 9.11. A single layer of eicosane core-shell particles were melted by convective air flow at four temperatures. The T_2 value was converted to a temperature using the correlation developed above (Fig. 9.7 black dashed line). Dark blue represents any temperature below 32°C and dark red any temperature above 38°C.

Conclusions

The T_2 values obtained from spin-warp T_2 imaging experiments are inherently different from CPMG results due to the inclusion of diffusive attenuation effects during application of the imaging gradients. The attenuation component from the imaging gradients can be calculated and an estimate for $T_{2,obs}$ made. Results of $T_{2,obs}$ substantially lower than expected using the read gradient diffusion induced correction, indicate all imaging gradients need to be accounted for. The effects of imaging gradient strength and resolution were investigated using phantoms of different $CuSO_4$ concentrations. Those results demonstrated the influence gradient timing and amplitude parameters have on the observed T_2 and how the longer T_2 populations are disproportionally affected. Micro-encapsulated eicosane particles were demonstrated to be useful for temperature measurement. A correlation between eicosane T_2 and temperature was developed which had high T_2 relief over a 4°C temperature range (during melt) and 0.3%/°C dependence outside of the melt range, consistent with results in the literature. A multi-echo spin-warp imaging sequence captured images of the internal temperature distribution of heated particles in 137 second intervals at a 300 μm resolution. This speed was rapid enough to capture the transient melt processes in the particles and could be used to quantify local temperature variations during heat transfer.

CHAPTER 10

CONCLUSIONS AND RECOMMENDATIONS

The presented studies applied MRI techniques to non-invasively investigate convective heat transfer in a packed bed and column of pure fluid. A novel experimental technique was pioneered that provided a means to selectively probe the pore-fluid or solid-packing domains via MRI without signal interference. This technique incorporated a fluorinated pore-filling fluid with a packed bed of hydrogen-rich phase change material (PCM) particles. The PCM particles were composed of micro-scale core-shell capsules agglomerated with a binder to form semi-spherical particles with a mean diameter of 3.5 mm. Either eicosane or octadecane wax formed the core of the core-shell particles. This hydrogen-rich wax provided magnetic resonant signal that was indicative of its liquid fraction and proportional to the amount of energy absorbed by the particles. Hydrogen and fluorine are both NMR-active nuclei that can be imaged with the same experimental equipment by adjusting the excitation resonant frequency. The combination of fluorinated fluid and wax-bound hydrogen provided a means to spatially and temporally resolve pore-fluid velocities and particle-bed energy absorbed at pore-scale resolutions, a feat not accomplished by any other experimental method. The experimental results were compared to CFD models in two of the studies with the purpose of evaluating the accuracy the numerical method in simulating convective heat transfer. The opening Chapters, 1-4, developed the theory on convective heat transfer and magnetic resonance applied in the central Chapters 5-9. These focal Chapters were composed of peer-reviewed journal articles published, under-review or in preparation for submission. Additionally, an appendix is included that describes the design of an experimental apparatus useful in future research endeavors.

The novel experimental technique discussed above was first demonstrated in the 2018 *Chemical Engineering Science* article [16]. It established how a packed bed composed of a fluorinated fluid and hydrogen-rich packed bed allowed imaging of the pore-fluid and particle-wax in the same packed bed without signal interference. In the forced convection experiment at the ^{19}F resonant frequency, pore-velocity images were acquired of the heated fluid in the packed bed oriented longitudinally and transverse to the main flow direction. At the ^{1}H resonant frequency, multi-slice images were acquired in both orientations of the particle-bound wax as it was melted by the heated pore-fluid. The solid-liquid phase transition of the wax caused a significant increase in signal intensity, resolved spatially in the images. This signal was directly proportional to the energy absorbed by the wax from the fluid, resulting in 2D images that provided high resolution spatial information on heat transfer variations in the packed bed. The accompanying pore-resolved velocity maps allowed correlation between areas of high flow and accelerated heat transfer at a length-scale smaller than any existing experimental method. One-dimensional signal intensity profiles were also acquired at the ^{1}H resonance. These profiles provided high temporal resolution of the advancement of the melt front through the packed bed. These profiles could be used to characterize the axial transport of energy and could provide narrow-range temperature information without the need for extensive correlation.

The above technique was utilized to assess the accuracy of CFD models in simulating convective heat transfer in low N packed beds. Three experimental packed beds were heated above the melting temperature of the wax in triplicate at two flow rates corresponding to Re = 2.3 and Re = 4.5. These results were compared to five simulated packed beds generated using DEM techniques. The PCM particles were extensively analyzed with DSC and NMR

measurements to determine the temperature range over which the wax solid-liquid phase transition occurred and the particle's enthalpy of fusion on a per mass basis. These values were used to set the Eulerian multiphase physics in the CFD solver STAR CCM+. The similarity of the DEM generated packed bed was determined by a combination of qualitative and quantitative metrics. The packed bed particle count, and mean and maximum velocities all agreed well with the experimental values. Experiments with MRI monitored over time both the energy absorbed by the bed and the vertical position where encapsulated wax was fully melted using a combination of 2D images and 1D intensity profiles. Similar data was extracted from the simulation. It was found that the energy absorbed by the simulated bed agreed well with the experiment at both flow rates but there was poor agreement with the position of the fully melted front. At Re = 2.3, the melt front progressed at the same rate but movement of the front initiated at a later time resulting in a vertical offset of ~5mm. At Re = 4.5, the advancement of the melt front again initiated at a later time but also propagated at a faster rate. These results suggest a difference in thermal dispersion occurring in the system. This work is in preparation for submission.

In addition to forced convection studies, this work also studied natural convection. In the 2020 article published in the *International Communications in Heat and Mass Transfer [230],* Rayleigh-Bénard convection (RBC) was investigated in a long, narrow cylindrical column of water. In RBC, the enclosed fluid is heated from below, inducing a density instability that generates fluid convection when a critical value is exceeded. In the experiment, the circulation pattern was observed with velocity maps oriented both longitudinally and transversely. Two longitudinal images were acquired at perpendicular orientations, and five transverse images were

acquired distributed axially. These images were taken at four different *Ra* numbers. Additionally, a simulation of the fluid was developed in STAR CCM+ for comparison to the results. It was found that the circulation pattern was dependent on axial position in the column, an aspect of RBC that is not discussed in literature and could be undetected in many investigations where imaging is performed in only a single plane, position or orientation. The simulation results were found to agree well with the experiment. In both, the observed flow patterns were symmetric two-cell, asymmetric two-cell ('C' shaped), concentric two-cell and four cell.

Natural convection was further investigated in another *International Communications on Heat and Mass Transfer* article currently under-review. In this article the effects of variable thermophysical properties on heat transfer were investigated in a packed bed of similar arrangement to the forced convection studies. In this study, the pore-fluid was the refrigerant C_2F_6 compressed to its sub-, near- and super-critical phases, and the PCM particle contained octadecane wax. The particles melted over the temperature range of 22-24^{o}C, just above the critical temperature of the fluid (19.5^{o}C). In this investigation a combination of pore-fluid velocity images, 2D particle intensity images and 1D particle intensity profiles were used to monitor the energy transferred to the bed over time by the fluid in its three phases. The pore-fluid was shown to change its circulation pattern with height in a manner similar to the previous RBC study and maintained a consistent arrangement over time. Thermal diffusivity changes rapidly in near-critical fluids due to the divergence of heat capacity at the critical point where thermal diffusivity goes to zero. The effects of the variable thermal diffusivity are quantified in this paper through the wax signal intensity, which is indicative of its internal energy. The observed rates of heat transfer are shown to correlate with the changing fluid thermal diffusivity.

In these studies, heat transfer was quantified through the melt processes of the PCM particles. The signal intensity from the hydrogen-bound wax was directly dependent on its energy and could therefore be used to estimate energy absorbed by the bed. However, the majority of heat transfer studies and experimental results report temperature. It would therefore be useful to measure temperature in the PCM packed bed. The final study presented discussed how qualitative T_2 maps can be acquired and transformed into temperature maps. It details how the signal attenuation caused by imaging gradients can be estimated and used to calculate the intrinsic T_2 relaxation rate from the observed T_2 value. This is demonstrated for phantoms of various $CuSo_4$ concentrations and for particle-wax temperature.

Recommendations

The experimental technique established and applied in this dissertation offers a variety of avenues for future research in packed bed forced convection, porous media free convection, and the study of heat transfer near the critical point and in supercritical fluids. There are potential research ventures utilizing only the resources currently available and many more which would require additional equipment and improved materials.

The greatest limitation in the above studies has been the inability to image temperature in the packed bed or pore-fluid. Advancement of the method to provide a temperature measurement would have the greatest impact and is the suggested direction for future research. An initial correlation for PCM37's T_2 relaxation time to temperature is presented in Chapter 9. This correlation was demonstrated to work in a simple system; however, the equipment available at the time did not provide the homogeneous temperature distribution necessary for precise temperature correlation of $<1^{o}C$. A new device designed, constructed and tested in the last

months of this PhD work provides the means for a more precise temperature correlation to be developed by providing accurate and stable boundary temperatures. A further complication was the existence of variance in the PCM particles, which leads to different dependence of $T(T_2)$. This affect could be negated by verifying the correlation with batches of PCMs, selecting only particles that allow the desired trend.

Another option for future research would be the design of a core-shell particle specifically tailored for NMR temperature measurement. The current particles are of an irregular shape, they are too large to form a true packed bed, are no longer available for purchase and they have variability in their T_2 relaxation rate. The phase transition is both a positive and negative trait as it allows for heat transfer to be quantified without extensive correlation with temperature but adds complexity to the system and uncertainty to the modelling effort. Micro-encapsulation is a benefit as it prevents particle scale convection. Ideally, particles could be constructed with a range of isometric diameters with interior fluid composed of either ^{1}H or ^{19}F. The temperature dependence would be strong and the other important characteristics i.e. SNR, T_1/T_2 relaxation times could be specifically tailored.

Forced convection packed beds are of importance in many industrial applications making spatially resolved experimental data and numerical validation of great interest. Future research in this area should focus on heat transfer with gas (as this fluid is commonly employed in industry), supercritical or near-critical working fluids, as these are of greatest scientific interest. Increased flow rates so higher *Re* flows could be investigated would also be of interest, including turbulent and transition to turbulent conditions. At high flow rates the melt rate will be too rapid for MR imaging. Instead, the analysis would rely on 1D profiles used for quantification in this work.

Inclusion of the pressure drop across the bed would be a useful metric for model validation. Additionally, a NMR viewable ruler would also be useful to easily verify axial location. A 3D printed tube of variable diameter is one idea for how this could be accomplished.

To enhance the control and measurement accuracy in natural convection experiments, a pressure vessel designed for MRI studies of RBC in the SWB system was constructed and tested. This system allows for more accurate temperature control, heat flux measurement at the bottom boundary, top and bottom boundary temperatures from 10-75^{o}C, and height adjustment in the magnet bore. Current experiments are investigating RBC in a packed bed of PCMs with C_2F_6 under gas, near and supercritical conditions. The timeline for experimentation with this device will leave many studies on packed bed heat transfer for future projects e.g. pure fluid convection of sub-, near-, super-critical fluids, porous media convection with different *N*, the development of a temperature correlation in fluid or PCM. Development of a simulation of this system would be very valuable. For example, the effects of divergent thermophysical properties near a fluid's critical point, as investigated in Chapter 8, can lead to thermomechanical heat transfer through a fluid at the speed of sound in a mechanism called the piston effect. The study of near-critical RBC in both the pure fluid and packed bed could reveal anomalous heat transfer resulting from this effect. Research in this direction would be difficult due to the sensitivity of the system to perturbation and the precision required. However, this research could be very valuable to the supercritical fluids community as few other techniques could provide the same experimental results.

A final direction for future work lies in the combination of 3D printing with micro PCM material. This could allow the heat transfer studies in specifically designed channels e.g.

sinusoidal, expansions, contractions. Particles of different shapes e.g. rings, hollow cylinders, multi-lobed, could also be printed to better represent those in industrial applications like catalytic beds. By including micro PCMs of different waxes, the range over which temperature can be measured could be increased. Initial investigations into this concept revealed inhomogeneous particle distributions. It was unclear whether this was due to interaction between the specific PCM and resin or if this is a more widespread problem with the 3D printing technique. These spatial distributions in particle density and methods for preventing them are also of scientific interest.

REFERENCES CITED

1. Solomon, L., et al., *Analysis of an encapsulated phase change material-based energy storage system for high-temperature applications.* International Journal of Energy Research, 2018.
2. Li, M.-J., et al., *Experimental and numerical study on the performance of a new high-temperature packed-bed thermal energy storage system with macroencapsulation of molten salt phase change material.* Applied Energy, 2018. **221**: p. 1-15.
3. Bhuvaneswari, E. and C. Anandharamakrishnan, *Heat transfer analysis of pasteurization of bottled beer in a tunnel pasteurizer using computational fluid dynamics.* Innovative Food Science & Emerging Technologies, 2014. **23**: p. 156-163.
4. Berthold, S. and C. Resagk, *Investigation of thermal convection in water columns using particle image velocimetry.* Experiments in fluids, 2012. **52**(6): p. 1465-1474.
5. Mellor, A., et al., *Roadmap for the next-generation of hybrid photovoltaic-thermal solar energy collectors.* Solar Energy, 2018. **174**: p. 386-398.
6. Accary, G., P. Bontoux, and B. Zappoli, *Convection in a supercritical fluid: a reduced model for geophysical flows.* Physics of Fluids, 2007. **19**(1): p. 014104.
7. El Khouri, L. and P. Carlès, *Supercritical fluids as experimental models for geophysical flows.* International journal of thermophysics, 2003. **24**(3): p. 683-693.
8. Dixon, A.G. and B. Partopour, *Computational fluid dynamics for fixed bed reactor design.* Annual review of chemical and biomolecular engineering, 2020. **11**: p. 109-130.
9. Noah, O.O., J.F. Slabber, and J.P. Meyer, *Modeling a Porous Region for Natural Convection Heat Transfer and Experimental Validation in Slender Cylindrical Geometries.* Nuclear Technology, 2016. **193**(3): p. 375-390.
10. Accary, G. and I. Raspo, *A 3D finite volume method for the prediction of a supercritical fluid buoyant flow in a differentially heated cavity.* Computers & Fluids, 2006. **35**(10): p. 1316-1331.
11. Ma, D., D. Henry, and H. Ben Hadid, *Three-dimensional numerical study of natural convection in vertical cylinders partially heated from the side.* Physics of Fluids, 2005. **17**(12): p. 124101.
12. Amiroudine, S., et al., *Direct numerical simulation of instabilities in a two-dimensional near-critical fluid layer heated from below.* Journal of Fluid Mechanics, 2001. **442**: p. 119-140.
13. Jurtz, N., M. Kraume, and G.D. Wehinger, *Advances in fixed-bed reactor modeling using particle-resolved computational fluid dynamics (CFD).* Reviews in Chemical Engineering, 2019. **35**(2): p. 139-190.
14. Thaker, A.H., G.M. Karthik, and V.V. Buwa, *PIV measurements and CFD simulations of the particle-scale flow distribution in a packed bed.* Chemical Engineering Journal, 2019. **374**: p. 189-200.
15. Boyce, C.M., et al., *Magnetic resonance imaging of single bubbles injected into incipiently fluidized beds.* Chemical Engineering Science, 2019. **200**: p. 147-166.
16. Skuntz, M.E., et al., *Melt-front propagation and velocity profiles in packed beds of phase-change materials measured by magnetic resonance imaging.* Chemical Engineering Science, 2018. **190**: p. 164-172.
17. Montague, J.A., et al., *Visualization and simulation of density driven convection in porous media using magnetic resonance imaging.* Journal of contaminant hydrology, 2018. **212**: p. 78-84.
18. Conradi, M.S., et al., *Low-field magnetic resonance imaging of roots in intact clayey and silty soils.* 2020.
19. Kuethe, D.O., J.M. Hix, and L.E. Fredenburgh, *T1, T1 contrast, and Ernst-angle images of four rat-lung pathologies.* Magnetic resonance in medicine, 2019. **81**(4): p. 2489-2500.
20. Thrane, L.W., et al., *NMR Relaxometry to Characterize the Drug Structural Phase in a Porous Construct.* Molecular pharmaceutics, 2018. **15**(7): p. 2614-2620.

21. Mailhiot, S.E., et al., *Pulsed gradient stimulated echo (PGStE) NMR shows spatial dependence of fluid diffusion in human stage IV osteoarthritic cartilage.* Magnetic resonance in medicine, 2018. **80**(3): p. 1170-1177.
22. Washburn, K.E. and Y. Cheng, *Detection of intermolecular homonuclear dipolar coupling in organic rich shale by transverse relaxation exchange.* Journal of Magnetic Resonance, 2017. **278**: p. 18-24.
23. Thrane, L.W., J.D. Seymour, and S.L. Codd, *Probing diffusion dynamics during hydrate formation by high field NMR relaxometry and diffusometry.* Journal of Magnetic Resonance, 2019. **303**: p. 7-16.
24. Terenzi, C., et al., *Spatially-resolved 1H NMR relaxation-exchange measurements in heterogeneous media.* Journal of Magnetic Resonance, 2019. **299**: p. 101-108.
25. Penn, A., et al., *Real-time magnetic resonance imaging of bubble behavior and particle velocity in fluidized beds.* Industrial & Engineering Chemistry Research, 2018. **57**(29): p. 9674-9682.
26. Gladden, L.F. and A.J. Sederman, *Recent advances in flow MRI.* Journal of Magnetic Resonance, 2013. **229**: p. 2-11.
27. Seymour, J.D. and P.T. Callaghan, *"Flow-diffraction" structural characterization and measurement of hydrodynamic dispersion in porous media by PGSE NMR.* Journal of Magnetic Resonance, Series A, 1996. **122**(1): p. 90-93.
28. Li, T.-Q., et al., *Turbulent pipe flow studied by time-averaged NMR imaging: measurements of velocity profile and turbulent intensity.* Magnetic resonance imaging, 1994. **12**(6): p. 923-934.
29. Jenner, C., et al., *Circulation of water within wheat grain revealed by nuclear magnetic resonance micro-imaging.* Nature, 1988. **336**(6197): p. 399.
30. Seymour, J.D., et al., *Anomalous fluid transport in porous media induced by biofilm growth.* Physical review letters, 2004. **93**(19): p. 198103.
31. Shiroishi, M.S., et al., *Principles of T2*-weighted dynamic susceptibility contrast MRI technique in brain tumor imaging.* Journal of Magnetic Resonance Imaging, 2015. **41**(2): p. 296-313.
32. MacKay, A., et al., *Insights into brain microstructure from the T2 distribution.* Magnetic Resonance Imaging, 2006. **24**(4): p. 515-525.
33. Gunnarsdóttir, A.B., et al., *Noninvasive In Situ NMR Study of "Dead Lithium" Formation and Lithium Corrosion in Full-Cell Lithium Metal Batteries.* Journal of the American Chemical Society, 2020. **142**(49): p. 20814-20827.
34. Sesti, E.L., et al., *A flow-through, elevated-temperature and -pressure NMR apparatus for in-situ CO2 sequestration studies.* Journal of Magnetic Resonance, 2017. **282**: p. 136-141.
35. Baker, L., et al., *Operando magnetic resonance studies of phase behaviour and oligomer accumulation within catalyst pores during heterogeneous catalytic ethene oligomerization.* Applied Catalysis A: General, 2018. **557**: p. 125-134.
36. Leclerc, S. and C. Métivier, *MRI temperature and velocity measurements in a fluid layer with heat transfer.* Experiments in Fluids, 2018. **59**(2): p. 34.
37. Darbouli, M., et al., *Natural convection in shear-thinning fluids: Experimental investigations by MRI.* International Journal of Heat and Mass Transfer, 2016. **95**: p. 742-754.
38. Shattuck, M., et al., *Onset and stability of convection in porous media: Visualization by magnetic resonance imaging.* Physical review letters, 1995. **75**(10): p. 1934-1937.
39. Nield, D.A. and A. Bejan, *Convection in porous media*. Vol. 3. 2006: Springer.
40. Bergman, T.L., et al., *Introduction to heat transfer*. 2011: John Wiley & Sons.
41. Munson, B.R., et al., *Fluid mechanics*. 2013: Wiley Singapore.
42. White, F.M. and I. Corfield, *Viscous fluid flow*. Vol. 3. 2006: McGraw-Hill New York.
43. Bird, R.B., W.E. Stewart, and E.N. Lightfoot, *Transport phenomena*. Vol. 1. 2006: John Wiley & Sons.
44. Deen, W.M., *Analysis of transport phenomena.* 1998.

45. Dixon, A.G. and M. Nijemeisland, *CFD as a design tool for fixed-bed reactors.* Industrial & Engineering Chemistry Research, 2001. **40**(23): p. 5246-5254.
46. Kummer, A. and T. Varga, *What do we know already about reactor runaway? – A review.* Process Safety and Environmental Protection, 2021. **147**: p. 460-476.
47. Dixon, A.G. and D.L. Cresswell, *Theoretical prediction of effective heat transfer parameters in packed beds.* AIChE Journal, 1979. **25**(4): p. 663-676.
48. Wakao, N., K. Tanaka, and H. Nagai, *Measurements of particle-to-gas mass transfer coefficients from chromatographic adsorption experiments.* Chemical Engineering Science, 1976. **31**(12): p. 1109-1113.
49. Miyauchi, T., H. Kataoka, and T. Kikuchi, *Gas film coefficient of mass transfer in low Peclet number region for sphere packed beds.* Chemical Engineering Science, 1976. **31**(1): p. 9-13.
50. Catton, I. *Natural convection in enclosures*. in *International Heat Transfer Conference Digital Library*. 1978. Begel House Inc.
51. MacGregor, R. and A.F. Emery, *Free convection through vertical plane layers—moderate and high Prandtl number fluids.* 1969.
52. Rayleigh, L., *LIX. On convection currents in a horizontal layer of fluid, when the higher temperature is on the under side.* The London, Edinburgh, and Dublin Philosophical Magazine and Journal of Science, 1916. **32**(192): p. 529-546.
53. Koschmieder, E.L., *Bénard cells and Taylor vortices*. 1993: Cambridge University Press.
54. Cordon, R.P. and M. Velarde, *On the (non linear) foundations of Boussinesq approximation applicable to a thin layer of fluid.* Journal de physique, 1975. **36**(7-8): p. 591-601.
55. Mihaljan, J.M., *A Rigorous Exposition of the Boussinesq Approximations Applicable to a Thin Layer of Fluid.* The Astrophysical Journal, 1962. **136**: p. 1126.
56. Spiegel, E.A. and G. Veronis, *On the Boussinesq approximation for a compressible fluid.* The Astrophysical Journal, 1960. **131**: p. 442.
57. Charlson, G. and R. Sani, *Finite amplitude axisymmetric thermoconvective flows in a bounded cylindrical layer of fluid.* Journal of Fluid Mechanics, 1975. **71**(2): p. 209-229.
58. Charlson, G.S. and R. Sani, *On thermoconvective instability in a bounded cylindrical fluid layer.* International Journal of Heat and Mass Transfer, 1971. **14**(12): p. 2157-2160.
59. Charlson, G.S. and R. Sani, *Thermoconvective instability in a bounded cylindrical fluid layer.* International Journal of Heat and Mass Transfer, 1970. **13**(9): p. 1479-1496.
60. Koschmieder, E. and S. Pallas, *Heat transfer through a shallow, horizontal convecting fluid layer.* International Journal of Heat and Mass Transfer, 1974. **17**(9): p. 991-1002.
61. Chen, M.M. and J.A. Whitehead, *Evolution of two-dimensional periodic Rayleigh convection cells of arbitrary wave-numbers.* Journal of Fluid Mechanics, 1968. **31**(1): p. 1-15.
62. Zappoli, B., *Near-critical fluid hydrodynamics.* Comptes Rendus Mécanique, 2003. **331**(10): p. 713-726.
63. Carlès, P. and B. Ugurtas, *The onset of free convection near the liquid–vapour critical point Part I: Stationary initial state.* Physica D: Nonlinear Phenomena, 1999. **126**(1-2): p. 69-82.
64. Zappoli, B. and A. Durand-Daubin, *Heat and mass transport in a near supercritical fluid.* Physics of Fluids, 1994. **6**(5): p. 1929-1936.
65. Assenheimer, M. and V. Steinberg, *Rayleigh-Bénard convection near the gas-liquid critical point.* Physical review letters, 1993. **70**(25): p. 3888.
66. Whitaker, S., *Theory and applications of transport in porous media: The method of volume averaging.* Theory and Application of Transport in Porous Media: The Method of Volume Averaging, 1999.
67. Georgiadis, J.G. and I. Catton, *Dispersion in cellular thermal convection in porous layers.* International journal of heat and mass transfer, 1988. **31**(5): p. 1081-1091.

68. Georgiadis, J.G., *Future research needs in convective heat and mass transport in porous media*, in *Convective Heat and Mass Transfer in Porous Media*. 1991, Springer. p. 1073-1088.
69. Hsu, C. and P. Cheng, *Thermal dispersion in a porous medium.* International Journal of Heat and Mass Transfer, 1990. **33**(8): p. 1587-1597.
70. de Gracia, A. and L.F. Cabeza, *Numerical simulation of a PCM packed bed system: A review.* Renewable and Sustainable Energy Reviews, 2017. **69**: p. 1055-1063.
71. Yang, X., et al., *Direct numerical simulation of pore-scale flow in a bead pack: Comparison with magnetic resonance imaging observations.* Advances in water resources, 2013. **54**: p. 228-241.
72. Wang, Z., et al., *Porosity distribution in random packed columns by gamma ray tomography.* Chemical Engineering and Processing: Process Intensification, 2001. **40**(3): p. 209-219.
73. Freund, H., et al., *Numerical simulations of single phase reacting flows in randomly packed fixed-bed reactors and experimental validation.* Chemical engineering science, 2003. **58**(3-6): p. 903-910.
74. Soppe, W., *Computer simulation of random packings of hard spheres.* Powder technology, 1990. **62**(2): p. 189-197.
75. Bai, H., et al., *A coupled DEM and CFD simulation of flow field and pressure drop in fixed bed reactor with randomly packed catalyst particles.* Industrial & Engineering Chemistry Research, 2009. **48**(8): p. 4060-4074.
76. Cundall, P.A. and O.D. Strack, *A discrete numerical model for granular assemblies.* geotechnique, 1979. **29**(1): p. 47-65.
77. Caulkin, R., et al., *Impact of shape representation schemes used in discrete element modelling of particle packing.* Computers & Chemical Engineering, 2015. **76**: p. 160-169.
78. Marigo, M. and E.H. Stitt, *Discrete element method (DEM) for industrial applications: comments on calibration and validation for the modelling of cylindrical pellets.* KONA Powder and Particle Journal, 2015. **32**: p. 236-252.
79. Partopour, B. and A.G. Dixon, *An integrated workflow for resolved-particle packed bed models with complex particle shapes.* Powder Technology, 2017. **322**: p. 258-272.
80. Boccardo, G., et al., *Validation of a novel open-source work-flow for the simulation of packed-bed reactors.* Chemical Engineering Journal, 2015. **279**: p. 809-820.
81. Flaischlen, S. and G.D. Wehinger, *Synthetic packed-bed generation for CFD simulations: Blender vs. STAR-CCM+.* ChemEngineering, 2019. **3**(2): p. 52.
82. Eppinger, T., N. Jurtz, and R. Aglave. *Automated workflow for spatially resolved packed bed reactors with spherical and non-spherical particles*. in *Proceedings of the 10th International Conference on CFD in Oil & Gas, Metallurgical and process Industries SINTEF, Trondheim, Norway*. 2014.
83. Dixon, A.G., M. Nijemeisland, and E.H. Stitt, *Systematic mesh development for 3D CFD simulation of fixed beds: Contact points study.* Computers & Chemical Engineering, 2013. **48**: p. 135-153.
84. Eppinger, T., K. Seidler, and M. Kraume, *DEM-CFD simulations of fixed bed reactors with small tube to particle diameter ratios.* Chemical Engineering Journal, 2011. **166**(1): p. 324-331.
85. Ookawara, S., et al. *High-fidelity DEM-CFD modeling of packed bed reactors for process intensification*. in *Proceedings of European Congress of Chemical Engineering (ECCE-6), Copenhagen*. 2007.
86. Pichler, M., et al., *Effect of particle contact point treatment on the CFD simulation of the heat transfer in packed beds.* Chemical Engineering Research and Design, 2021. **165**: p. 242-253.
87. Dixon, A.G., et al., *Experimental validation of high Reynolds number CFD simulations of heat transfer in a pilot-scale fixed bed tube.* Chemical Engineering Journal, 2012. **200**: p. 344-356.

88. Cascetta, M., et al., *A comparison between CFD simulation and experimental investigation of a packed-bed thermal energy storage system.* Applied Thermal Engineering, 2016. **98**: p. 1263-1272.
89. Niu, Q. and N.-X. Wang, *Study of heat transfer by using DEM–CFD method in a randomly packed pebble-bed reactor.* Nuclear Science and Techniques, 2019. **30**(2): p. 28.
90. Hassan, Y.A. and E. Dominguez-Ontiveros, *Flow visualization in a pebble bed reactor experiment using PIV and refractive index matching techniques.* Nuclear Engineering and Design, 2008. **238**(11): p. 3080-3085.
91. Khayamyan, S., et al., *Measurements of transitional and turbulent flow in a randomly packed bed of spheres with particle image velocimetry.* Transport in Porous Media, 2017. **116**(1): p. 413-431.
92. Callaghan, P.T., *Translational dynamics and magnetic resonance: principles of pulsed gradient spin echo NMR*. 2011: Oxford University Press.
93. Rieke, V. and K. Butts Pauly, *MR thermometry.* Journal of Magnetic Resonance Imaging, 2008. **27**(2): p. 376-390.
94. Gladden, L.F. and A.J. Sederman, *Magnetic Resonance Imaging and Velocity Mapping in Chemical Engineering Applications.* Annual review of chemical and biomolecular engineering, 2017. **8**: p. 227-247.
95. Song, Y.-Q., et al., *Magnetic resonance in porous media: Recent progress.* The Journal of chemical physics, 2008. **128**(5): p. 02B618.
96. Purcell, E.M., H.C. Torrey, and R.V. Pound, *Resonance Absorption by Nuclear Magnetic Moments in a Solid.* Physical Review, 1946. **69**(1-2): p. 37-38.
97. Bloch, F., W.W. Hansen, and M. Packard, *The Nuclear Induction Experiment.* Physical Review, 1946. **70**(7-8): p. 474-485.
98. Lauterbur, P.C., *Image formation by induced local interactions: examples employing nuclear magnetic resonance.* nature, 1973. **242**(5394): p. 190-191.
99. Mansfield, P. and P.K. Grannell, *NMR'diffraction'in solids?* Journal of Physics C: solid state physics, 1973. **6**(22): p. L422.
100. Callaghan, P.T., *Principles of nuclear magnetic resonance microscopy*. 1993: Oxford University Press on Demand.
101. Blümich, B., *NMR imaging of materials*. 2004.
102. Keeler, J., *Understanding NMR spectroscopy*. 2011: John Wiley & Sons.
103. Fabich, H.T., et al., *NMR of petrochemical-type chemical reactions.* Journal of Magnetic Resonance, 2020. **311**: p. 106665.
104. Colucci, L.A., et al., *Fluid assessment in dialysis patients by point-of-care magnetic relaxometry.* Science translational medicine, 2019. **11**(502): p. eaau1749.
105. Seymour, J.D., S.L. Codd, and R. Kimmich, *Peclet number dependent superdiffusive hydrodynamic dispersion in a site percolation porous media measured by NMR.* Microporous and Mesoporous Materials, 2018. **269**: p. 56-59.
106. Zhu, M., Z. Sun, and C.K. Ng, *Image-guided thermal ablation with MR-based thermometry.* Quantitative imaging in medicine and surgery, 2017. **7**(3): p. 356.
107. Williams, E.T., et al., *Magnetic resonance thermometry experimental setup: a portable heat transfer experiment.* Proceedings of the ASMA, 2016: p. 11-17.
108. Koptyug, I.V., et al., *Spatially resolved NMR thermometry of an operating fixed-bed catalytic reactor.* Journal of the American Chemical Society, 2008. **130**(32): p. 10452-10453.
109. Callaghan, P.T. and Y. Xia, *Velocity and diffusion imaging in dynamic NMR microscopy.* Journal of Magnetic Resonance (1969), 1991. **91**(2): p. 326-352.
110. Carr, H.Y. and E.M. Purcell, *Effects of Diffusion on Free Precession in Nuclear Magnetic Resonance Experiments.* Physical Review, 1954. **94**(3): p. 630-638.

111. Stejskal, E.O. and J.E. Tanner, *Spin diffusion measurements: spin echoes in the presence of a time-dependent field gradient.* The journal of chemical physics, 1965. **42**(1): p. 288-292.
112. Torrey, H.C., *Bloch equations with diffusion terms.* Physical review, 1956. **104**(3): p. 563.
113. Rieke, V., *MR thermometry.* Interventional Magnetic Resonance Imaging, 2011: p. 271-288.
114. Buchenberg, W.B., et al., *Acquisition of 3D temperature distributions in fluid flow using proton resonance frequency thermometry.* Magnetic resonance in medicine, 2016. **76**(1): p. 145-155.
115. Wasserman, F., et al. *Applying Magnetic Resonance Thermometry to Engineering Flows*. in *17th International Symposium on Applications of Laser Techniques to Fluid Mechanics*. 2014.
116. Mitchell, J. and M.L. Johns, *Rapid measurements of diffusion using PFG: developments and applications of the difftrain pulse sequence.* Concepts in Magnetic Resonance Part A: An Educational Journal, 2009. **34**(1): p. 1-15.
117. Zanganeh, G., et al., *Packed-bed thermal storage for concentrated solar power–Pilot-scale demonstration and industrial-scale design.* Solar Energy, 2012. **86**(10): p. 3084-3098.
118. Singh, H., R. Saini, and J. Saini, *A review on packed bed solar energy storage systems.* Renewable and Sustainable Energy Reviews, 2010. **14**(3): p. 1059-1069.
119. Shigaki, N., S. Ozawa, and I. Sumi, *Effect of Gas Velocity Distribution on Heat Recovery Process in Packed Bed of Plate-Shaped Slag.* Energies, 2017. **10**(6): p. 755.
120. Wehinger, G.D., T. Eppinger, and M. Kraume, *Detailed numerical simulations of catalytic fixed-bed reactors: Heterogeneous dry reforming of methane.* Chemical Engineering Science, 2015. **122**: p. 197-209.
121. Yang, J., et al., *Experimental analysis of forced convective heat transfer in novel structured packed beds of particles.* Chemical engineering science, 2012. **71**: p. 126-137.
122. Anderson, R., et al., *Experimental results and modeling of energy storage and recovery in a packed bed of alumina particles.* Applied Energy, 2014. **119**: p. 521-529.
123. Wen, D. and Y. Ding, *Heat transfer of gas flow through a packed bed.* Chemical Engineering Science, 2006. **61**(11): p. 3532-3542.
124. Achenbach, E., *Heat and flow characteristics of packed beds.* Experimental Thermal and Fluid Science, 1995. **10**(1): p. 17-27.
125. Rassi, E.M., S.L. Codd, and J.D. Seymour, *Nuclear magnetic resonance characterization of the stationary dynamics of partially saturated media during steady-state infiltration flow.* New Journal of Physics, 2011. **13**(1): p. 015007.
126. Gladden, L.F. and J. Mitchell, *Measuring adsorption, diffusion and flow in chemical engineering: applications of magnetic resonance to porous media.* New Journal of Physics, 2011. **13**(3): p. 035001.
127. Bijeljic, B. and M.J. Blunt, *Pore-scale modeling of transverse dispersion in porous media.* Water Resources Research, 2007. **43**(12).
128. Götz, J., et al., *Visualisation of flow processes in packed beds with NMR imaging: determination of the local porosity, velocity vector and local dispersion coefficients.* Chemical Engineering and Processing: Process Intensification, 2002. **41**(7): p. 611-629.
129. Manz, B., L. Gladden, and P. Warren, *Flow and dispersion in porous media: Lattice-Boltzmann and NMR studies.* AIChE journal, 1999. **45**(9): p. 1845-1854.
130. Sederman, A., et al., *Structure-flow correlations in packed beds.* Chemical Engineering Science, 1998. **53**(12): p. 2117-2128.
131. Seymour, J.D. and P.T. Callaghan, *Generalized approach to NMR analysis of flow and dispersion in porous media.* AIChE Journal, 1997. **43**(8): p. 2096-2111.
132. Sederman, A.J., et al., *Magnetic resonance imaging of liquid flow and pore structure within packed beds.* Chemical Engineering Science, 1997. **52**(14): p. 2239-2250.
133. Sen, P.N., L. Schwartz, and P.P. Mitra, *Probing the structure of porous media using NMR spin echoes.* Magnetic resonance imaging, 1994. **12**(2): p. 227-230.

134. Webb, A., *Temperature measurements using nuclear magnetic resonance.* Annual Reports on NMR Spectroscopy, 2002. **45**: p. 1-67.
135. Spirnak, J., et al. *Validation of Magnetic Resonance Thermometry through Experimental and Computational Approaches*. in *52nd AIAA/SAE/ASEE Joint Propulsion Conference*. 2016.
136. Jarenwattananon, N.N., et al., *Thermal maps of gases in heterogeneous reactions.* Nature, 2013. **502**(7472): p. 537-540.
137. Nott, K.P. and L.D. Hall, *Validation and cross-comparison of MRI temperature mapping against fibre optic thermometry for microwave heating of foods.* International journal of food science & technology, 2005. **40**(7): p. 723-730.
138. Ye, X., et al., *MRI Temperature Mapping and Determination of Liquid-particulate Heat Transfer Coefficient in an Ohmically Heated Food System.* Journal of food science, 2003. **68**(4): p. 1341-1346.
139. Nott, K.P., et al., *MRI phase mapping of temperature distributions induced in food by microwave heating.* Magnetic Resonance Imaging, 2000. **18**(1): p. 69-79.
140. Bertsch, F., et al., *Non-invasive temperature mapping using MRI: comparison of two methods based on chemical shift and T1-relaxation.* Magnetic resonance imaging, 1998. **16**(4): p. 393-403.
141. HULBERT, G.J., J.B. Litchfield, and S.J. SCHMIDT, *Temperature mapping in carrot using T1 weighted magnetic resonance imaging.* Journal of food science, 1995. **60**(4): p. 780-785.
142. SUN, X., J.B. LITCHFIELD, and S.J. SCHMIDT, *Temperature mapping in a model food gel using magnetic resonance imaging.* Journal of food science, 1993. **58**(1): p. 168-172.
143. Boyce, C., et al., *Magnetic resonance characterization of coupled gas and particle dynamics in a bubbling fluidized bed.* Physical Review Fluids, 2016. **1**(7): p. 074201.
144. Abragam, A., *The principles of nuclear magnetism*. 1961: Oxford university press.
145. Parker, D.L., *Applications of NMR imaging in hyperthermia: an evaluation of the potential for localized tissue heating and noninvasive temperature monitoring.* Ieee transactions on biomedical engineering, 1984(1): p. 161-167.
146. Allen, K., T. Von Backström, and D. Kröger, *Rock bed pressure drop and heat transfer: Simple design correlations.* Solar Energy, 2015. **115**: p. 525-536.
147. Ettouney, H., H. El-Dessouky, and A. Al-Ali, *Heat transfer during phase change of paraffin wax stored in spherical shells.* Journal of solar energy engineering, 2005. **127**(3): p. 357-365.
148. Zhang, Z., et al., *The Shandong Shidao Bay 200 MWe High-Temperature Gas-Cooled Reactor Pebble-Bed Module (HTR-PM) Demonstration Power Plant: An Engineering and Technological Innovation.* Engineering, 2016. **2**(1): p. 112-118.
149. Sharma, A., et al., *Review on thermal energy storage with phase change materials and applications.* Renewable and Sustainable Energy Reviews, 2009. **13**(2): p. 318-345.
150. Zare, M. and S.H. Hashemabadi, *Particle-fluid heat transfer close to the bed wall: CFD simulation and experimental study of particle shape influence on the formation of hot zones.* International Journal of Thermal Sciences, 2020. **150**: p. 106223.
151. Partopour, B. and A.G. Dixon, *Computationally efficient incorporation of microkinetics into resolved-particle CFD simulations of fixed-bed reactors.* Computers & Chemical Engineering, 2016. **88**: p. 126-134.
152. Zhang, M., H. Dong, and Z. Geng, *Computational study of flow and heat transfer in fixed beds with cylindrical particles for low tube to particle diameter ratios.* Chemical Engineering Research and Design, 2018. **132**: p. 149-161.
153. Wehinger, G.D., *Radiation Matters in Fixed-Bed CFD Simulations.* Chemie Ingenieur Technik, 2019. **91**(5): p. 583-591.
154. Fernengel, J. and O. Hinrichsen, *Influence of material properties on voidage of numerically generated random packed beds.* Chemical Engineering Science, 2021. **233**: p. 116406.

155. Dixon, A., *COMSOL Multiphysics Simulation of 3D Single-3hase Transport in a Random Packed Bed of Spheres*.
156. Dabiri, D., *Digital particle image thermometry/velocimetry: a review.* Experiments in Fluids, 2009. **46**(2): p. 191-241.
157. Xi, H.-D., S. Lam, and K.-Q. Xia, *From laminar plumes to organized flows: the onset of large-scale circulation in turbulent thermal convection.* Journal of Fluid Mechanics, 2004. **503**: p. 47-56.
158. Xia, K.-Q., C. Sun, and S.-Q. Zhou, *Particle image velocimetry measurement of the velocity field in turbulent thermal convection.* Physical review E, 2003. **68**(6): p. 066303.
159. Ataei-Dadavi, I., et al., *Flow and heat transfer measurements in natural convection in coarse-grained porous media.* International Journal of Heat and Mass Transfer, 2019. **130**: p. 575-584.
160. Elkins, C.J. and M.T. Alley, *Magnetic resonance velocimetry: applications of magnetic resonance imaging in the measurement of fluid motion.* Experiments in Fluids, 2007. **43**(6): p. 823-858.
161. Seymour, J.D., B. Manz, and P.T. Callaghan, *Pulsed gradient spin echo nuclear magnetic resonance measurements of hydrodynamic instabilities with coherent structure: Taylor vortices.* Physics of Fluids, 1999. **11**(5): p. 1104-1113.
162. Aussillous, P., et al., *Magnetic resonance imaging of structure and convection in solidifying mushy layers.* Journal of Fluid Mechanics, 2006. **552**: p. 99-125.
163. Mantle, M.D., A.J. Sederman, and L.F. Gladden, *Single- and two-phase flow in fixed-bed reactors: MRI flow visualisation and lattice-Boltzmann simulations.* Chemical Engineering Science, 2001. **56**(2): p. 523-529.
164. Gladden, L.F., et al., *MRI: operando measurements of temperature, hydrodynamics and local reaction rate in a heterogeneous catalytic reactor.* Catalysis Today, 2010. **155**(3-4): p. 157-163.
165. Lysova, A.A., et al., *Quantitative temperature mapping within an operating catalyst by spatially resolved 27Al NMR.* Chemical Communications, 2012. **48**(46): p. 5763-5765.
166. Eppinger, T. and G.D. Wehinger, *A Generalized Contact Modification for Fixed-Bed Reactor CFD Simulations.* Chemie Ingenieur Technik, 2021. **93**(1-2): p. 143-153.
167. Dixon, A.G., *Correlations for wall and particle shape effects on fixed bed bulk voidage.* The Canadian Journal of Chemical Engineering, 1988. **66**(5): p. 705-708.
168. von Seckendorff, J., et al., *Experimental Characterization of Random Packed Spheres, Cylinders and Rings, and their Influence on Pressure Drop.* Chemical Engineering Science, 2020: p. 115644.
169. Churchill, S.W. and H.H. Chu, *Correlating equations for laminar and turbulent free convection from a vertical plate.* International journal of heat and mass transfer, 1975. **18**(11): p. 1323-1329.
170. McGreavy, C., E. Foumeny, and K. Javed, *Characterization of transport properties for fixed bed in terms of local bed structure and flow distribution.* Chemical Engineering Science, 1986. **41**(4): p. 787-797.
171. Hof, B., P. Lucas, and T. Mullin, *Flow state multiplicity in convection.* Physics of Fluids, 1999. **11**(10): p. 2815-2817.
172. Lohse, D. and K.-Q. Xia, *Small-scale properties of turbulent Rayleigh-Bénard convection.* Annual Review of Fluid Mechanics, 2010. **42**: p. 335-364.
173. Ahlers, G., S. Grossmann, and D. Lohse, *Heat transfer and large scale dynamics in turbulent Rayleigh-Bénard convection.* Reviews of modern physics, 2009. **81**(2): p. 503-537.
174. Xi, H.-D. and K.-Q. Xia, *Azimuthal motion, reorientation, cessation, and reversal of the large-scale circulation in turbulent thermal convection: a comparative study in aspect ratio one and one-half geometries.* Physical Review E, 2008. **78**(3): p. 036326.
175. Brown, E., A. Nikolaenko, and G. Ahlers, *Reorientation of the large-scale circulation in turbulent Rayleigh-Bénard convection.* Physical review letters, 2005. **95**(8): p. 084503.

176. Buell, J. and I. Catton, *The effect of wall conduction on the stability of a fluid in a right circular cylinder heated from below.* Journal of Heat Transfer, 1983. **105**(2): p. 255-260.
177. Rosenblat, S., *Thermal convection in a vertical circular cylinder.* Journal of Fluid Mechanics, 1982. **122**: p. 395-410.
178. Catton, I. and D.K. Edwards, *Initiation of thermal convection in finite right circular cylinders.* AIChE Journal, 1970. **16**(4): p. 594-601.
179. Müller, G., G. Neumann, and W. Weber, *Natural convection in vertical Bridgman configurations.* Journal of Crystal Growth, 1984. **70**(1-2): p. 78-93.
180. Andreades, C., et al., *Design Summary of the Mark-I Pebble-Bed, Fluoride Salt–Cooled, High-Temperature Reactor Commercial Power Plant.* Nuclear Technology, 2016. **195**(3): p. 223-238.
181. Koschmieder, E. and S. Prahl, *Surface-tension-driven Bénard convection in small containers.* Journal of Fluid Mechanics, 1990. **215**: p. 571-583.
182. Zaleski, S., Y. Pomeau, and A. Pumir, *Optimal merging of rolls near a plane boundary.* Physical Review A, 1984. **29**(1): p. 366-370.
183. Stork, K. and U. Müller, *Convection in boxes: an experimental investigation in vertical cylinders and annuli.* Journal of Fluid Mechanics, 1975. **71**(2): p. 231-240.
184. Stork, K. and U. Möller, *Convection in boxes: experiments.* Journal of Fluid Mechanics, 1972. **54**(4): p. 599-611.
185. Bénard, H., *Les tourbillons cellulaires dans une nappe liquide propageant de la chaleur par convection: en régime permanent*. 1901: Gauthier-Villars.
186. Naghib, A., et al., *Natural convection induced by radiation in a water filled square cavity: Experimental observations.* Experimental Thermal and Fluid Science, 2017. **80**: p. 105-116.
187. Funfschilling, D. and G. Ahlers, *Plume motion and large-scale circulation in a cylindrical Rayleigh-Bénard cell.* Physical review letters, 2004. **92**(19): p. 194502.
188. Tilgner, A., A. Belmonte, and A. Libchaber, *Temperature and velocity profiles of turbulent convection in water.* Physical Review E, 1993. **47**(4): p. R2253-R2256.
189. Xi, H.-D. and K.-Q. Xia, *Cessations and reversals of the large-scale circulation in turbulent thermal convection.* Physical Review E, 2007. **75**(6): p. 066307.
190. Jerschow, A., *Thermal Convection Currents in NMR: Flow Profiles and Implications for Coherence Pathway Selection.* Journal of Magnetic Resonance, 2000. **145**(1): p. 125-131.
191. Manz, B., J. Seymour, and P. Callaghan, *PGSE NMR measurements of convection in a capillary.* Journal of Magnetic Resonance, 1997. **125**(1): p. 153-158.
192. Weber, M. and R. Kimmich, *Rayleigh-B\'enard percolation transition of thermal convection in porous media: Computational fluid dynamics, NMR velocity mapping, NMR temperature mapping.* Physical Review E, 2002. **66**(5): p. 056301.
193. Mohorič, A. and J. Stepišnik, *Effect of natural convection in a horizontally oriented cylinder on NMR imaging of the distribution of diffusivity.* Physical Review E, 2000. **62**(5): p. 6628-6635.
194. Weis, J., R. Kimmich, and H.-P. Müller, *NMR imaging of thermal convection patterns.* Magnetic resonance imaging, 1996. **14**(3): p. 319-327.
195. Gibbs, S.J., T.A. Carpenter, and L.D. Hall, *Magnetic Resonance Imaging of Thermal Convection.* Journal of Magnetic Resonance, Series A, 1993. **105**(2): p. 209-214.
196. Borońska, K. and L.S. Tuckerman, *Extreme multiplicity in cylindrical Rayleigh-Bénard convection. I. Time dependence and oscillations.* Physical Review E, 2010. **81**(3): p. 036320.
197. Borońska, K. and L.S. Tuckerman, *Extreme multiplicity in cylindrical Rayleigh-Bénard convection. II. Bifurcation diagram and symmetry classification.* Physical Review E, 2010. **81**(3): p. 036321.
198. Ma, D.-J., D.-J. Sun, and X.-Y. Yin, *Multiplicity of steady states in cylindrical Rayleigh-Bénard convection.* Physical Review E, 2006. **74**(3): p. 037302.

199. Touihri, R., H. Ben Hadid, and D. Henry, *On the onset of convective instabilities in cylindrical cavities heated from below. I. Pure thermal case.* Physics of Fluids, 1999. **11**(8): p. 2078-2088.
200. Stringano, G. and R. Verzicco, *Mean flow structure in thermal convection in a cylindrical cell of aspect ratio one half.* Journal of Fluid Mechanics, 2006. **548**: p. 1-16.
201. Crespo del Arco, E. and P. Bontoux, *Numerical solution and analysis of asymmetric convention in a vertical cylinder: An effect of Prandtl number.* Physics of Fluids A: Fluid Dynamics, 1989. **1**(8): p. 1348-1359.
202. Yu, J., et al., *Onset of Rayleigh-Bénard convection for intermediate aspect ratio cylindrical containers.* Physics of Fluids, 2017. **29**(2): p. 024107.
203. Stevens, R.J., H.J. Clercx, and D. Lohse, *Effect of plumes on measuring the large scale circulation in turbulent Rayleigh-Bénard convection.* Physics of fluids, 2011. **23**(9): p. 095110.
204. Xi, H.-D. and K.-Q. Xia, *Flow mode transitions in turbulent thermal convection.* Physics of Fluids, 2008. **20**(5): p. 055104.
205. Manz, B., P. Alexander, and L. Gladden, *Correlations between dispersion and structure in porous media probed by nuclear magnetic resonance.* Physics of Fluids, 1999. **11**(2): p. 259-267.
206. Kimmich, R., A. Klemm, and M. Weber, *Flow, diffusion, and thermal convection in percolation clusters: NMR experiments and numerical FEM/FVM simulations.* Magnetic resonance imaging, 2001. **19**(3-4): p. 353-361.
207. Callaghan, P., et al., *Earth's field NMR in Antarctica: a pulsed gradient spin echo NMR study of restricted diffusion in sea ice.* Journal of Magnetic Resonance, 1998. **133**(1): p. 148-154.
208. Onuki, A., *Phase transition dynamics*. 2002: Cambridge University Press.
209. Stanley, H., *Introduction to Phase Transitions and Critical Phenomena Oxford Univ.* Press, New York, 1987.
210. Reverchon, E. and I. De Marco, *Supercritical fluid extraction and fractionation of natural matter.* The Journal of Supercritical Fluids, 2006. **38**(2): p. 146-166.
211. Cocero, M.J., *Supercritical water processes: Future prospects.* The Journal of Supercritical Fluids, 2018. **134**: p. 124-132.
212. Irwin, L. and Y. Le Moullec, *Turbines can use CO2 to cut CO2.* Science, 2017. **356**(6340): p. 805-806.
213. Trevisan, S., R. Guédez, and B. Laumert. *Supercritical CO2 Brayton Power Cycle for CSP With Packed Bed TES Integration and Cost Benchmark Evaluation*. in *ASME Power Conference*. 2019. American Society of Mechanical Engineers.
214. Wang, Y., et al., *Thermal performance analysis of fin-and-tube heat exchanger circuit in supercritical hydrogen refrigeration cycle system.* International Journal of Hydrogen Energy, 2019. **44**(56): p. 29765-29775.
215. Johnson, E., et al., *Thermal energy storage with supercritical carbon dioxide in a packed bed: Modeling charge-discharge cycles.* The Journal of Supercritical Fluids, 2018. **137**: p. 57-65.
216. Haberbusch, M.S., et al. *Thermoacoustic Duplex Technology for Cooling and Powering a Venus Lander*. in *12th International Energy Conversion Engineering Conference*. 2014.
217. Carlès, P., *A brief review of the thermophysical properties of supercritical fluids.* The Journal of Supercritical Fluids, 2010. **53**(1-3): p. 2-11.
218. Zappoli, B., D. Beysens, and Y. Garrabos, *Heat transfers and related effects in supercritical fluids*. Vol. 108. 2015: Springer.
219. Forster, D., *Hydrodynamic fluctuations, broken symmetry, and correlation functions*. 2018: CRC Press.
220. Amiroudine, S. and B. Zappoli, *Piston-Effect-Induced Thermal Oscillations at the Rayleigh-Bénard Threshold in Supercritical H e 3.* Physical review letters, 2003. **90**(10): p. 105303.
221. Codd, S. and S. Altobelli, *A PGSE study of propane gas flow through model porous bead packs.* Journal of Magnetic Resonance, 2003. **163**(1): p. 16-22.

222. Rassi, E.M., S.L. Codd, and J.D. Seymour, *MR measurement of critical phase transition dynamics and supercritical fluid dynamics in capillary and porous media flow.* Journal of Magnetic Resonance, 2012. **214**: p. 309-314.
223. Wlodarczyk, W., et al., *Comparison of four magnetic resonance methods for mapping small temperature changes.* Physics in Medicine & Biology, 1999. **44**(2): p. 607.
224. Poorter, J.D., *Noninvasive MRI thermometry with the proton resonance frequency method: study of susceptibility effects.* Magnetic resonance in medicine, 1995. **34**(3): p. 359-367.
225. Hindman, J., *Proton resonance shift of water in the gas and liquid states.* The Journal of Chemical Physics, 1966. **44**(12): p. 4582-4592.
226. Mitchell, J., M. Hürlimann, and E. Fordham, *A rapid measurement of T1/T2: the DECPMG sequence.* Journal of Magnetic Resonance, 2009. **200**(2): p. 198-206.
227. II′ yasov, K.A. and J.H. Prof, *Single-shot diffusion-weighted RARE sequence: Application for temperature monitoring during hyperthermia session.* Journal of Magnetic Resonance Imaging, 1998. **8**(6): p. 1296-1305.
228. Matthew S. Skuntz, S.L.C., Ryan Anderson, Joseph D. Seymour, *Quantitative T2 MR imagingMulti-EchoT2 Thermometry of Micro-encapsualted Wax Particles.* Applied Magnetic Resonance, 2021.
229. Achenbach, E., *Heat and flow characteristics of packed beds.* Experimental Thermal and Fluid Science, 1993. **7**(2): p. 129.
230. Skuntz, M.E., et al., *Axial variability of pattern formation in Rayleigh-Bénard convection: MRI velocimetry in a low aspect ratio cylinder.* International Communications in Heat and Mass Transfer, 2020. **118**: p. 104869.
231. Marcone, M.F., et al., *Diverse food-based applications of nuclear magnetic resonance (NMR) technology.* Food Research International, 2013. **51**(2): p. 729-747.
232. Kuballa, T., et al., *Application of NMR for authentication of honey, beer and spices.* Current Opinion in Food Science, 2018. **19**: p. 57-62.
233. Edzes, H.T., D. Van Dusschoten, and H. Van As, *Quantitative T 2 imaging of plant tissues by means of multi-echo MRI microscopy.* Magnetic resonance imaging, 1998. **16**(2): p. 185-196.
234. MacKay, A.L. and C. Laule, *Magnetic resonance of myelin water: an in vivo marker for myelin.* Brain Plasticity, 2016. **2**(1): p. 71-91.
235. Callaghan, P.T., et al., *Diffraction-like effects in NMR diffusion studies of fluids in porous solids.* Nature, 1991. **351**(6326): p. 467.
236. Edzes, H.T., D. Van Dusschoten, and H. Van As, *Quantitative T2 imaging of plant tissues by means of multi-echo MRI microscopy.* Magnetic resonance imaging, 1998. **16**(2): p. 185-196.
237. Loskutov, V. and S. Zhakov, *Dependence of the liquid transverse relaxation time T2 in porous media on fluid flow velocity.* International Journal of Heat and Mass Transfer, 2016. **101**: p. 692-698.
238. Fenrich, F., C. Beaulieu, and P. Allen, *Relaxation times and microstructures.* NMR in Biomedicine: An International Journal Devoted to the Development and Application of Magnetic Resonance In Vivo, 2001. **14**(2): p. 133-139.
239. Whittall, K.P., et al., *In vivo measurement of T2 distributions and water contents in normal human brain.* Magnetic resonance in medicine, 1997. **37**(1): p. 34-43.
240. Vavasour, I.M., et al., *A comparison between magnetization transfer ratios and myelin water percentages in normals and multiple sclerosis patients.* Magnetic resonance in medicine, 1998. **40**(5): p. 763-768.
241. Williamson, N.H., et al., *Magnetic resonance measurements of cellular and sub-cellular membrane structures in live and fixed neural tissue.* Elife, 2019. **8**: p. e51101.
242. Lewis, M.A., R.M. Staruch, and R. Chopra, *Thermometry and ablation monitoring with ultrasound.* International Journal of Hyperthermia, 2015. **31**(2): p. 163-181.

243. Brandl, M. and A. Haase, *Molecular diffusion in NMR microscopy.* Journal of Magnetic Resonance, Series B, 1994. **103**(2): p. 162-167.
244. Seland, J.G., et al., *Correlations between diffusion, internal magnetic field gradients, and transverse relaxation in porous systems containing oil and water.* Physical Review E, 2004. **70**(5): p. 051305.

APPENDIX A

HIGH PRESSURE VESSEL DESIGN FOR NATURAL CONVECTION EXPERIMENTS IN A SUPER-WIDE-BORE MAGNET

Background

Experimentation is often limited by the tools available. This is especially true in high-field NMR spectrometer where space and allowable materials are highly restricted. These limitations are the reason there are many valuable NMR measurement and applications yet to be realized. This report details the development of a high pressure, temperature controlled vessel which will allow high precision experimental studies on Rayleigh-Bénard and porous media convection, areas ripe for pioneering NMR experiments. Previous natural convection studies performed by our group relied on a vessel designed for pressure driven flow, which had thick PEEK plastic at the top and bottom boundaries. The poor thermal conductivity of the material caused undesirable temperature variations at those boundaries and prevented temperature from being measured accurately. Other groups have developed methods for studying RBC and PMC in NMR spectrometers but the published studies have been limited to liquid convection. Interest from NASA in porous media heat transfer of super- and near- critical fluids provided the means to design a system specifically for the study of gas, near-, and super-critical Rayleigh-Bénard and porous media natural convection flows. The main design aims for this vessel included: accurate, homogeneous temperatures at the top and bottom boundaries; a maximum applied temperature differential of 70^{o}C; investigation of multiple aspect ratios; pressures up to 7 MPa; compatibility with Bruker Avance III super-wide-bore (SWB) NMR spectrometer.

Pressure vessels have been used in NMR spectrometers for decades. Primarily, they are constructed of either thick walled glass or plastic, are used for spectroscopy, have small diameters, and contain small volumes. The most popular design is a 5 mm diameter hole drilled into a PEEK cylinder. Threads are machined into the exterior of this cylinder, and a cap attached

to a pressurized line is screwed on. A larger version of this design was used for our first pressure vessel (with hole in bottom for pressure-driven flow experiments), shown in Fig. A.1. The large outer diameter of the vessel prevented it from being fully lowered into the RF coil, limiting imaging to the bottom 60 mm. The design had a fixed aspect ratio and did not have a means for controlling boundary temperature, both of these issues are addressed in the new design.



Fig. A.1. Previous PEEK Pressure vessel with external threads.

Size and material choices are highly constrained in spectrometer experiments. PEEK plastic, aluminum (6061-T6) and austenitic stainless steel (e.g. 304, 316) were selected to be the primary materials for their high magnetic permeability. PEEK plastic has been widely used in NMR studies for its favorable magnetic, mechanical, machining, and thermal resistance properties. Aluminum and stainless steel are also used in probe construction and have suitable relative magnetic permeability's of 1.000022 and 1.003, respectively, near that of free space. However, our intended use of aluminum within the RF coil is unusual. In preliminary experiments, performed with the Avance III spectrometer in wide-bore configuration and a

micro2.5 probe, proved that an aluminum plate could be lowered 5 mm into the RF coil with minimal disruption to NMR imaging. SNR is not dramatically effected until the aluminum is more than 10 mm into the coil. Aluminum was found to be the best option for the interface between the heat transfer fluid and the RBC chamber due to its combination of high thermal conductivity, machinability and cost.

Designing the vessel for use with the SWB configured spectrometer provided the most space for temperature control fluid hookups and instrumentation. The SWB RF coils have interior diameters (ID) of 60-66 mm in diameter and a new dual-tune RF coil (ID 66 mm) was manufactured by Bruker for use with this pressure vessel. The new coil allows both ^{1}H and ^{19}F nuclei to be imaged. For the pressure vessel an OD of 58 mm was chosen to ensure fit in any SWB probe, allowing expansion due to thermal effects and internal pressure. The gap also allows for ease of height adjustment, and improved thermal isolation from the spectrometer. The length of the vessel will vary depending on the aspect ratio studied at 2, 3, and 5 times the interior diameter. The aspect ratios ½ and 1/3 have been investigated often numerically and via other experimental techniques (PID, multi-temperature probe), which will allow for direct comparison.

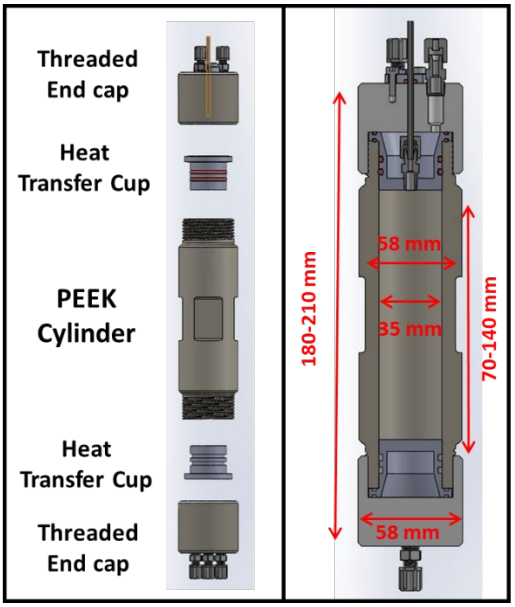


Fig. A.2. Exploded pressure vessel assembly at left and collapsed assembly with dimensions at right.

The ability to observed different aspect ratios was a primary goal of the design and this was accomplished by designing the parts to be modular. In accordance to this, the vessel was broken into three parts: a top cap which could be heated or cooled; a central cylindrical body to be constructed from PEEK which could be replaced with cylinders of different aspect ratios; and bottom endcap with temperature control. Two methods of attaching these parts were primarily considered. External threads similar to the previous design or six equally spaced bolts anchored to holes tapped in the PEEK cylinder. The exterior thread design has been employed many times in small diameter devices as well as large diameter devices such as Behr's NMR compatible 'autoclave.' The bolted connection has been successfully employed by Horch *et al.* in an NMR compatible autoclave designed to be pressurized to 30 MPa. It used six M4 bolts, 30 mm long, tapped into walls 10 mm thick. The vessel had an OD of 40 mm. The bolted connection was first pursued as it was assumed it could provide a larger interior diameter. However, the smaller

thread surface area in shear resulted in higher stress on the interior PEEK threads. In addition, the mismatch in thermal expansion of PEEK vs metals led to a decrease in thread overlap, and preload with heating. This weakens the joint with elevated temperatures, and made worse by PEEK's strength's inverse relation with temperature. For these reasons the exterior thread design was chosen. This joint provides a greater shear area, keeping stresses lower, has no thermal expansion induced loss of strength, is easier to assemble, and provides more room for instrumentation on the end caps.

Different methods of temperature control were considered, including resistance wires, and fluid channels cut into an aluminum block. Previous studies in low field systems have used resistance wires for heating. This necessitated heating through acoustic amplifiers so AC frequency could be set away from NMR frequency. Heating and cooling is most often achieved using a fluid system, and this is the solution employed here. A turbulent mixing chamber is both simple and minimized aluminum mass. This system does not interfere with NMR measurement and uses readily available equipment.

A detailed description of the design, the stress analysis of individual parts, thermal effects, and O-rings sizing are presented in the following sections. A discussion on the heating and instrumentation systems as well as a timeline of expected experimentation is also included.

Design

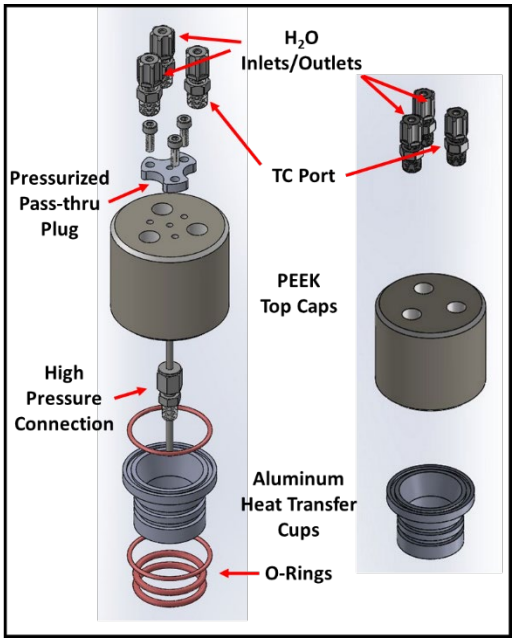


Fig. A.3. Detailed view of top (left) and bottom (right) pressure vessel assembles.

The final design is composed of a hollow, central PEEK cylinder with thread cut into the exterior at the top and bottom (see Fig. A.2). The threaded end caps clamp flanged aluminum cups as shown in Fig. A.3. The aluminum cups divides the heat transfer fluid from the central chamber, where the fluid instability of interest occurs. The temperature of the outer can be set between 10 and 70°C. The top boundary temperature can be measured via a thermocouple inserted into the heat transfer fluid mixing chamber through the top cap. Both heat flux and temperature can be measured at the bottom boundary through an encapsulated thermopile fixed on the temperature control side of the aluminum cup. The design is modular to allow central cylinders of different aspect ratios (d/L) to be used with the same end caps. The heat caps are composed the flanged aluminum cup that seats inside of the PEEK cylinder and the PEEK end cap which is screwed onto the cylinder. The aluminum cup has four glands for O-rings. Two on the vertical walls of the cup which provide the main seal for the pressurized chamber. The other two are on opposing sides of the flange providing a seal for the heating fluid chamber and a

back-up seal for the pressurized chamber. The top and bottom PEEK plates have three tapped holes for 1/8 NPT threads, which allow attachment of quick-connect fittings for heat transfer fluid inlet/outlet and a thermocouple (or heat flux meter) access. The top cap has four additional holes, one for the pressurized line to pass through and the others to secure the sealing plate which compresses an O-ring around the pressurized line to prevent water leakage.

PEEK Cylinder Stress Analysis

The entire vessel has been designed based on guidance from *Roark's Formulas for Stress and Strain*, *Shigley's Mechanical Engineering Design*, and a number of papers. Safety was a top priority due to the high cost of failure, and intended use with pressurized gas/supercritical fluids. All safety factors were kept greater than three and extra O-rings were added to minimize risk of leakage. The pressure vessel is designed to operate at pressures up to 7 MPa and temperatures up to 70ºC. The tensile strength of PEEK is known to decrease with temperature from 90-100 MPa at 23ºC down to 65 MPa at 100ºC. All safety factors are reported based on this temperature reduced value. Creep is an additional concern in PEEK at elevated temperatures. However, by keeping the strain low, ~0.1-0.3%, creep is negligible. To keep the strain below the 0.3%, stress must remain below 25 MPa.

In most pressure vessels the highest stress concentration is at the interface of the cylinder wall and cap. In this case the cap of the pressure vessel is isolated from the cylinder walls, removing this stress zone there. The highest stress in the cylinder will occur at the threads where the wall is thinnest, and there is the potential for both hoop stress from the internal pressure and shear stress from the end cap.

As the thickness of the cylinder walls will be greater than 1/10 the inner radius of curvature wall stresses are appropriate instead of the simpler membrane stresses used in thin-walled vessels. This means there are three non-negligible principle stresses, the longitudinal stress σ_1, hoop stress σ_2, and radial stress σ_3 (which will vary in the radial direction) all defined as:

$$\sigma_1 = \frac{qb^2}{(a^2-b^2)}, \qquad \sigma_2 = \frac{qb^2(a^2+r^2)}{r^2(a^2-b^2)}, \qquad \sigma_3 = \frac{-qb^2(a^2-r^2)}{r^2(a^2-b^2)} \qquad \textit{Eq. 161}$$

where q is the internal pressure, a the outer radius, and b the inner radius. The maximum stresses will be at $r = b$, and calculated as,

$$\sigma_{2,max} = q\frac{(a^2+b^2)}{(a^2-b^2)}, \qquad \sigma_{3,max} = -q \qquad \textit{Eq. 162}$$

By far the greatest stress is the hoop stress. The hoop stress equation can be rearranged to solve for inner diameter to provide an estimate for the minimum required thickness for a chosen outer diameter (which is a limiting factor in our design). Using the temperature-reduced PEEK strength of 65 MPa, the thinnest vessel allowable wall would be 3 mm. However, we want to keep the stress below 25 MPa to eliminate the worry of creep. A wall thickness of 7.5 mm provided a stress of 20.5 MPa and a still acceptable stress of 24 MPa in the threaded areas. This provided an interior diameter of 35 mm. Stress analysis followed the guidelines in *Roark's Formulas for Stress and Strain* and are detailed in the Appendix.

A complete CAD model of the pressure vessel assembly was created in SolidWorks and a stress analysis simulation was performed on each individual part. These results were compared to our hand calculations to give us confidence in the complete analysis. The results for the cylinder are shown in Fig. A.4. The internal pressure was applied to the entire cylinder which would only occur if the O-rings fail. The material stress is shown at the left. The maximum of 20 MPa in the

walls matches our hand calculations. The displacement in the *x* direction is shown in the right figure; a maximum of 0.1 mm occurs due to the internal pressure. The lateral expansion is most relevant as it will increase the gap between the inner cup and outer cylinder. This gap must remain below 0.45 mm to prevent the O-rings from extruding, which increases the potential for leakage and decreases O-ring life.

Thread Stress Analysis

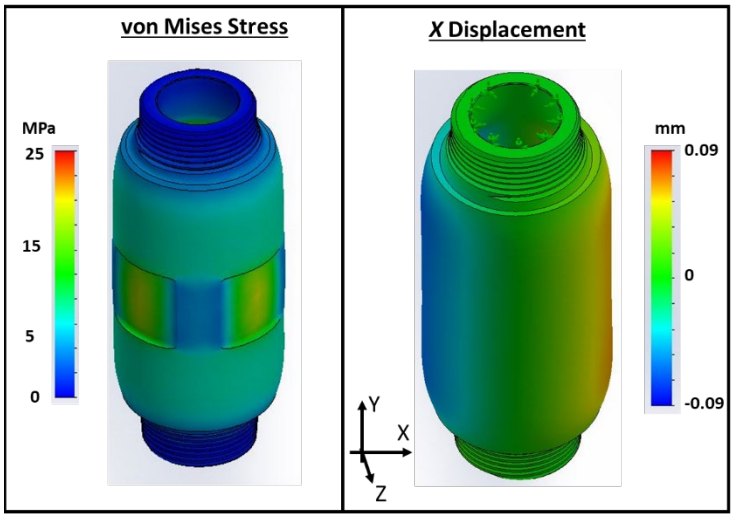


Fig. A.4. SolidWorks simulation results for stress (left) and displacements (right) of the PEEK cylinder walls under 7 MPa internal pressure.

The top and bottom heat caps are attached to the cylindrical body by M50x3 threads cut into the exterior of the cylinder. The threads have a pitch of 3 mm, are cut with a 60^{o} aperture, and have a depth of 1.27. The shear area can be found by multiplying the pitch diameter by the thread thickness there for a result of 226 mm^2/thread. When the internal pressure is 7 MPa, the force on the upper plate is 6.74 kN. Dividing this by the shear area yields a stress of 10 MPa if there are three engaged threads. This results in a safety factor against yielding of 6.5. The threads were also modeled in SolidWorks, however the results were not entirely as expected. It is

suspected that this was due to the method of applying fixtures and forces and was not an accurate representation. It was revealed that there are some asymmetric reactions due to the pitch of the threads. This torque will be countered by the aluminum cup which will reduce the overall displacement.

Heat Cap Stress Analysis

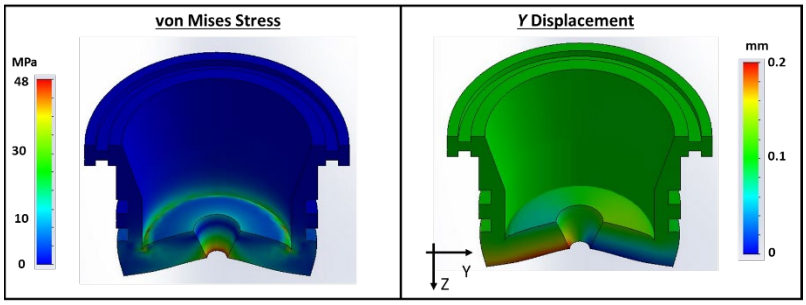


Fig. A.5. SolidWorks simulation results for the top and bottom aluminum heat transfer cups. Left column shows stresses and right displacements.

The two parts of the heat caps are both important to the structural integrity of the pressure vessel. The metal cup through which heat is transferred to the central fluid must resist the full pressure. The metal cup houses the O-ring glands, which seal the pressurized fluid. Distortion of these glands must not increase the gap size to the point where the O-ring extrudes plastically (see thermal effects section). The bottom plate of the cup experiences bending forces while its sides (up to the O-ring glands) experience compressive forces. The point of highest stress concentration will be on the interior wall at the joint of these two faces. The first O-ring was positioned below the turbulent mixing chamber to limit the stress at the junction of the inner wall and flat bottom. Again from Roark's, $\sigma_{2,max} = \frac{-q2a^2}{a^2-b^2}$ which yields an expected wall stress of 65 MPa. Higher stresses are expected at discontinuity points. SolidWorks simulation results shown

at left match these expected values well. Maximum stress is 48 MPa for the two parts. This is below the yield stress of Aluminum 6061-T6, with a safety factor of 2.75. Displacements near the O-rings are an acceptably small 0.04 mm.

Thermal Effects

Heating and cooling of the pressure vessel will cause changes to part dimensions and thermal stresses to develop. PEEK expands at roughly twice the rate of aluminum (5 e-5 vs 2.36 e -5 m/m-^{o}C). The relative expansion rates indicate the gap between the PEEK cylinder and Al cup will increase in size with heating from 0.1 mm to 0.25 mm. The gap is additionally expanded due to fluid pressure by approximately 0.1 mm for a total gap size 0.35 mm. This is within the acceptable limits for an O-ring with back-up O-ring of Hardness Shore 75 up to a pressure of 10.5 MPa (Parker Figure 3-2).

No thermal stresses are expected to develop at the threaded joint as the internal and external threads are made from the same material. The compressive forces on the aluminum flange will decrease. Expansion of joints and thermal expansion driven stresses are within acceptable limits.

Pressure Vessel Sealing

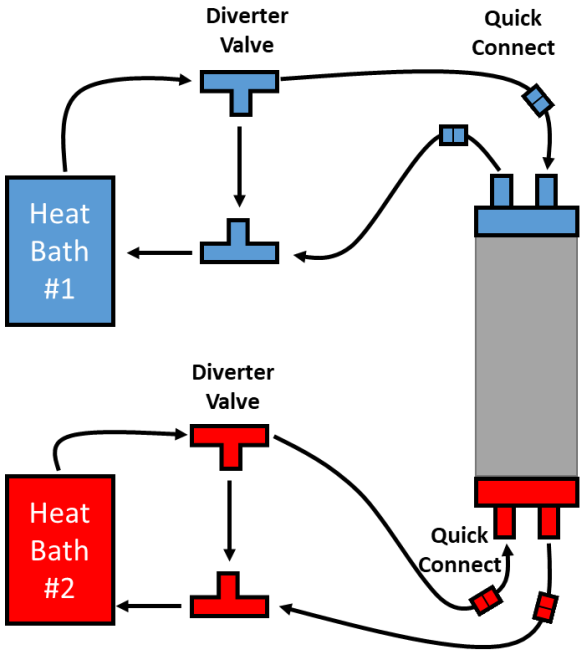
O-Ring Selection

The vessel will be sealed with four O-rings, two opposing O-rings positioned on the heat transfer cup flange and two O-rings seated in glands on a vertical portion of the aluminum heat transfer cup. The Parker O-ring manual was used to select appropriate O-ring and gland sizes (manual section IV) as well as acceptable tolerances for fit. According to the manual,

temperature and chemical resistance to the sealed fluid are the most important considerations for base polymer selection. Vitron fluorocarbon rubber was selected for having satisfactory compatibility with fluorinated oils, water and silicone oils as well as fair compatibility with Hexafluoroethane. The O-rings located on the flange are 2 mm in diameter, 37.5 mm ID, on vertical walls of cup 3 mm diameter and ID of 30 mm, and for sealing the high pressure pass through line a 2mm square O-ring with 3 mm ID.

Flow Loop

Top and bottom boundary temperatures are controlled by water pumped through the mixing chambers. Each of the flow loops have incorporates a diverter valve allows the heat transfer fluid to bypass the pressure vessel. This allows the heater/chiller to reach temperature before being directed to the pressure vessel boundaries. Fig. A.5 is a schematic of the hot and cold flow loops with parts lists. Rigid stainless 1/8” thermocouples can be inserted into the heating chambers via compression fittings. A heat flux sensor (FluxTeq) can also be attached in a similar way. Half inch, clear PVC tubing is used for the majority of the flow loop length, reducing to ¼ polyethylene tubing for the last couple feet. This decreases the pressure drop in the loop, allowing for higher flow rates, and better thermal transport. Tubes are wrapped in rubber foam insulation to prevent excessive heat loss.



Parts List – Heat Loops

- Cole-Palmer Chiller
- Fischer Scientific Heat Bath
- ½" PVC Clear tubing [Mcmstr] ~30'
- ¼" Polyethylene Tubing [Mcmstr 5181K24] ~15'
- 3/8" npt Diverter valve [Mcmstr 46095K43] (2)
- Quick Disconnect Fitting [Mcmstr 5012K125] (4)
- ½" barb to ¼" npt female plastic [mcstr 5372K181] (4)
- ½" Barbed to 3/8" npt Brass Fitting (mcstr 5346K23] (6)
- 3/8" npt PVC Tee (2)
- ½" barb to 3/8 npt PVC [mcstr 53055K218] (6)
- ¼" Tube Compression Fitting Plastic (mcstr 5694T11] (6)

Parts List – Vessel

- 2.5" dia x 12" PEEK Cylinder [Mcmstr 8503K88]
- 2 5/8" dia x 12" 6061-T6 Al Cylinder [Mcmstr 8974K53]

Instrumentation

- National Instruments DAQ
- FluxTeq PHFS-OEMe Heat flux meter
- Omega Thermocouple

Fig. A.6 Flow diagram for heat and cooling top and bottom boundaries of the interior chamber

Bolt Stress Analysis :

Bolt Dimensions :

$d := 0.25 \cdot in$ $D1 := 1.5 \cdot d$

$D2 := a - b$

Must find stiffness of bolt and clamped members. This is done first using method of frustums outlind in Shigley's, then as suggested by Musto and Konkle:

Define thickness of clamped members

$t_{peek} := 15 \cdot mm$ $t_{washer} := 2.413 \cdot mm$ $t_{al} := 3.175 \cdot mm$

$t_{total} := t_{peek} + t_{al} + t_{washer}$

Stiffness of bolt: $A_{tbolt} := 0.0318 \cdot in^2$ $l_t := t_{total} + \frac{d}{2} = 0.024\,m$

$$k_{bolt} := \frac{A_{tbolt} \cdot E_{al}}{l_t} = 3.397 \times 10^5 \frac{lbf}{in}$$

Now stiffness of members using fixed pressure cone angle of 30deg

First frustum contains al washer and peek, stiffness of these two portions if found as: $t_{peek1} := 0.5 \cdot t_{total} - t_{washer}$

$$k_{wsher} := \frac{0.5774 \cdot \pi \cdot E_{al} \cdot d}{\ln\left[\frac{(1.155 \cdot t_{washer} + D1 - d) \cdot (D1 + d)}{(1.155 \cdot t_{washer} + D1 + d) \cdot (D1 - d)}\right]} \qquad k_{peek1} := \frac{0.5774 \cdot \pi \cdot E_{peek} \cdot d}{\ln\left[\frac{(1.155 \cdot t_{peek1} + D2 - d) \cdot (D2 + d)}{(1.155 \cdot t_{peek1} + D2 + d) \cdot (D2 - d)}\right]}$$

Second Frustum contains PEEK and aluminum: $t_{peek2} := 0.5 \cdot t_{total} - t_{al}$

$$k_{al} := \frac{0.5774 \cdot \pi \cdot E_{al} \cdot d}{\ln\left[\frac{(1.155 \cdot t_{al} + D2 - d) \cdot (D2 + d)}{(1.155 \cdot t_{al} + D2 + d) \cdot (D2 - d)}\right]} \qquad k_{peek2} := \frac{0.5774 \cdot \pi \cdot E_{al} \cdot d}{\ln\left[\frac{(1.155 \cdot t_{peek2} + D2 - d) \cdot (D2 + d)}{(1.155 \cdot t_{peek2} + D2 + d) \cdot (D2 - d)}\right]}$$

Total stiffness of members:

$$k_m := \left[\left(\frac{1}{k_{wsher}}\right) + \left(\frac{1}{k_{peek1}}\right) + \left(\frac{1}{k_{peek2}}\right) + \left(\frac{1}{k_{al}}\right)\right]^{-1} = 61.095\,m\,MPa$$

The stiffness constant of the joint, C: $C := \frac{k_{bolt}}{k_{bolt} + k_m} = 0.493$

This seems a bit low!

This can aslo be found using approach of Musto and Konkle

$t_{ls} := 15 \cdot mm \quad t_{ms} := 3.175 \cdot mm \qquad n := \frac{t_{ls}}{t_{ls} + t_{ms}} = 0.825$

$E_{eff} := \frac{1}{\left[\frac{1}{E_{al}} + n \cdot \left(\frac{1}{E_{peek}} - \frac{1}{E_{al}}\right)\right]} = 4.314 \times 10^3 \, MPa \qquad temp := \frac{d}{t_{ls} + t_{ms}} = 0.349$

$M := 0.968 \qquad B := 0.725$

M and B are constants taken from Musto and Konkle, 2006

$k_{musto} := E_{eff} \cdot d \cdot (temp \cdot M + B) = 1.663 \times 10^5 \, \frac{lbf}{in}$

$C_{musto} := \frac{k_{bolt}}{k_{bolt} + k_{musto}} = 0.671$

This value is more what I would expect, given the complexity of the frustum method i believe this value more

Now that the stiffness is known we must calulate the force on the bolt from the internal pressure of the vessel:

$Dia_{top} := 2 \cdot b = 35 \, mm \qquad A_{top} := \frac{\pi}{4} \cdot Dia_{top}^2 = 962.113 \, mm^2$

$F_{top} := q \cdot A_{top} = 6.735 \times 10^3 \, N \qquad F_{per_bolt} := \frac{F_{top}}{6} = 1.122 \times 10^3 \, N$

With this force we calculate the load on the bolt and members respectively, keeping in mind there must be enough preload to maintain some clamping force.

$F_{preload1} := 600 \cdot N$

$F_{bolt} := C \cdot F_{per_bolt} + F_{preload1} = 1.154 \times 10^3 \, N$

$F_{members} := (1 - C) \cdot F_{per_bolt} - F_{preload1} = -31.277 \, N$

Or using the C value from Musto Method:

$$F_{preload} := 500 \cdot N$$

$$F_{bmusto} := C_{musto} \cdot F_{per_bolt} + F_{preload} = 1.254 \times 10^{3}\,N$$

$$F_{mmusto} := \left(1 - C_{musto}\right) \cdot F_{per_bolt} - F_{preload} = -131.044\,N$$

Torques required to produce these preloads are:

$$T_1 := 0.2 \cdot d \cdot F_{preload1} = 0.762\,N \cdot m \qquad T_{musto} := 0.2 \cdot d \cdot F_{preload} = 0.635\,N \cdot m$$

We can now find the length of threads necessary to prevent thread stripping:

$$n := 20 \cdot \frac{1}{in} \ \frac{teeth}{in}$$

$k_{nmax} := 0.185 \cdot in$	max minor dia internal threads
$E_{smin} := 0.2127 \cdot in$	min pitch dia external threads
$E_{nmax} := 0.2164 \cdot in$	max pitch dia internal threads
$d_{smin} := 0.245 \cdot in$	min major dia external threads

$$L_e := \frac{2 \cdot A_{tbolt}}{k_{nmax} \cdot \pi \cdot \left[0.5 + 0.57735 \cdot n \cdot \left(E_{smin} - k_{nmax}\right)\right]} = 3.39\,mm$$

But this is for internal/external threads of the same strength, to compensate:

$$A_s := \pi \cdot n \cdot L_e \cdot k_{nmax} \cdot \left[\frac{1}{2 \cdot n} + 0.57735 \cdot \left(E_{smin} - k_{nmax}\right)\right] = 41.032\,mm^2$$

$$A_n := \pi \cdot n \cdot L_e \cdot d_{smin} \cdot \left[\frac{1}{2 \cdot n} + 0.57735 \cdot \left(d_{smin} - E_{nmax}\right)\right] = 55.029\,mm^2$$

$$j := \frac{A_s \cdot S_{al}}{A_n \cdot S_{peek}} = 2.983$$

$$L_{threads} := j \cdot L_e = 10.112\,mm$$

As a further check, we can estimate the average stress over the full internal thread area, and the stress in the first thread.

$$\sigma_{intnlThrds} := \frac{F_{bolt}}{A_n} = 20.966\,MPa$$

To look at the first thread we will find stress at root of thread, as this is where stripping will occur when bolt is stronger than tapped material.

$$A_{1thread} := \frac{\pi}{n} d_{smin} = 24.829\,mm^2 \qquad \sigma_{1stThread} := \frac{0.34 \cdot F_{bolt}}{A_{1thread}} = 15.799\,MPa$$

This is assuming 34% load taken by first thread, given ductility of PEEK first thread will probably take less of the load

Factor of Saftey's can be calculated for both the Aluminum bolt and PEEK threads:

For Aluminum:

$$FOS_{yieldAl} := \frac{S_{al} \cdot A_{tbolt}}{C_{musto} \cdot F_{bmusto} + F_{preload}} = 3.976$$

$$FOS_{loadAl} := \frac{S_{al} \cdot A_{tbolt} - F_{preload}}{C_{musto} \cdot F_{bmusto}} = 5.745$$

$$FOS_{seperation} := \frac{F_{preload}}{F_{bmusto} \cdot (1 - C_{musto})} = 1.214$$

For PEEK:

$$FOS_{yieldPeek} := \frac{S_{peek} \cdot A_n}{C_{musto} \cdot F_{bmusto} + F_{preload}} = 2.666$$

$$FOS_{loadPeek} := \frac{S_{peek} \cdot A_n - F_{preload}}{C_{musto} \cdot F_{bmusto}} = 3.656$$